UNIVERSITY OF Southampton

Faculty of Engineering and Physical Sciences
National Centre for Advanced Tribology
Engineering Materials

Phase and Dissipative Behaviour of Complex 2D Materials

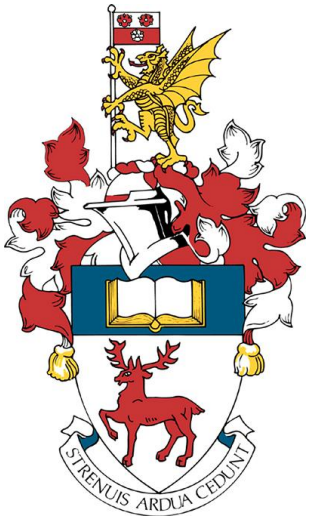

Supervisor: Prof. Denis Kramer

Co-supervisor: Prof. Tomàš Polcar

Author: Andrea Silva

University of Southampton

Faculty of Engineering and Physical Sciences
School of Engineering

Phase and Dissipative Behaviour of Complex 2D Materials

DOI: -pending-

by

Andrea Silva
MSc in Physics
ORCiD: 0000-0001-6699-8115

A thesis for the degree of
Doctor of Philosophy

January 12, 2021

University of Southampton

Abstract

Faculty of Engineering and Physical Sciences
School of Engineering

Doctor of Philosophy

Phase and Dissipative Behaviour of Complex 2D Materials

by Andrea Silva

Being a relatively new field, the vast chemical space spanned by two-dimensional materials has so far only seen limited exploitation to optimise properties. In the field of tribology, layered materials have been used for decades as solid lubricants, but the design of optimised surfaces for friction in a systematic way, which relies on a predictive model of friction that scales from the nanoscale up to micro/macro-scales, remained elusive. This thesis makes a step in exploring the chemical space and stacking possibilities of two-dimensional materials, informing experimental efforts to design tribological contacts. Moreover, it extends the fundamental understanding of lubrication mechanisms, on which the design of solid lubricants can be built.

The materials design aspects of this thesis focus on the phase behaviour of monolayers and the inter-layer phase stability of twisted heterostructures. A framework was developed to identify novel compounds obtained from substitutional alloys on transition metal sites in dichalcogenide crystals, yielding a road-map for experimental efforts. A generalised theory of epitaxy developed here rationalises the behaviour of heterostructures observed as a function of the twist angle introduced between the lattices.

To advance the fundamental understanding of solid lubrication, the dissipative behaviour of two-dimensional materials has been studied both in hetero- and homo-structures. Superlubric behaviour in large-mismatched heterostructures has been rationalised in terms of edge effects and identified as a promising road to robust superlubricity. A novel framework, based on the Prandtl-Tomlinson model and stochastic thermodynamics, allows evaluation of a set of thermodynamic quantities in homostructures, providing a clear picture of the dissipation in the system and a straightforward way to test the model against experiments.

In conclusion, the phase behaviour analysis shows that alloyed transition metal dichalcogenides offer many opportunities for material science research, thanks to the densely populated chemical space. Flexural phonons play an important role in the stability of misaligned heterostructures, with implications for novel twistronic devices. The analysis of tribological contacts highlights the importance of potential energy surface topology, in addition to simple energy barriers, and of edge effects in determining the dissipative behaviour of the system.

Contents

List of Figures

List of Tables

Abbreviations

AC	Amontons-Coulomb
AFM	Atomic Force Microscopy
APW	Augmented-plane waves
ATAT	Alloy Theory Automated Toolkit
BM	Birch-Murnaghan
BZ	Brillouin Zone
BL	Bi-layer
CE	Cluster Expansion
CF	Crystal Field
CoF	Coefficient of Friction
CoM	Centre of Mass
CV	Cross Validation
CVD	Chemical Vapour Deposition
DFT	Density Functional Theory
DOS	Density of States
ECI	Effective Cluster Interactions
EoS	Equation of State
F	Flexural
FF	Force Field
FFM	Frictional Force Microscopy
FK	Frenkel-Kontorova
G	Graphene
GGA	Generalized Gradient Approximation
GS	Ground State
HK	Hohenberg-Kohn
HRTEM	High-Resolution Transmission Electron Microscopy
JT	Jahn-Teller
KC	Kolmogorov-Crespi
KS	Kohn-Sham
L	Longitudinal
LDA	Local Density Approximation
LJ	Lennard-Jones
MD	Molecular Dynamics
ML	Mono-layer
MM	Molecular Mechanics
MP	Materials Project
NM	Novaco-McTague
PAW	Projector Augmented-plane Waves
PBC	Periodic Boundary Condition

PES	Potential Energy Surface
PP	Pseudo-potential
PT	Prandtl-Tomlinson
REBO	Reactive Empirical Bond Order
SCAN	Strongly Constrained and Appropriately Normed
STEM	Scanning Transmission Electron Microscopy
SW	Stilling-Weber
T	Transverse
TM	Transition Metal
TMD	Transition-metal dichalcogenide
VASP	Vienna *ab initio* Software Package

Declaration of Authorship

I declare that this thesis and the work presented in it is my own and has been generated by me as the result of my own original research.

I confirm that:

1. This work was done wholly or mainly while in candidature for a research degree at this University;
2. Where any part of this thesis has previously been submitted for a degree or any other qualification at this University or any other institution, this has been clearly stated;
3. Where I have consulted the published work of others, this is always clearly attributed;
4. Where I have quoted from the work of others, the source is always given. With the exception of such quotations, this thesis is entirely my own work;
5. I have acknowledged all main sources of help;
6. Where the thesis is based on work done by myself jointly with others, I have made clear exactly what was done by others and what I have contributed myself;
7. Parts of this work have been published as: Andrea Silva, Tomas Polcar, and Denis Kramer. Phase behaviour of (Ti:Mo) S2 binary alloys arising from electron-lattice coupling. *Computational Materials Science*, 186(July 2020):110044, 1 2021,Andrea Silva, Victor E. P. Claerbout, Tomas Polcar, Denis Kramer, and Paolo Nicolini. Exploring the Stability of Twisted van der Waals Heterostructures. *ACS Applied Materials & Interfaces*, 12(40):45214–45221, 10 2020

Signed:..... Date:.....

1

Introduction

Since the discovery of graphene [3], low-dimensional materials have gained significant attention from the scientific community. The reduced dimensionality of graphene compared to its well-known bulk counterpart, graphite, yields exciting and unexpected changes in the materials electronic and mechanical properties [3]. Shortly after, the same interest was sparked by atomically flat sheets of transition metal dichalcogenides (TMDs) [4]. Beyond the academic interest in this new and exotic polymorph, two-dimensional materials bring the prospect of significant technological advancement. As showcased in Fig. 1.1, reduced dimensionality is linked to properties sought after by engineers for real-life applications, like superior flexibility and strength [5] or enhanced thermal transport [6].

Two-dimensional materials are critical players in the technological effort towards miniaturisation that has accompanied human progress for ages. Fig. 1.2 sketches the progress of human technology with time and the progressive reduction of the typical length-scale, from macroscopic tools in the bronze age to microscopic transistors in the past century. Nowadays, technology advancement stands on a figurative edge, only a few nanometers wide, with progress towards atom-based technology in tribology [8], electronics [9], catalysis [10], and energy-storage [11]. Understanding the thermodynamics of low-dimensional materials and the laws of dissipation at the nanoscale scale is an essential step in advancing nanoscale engineering.

In the field of electronics, 2D materials promise to help engineers to achieve 'more-than-Moore' nanoelectronics [12]. Transistors can be built from atomically-thin sheets, as shown by Schwierz [13] for graphene and by Radisavljevic *et al.* [9] for MoS_2, sketched in Fig. 1.3a. With improvements of traditional Si-based transistors starting to deviate from the Moore's law (the number of transistors on a chip doubles about every 18 to 24

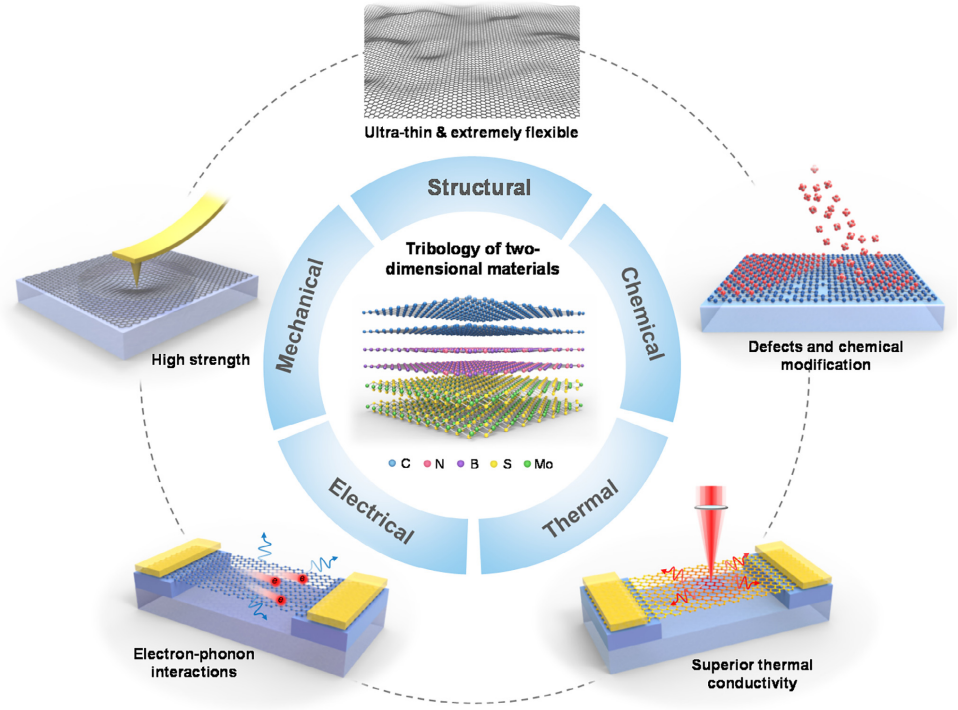

Figure 1.1: Showcase of enhanced properties of two-dimensional materials. Adapted from Ref. [7].

months [14]), the need for next-generation devices is growing stronger. Because of this need, the Graphene Flagship (the €1 billion European investment into 2D-materials-based technology) is supporting pilot projects to move graphene-based electronic devices from laboratory testing to industrial reality [15]. The main goal is a graphene-CMOS technology able to seamlessly integrate with existing electronics [12], like the processor prototype shown in Fig. 1.3b.

In the field of tribology, the study of friction, layered bulk phases of graphene and MoS_2 have been used in industrial applications for many decades [17]. Devices based on single layers have the potential to make superlubricity a reality. First introduced by Hirano in the early 90s [18], superlubricity is a state of sliding without dissipation that would eliminate dissipative energy leakage in tribological contact. The reliable realisation of

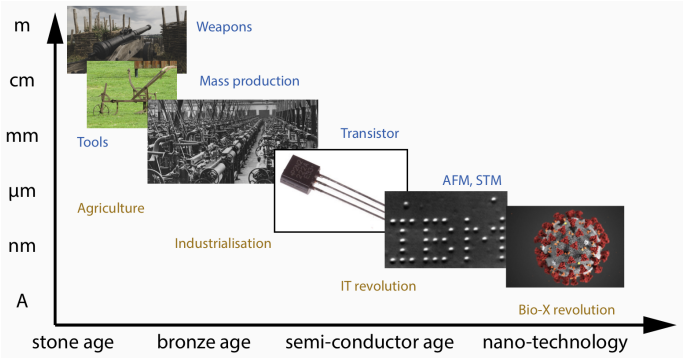

Figure 1.2: Length scales of human technologies throughout our history.

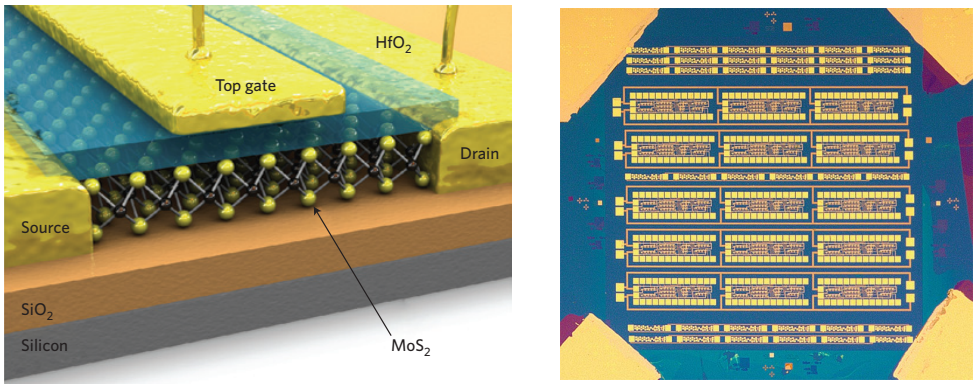

(a) (b)

Figure 1.3: (a) A sketch of a single-layer MoS_2 transistor. The MoS_2 layer is not in scale. Adapted from Ref. [16]. (b) A functional microprocessor comprising 115 integrated transistors based on atomically thin material. Adapted from Ref. [12].

this state has proven elusive, but micro-scale boron-nitride and graphene contact recently shown promising result [19].

The SOLUTION programme [20], of which this project is part, is a small-scale framework with a similar ambition to the Graphene Flagship in the field of tribology. The ultimate goal of the SOLUTION project is to advance the fundamental understanding of solid lubrication and to bring innovations closer to industrial applications. At the core of the project is a drive to familiarise a new generation of scientists with a cross-disciplinary attitude and promote collaboration between the research groups involved. Thus, this framework has encouraged, during this PhD, collaborations with other institutions and the synergy between multi-scale simulation techniques and experiments.

1.1 2D Materials

Following the discovery of graphene, the number of 2D material proposed by computational studies numbers in the thousands [21, 22], and dozens materials have been synthesised [23, 24]. The proposed 2D materials span the whole periodic table: they include more than 300 binary compounds and more than 700 ternary ones, with different crystal structures and electronic characteristics [21]. The chemical and structural complexity is expanded even further if one considers heterostructures: the strong intralayer covalent bond and weak van der Waals interlayer coupling make it relatively easy to manipulate 2D flakes and stack them with a high degree of control [25].

The stacking process can be decorated with a twisting angle between the crystal planes, introducing a novel continuous degree of freedom. This misalignment angle led Cao and coworkers [26] to the discovery of a novel superconductive phase in bilayer graphene when the two sheets are twisted at the *magic angle* of 1.1°, as shown in Fig. 1.4. Understanding the emergence of superconductivity in such a simple, carbon-only material promises to shed light on the origin of unconventional superconductivity observed in more complex high T_c cuprates [27, 28]. More generally, this rotational degree of freedom has led to

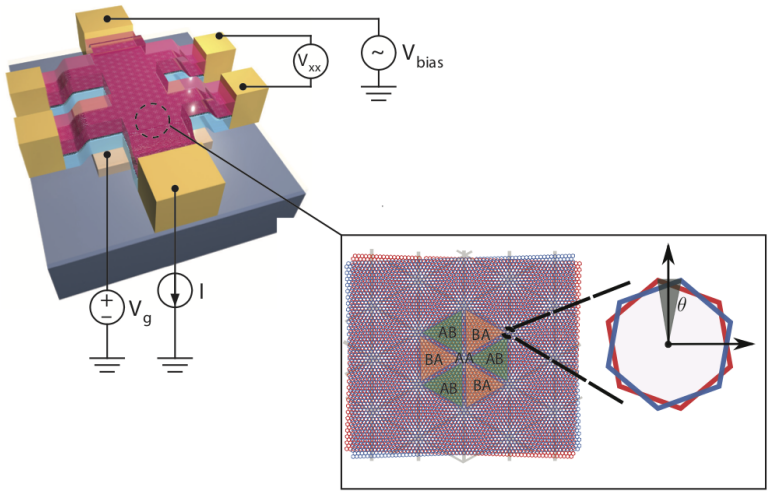

Figure 1.4: Sketch of the experimental setup of the superconducting twisted bilayer graphene, adapted from Ref. [26]. The inset is a snapshot of a simulation of the system showing different stacking regions, adapted from Ref. [27].

the flourishing field of *twistronics*, which aims to understand how to use this mismatch angle to tune electronic properties [29] and optical emission properties [30] of homo- and heterostructures.

Graphite and Graphene

Graphite is a layered material made solely from carbon atoms. The four carbon atoms per unit cell are trigonally (sp^2) bonded, resulting in the typical lamellar structure belonging to the hexagonal $P6_3/mmc$ space group [31]. The layers themselves are AB stacked, with one carbon atom in each layer sitting over a corresponding one in the neighbouring layer (full A and A' circles in Fig. 1.5) and the other carbon atom in each layer placed over the centres of the hexagons of the neighbouring layers (hollow B and B' circles in Fig. 1.5). In the other high-symmetry stacking, AA, both carbon atoms in each layer sit over their counterparts in the neighbouring layer; this stacking results in higher energy. Whereas the atoms within a layer are covalently bonded with a bond distance of 1.42 Å, van der Waals interactions between the layers lead to a layer spacing of 3.35 Å [31]. The unit cell of graphite contains four carbon atoms, has a planar lattice constant of $a = b = 2.46$ Å and a perpendicular lattice constant of $c = 6.71$ Å [31]. While the basal planes are chemically inert, edges show pronounced reactivity [31]. Graphene layers show armchair and zig-zag termination, with the former having a lower formation energy [32].

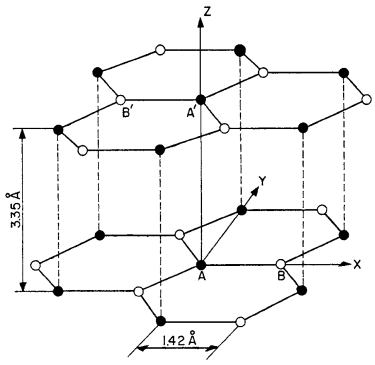

Figure 1.5: Crystal structure of graphite. Adapted from Ref. [31]

The discovery of graphene has led to a new chapter in the study of solid lubricants. Its mechanical strength, among the best (tensile strength of 130 GPa), prevents wear of both itself and the substrate, although the lifetime is reduced at higher loads and defects can affect the strength [33].

Transition Metal Dichalcogenides

The discovery of graphene and its dimensionality-dependent properties sent ripples through the scientific world [4]. Although graphene exhibits enormous potential, its chemical inertness is not always desired. The material science community quickly started searching for other atomically thin materials, leading to the discovery of transition metal dichalcogenide monolayers, which are more chemically versatile [4].

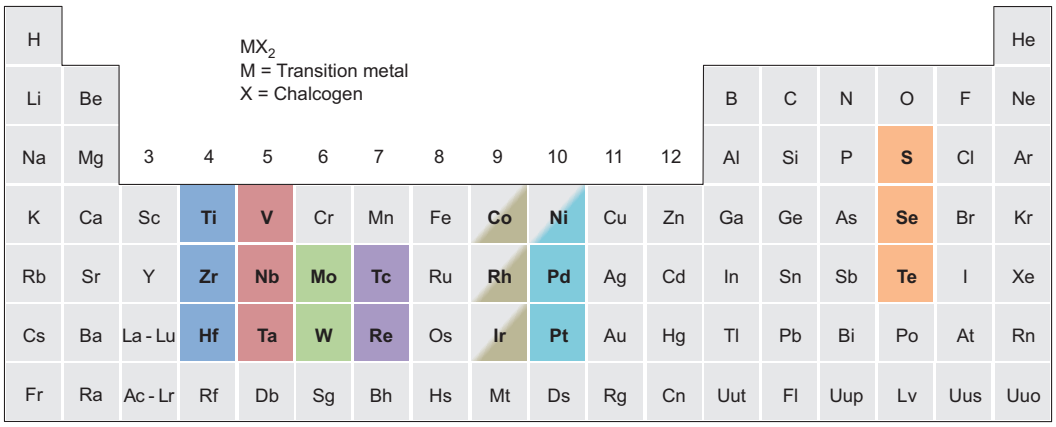

Figure 1.6: Atom species forming the TMDs family. The slots colour-code refers to different groups. Half-filled slots (Co, Rh, Ir and Ni) indicate that not all metal-dichalcogenides combinations form layered structures, e.g. NiS_2 crystallises in a pyrite structure while $NiTe_2$ is a layered compound. Adapted from Ref. [4]

Transition metal dichalcogenides (TMDs) are binary compounds with the general form MX_2, with M being a transition metal (TM) and X a chalcogenide. Fig. 1.6 reports the TMs found to crystallise in layered structures that closely resemble graphite. Two-dimensional sheets are formed by a metal layer sandwiched between two layers of chalcogenide atoms; covalent bonds between metal and chalcogenide atoms hold these monolayers together.

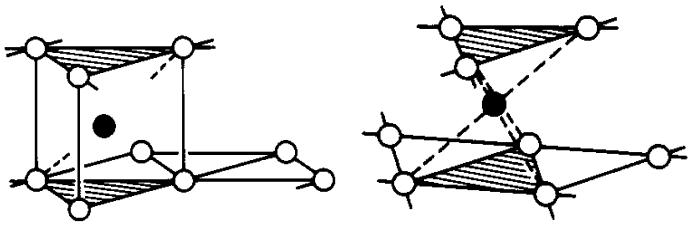

(a) Prismatic **(b)** Octahedral

Figure 1.7: Prismatic (a) and octahedral (b) coordination. Adapted from Ref. [34]

Figures 1.7a and 1.7b show two common coordinations within the mono-layers (MLs). Fig. 1.7a shows the prismatic coordination, where chalcogenide planes are oriented in the

same direction, and X atoms sit on top of each other. Fig. 1.7b shows the octahedral coordination, where chalcogenides planes are mutually rotated by 180°, leading to less steric hindrance between X atoms compared to the prismatic solution [34]. The layers can then organise themselves into many different polymorphs [35]. Fig. 1.8 reports the three most common stacking patterns found in the TMDs family: $1T$, $2H$ and $3R$, where the digit indicates the number of layers in the unit cell and the letter the symmetry [35]. The $1T$ polymorph, in Fig. 1.8a, is constructed by piling up layers with octahedral geometry. The TM sites are vertically aligned between layer, as shown in Fig. 1.8a. The stacking sequence is /AbC/AbC/, where the letter refers to a position in the cell; uppercase letters refer to chalcogen atoms, lowercase ones to metals. This results in a unit cell comprising three atoms and belonging to $P\bar{3}m1$ (or D^3_{3d}) layer group [35]. The $2H$ polymorph comprises of prismatic coordinated layers stacked with a 180° misalignment between them, as shown in Fig. 1.8b. The unit cell is composed of six atoms, and it belongs to the $P6_3/mmc$ (or D^4_{6h}) space group. The $2H$ is found in two variations: $2H_a$ (/AbA/CbC/), in which metal sites in one layer are on top of the metal sites in the next layer, and $2H_c$ (/CaC/AcA/), in which the metal site is located on top of the chalcogenides atom in the neighbouring layer (Fig. 1.8b) [35]. The $3R$ polymorph comprises prismatic layers stacked in the same orientation, yielding the three-ML unit cell shown in Fig. 1.8c.

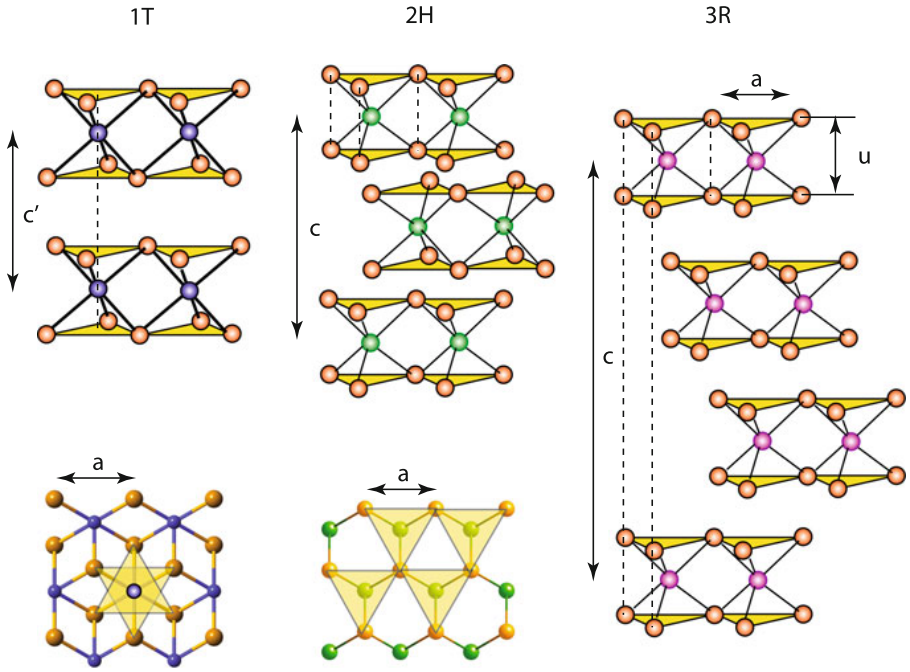

Figure 1.8: Side (upper row) and top (lower row) views of common stacking in the TMDs family. Adapted from Ref. [35]

While the sizeable bandgap of single-layer TMDs make them attractive for electronic applications [16], the interplay between the strong intra-layer covalent bonding and weak inter-layer van der Waals interaction is the key feature that makes TMDs excellent solid lubricants [36]. They have been widely used in those industrial applications where traditional oil lubrication is impossible, like space vehicles operating in vacuum, or when the

risk of contamination discourages the use of oils.

1.1.1 Phase Behaviour

This thesis will focus on an aspect of *first-principles* material design often neglected: are these materials with remarkable properties thermodynamically stable, and how feasible it is to synthesise them? Can one develop a protocol and a deeper understanding of structural changes and electronic effect determining stability in heterostructures and multi-component ML systems? The description of the thermodynamics of a multi-component crystalline material is a formidably difficult task. One crucial aspect is the complexity of the configurational space of these materials, i.e. the combinatorial problem of describing the energetics of different orderings of components within a given crystal. In order to address this problem, a multi-scale approach is needed: knowledge is transferred from lower, more advanced level approximation to simpler higher-level models, where some degrees of freedom are averaged out. This approach allows building a consistent description of processes happening on different scales.

Strong anisotropy of two-dimensional materials leads to a decoupling of properties between in-plane and out-of-plane directions. Thus, phase stability shows different behaviour in these two directions, as outlined in the following.

Intralayer aspects of TM substitution Strong in-plane bonding leans towards tailoring of properties by chemical substitution of elements in the parent lattice. Alloy and doping are helpful tools to tailor material properties for specific applications, like adjusting the bandgap of 2D transistors [37] or creating magnetic materials suitable for spintronic devices [38]. In tribology, experiments have found that mixing transition metals in low-friction coatings may lead to an improvement in hardness and density, yielding better performance [39].

Designing improved materials at an experimental level is often a costly trial-and-error process. Layered materials are no exception: the space of possible chemical compounds for pristine materials is already vast, adding doping possibilities and heterostructure stacking makes it practically impossible for experimentalists to explore even a fraction of it. In this scenario, input from theoretical studies identifying viable candidates and guiding synthesis efforts are absolutely necessary.

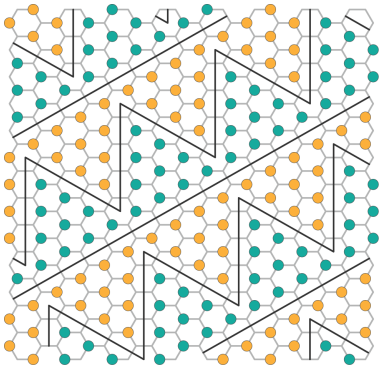

Figure 1.9: Ground-state ordering of Na ions between TiS_2 planes. Green and orange circles represent Na ions and vacancies within the honeycomb lattice formed by the interstitial spaces. Adapted from Ref. [40]

First-principles alloy theory is a well-established field in metals [41, 42, 43] correctly predicting the phase diagram of mixtures of two [44] and three [45] metals. In these mixtures, the key to correctly describing the stability of competing phases is to accurately describe the energy of different orderings of the ions on the lattice and to reliably estimate the entropic contributions, which arise primarily from occupational degrees of freedom on the parent lattice and vibrational effects [44]. Moreover, a modification of the alloy theory has been successfully applied to transition metal oxides [46] and intercalation compounds used in Li-ion batteries [40]. Only limited attempts to apply the same formalism to TMDs are reported in the literature. For example, Raffone *et al.* [37] analysed Sn-alloyed MoS_2 to stabilise the metallic 1T polymorph over the 2H stable configuration. The authors identify a dependence of the bandgap from the TM-site impurity concentration, devising a strategy to tune the electronic properties for tailored applications. In another example, Burton and Singh [47] studied substitution on the chalcogenide site and computed the finite-temperature phase diagram of the alloys $MoS_{2-2x}Te_{2x}$. The authors show an intriguing coexistence of incommensurate orderings up to 600 K before disordered structures are stabilised by entropy.

While no coherent knowledge of substitutional alloys in TMDs is found in literature, it is possible to adapt findings from oxides and metals, keeping in mind the different type of bonding occurring in this system. While in metal alloys interactions shaping the configurational landscape are defined mainly by the direct overlap of electron orbitals, the situation in chalcogenides is different due to the small size of the d orbitals of cations compared to distances between them in the anion framework. In compounds of the form $M_xN_{1-x}X_2$, M and N being transition metals, the covalent nature of bonds between metals and chalcogenides means interactions between metal cations in the sub-lattice is mainly mediated by the chalcogenide anion framework. Thus, the direct overlap of metal orbitals is expected to be less pronounced, albeit more than in oxides where marked electronegativity of oxygen anions results in more ionic bonds [46]. Charge localisation resulting from the covalent bonding, as opposite to delocalised metallic bonds, may result in electrostatic interaction, as found in some perovskite systems [48], and magnetic effects [38]. While these effects have a significant impact on the magnetic ground states in oxides [46], the effect on the formation energy of alloys is of second order. Due to the less localised bonds in chalcogenides compared to oxides, magnetic effects are expected to be less pronounced, although they cannot be ruled out [38, 21]. On the other hand, less stiff chalcogenide-metal bonds make them more prone to electron-lattice coupling effects, with anharmonic effects like Jahn-Teller distortions potentially playing an important role in stabilising orderings [49].

Interlayer The strong asymmetry in strength between intralayer and interlayer interactions in layered materials makes it possible to play LEGO® on the atomic scale, stacking different crystals on top of each other in heterostructures, as shown in Fig. 1.10. Different types of single layers can be mixed and matched to create new superstructures, termed

heterostructures [25, 50, 51, 52]. A key feature affecting the behaviour of multi-layered structures is the relative orientational mismatch between layers. While heterostructures are intrinsically incommensurate due to the different lattice constants of the parent layers, incommensurability can also arise in homostructrures due to relative misalignment of the single layers [53].

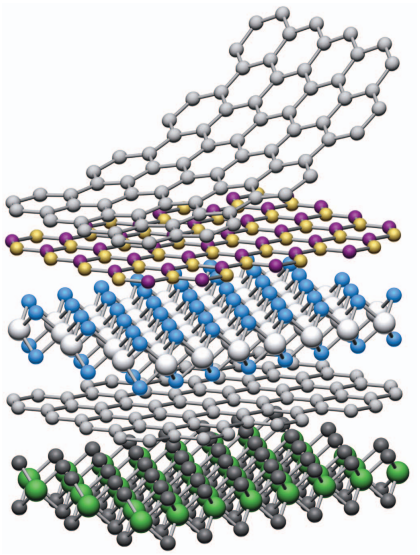

Figure 1.10: Atomic scale LEGO® with 2D materials heterostructures, adapted from Ref. [25]

The relative mismatch between layers, both for homo- and heterostructures, has been related to a range of electronic and mechanical properties [54, 55, 56, 53, 57, 55, 58]. A flourishing new branch in the field of condensed matter, known as *twistronics*, promises to allow fine-tuning of the electronic properties using the rotational misalignment between layers [56, 26]. A notable example is the recent discovery of unconventional superconductivity in bilayer graphene twisted at the *magic angle* of 1.1° [26]. Another study found that the vertical conductivity of bilayer MoS_2/G heterostructures varies by a factor of five when imposing an angle of 30° between the layers [59]. Finally, a pioneering work [53] showed that, by switching from commensurate to incommensurate orientation in graphite systems, it is possible to achieve a state in which the coefficient of friction vanishes, the so-called *superlubric* regime.

An often overlooked question in these novel twisted heterostructures is whether this orientational ordering is stable and what underpins the energy landscape as a function of the mismatch angle. Chapter 3 explores this problem by means of classical MD and *first principles* calculations. While calculations are carried out on a specific system (MoS_2/graphene), the conclusions and the proposed generalisation of known epitaxy theory are general in nature.

Synthesis of 2D Materials

Mono- and few-layer thick crystals are mostly obtained in two ways [60]: micromechanical exfoliation and chemical vapour deposition (CVD). With the so-called Scotch-tape exfoliation method [3, 61], crystalline flakes are removed from a bulk layered crystal and

transferred to a substrate material. The method yields highly crystalline flakes, as the origin is a fully crystalline bulk, but offers little control over the size and chemical composition.

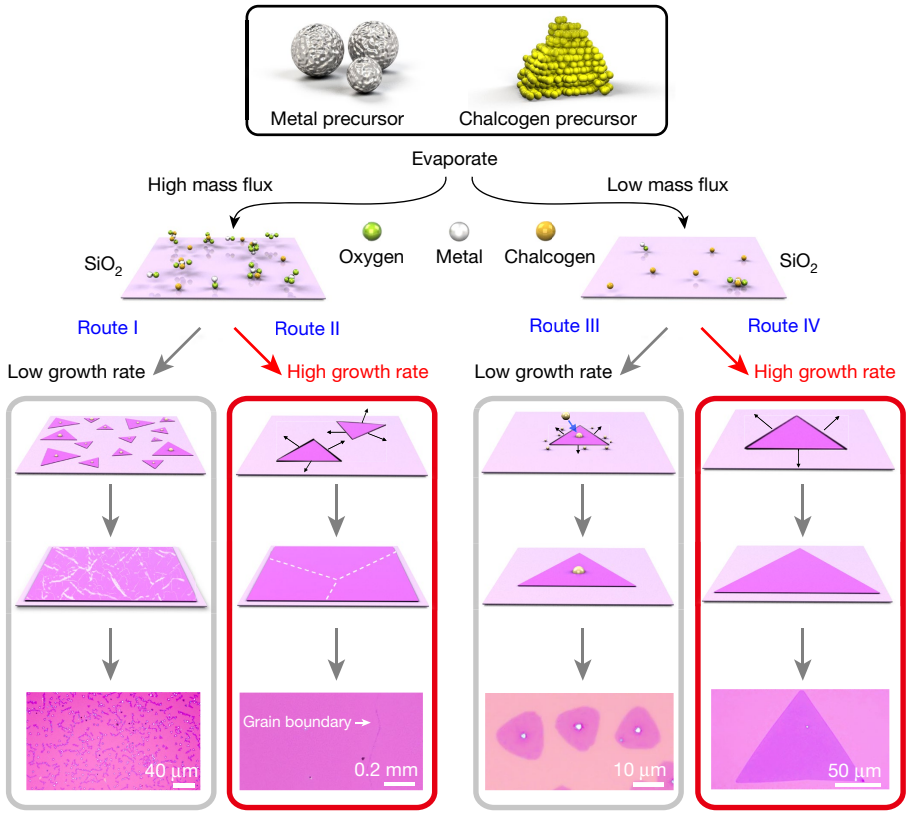

Figure 1.11: Sketch of the CVD techniques and resulting samples. Adapted from Ref. [23].

In CVD synthesis [62], sketched in Fig. 1.11, material precursors are evaporated, channelled into a high-temperature chamber ($400\,^{\circ}\mathrm{C} \div 900\,^{\circ}\mathrm{C}$), where they are then allowed to recombine onto a substrate, usually silicon oxides. While samples obtained by CVD are more prone to defects compared to exfoliated ones, high quality is achievable, and using different precursors and protocols allows for great freedom in chemical composition and sample sizes. In 2018, Zhou *et al.* [23] showed the power of CVD by compiling an experimental library of known TMDs in monolayer form. The author showed how having high level of control over the process allows for tuning between μm-sized high-quality isolated flakes (right branch of Fig. 1.11) and full-coverage poly-crystalline layers up to a fraction of mm in the lateral dimension (left side of Fig. 1.11). Moreover, the authors show the capabilities of CVD to synthesise TMD alloys, e.g. $\mathrm{Mo}_x\mathrm{Nb}_{1-x}\mathrm{S}_2$, albeit experiments provide little information about exact stochiometry or ordering of stable alloy configurations. Shortly after the work by Zhou and coworkers, Shivayogimath *et al.* [63] developed a modified CVD technique that could offer more control of TMD alloy synthesis. The authors used an Au-M alloy as a substrate, where M is one of the metals in Fig. 1.6, and subsequently exposed it to the chalcogenide precursor. The authors show that, since Au shows low reactivity with chalcogenides, high-quality TMD flakes are formed on the substrate. In principle, by using an alloy as a substrate, based on the TM in Fig. 1.6, one could obtain TMD alloys using this technique. Preliminary tests are underway at a

partner of the SOLUTION framework, the Forth laboratories in Patras, Greece, which could validate the results shown in chapter 4.

TMD-based coatings used in industrial applications are mainly obtained from physical vapour deposition techniques, like magnetron sputtering [64, 65]. The process is based on precursor targets ionised by accelerated Ar ions and subsequently accelerated towards a heated substrate by an electric field. The process is highly kinetic: ions impact the substrate with kinetic energy in the order of 10 eV and have little time to diffuse and recombine towards the thermodynamically stable phase. The result is the formation of metastable amorphous films, like the one shown on the left of Fig. 1.12a. Since amorphous films lack by definition periodicity, any model of such structures requires a large number of atoms to be considered. The lack of periodicity puts amorphous film beyond the reach of standard DFT techniques, requiring computationally more efficient approaches like empirical potentials [66] or linear scaling DFT [67, 68]. Nonetheless, experiments showed that amorphous coatings can re-organised in crystalline layers at the sliding interface, see Fig. 1.12a [39]. Computational analysis showed that the heat at the sliding interface promotes crystallisation towards thermodynamically stable structures while out-of-equilibrium effects due to the moving interface can be neglected. Thus, simulations utilising highly crystalline interfaces have implications for amorphous contact as well.

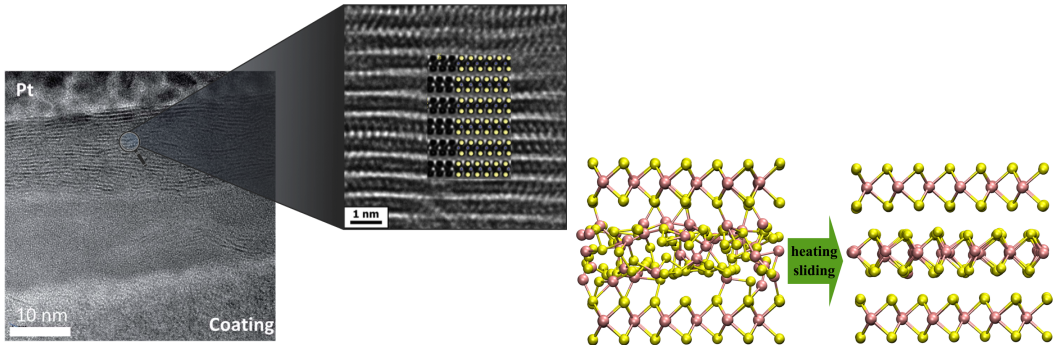

Figure 1.12: (a) High-Resolution Transmission Electron Microscopy (HRTEM) of a sputtered WS_2 coating at the sliding interface. The inset shows a magnification of the layered structure emerging from the amorphous matrix at the contact; adapted from Ref. [39]. (b) Sketch of the simulated re-crystallisation of MoS_2, adapted from Ref. [66].

1.2 Tribology

In 1966, Jost *et al.* [69] coined the word tribology, which means the study of 'rubbing' when two surfaces are in contact and in relative motion. It is estimated that 23% of the world's total energy consumption originates from tribological contacts [70], making the study of friction a relevant field from an engineering perspective. While the classical way to address this problem is via oil-based lubricants, these are linked to severe environmental problems and are not suited for operating under demanding conditions, e.g. high temperature or contact pressure [7]. A relevant example of an application of tribology, and specifically

TMD-based lubricants, is spacecraft. In this context, the temperature can quickly shift from a cryogenic regime to several hundred Kelvin, and the pressure ranges from atmospheric to high vacuum, making conventional oil-based lubricants impractical [17]. In this case, solid lubricants, in the form of a thin layer, or *coating*, deposited on the surfaces in contact, provide a better technical solution. Frictional behaviour of 2D material also relates to the development of Micro-Electro-Mechanical Systems or MEMS. These microscale systems operate at nanometer precision and find applications as micro-actuators and sensors [71]. Considering the scale of these devices, the presence of liquid and devices to control them, like pumps, is not advisable due to capillary effects and limited space on the device itself [72, 73]. Thus, these devices often require atomically thin layers of crystalline materials to ease the movement of different components and to extend their lifetime [71]. Of course, there are several drawbacks to solid lubricants. In general, they have low wear resistance and are sensitive to environmental conditions [73]. For example, MoS_2 is found to have an increased coefficient of friction (CoF) in humid environments, whereas graphite requires humidity to achieve low CoFs [73]. Moreover, applying and replenishing a solid lubricant coating poses more difficulties than classical liquid-based counterparts [17].

To summarise, the ideal solid lubricant would have high wear resistance, low sensitivity to environmental conditions, and a technologically convenient strategy for replenishing it should be available [73]. The research for such materials is a material science problem, as these problems and targets can be addressed by careful tuning of the chemistry and structure of the materials [65, 64]. For example, it has been shown that Ti doping enhances the tribological performances of MoS_2-based coatings in humid environments [74], while Ta additions help improve fatigue resistance [75]. While these two represent trial-and-error experimental approaches, a theoretical investigation of underlying microscopic behaviour of different dopants and alloys is lacking. The phase stability analysis presented in chapter 4 makes a step in this direction. The main aim of this first step is to provide experimentalists with a guide in the chemical space of TMDs, identifying thermodynamically favoured chemical orderings and crystal structures that are expected to form at the tribological contact.

While the empirical laws of macroscopic friction are well known [76], the mechanisms governing dissipation on the atomistic scale are still unclear [77, 78]. Moreover, a microscopic understanding of the effect of chemical composition on friction is largely uncharted territory [79, 80]. These open questions make the quest for a coherent theoretical framework of friction an exciting field of physics. Such a framework would allow bridging the empirical description routinely deployed at different length-scales [81], as sketched in Fig. 1.13. This thesis alone will not provide such a framework. Nonetheless, section 6.2 presents an extension of a known model based on novel frameworks, which allow for a coherent evaluation from microscopic variables of thermodynamic quantities during violent frictional events.

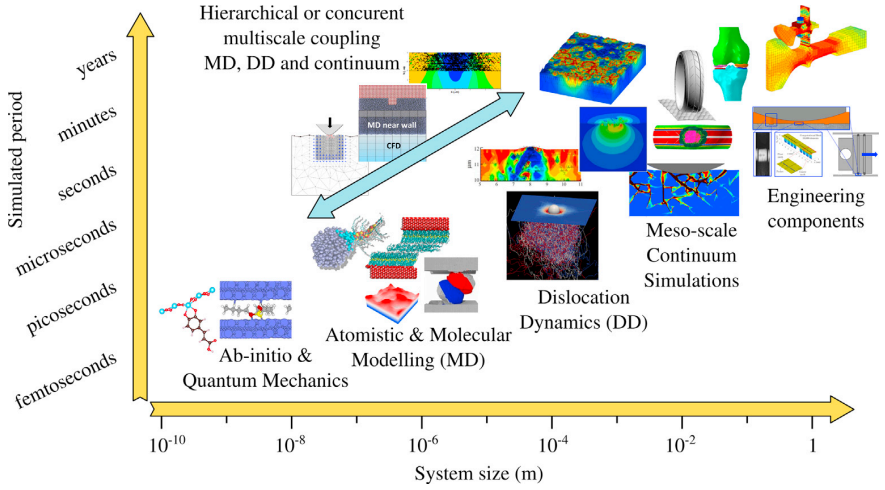

Figure 1.13: Approaches deployed at different scales to model frictional behaviour. Adapted from Ref. [81]

Friction Laws From a scientific point of view, friction, and more specifically 'dry' friction, is the thwarting force opposing the sliding motion between two solid surfaces in contact, as a result of the dissipation of energy (e.g. mechanical energy that is transformed into heat) and an irreversible loss of momentum [82]. In the empirical Amontons-Coulomb (AC) model [83, 84], friction is defined as the force opposing the relative motion of two objects. This is not a fundamental force, and it is artificially introduced in the equation of motion with suitable empirical coefficients. The AC model defines two different kinds of frictional forces: the static friction F_s and the dynamic friction F_d. The former describes the force barrier that a body in contact with another must overcome to start moving. The threshold to the body in motion depends linearly on the applied load:

$$F_\mathrm{s} = \mu_\mathrm{s} F_\mathrm{n}, \tag{1.1}$$

where μ_s is the static friction coefficient of the system, which depends on the materials in contact, the temperature, the possible pressure and type of lubrication. A similar relation holds for the dynamic friction, which applies when the two bodies are in relative motion:

$$F_\mathrm{d} = \mu_\mathrm{d} F_\mathrm{n}, \tag{1.2}$$

where μ_d is the dynamic friction coefficient, found to be smaller than the static one. In this simple model, both coefficients are constant. They are independent of the environment in which the sliding takes place, e.g. temperature and contamination. Moreover, the characteristics of the contact, i.e. sliding velocity and contact area, are not considered either.

1.2.1 Nanotribology

The familiar friction experienced at the macroscale arises from a set of different phenomena occurring at the microscopic sliding interface. When zoomed in, the apparent flat surfaces of the two macroscopic objects in contact appear as rough surfaces with multiple points of contact, as illustrated by the yellow and grey regions in Fig. 1.14. At this scale, processes take place at a set of contact points, termed *asperities*, rather than a single contact. Fig. 1.14 illustrates the processes that are captured by the umbrella term tribology: from fast quantum and electronic effects, happening on the order of picoseconds, to slower wear and ageing processes, stretching up to seconds. Moreover, most of the phenomena are out-of-equilibrium processes, where thermodynamics formalism finds limited applicability, or its meaning is ambiguous.

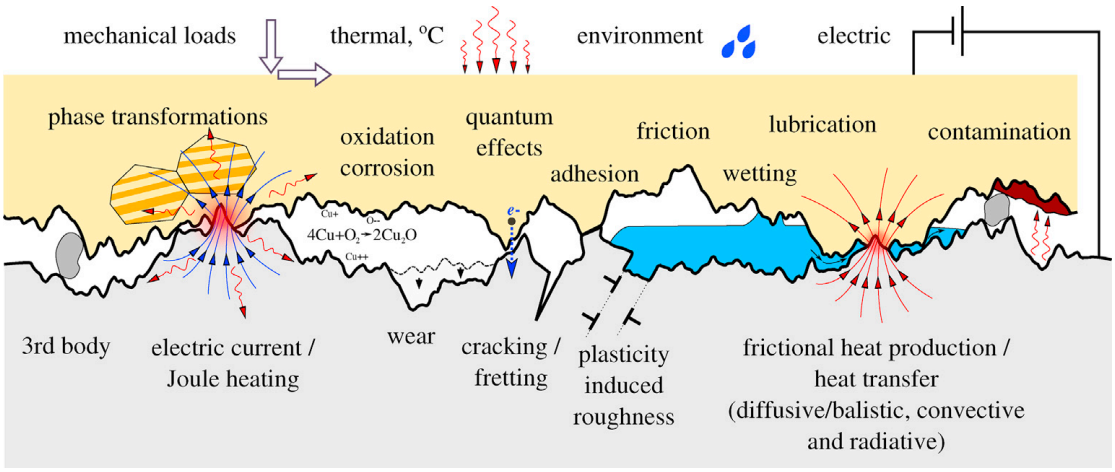

Figure 1.14: Phenomena occurring in a tribological contact formed by two rough surfaces (gray and orange regions). Adapted from Ref. [81]

Whether the AC model applies at the nano- and micro-scale is an ongoing debate. While it assumes the friction coefficients μ_i to be constant, it has been observed that they can vary with contact characteristic [81, 82]. Moreover, the frictional force at nanoscale has been shown to depend on the contact area [85, 86, 87], while the AC model assumes a linear relationship between load and force, Eq. (1.1) and (1.2), independent of the contact area. In the case of static friction, ageing of the contact results in μ_s increasing [88]. In the case of kinetic friction, μ_d decreases with increasing sliding velocity [81, 82]. Ad hoc corrections to the AC model can account for this [81]. On the other hand, Mo *et al.* [85] argued that the linear AC relation might be valid at the nanoscale given a correct definition of the area of contact. The authors showed with numerical calculations that AC still applies if the contact area is defined in terms of the atoms chemically interacting at the contact, shown as red dots in Fig. 1.15. This yields the relation $F_\mathrm{d} = \tau \sum A_\mathrm{atom}$, where τ is an effective shear strength for the contact and A_atom is the average surface area per atom (gray hexagons in Fig. 1.15), in contrast with the result of Bowden and Tabor [87] $F_\mathrm{d} = \tau \sum A_\mathrm{asp}$, where A_asp is the single asperity area, which is the region enclosed by the black polygon in Fig. 1.15, clearly different from the sum of the hexagons representing the

area per atom.

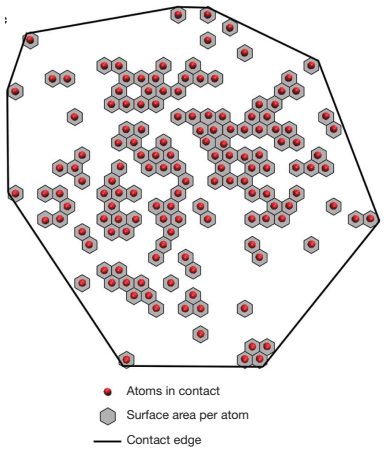

Figure 1.15: Asperity contact area (enclosed by black line) and atoms forming the real contact (red dots). Adapted from Ref. [85]

As hinted by this summary, the problem of surface roughness is a complex field, at the interface between atomistic, nanoscale tribology ($\approx 10^{-9}$m) and continuum, mesoscale tribology ($\approx 10^{-4}$m [89]). The common approach in nanotribology is to focus on a single asperity contact, limiting the size of the system to $10^{-9} \div 10^{-7}$ m and $10^{-9} \div 10^{-4}$ s. This single asperity can be modelled as a point-like object sliding over a substrate, allowing for an efficient description of the substrate and long-dynamical response [90, 91], or as two locally flat crystalline surfaces, focusing on contribution to the friction of intrinsic properties of the material [92, 93]. As sketched in Fig. 1.13, phenomena in this realm are described employing different techniques. Out-of-equilibrium effects are described by classical Molecular Dynamics (MD) simulations, powered by carefully parametrised classical potentials, termed Force Fields (FF), [94, 95], or by low-order models, such as the Prandtl-Tomlinson (PT) model [96, 77]. Descriptors based on electronic structure calculations, like Potential Energy Surfaces (PES) [93, 97] or phonon-based quantities [80, 98] tackle intrinsic friction properties.

Friction Force Microscopy The most common methods to investigate nanoscale friction is Atomic Force Microscopy (AFM), first proposed in 1986 by G. Binnig *et al.* [99] as a modification of Scanning Tunnelling Microscopy. The working principle of AFM is shown in Fig. 1.16a: an atomically sharp tip ($\approx 10\,$nm [100]) slides over a substrate, yielding $\mathring{A}$ resolution of the topography [99]. Shortly after the work of Binning and coworkers, Mate *et al.* [101] were the first to develop a modified version of the AFM to observe the atomic-scale friction of a tungsten tip on a graphite surface. The authors' Friction Force Microscopy (FFM) exploits the lateral deflection of the tip to measure the force opposing the sliding of the tip over the substrate [101]. The simplest way to model FFM experiments is via a PT model, which can qualitatively explain the bulk of the frictional behaviour [90, 102, 103]. Nowadays, large-scale atomistic simulations allow the explicit description of an entire AFM tip explicitly, shedding light on mechanisms which are not describable by PT-like models. For example, it is possible to investigate the role of the finite size of tips and mechanical properties in the formation/rupture dynamics of contacts and as channels for dissipation

and wear [104].

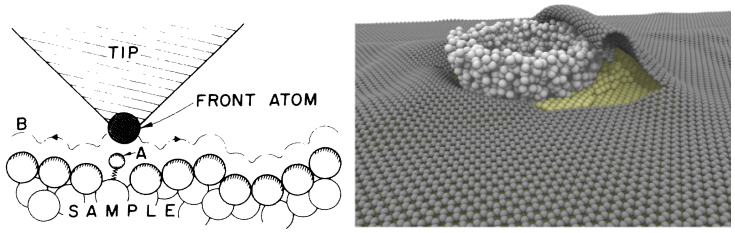

Figure 1.16: (a) Sketch of the AFM idea of a tip sliding at speed $\boldsymbol{v}$ over a substrate material. Adapted from Ref. [99] (b) Finite AFM tip sliding at speed $\boldsymbol{v}$ over a graphene layer protecting a Pt metal substrate. Adapted from Ref. [104]

Non-linear dynamics

As sketched in Fig. 1.14 a contribution to frictional dissipation is energy dissipation, transforming the kinetic energy of the sliding bodies into forms of heat. These are out-of-equilibrium processes challenging the classical thermodynamic framework. A vital distinction runs between dissipative phenomena related to linear- or non-linear dynamics [105]. Linear dissipation can be addressed with linear response tools, which, in simple cases, allow for analytical solution [78]. On the other hand, non-linear dynamics pose theoretical problems [105]. A classic example is the stick-slip dynamics observed in crystalline interfaces: the contact alternates for long time periods around the energy minima (stick) with sudden snaps over the energy barrier in the PES (slip). These decoupled time scales between stick and slip mean the linear response theory hypothesis of smooth deviation from equilibrium behaviour is broken [105]. The stick-slip dynamics is thus usually treated by direct integration of the equation of motion of empirical models, most notably the PT model [106, 90, 103], mimicking a single asperity sliding over a substrate as sketched in Fig. 1.17, and the Frenkel–Kontorova (FK) model [107, 108], describing an extended contact (multiple asperities or a soft crystal) sliding over a rigid crystalline substrate. Section 6.2 introduces a generalisation of the PT model based on state-rate theory and stochastic thermodynamics [109] which provides a derivation of thermodynamic quantities in non-equilibrium processes, e.g. entropy production, from microscopic variables.

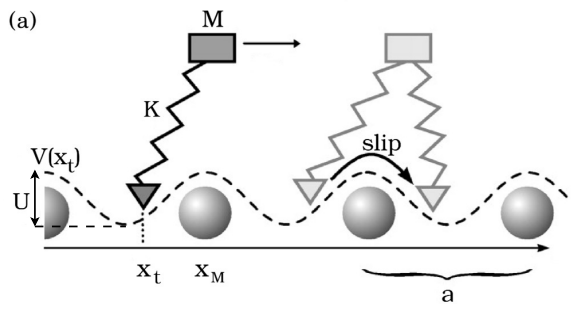

Figure 1.17: One-dimensional Prandtl-Tomlinson model. A point-like mass M is connected via a spring of constant K to a body moving at constant velocity v while and interacting with a static potential $V(x)$ of amplitude U and periodicity a, mimicking the sliding of an AFM tip over an atomic surface. Adapted from Ref. [110].

Structural Superlubricity

Within the AC model, frictional response is defined by the dimensionless parameters $\mu_s \geq \mu_d$. For example, the dynamic coefficient of friction for wood planks in relative motion is of 0.2 and larger, whereas for two metal surfaces it is 1.0 and larger [57]. For interfaces treated with solid lubricant coatings, this can be lowered to 0.05 [7]. Assuming the AC captures the dissipation at this scale, one may wonder how small these coefficients can be. Going even further, can they physically be *exactly* zero, yielding dissipation-free interfaces?

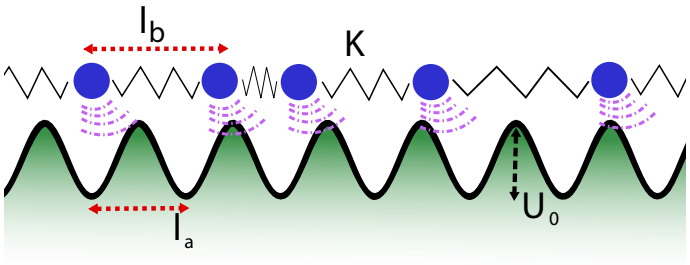

Figure 1.18: A sketch of the Frenkel-Kontorova model. A linear chain of point-like masses M are connected via springs of constant K and equilibrium spacing l_b. The masses interact with a periodic potential $V(x)$ of amplitude U_0 and spacing l_a.

In 1983, Peyrard and Aubry [111] showed emergence of a state characterised by a vanishing static friction coefficient in the one-dimension incommensurate FK model, depicted in Fig. 1.18. The core idea behind this free-sliding state is an underlying cancellation of forces opposing the motion of the atoms from the ground state: for every atom going up the substrate potential, there is always another atom somewhere in the infinite chain going down, resulting in an exact energy balance and an unconventional 'effective' translational invariance. Numerical simulations have shown that the vanishing static friction is accompanied by a small yet finite dynamic friction dissipation [112]. From an operative and experimental point of view, the onset of the structural superlubricity is defined as the friction coefficient falling below $10^{-4} \div 10^{-3}$ [72].

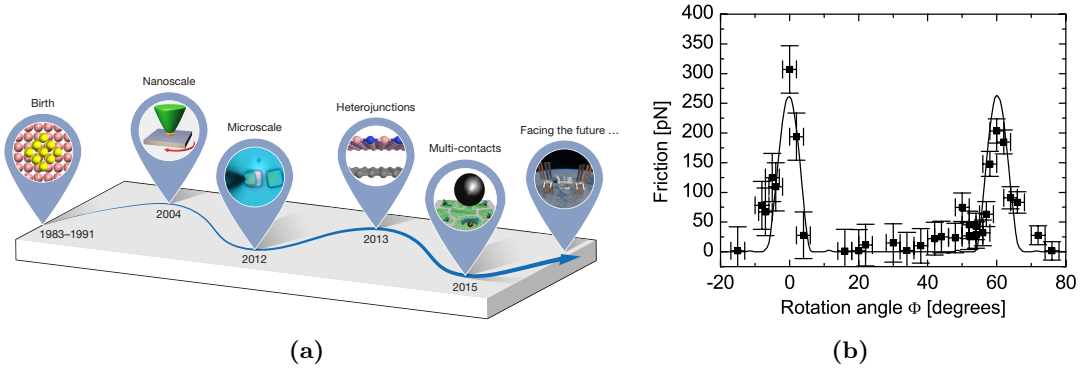

(a) **(b)**

Figure 1.19: (a) Adapted from Ref. [113]. (b) Friction signal in AFM experiments from graphene flake on graphite as a function of the imposed rotation. Adapted from Ref. [114].

As a historical note, the term superlubricity was first introduced by Hirano and Shinjo a decade after the Peyrard and Aubry paper, marking the official start of the quest to

frictionless sliding, sketched in Fig. 1.19a Another decade later, experimental validation of these theoretical predictions was given by Dienwiebel *et al.* [53]. Using AFM in high vacuum, the authors measured the coefficient of friction between a graphite substrate and a graphite-covered tip as a function of misalignment angle. Fig. 1.19b reports the frictional signal versus the imposed angle. It shows how frictional forces away from the aligned configuration, 0° and 60°, are reduced below the accuracy of the instrument [53].

The experiment by Dienwiebel and coworkers shows how the argument underpinning the Aubry argument in the 1D model is extended to higher dimensions. Consider two atomically flat layers, free of contaminants and dangling bonds. The PES that the sliding layer experiences, due to the presence of the static one, is purely the result of interatomic interactions [57]. These electrostatic and van der Waals interactions result in preferential positions and orientations of one surface atop another.

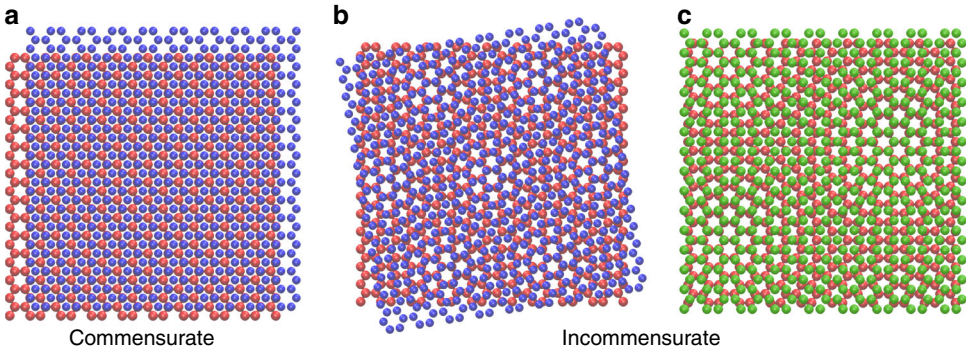

Figure 1.20: Schematic representation of different ways to position periodic surfaces above each other. a) Homogeneous commensurate minimum energy configuration. b) Homogeneous incommensurate structure through a mismatch angle between the layers. c) Heterogeneous incommensurate contact where both surfaces have the same symmetry but different lattice constant. Adapted from Ref. [115]

Fig. 1.20 shows the possible ways in which the two atomic surfaces can be brought into contact to form a tribological contact. Fig. 1.20a is a schematic of two identical, aligned structures, positioned above each other, in a minimum energy configuration. This orientation, where the bottom and top layer are aligned in the parallel plane, is called a commensurate structure. As one might expect, this configuration is very stable, which implies a relatively high resistance to making the top layer slide. This resistance is due to the energy barriers resulting from the atomic interlayer interactions that all have to be overcome simultaneously, causing high frictional forces in order to start sliding. Whenever a misalignment angle between the relative orientation of the layers is introduced, as depicted in Fig. 1.20b, the contact becomes incommensurate. As a result, pairs of atoms can be found at any possible relative distance, bringing back the Aubry argument about cancelling forces outlined at the beginning of the section. Rotating one of the two layers is not the only way of achieving this symmetry breaking. If one, for example, considers a heterostructure of two different materials, possibly with the same symmetry but with a different lattice constant, the same effect can be achieved, see Fig. 1.20c. In conclusion, misalignment angles or lattice mismatch introduce the structural incommensurability required by the

Aubry theory and represent a possible pathway to achieving superlubricity in real contacts.

An example of robust superlubricity in mismatched heterostructures has been recently reported by Song *et al.* [19]. The authors focused on hBN/graphene heterostructures, which are characterised by a small mismatch of $l_{\mathrm{hBN}}/l_{\mathrm{G}} \approx 1.1$. They tested the frictional properties of extended contacts, $(3 \times 3\,\mu\mathrm{m}^2)$ flakes over a larger substrate obtained by exfoliation methods, finding a vanishingly small frictional coefficient via AFM measurements. MD simulations reproduced the observation and rationalised the finding. In commensurate graphitic contacts, large dissipation is related to the stick-slip of the layers' centre of mass (CoM). On the other hand, in hBN/G heterostructures the CoM cruises over the substrate undisturbed, while the small dissipation detected is due to internal degrees of freedom of the layers [19]. Section 6.1 further explores the pathway towards robust superlubricity by focusing on the large mismatch limit. The dissipation of MoS_2/G heterostructures $l_{\mathrm{hBN}}/l_{\mathrm{G}} \approx 0.8$ is compared with the near-commensurate G/hBN case in a joint experimental and computation work carried out in collaboration with groups in Prague, Czech Republic and Beijing, China.

1.3 Aims

This project aims to study the phase behaviour and frictional properties of (novel) 2D materials. Particular attention is given to the application of TMD as solid lubricants. Numerical techniques can create fully controlled 'in silico' experiments, not only regarding the environment but also the interactions within the system. They can thus act as a magnifying lens for experiments and, by tuning the physics underpinning different phenomena, test hypotheses in ways not possible in experiments. Thus, experiments and theory do not exclude one another, but it is the synergy between them that creates real scientific power.

The goal of the interlayer phase behaviour investigation is to understand the mechanisms defining the energy landscape of heterostructures based on TMDs and other 2D materials. In particular, the focus is on the dependence of energy on the imposed misalignment angle at the base of the emerging twistronic field.

The in-plane phase behaviour investigation aims to develop a framework to understand and predict the thermodynamic behaviour of substitutional alloys in TMDs. The knowledge gained should help to identify possible binary alloys and predict their phase behaviour, guiding synthesis efforts.

The goal of the investigation of nanoscale tribological contacts is to rationalise AFM experiments, relating measured frictional forces to dissipation mechanism within the system and with the surrounding. Thus, making a step in developing a fundamental understanding of the lubrication mechanism, on which design of solid lubricants can be built.

1.4 Thesis Outline

Most of this thesis represents a compilation of results presented or submitted to scientific journals. It addresses the issues of phase stability and alloying in two-dimensional materials and their frictional behaviour during dry sliding.

Chapter 2 presents the theoretical frameworks and numerical techniques deployed to address these questions. Density Functional Theory was used to describe the electronic structure and total energy of the crystalline system; it also represents the reference for statistical mechanics models of formation energy and finite temperature behaviour.

Chapter 3 explores the problem of phase stability in heterostructures, focusing on the rotational degree of freedom. The limits of a known theory of epitaxial stacking are tested on a specific system. A novel argument rationalises the breakdown of the known theory, and an extension of the known theory is outlined. This chapter is based on the publication "Exploring the stability of twisted van der Waals heterostructures" by **A. Silva**, V. E. P. Claerbout, T. Polcar, D. Kramer, and P. Nicolini, *ACS Appl. Mater. Interfaces* 12, 45214 (2020).

Chapter 4 reports a systematic analysis of phase behaviour of possible TMDs. Computational screening of selected TMs in known layered prototypes yields a bird-eye perspective of possible alloys system. The chapter continues with a detailed analysis of selected stable orderings and miscibility gaps in a set of ternary systems. This section is based on the manuscript "High-throughput Design of TMDs Alloys" by **A. Silva**, T. Polcar, and D. Kramer, in preparation for *Npj Comput. Mater.*

Chapter 5 builds on the protocol outlined in the previous chapter and presents an in-depth analysis of the (Mo:Ti)S_2 system, relevant to the tribology community. Zero- and high-temperature behaviour is studied and rationalised in terms of electronic effects. This chapter is based on the publication "Phase behaviour of (Ti:Mo)S_2 binary alloys arising from electron-lattice coupling" by **A. Silva**, T. Polcar, and D. Kramer, *Comput. Mater. Sci.* 186, 110044 (2021).

Chapter 6 addresses the problem of simulating tribology experiments. Section 6.1 presents a joined experimental and computational characterisation of the frictional properties of large-mismatch heterostructures. The study focuses on describing scaling laws of observed superlubricity, and the developed classical model rationalises the trends in terms of enhanced flake-edge mobility. This section is based on the manuscript "Ultra-low friction and edge pinning effect at large lattice mismatch van der Waals heterostructure interfaces" by M. Liao, P. Nicolini, L. Du, J. Yuan, S. Wang, H. Yu, J. Tang, P. Cheng, K. Watanabe, T. Taniguchi, L. Gu, V. E. P. Claerbout, **A. Silva**, D. Kramer, T. Polcar, R. Yang, D. Shi and G. Zhang, under review in *Nat. Mater.*

Section 6.2 introduces a modified model for AFM measurements. The combination of DFT-based material descriptions with stochastic thermodynamics allows for a coherent description of the dissipation on single experimental trajectories. The results of the model can be validated experimentally with known techniques. This section is based on the manuscript "Multi-scale Model for Nano-friction Measurements" by P. C. Torche, **A. Silva**,

T. Polcar, D. Kramer and O. Hovorka, in preparation for *Phys. Rev. Mater.*

2
Methods

The first three sections of this chapter are dedicated to the theoretical frameworks used to describe the physics underpinning materials behaviour at different length- and time-scales. The last section introduces the approximate models used to describe materials properties.

2.1 Density Functional Theory

The Density Functional Theory (DFT) is a formulation of the quantum theory of electronic structure, in which the electron density $n(\boldsymbol{r})$, rather than the many-electron wave function Ψ, plays a central role. This alternative viewpoint, which earned Kohn and Pople the Nobel Price in 1998 [116], is an exact formulation of the electron problem, but it also has the advantage of providing a formalism that naturally lends itself to approximate solutions.

The starting point to introduce DFT is the standard formulation of the Schrödinger equation for the wave function of a N_e-electron system within the Born-Oppenheimer approximation:

$$\left[\sum_i \left(-\frac{h^2\nabla^2_{\boldsymbol{r}_i}}{2m} + v(\boldsymbol{r}_i)\right) + \sum_{ij} U(\boldsymbol{r}_i, \boldsymbol{r}_j)\right] \Psi(\boldsymbol{r}_1, ..., \boldsymbol{r}_{N_\mathrm{e}}) = E\Psi(\boldsymbol{r}_1, ..., \boldsymbol{r}_{N_\mathrm{e}}), \tag{2.1}$$

where $v(\boldsymbol{r}_i) = \sum_k \frac{Q_k e}{|\boldsymbol{r}_i - \boldsymbol{R}_k|}$ is the external potential generated by the nuclei of charge Q_k at positions $\boldsymbol{R}_k$, and $U(\boldsymbol{r}_i, \boldsymbol{r}_j) = \frac{e^2}{|\boldsymbol{r}_i - \boldsymbol{r}_j|}$ is the Coulomb electron-electron interaction potential. In Dirac notation, Eq. (2.1) can be understood as an eigenvalue problem for the Hamiltonian operator

$$\hat{H}|\Psi\rangle = E|\Psi\rangle, \tag{2.2}$$

where $\hat{H}$ is composed of the terms in squared brackets in Eq. (2.1).

The widespread use of DFT compared to methods based on multiparticle wavefunctions is rooted in the manageable scaling of the computational time T_{simul}. The time needed to obtain the electron density scales as $T_{\text{simul}} \approx N_{\text{e}}^{\alpha}$ with $\alpha = 2 - 3$, while, in a wavefunction-based framework, the scaling is exponential with the number of electrons. Recent developments are focusing on achieving true linear scaling, $\alpha = 1$, making DFT able to treat larger systems usually requiring classical mechanics methods [67]. Moreover, the wave-function $\Psi(\boldsymbol{r}_1, ..., \boldsymbol{r}_{N_{\text{e}}})$ of N_{e} electrons is an incredibly complex object going from $3N_{\text{e}}$ space of electron coordinates to $\mathbb{C}$, making it a difficult object to treat and store [116]. Physical quantities of interest are obtained by integrating degrees of freedom from Ψ. As an example, the electron density itself is given by

$$n(\boldsymbol{r}) = N_{\text{e}} \int |\Psi^*(\boldsymbol{r}, \boldsymbol{r}_2, ..., \boldsymbol{r}_{N_{\text{e}}})\Psi(\boldsymbol{r}, \boldsymbol{r}_2, ..., \boldsymbol{r}_{N_{\text{e}}})|\, d\boldsymbol{r}_2 ... d\boldsymbol{r}_{N_{\text{e}}}, \tag{2.3}$$

which is a scalar function of the 3D vector $\boldsymbol{r}$.

The Hohenberg-Kohn Theorems

The Hohenberg-Kohn (HK) theorems are the foundation of DFT. They prove that Ψ_0 and all the other observables of the system can be computed in terms of $n_0(\boldsymbol{r})$. This means that $n_0(\boldsymbol{r})$, a function of a single 3D vector variable $\boldsymbol{r}$, contains the same information as a function of $\boldsymbol{r}_1, ..., \boldsymbol{r}_{N_{\text{e}}}$. The apparent paradox is explained from considering that Ψ_0 not only yields the ground state density according to Eq. (2.3), but must also minimise the energy as expressed by the variational formulation of Eq. (2.1)

$$E_{\text{GS},v} \leq \langle \Psi | \hat{H} | \Psi \rangle, \tag{2.4}$$

where $E_{\text{GS},v}$ indicates the ground state energy with external potential $v(\boldsymbol{r})$. The Hamiltonian of the system can be divided as

$$\hat{H} = \hat{T} + \hat{U} + \hat{V}, \tag{2.5}$$

where $\hat{T} = \sum_i \frac{h^2 \nabla_i^2}{2m}$ is the kinetic energy operator, $\hat{U} = \sum_{ij} \frac{e^2}{|\boldsymbol{r}_i - \boldsymbol{r}_j|}$ is the electron-electron potential and $\hat{V} = \sum_i v(\boldsymbol{r}_i)$ is the external potential energy. The $\hat{T} + \hat{U}$ part of the Hamiltonian is universal, and the specific system is defined only by the potential $\hat{V}$. The energy of the system can be expressed as a functional of the electron density as

$$E[n(\boldsymbol{r})] = \int n(\boldsymbol{r}) v(\boldsymbol{r}) d\boldsymbol{r} + F[n(\boldsymbol{r})], \tag{2.6}$$

where $F[n(\boldsymbol{r})]$ is an unknown, universal functional expression for the kinetic energy and electron-electron interactions.

The first theorem states that the external potential $v(\boldsymbol{r})$, and hence the total energy, is uniquely determined by the electron density $n(\mathbf{r})$. The proof of the theorem if found by

reductio ad absurdum. Assume there are two different external potentials $v_1(\boldsymbol{r})$ and $v_2(\boldsymbol{r})$ resulting in the same density $n(\boldsymbol{r})$. In turn, the two Hamiltonians $\hat{H}_1$ and $\hat{H}_2$ associated with the two potentials have different ground-state wave-functions Ψ_1 and Ψ_2, both yielding $n(\boldsymbol{r})$. The variational principle in Eq. (2.4) and (2.5) for the first Hamiltonian $\hat{H}_1$ evaluated on the second ground-state Ψ_2 yields

$$E_{\mathrm{GS},v_1} \leq \langle\Psi_2|\hat{H}_1|\Psi_2\rangle = \langle\Psi_2|\hat{H}_2|\Psi_2\rangle + \langle\Psi_2|\hat{H}_1 - \hat{H}_2|\Psi_2\rangle \tag{2.7}$$

$$= E_{\mathrm{GS},v_2} + \int n(\boldsymbol{r})(v_1(\boldsymbol{r}) - v_2(\boldsymbol{r}))d\boldsymbol{r}. \tag{2.8}$$

An equivalent relation is found for the opposite situation, i.e. $\hat{H}_2$ evaluated on the ground-state Ψ_1. Adding the two inequalities yields

$$E_{\mathrm{GS},v_1} + E_{\mathrm{GS},v_2} \leq E_{\mathrm{GS},v_1} + E_{\mathrm{GS},v_1}, \tag{2.9}$$

which is impossible, and thus the ground-state density uniquely determines the external potential $v(\boldsymbol{r})$.

The second theorem shows that the variational principle in terms of wave-functions, Eq. (2.4), holds for the density as well

$$n' \neq n_0 \rightarrow E[n_0]_v < E[n']_v \tag{2.10}$$

This property is essential as it assures that by minimizing the energy from a trial density one only gets closer and closer to the actual ground state.

The Kohn-Sham Equations

The HK theorem results can be implemented in different frameworks. A widely used choice is the one created by Kohn and Sham [117], as it casts the problem in a one-body formalism and expresses the density $n(\boldsymbol{r})$ in terms of single-particle orbitals $\{\phi_i(\boldsymbol{r})\}$, reducing the problem to a set of coupled differential equations that can be solved iteratively. The kinetic energy term in Eq. (2.4) can be written as $T = T_s + T_c$, where T_s is the kinetic energy of a non-interacting electronic system[1]. The non-interacting kinetic energy is expressed in orbitals $\{\phi_i(\boldsymbol{r})\}$ by the functional

$$T_s = -\frac{\hbar^2}{2m}\sum_i^{N_\mathrm{e}} \int d\boldsymbol{r}\phi_i^*(\boldsymbol{r})\nabla^2\phi_i(\boldsymbol{r}), \tag{2.11}$$

and $T_c = T - T_s$ includes all the correlation effects not included in the non-interacting system. Likewise, $U = U_H + U_c$, where U_H is the mean-field Hartree potential for the electrostatic Coulomb interaction, is expressed in terms of the density as

$$U_H = \frac{q^2}{2}\int\int d\boldsymbol{r}d\boldsymbol{r'}\frac{n(\boldsymbol{r})n(\boldsymbol{r'})}{|\boldsymbol{r} - \boldsymbol{r'}|}. \tag{2.12}$$

[1]We shall use the subscript s in the rest of the chapter to indicate quantities of non-interacting systems.

The energy of the system then becomes

$$E[n] = T_s[\{\phi_i[n]\}] + U_H[n] + V[n] + E_{xc}[n], \tag{2.13}$$

where the functional $E_{xc}[n]$ is called *exchange-correlation* (xc) energy and it contains the neglected parts $T - T_s$ and $U - U_H$. Equation (2.13) is still exact and equivalent to the full Schrödinger equation, Eq. (2.1), but the exact expression for $E_{xc}[n]$ is unknown. Nonetheless, the beauty of this scheme is that if $E_{xc}[n]$ is small compared to other terms (as it usually is), then it is possible to rely on some approximation for this unknown functional to obtain physical results. In order to obtain the celebrated Kohn-Sham (KS) equations, Eq. (2.13) is minimised with respect to $n(\boldsymbol{r})$, yielding

$$0 = \frac{\delta E[n]}{\delta n} = \frac{\delta T_s[n]}{\delta n} + v(\boldsymbol{r}), \tag{2.14}$$

which describes the full-interacting electron system with $v(\boldsymbol{r}) = v(\boldsymbol{r}) + v_H(\boldsymbol{r}) + v_{xc}(\boldsymbol{r})$.

Consequently, the density of the interacting, many-body system of Eq. (2.1) is obtained by solving the set of coupled-equations

$$\left[-\frac{\hbar^2\nabla^2}{2m} + v_s(\boldsymbol{r})\right]\phi_i(\boldsymbol{r}) = \epsilon_i\phi_i(\boldsymbol{r}), \tag{2.15}$$

together with

$$n(\boldsymbol{r}) = \sum_i^{N_\mathrm{e}} f_i|\phi_i(\boldsymbol{r})|^2, \tag{2.16}$$

where f_i is the occupation number of the single-particle orbital $\phi_i(\boldsymbol{r})$. Because v_s and $\phi_i(\boldsymbol{r})$ depend on each other through n, this is a set of non-linear equations and is solved self-consistently: using an initial guess for $n^{(0)}$, a new density $n^{(1)}$ is obtained by solving Eq. (2.15), which can be used as new starting point to solve the equations again. This procedure is repeated until the new solution is not too different from the previous step, i.e. the system has reached the desired level of convergence.

From Electrons to Ions: Hellmann-Feynman Theorem

It is time to deal with one side of the Born-Oppenheimer approximation: while DFT yields the solution to the fast electron motion in the field of fixed ions, the positions of the ions themselves must be updated. Together with the electron density $n(\boldsymbol{r})$, the $3N$ ionic coordinates R_i define a hyper-surface, the PES, $E = E[\{\boldsymbol{R}_i\}, n(\boldsymbol{r})]$. The total energy of the system E is given by the sum of the electronic parts in Eq. (2.1) and the ion-ion interactions:

$$V_\mathrm{ion} = \sum_{i\neq j}\frac{Q_iQ_j}{|\boldsymbol{R}_i - \boldsymbol{R}_j|}. \tag{2.17}$$

The force acting on the ions can be connected directly with the electron density via

the Hellman-Feynman theorem [118], which states that

$$\frac{dE_\lambda}{d\lambda} = \left\langle \Psi \left| \frac{d\hat{H}}{d\lambda} \right| \Psi \right\rangle . \tag{2.18}$$

The proof follows from the differentiation chain rule and the properties of normalised wave-functions:

$$\langle \psi_\lambda | \psi_\lambda \rangle = 1 \Rightarrow \frac{\mathrm{d}}{\mathrm{d}\lambda} \langle \psi_\lambda | \psi_\lambda \rangle = 0. \tag{2.19}$$

When the parameter λ corresponds to the coordinates of the nuclei, Eq. (2.18) yields the force acting on the ion [118]

$$F_i = \nabla_{\boldsymbol{R}_i} E = -\left\langle \Psi \left| \frac{\partial \hat{H}}{\partial \boldsymbol{R}_i} \right| \Psi \right\rangle - \nabla_{\boldsymbol{R}_i} V_{\text{ion}} \tag{2.20}$$

$$= -\int n(\boldsymbol{r}) \nabla_{\boldsymbol{R}_i} v(r) d\boldsymbol{r} - \nabla_{\boldsymbol{R}_i} V_{\text{ion}}, \tag{2.21}$$

where only the electron-ion interaction $v(\boldsymbol{r}_i) = \sum_k \frac{Q_k e}{|\boldsymbol{r}_i - \boldsymbol{R}_k|}$ in Eq. (2.1) depends on the nuclei position. The forces acting on ions depends explicitly on the electron density and how accurately this has been computed. Once forces are extracted from $n_{\{\boldsymbol{R}\}}(\boldsymbol{r})$, the positions of the N ions can be updated in many ways: for example, via a minimization algorithm if the goal is to find the minimal energy [119] or using the Car-Parrinello scheme if one is interested in the dynamics of the ion system [120].

2.1.1 Implementation

In the previous sections, the complex and numerically intractable problem Eq. (2.1) has been cast into the equivalent set of coupled differential equations Eq. (2.15). The exchange does not come for free, as the new formalism does not have an explicit analytic form and a set of approximations need to be implemented to find a solution of Eq. (2.15) on a computer, as outlined in Fig. 2.1.

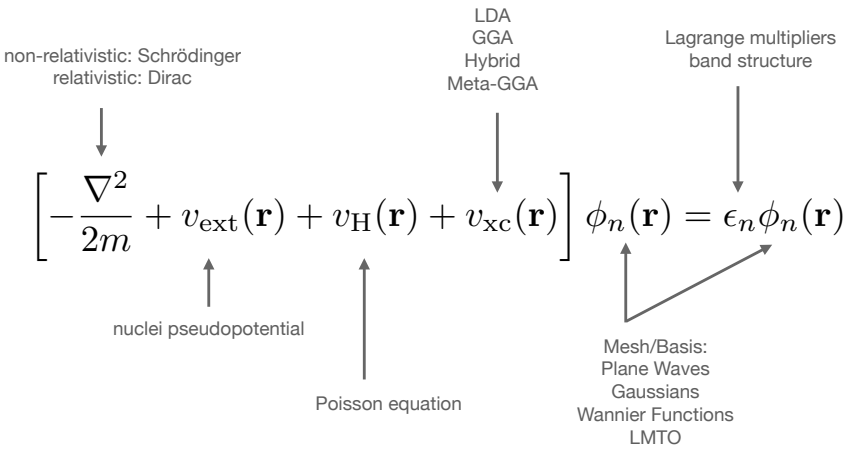

Figure 2.1: Some possibilities used to approximate the exact KS problem. Adapted from Ref. [121].

Basis Set

The Kohn orbitals $\phi_i(\boldsymbol{r})$ can be expanded onto a set of known functions, and the KS equations can be written in terms of the expansion coefficients. The possible sets of functions are usually divided into two categories: localized and plane-wave basis. These are in principles equivalent. In practice, each one provides a better approximation of different electronic behaviours, and one should choose the basis that better describes the system under consideration.

In a localized basis set the electron density is described in terms of functions centred on the atomic positions, like Gaussian- or Slater-type orbitals. Note that Gaussian-type orbitals are a convenient representation from a numerical point of view, although they do not represent a complete basis set and, thus, the precision might not increase with the number of elements of the orbitals. Localized sets are the preferred choice when electrons are confined around ions, like in the case of metal oxides and molecules.

In a plane-wave basis set, the density is expressed in terms of periodic, oscillatory wave functions that form a complete representation of the Hilbert space. This set is the preferred choice when electron wavefunctions are delocalized within periodic systems, like crystalline metals.

Wannier functions [122, 123] represent a mid-point between these two approaches. These functions represent a complete set and can be thought of as the Fourier transform of Bloch states

$$\Xi_{\boldsymbol{R}}(\boldsymbol{r}) = \frac{1}{N} \sum_{\boldsymbol{k}} e^{i\boldsymbol{R}\cdot\boldsymbol{k}} \psi_{\boldsymbol{k}}(\boldsymbol{r}), \tag{2.22}$$

where $\boldsymbol{R}$ are the direct lattice vectors, the sum in $\boldsymbol{k}$ is extended over the Brillouin Zone (BZ) and $\psi_{\boldsymbol{k}}(\boldsymbol{r}) = e^{i\boldsymbol{r}\cdot\boldsymbol{k}} u_{\boldsymbol{k}}(\boldsymbol{k})$ is a Bloch state function, which has the same periodicity as the crystal structure. Because the set $\psi_{\boldsymbol{k}}(\boldsymbol{r})$ is defined up to a phase factor, the definition of the Wannier functions remains somewhat arbitrary. ONETEP [67], a linear-scaling implementation of DFT, takes advantage of the hybrid character of Wannier functions. A set of non-orthogonal generalized Wannier functions is optimized for the specific environment simulated and used as a basis set for the electron density expansion. These functions are then truncated outside a sphere of radius r_{cut}, preserving the overlap with neighbouring Wannier functions. This approach allows the code to range in accuracy from plane-wave to localized orbitals and yield linear scaling with the size of the system.

Pseudo Potentials

Due to the point-like positive charge of the nuclei, the ion potential around them is steep, and the electron density in this region varies fast. Although this is a physical behaviour, it can constitute a problem for a numerical solution of the problem, as a large number of basis functions, e.g. plane-waves, is needed to describe the rapid variation in real space. If the behaviour of the density close to the nuclei is not of interest, pseudo-potentials (PP) are a way to overcome this numerical difficulty. Chemical binding is dominated by the outer (valence) electrons of atoms, while inner (core) electrons retain an atomic-like

configuration in different environments. The idea behind PP is to solve the problem of the nucleus and core electrons once and then consider this part of the system as frozen. The remaining valence electrons feel a softer potential $v_s(\boldsymbol{r})$ in Eq. (2.15) and their density can be described with fewer plane-waves, making the calculation faster.

The augmented-plane waves (APW) and projector augmented-plane waves (PAW) [124] methods are generalizations of the PP concept. In the APW, space is divided into atom-centred augmentation spheres, and inter-atomic space and the wavefunctions are described differently in these two regions. In the PAW method, the valence wavefunctions rapidly oscillating near the nuclei are transformed through a linear transformation $\hat{\mathcal{T}}$ into smooth functions. This transformation can be inverted, allowing for the calculation of all-electron properties. In the PAW method, the creation of a PP consists of tabulating atom-specific transformations $\hat{\mathcal{T}}$.

Exchange Correlation Functional

Probably the most delicate step in the implementation of the KS equation is to define an analytical form for the exchange-correlation functional. The simplest approximation of v_{xc} is known as the local density approximation (LDA), in which the results of the homogeneous electron gas are applied locally to the system under study. The LDA can be regarded as an extension of the Thomas-Fermi electron model [125, 126], in which the constant density of kinetic energy is artificially made local

$$t_s^{\text{hom}}(n) \approx t_s\left(n(\boldsymbol{r})\right) = \frac{3\hbar}{10m}(3\pi^2)^{2/3} n(\boldsymbol{r})^{5/3}. \tag{2.23}$$

where t_s is now a function of the density $n(\boldsymbol{r})$. Once an analytical expression for the kinetic energy is known, LDA exchange-correlation energy is then defined as

$$E_{xc}^{\text{LDA}}[n](\boldsymbol{r}) = \int d\boldsymbol{r}\, \epsilon_{xc}^{\text{hom}}[n(\boldsymbol{r})], \tag{2.24}$$

where $\epsilon_{xc}^{\text{hom}} = \epsilon_x^{\text{hom}} + \epsilon_c^{\text{hom}}$, where the exchange part can be computed analytically, while the correlation function is parametrised from quantum Monte Carlo simulations.

The natural step forward from LDA is to include information on the variation of the density as well, much like in a Taylor expansion. The Generalized Gradient Approximation (GGA) [127] also exploit the information of how the density varies through space, i.e. $\nabla n(\boldsymbol{r})$, to build the exchange correlation functional. The energy is written as a general functional of the density and its gradient

$$E_{xc}^{\text{GGA}}[n](\boldsymbol{r}) = \int d\boldsymbol{r}\, f(n(\boldsymbol{r}), \nabla n(\boldsymbol{r})) \tag{2.25}$$

and different GGA flavours rely on different choices for $f(n, \nabla n)$, based on fitting against a reference set and/or satisfying known constraints for the real density $n_0(\boldsymbol{r})$.

Following the same reasoning, one could include more information in the functional form of E_{xc}. Meta-GGA functionals are an example of this approach, like Strongly Constrained

and Appropriately Normed (SCAN) [128]. These functionals include kinetic energy density τ_{kin} explicitly in the functional:

$$E_{xc}^{\text{meta-GGA}}[n](\boldsymbol{r}) = \int d\boldsymbol{r} f(n(\boldsymbol{r}), \nabla n(\boldsymbol{r}), \tau_{\text{kin}}). \tag{2.26}$$

The additional information used to compute the density improves the performance of SCAN in describing complex systems, like metal oxides and layered materials, but results in more expensive calculations and slower convergence [129].

van der Waals Interactions

It is challenging to capture van der Waals (vdW) interactions within the DFT framework with local or semi-local functionals, due to their non-local and long-range nature.This problem can be tackled in two ways: empirical correction and non-local functionals.

An empirical correction is added a posteriori to the solution of the KS equations. In the case of DFT-D2, a popular choice implemented by Grimme [130], the correction as a function of the inter-atomic distances R_{ij} reads

$$E_{\text{D2}} = -s_6 \sum_{ij} \frac{C_6(ij)}{R_{ij}^6} f_{\text{damp}}(R_{ij}), \tag{2.27}$$

where s_6 is a scaling factor, and $C_6(ij)$ is the strength of the interaction between i and j atom types. The function $f_{\text{damp}}(R_{ij})$ tempers the attractive interactions as the atoms get close. This methods provides a computationally inexpensive solution but decouples the vdW description from the electron density completely. Moreover, it can suffer from transferability problems between different functionals, because it relies on the fine parametrization of the empirical potential.

A non-local functional of the form

$$E_c^{nl} = \int d\boldsymbol{r} d\boldsymbol{r'} n(\boldsymbol{r}) \Theta(\boldsymbol{r}, \boldsymbol{r'}) n(\boldsymbol{r'}) \tag{2.28}$$

based on the kernel $\Theta(\boldsymbol{r}, \boldsymbol{r'})$ can be included explicitly in the KS equation, thus providing a vdW correction directly from the electron density [131, 132]. In the case of rVV10 correction, proposed by Vydrov and Van Voorhis [132], the kernel combines the local plasma frequency of the electron gas $\omega_{\text{p}}(\boldsymbol{r})$, the local band gap given $\omega_{\text{g}}(\boldsymbol{r})$ and the local Fermi velocity $v_{\text{F}}(\boldsymbol{r})$. The functional form of the kernel assures damping at a short distance and vdW $\sim 1/R^6$ behaviour for $R \to \infty$. This method is computationally more expensive but more transferable than the empirical approach.

Fig. 2.2 reports the binding energy $E(d)$ as a function of bilayer distance d for MoS_2 and Ti_2 bilayers, with and without vdW corrections. The curve with rVV10 correction, solid lines, show a clear bounded state for both compounds, with negative formation energy compared to isolated monolayers $E(\infty)$. In contrast, the curves obtained with a non-correct GGA kernel, dashed ones, show no bounded state, only repulsion at a short distance. This

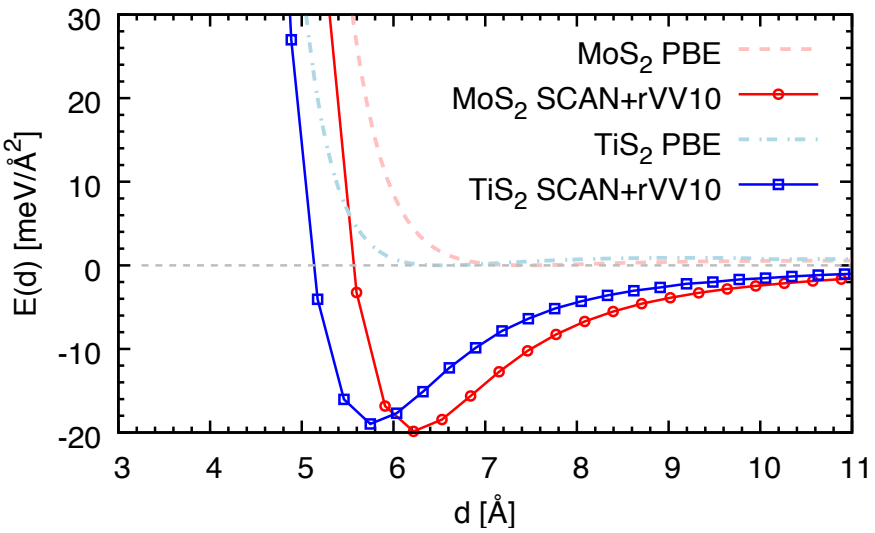

Figure 2.2: Binding energy $E(d)$, in meV/$\mathring{A}$ as a function of bilayer distance d, in $\mathring{A}$. Compounds and model are reported in the legend.

test confirms the need for vdW correction in layered materials.

2.2 Cluster Expansion

DFT simulations are a powerful tool, providing a great amount of information about a system relying on minimal approximations and almost no empirical parameters. This accuracy, in turn, limits the size of the system one can treat: a few hundred of atoms for standard DFT codes or thousands for linear-scaling solutions [67, 133]. The time-scale is also limited to pico- or nano-seconds. Classical MD simulations can reach hundreds of thousands of atoms and a time-scale in the order of microseconds. While valuable thermodynamics information can be gained at this level, rare events, like dopant diffusion and phase transitions, are difficult to sample. A solution to this problem is found in statistical mechanical tools, and the concept of coarse-grained models: information from *First Principles* calculations is transferred to a classical model, simple enough to be computationally cheap compared to DFT, but accurate enough to describe the property of interest.

The Connolly-Williams or cluster expansion (CE) method falls into this idea of multi-scale modelling [41]. It was initially developed to describe different phases of metal alloys characterized by different arrangements of the species within a fixed underlying lattice. It is thus suitable to handle configurational problems and discrete phase spaces. The configurational energy of the system is mapped on a generalized Ising model

$$E^{(\mathrm{DFT})}(\boldsymbol{R}_1, \ldots, \boldsymbol{R}_N) \rightarrow E^{(\mathrm{CE})}(\sigma_1, \ldots, \sigma_N), \tag{2.29}$$

where $\boldsymbol{R}_i$ is position of ion i in 3D space and σ_i is the occupancy of lattice sites i. In doing so, the information about the exact position of the ions in space is discarded, and only information about the atom type occupying each lattice site is retained. Fig. 2.3 sketches this approximation, with displaced positions of blue and white atoms mapped onto a square lattice. A spin variable, +1 for blue atoms and -1 for white ones, is associated with each lattice site. Any local relaxation of the lattice is treated implicitly [134].

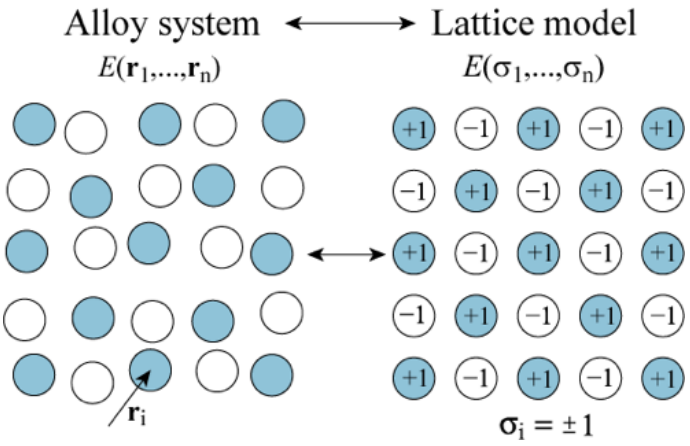

Figure 2.3: Sketch of the CE mapping of a real crystal system onto a fixed-lattice Ising model.

2.2.1 Cluster Algebra

The CE approach emerges from introducing a suitable change of basis for the functions defined on a lattice [135]. The goal is to be able to write any function defined on the lattice as a series expansion onto a 'convenient' basis set, where convenient here means that the series converges fast with respect to the number of basis functions considered and is easy to parametrize. This section focuses on the binary system where each lattice site can assume two distinct values and a brief comment about multi-component systems is given at the end of the section.

Let L be a lattice of N sites. The configuration of the lattice is fully specified by the vector $\boldsymbol{\sigma} = (\sigma_1, \ldots, \sigma_N)$ assigning a value $\sigma_i = \pm 1$ to each site. The phase space of the system is thus composed of 2^N configurations. The first step in developing a basis for the space of functions on the lattice is to define an inner product on it. Let $g(\boldsymbol{\sigma})$ and $f(\boldsymbol{\sigma})$ be general functions on L, the inner product is defined:

$$\langle g, f \rangle = 2^{-N} \sum_{\{\boldsymbol{\sigma}\}} g(\boldsymbol{\sigma}) f(\boldsymbol{\sigma}), \tag{2.30}$$

where the sum is take over the set of all possible configurations $\{\boldsymbol{\sigma}\}$.

Single site function Firstly, consider a lattice with a single site $N = 1$. Since the phase space is composed of two configurations and two possible values of the site, consider an ortho-normal basis of two functions:

$$\varphi_0(\sigma) = 1 \tag{2.31}$$

$$\varphi_1(\sigma) = \sigma. \tag{2.32}$$

It is readily verified that the set $\varphi_i(\sigma)$ satisfied ortho-normality and completeness under the product defined in Eq. (2.30):

$$\langle \varphi_i(\sigma), \varphi_j(\sigma) \rangle = \frac{1}{2} \left[\varphi_i(+1) \cdot \varphi_j(+1) + \varphi_i(-1) \cdot \varphi_j(-1) \right] = \delta_{ij} \tag{2.33}$$

$$\sum_s \varphi_s(\sigma) \varphi_s(\sigma') = 1 \cdot 1 + \sigma \cdot \sigma' = 2\delta_{\sigma\sigma'} \tag{2.34}$$

For example, a function of the single lattice site can be expanded on this basis set:

$$f(\sigma) = \sum_s a_s \varphi_s(\sigma) \tag{2.35}$$

$$a_s = \langle f, \varphi_s \rangle. \tag{2.36}$$

Explicitly, the coefficients are

$$a_0 = \frac{1}{2}[f(+1)\varphi_0(+1) + f(-1)\varphi_0(-1)] = \frac{1}{2}[f_+ + f_-] \tag{2.37}$$

$$a_1 = \frac{1}{2}[f(+1)\varphi_1(+1) + f(-1)\varphi_1(-1)] = \frac{1}{2}[f_+ - f_-], \tag{2.38}$$

where the subscript $f_\pm$ is shortcut for the value of the lattice site. Any function of the single site can thus be written as

$$f(\sigma) = \sum_s a_s \varphi_s(\sigma) = \frac{1}{2}[(f_+ + f_-) + (f_+ - f_-)\sigma]. \tag{2.39}$$

Cluster functions We shall now build a basis set for a lattice of arbitrary size. This choice is not unique, and here we build the basis as the product of single-site functions:

$$\Phi_{\boldsymbol{s}} = \varphi_{s_1}(\sigma_1)\varphi_{s_2}(\sigma_2)\dots\varphi_{s_N}(\sigma_N) = \prod_{i=1}^{N}\varphi_{s_i}(\sigma_i), \tag{2.40}$$

where the vector $\boldsymbol{s}$ defines which function φ_{s_i} in Eq. (2.31) is associated with each site σ_i. The set of functions defined in Eq. (2.40) is ortho-normal

$$\langle \Phi_{\boldsymbol{s}}, \Phi_{\boldsymbol{p}} \rangle = 2^{-N} \sum_{\boldsymbol{\sigma}} \Phi_{\boldsymbol{s}}(\boldsymbol{\sigma})\Phi_{\boldsymbol{p}}(\boldsymbol{\sigma}) \tag{2.41}$$

$$= 2^{-N} \sum_{\sigma_1=-1}^{+1} \cdots \sum_{\sigma_N=-1}^{+1} \varphi_{s_1}(\sigma_1)\dots\varphi_{s_N}(\sigma_N)\cdot\varphi_{p_1}(\sigma_1)\dots\varphi_{p_N}(\sigma_N) \tag{2.42}$$

$$= 2^{-N} \sum_{\sigma_1=-1}^{+1} \varphi_{s_1}(\sigma_1)\varphi_{p_1}(\sigma_1)\dots \sum_{\sigma_N=-1}^{+1} \varphi_{s_N}(\sigma_N)\varphi_{p_N}(\sigma_N) \tag{2.43}$$

$$= 2^{-N} \prod_i \langle \varphi_{s_i}(\sigma_i)\varphi_{p_i}(\sigma_i)\rangle = \delta_{\boldsymbol{sp}}, \tag{2.44}$$

where, in the last equality, Eq. (2.33) was used. The set of functions is also complete:

$$\sum_{\boldsymbol{s}} \Phi_{\boldsymbol{s}}(\boldsymbol{\sigma})\Phi_{\boldsymbol{s}}(\boldsymbol{\sigma'}) = \sum_{s_1=0}^{1} \cdots \sum_{s_N=0}^{1} \prod_i \varphi_{s_i}(\sigma_i) \prod_i \varphi_{s_i}(\sigma_i') \tag{2.45}$$

$$= \sum_{s_1=0}^{1} \varphi_{s_1}(\sigma_1)\varphi_{s_1}(\sigma_1')\cdots \sum_{s_N=0}^{1} \varphi_{s_N}(\sigma_N)\varphi_{s_N}(\sigma_N') \tag{2.46}$$

$$= 2^N \delta_{\boldsymbol{\sigma\sigma'}}, \tag{2.47}$$

where in the last equality Eq. (2.34) was used. Any function defined on the lattice can thus be written as

$$f(\boldsymbol{\sigma}) = \sum_{\boldsymbol{s}} a_{\boldsymbol{s}} \Phi_{\boldsymbol{s}}(\boldsymbol{\sigma}). \tag{2.48}$$

Because the identity with respect to the product $\varphi_0 = 1$ is included in the basis set, the expansion in Eq. (2.48) can be re-interpreted as a sum over all possible sub-clusters α of $n = 0, \ldots, N$ sites of the lattice L:

$$f(\boldsymbol{\sigma}) = a_0 + \sum_{\alpha \subseteq L} a_\alpha \Phi_\alpha(\boldsymbol{\sigma}) \tag{2.49}$$

$$a_0 = \langle f, 1 \rangle,\ a_\alpha = \langle f, \Phi_\alpha \rangle \tag{2.50}$$

$$\Phi_\alpha = \sigma_{\alpha_1} \ldots \sigma_{\alpha_n}, \tag{2.51}$$

where now φ_0 has effectively disappeared from the expansion. To better clarify the last passage, consider as an example a lattice of two sites $N = 2$ and consider a function of the pair sites

$$f(\sigma_1, \sigma_2) = \sum_{ij} a_{ij} \Phi_{ij}(\sigma_1, \sigma_2), \tag{2.52}$$

where by Eq. (2.36)

$$a_{00} = \frac{1}{4}[f_{++} + f_{-+} + f_{+-} + f_{--}] \tag{2.53}$$

$$a_{01} = \frac{1}{4}[f_{++} + f_{-+} - f_{+-} - f_{--}] \tag{2.54}$$

$$a_{10} = \frac{1}{4}[f_{++} - f_{-+} + f_{+-} - f_{--}] \tag{2.55}$$

$$a_{11} = \frac{1}{4}[f_{++} - f_{-+} - f_{+-} + f_{--}], \tag{2.56}$$

and thus

$$\begin{aligned} f(\sigma_1, \sigma_2) = \frac{1}{4}[&(f_{++} + f_{-+} + f_{+-} + f_{--}) \\ &+ (f_{++} + f_{-+} - f_{+-} - f_{--})\sigma_1 \\ &+ (f_{++} - f_{-+} + f_{+-} - f_{--})\sigma_2 \\ &+ (f_{++} - f_{-+} - f_{+-} + f_{--})\sigma_1\sigma_2], \end{aligned} \tag{2.57}$$

Symmetry of the lattice Since the inner product Eq. (2.30) retains the symmetry of the lattice L [135] all sub-cluster β equivalent to α under a symmetry operation of the lattice (including translations) will yield the same coefficient a_α in the expansion Eq. (2.49). The set $\Omega_L(\alpha)$ of clusters related to α by symmetry operation in the lattice point group Ω_L are termed *orbit of* α. We can thus write Eq. (2.49) as

$$f(\boldsymbol{\sigma}) = \sum_{\alpha} p_\alpha J_\alpha \Pi_\alpha(\boldsymbol{\sigma}), \tag{2.58}$$

where α runs over symmetry distinct clusters, p_α is the number of equivalent clusters, i.e. the multiplicity of each term, and the expansions coefficients J_α, termed Effective Cluster

Interactions (ECI), and are related to the $a_{\boldsymbol{s}}$ in Eq. (2.49) by

$$J_\alpha = N a_{\boldsymbol{s}}, \tag{2.59}$$

where $\boldsymbol{s}$ identifies one cluster in the orbit $\Omega_L(\alpha)$. The symmetry-averaged cluster function $\Pi_\alpha(\boldsymbol{\sigma})$ are called *orbit average* and are defined as

$$\Pi_0(\boldsymbol{\sigma}) = 1 \tag{2.60}$$

$$\Pi_\alpha(\boldsymbol{\sigma}) = \frac{1}{N p_\alpha} \sum_{\beta \in \Omega_L(\alpha)} \Phi_\beta(\boldsymbol{\sigma}), \tag{2.61}$$

where the factor N in the definition of Π_α accounts for the translational symmetry over the lattice. As an example consider the $N = 3$ triangular lattice in Fig. 2.4. In this example, the lattice is composed of three isolated sites, so that no translational symmetry is present in the system and only the point group is relevant. The lattice presents $3m$ point group symmetry, highlighted by the axes m_1, m_2 and m_3 in Fig. 2.4. The phase space contains $2^3 = 8$ configurations $\boldsymbol{\sigma}$ and thus the functional space of the lattice is spawned by the eight cluster functions: the empty cluster $\Phi_0 = 1$, three point function $\Phi_\alpha = \sigma_i$, three pair functions $\Phi_\alpha = \sigma_i \sigma_j$ and one triplet $\Phi_\alpha = \sigma_i \sigma_j \sigma_k$, as shown in Fig. 2.4. The point and pair cluster are equivalent under the reflections defined by the axes $\{m_i\}$, yield multiplicity $s_{1,2} = 3$ and, thus, from Eq. (2.58) any function on this lattice has the form

$$f(\boldsymbol{\sigma}) = J_0 + 3J_1\Pi_1(\boldsymbol{\sigma}) + 3J_2\Pi_2(\boldsymbol{\sigma}) + J_3\Pi_3(\boldsymbol{\sigma}). \tag{2.62}$$

For example, the pair symmetry-averaged function and the corresponding ECI read

$$\Pi_2(\boldsymbol{\sigma}) = \frac{1}{3}(\Phi_{12}(\boldsymbol{\sigma}) + \Phi_{13}(\boldsymbol{\sigma}) + \Phi_{23}(\boldsymbol{\sigma})) \tag{2.63}$$

$$\begin{aligned} J_2 =& \frac{1}{8}(f_{+++} + f_{++-} - f_{+-+} - f_{-++} \\ & - f_{+--} + f_{--+} - f_{-+-} + f_{---}) \end{aligned} \tag{2.64}$$

$$= \frac{1}{4}(\langle f_{++}\rangle - \langle f_{+-}\rangle - \langle f_{-+}\rangle + \langle f_{--}\rangle), \tag{2.65}$$

where the notation $\langle f_{++}\rangle$ in Eq. (2.65) indicates an average over all the configurations in which $\sigma_1 = +1$ and $\sigma_2 = +1$. Thus, the meaning of the term *effective interactions* for J_α is clear: the interaction is a result of "mean-field" approach, as the possible configurations of the cluster see an average value of the remaining lattice.

Expansion Convergence The expansion in Eq. (2.58) is written in terms of a complete, orthogonal basis set and is therfore exact. However, in the thermodynamic limit of infinite sites, the sum is infinite and thus of little practical utility. For any application, the series must be truncated. The hope is that the sum converges rapidly and a satisfying description of the system is retained when considering only a few clusters, deemed to be the dominant terms, and neglecting the rest. The convergence of the series can only be tested numerically

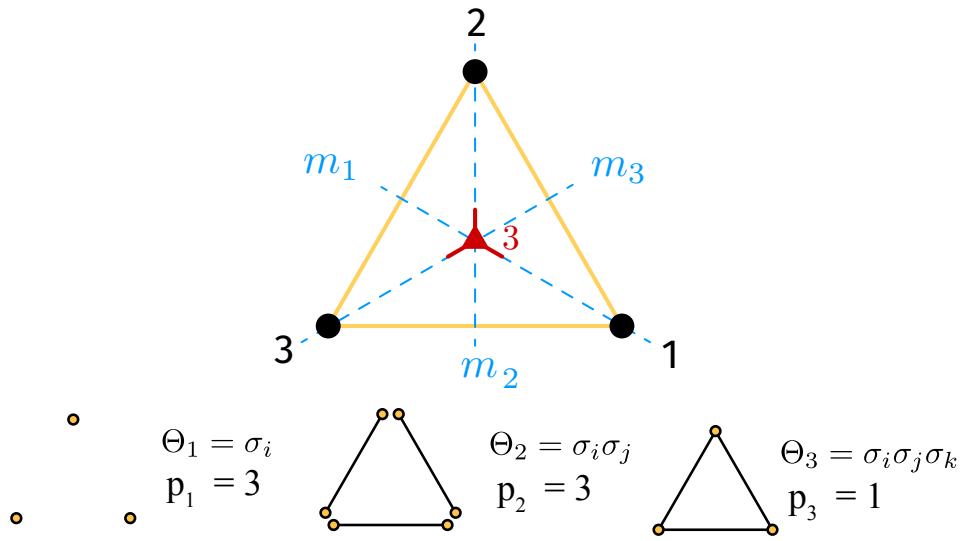

Figure 2.4: Example of symmetrically equivalent clusters in a three-points triangular lattice.

by checking that the ECI J_α decay with the radius of the cluster and the number of sites in them [42, 135]. As of now, the formalism has been developed in terms of general functions on the lattice L. In most cases, the quantity expanded is the total energy of a configuration $E(\boldsymbol{\sigma})$ in a substitutional alloy system. In this case, the convergence of the expansion in Eq. (2.58) is intuitively supported by the shortsightedness of the many-body interactions between the ions [116]. On the other hand, the discrete nature of the model makes the description of long-range elastic interaction challenging [136].

2.2.2 Hamiltonian Parametrisation

A common way to implement the theory outlined in the previous section is to fit the ECIs of relevant m clusters against the energies of n configurations, obtained with high-quality, expensive methods, e.g. DFT simulations, on small systems. Regardless of the choice of specific basis functions $\Phi_\eta(\boldsymbol{\sigma})$ and how the relevant figures are selected, the column vector of n computed energies $\boldsymbol{E}$ and the vector $\boldsymbol{J}$ of the m ECI are related via the matrix $\underline{\underline{Z}}$:

$$E_\sigma = \sum_\alpha Z_{\sigma\alpha} J_\alpha. \tag{2.66}$$

Each of the n rows $\boldsymbol{Z}_i$ of the matrix represents the m correlation functions of the selected cluster function for that configuration. The CE model fitting can be cast in the form of a minimisation problem

$$\boldsymbol{J}_\lambda = \min_{\boldsymbol{J}} \left[\sum_{\sigma=1}^{n} w_\sigma (E_\sigma - \boldsymbol{Z}_\sigma \cdot \boldsymbol{J})^2 + R(\lambda, \boldsymbol{J}) \right], \tag{2.67}$$

where $(E_\sigma - \boldsymbol{Z}_\sigma \cdot \boldsymbol{J})^2$ is the square distance between the computed energies and the fitted ones, weighed by w_i and $R(\lambda, \boldsymbol{J})$ is a regularisation function. The regularisation is useful because the dimensionality of the inversion problem, n structure for m coefficients, makes

the fitting an ill-posed problem [137]. Moreover, $R(\lambda, \boldsymbol{J})$ can also bias the minimization according to physical intuition.

The selection of relevant clusters α to include is based on the concept of cross-validation (CV) [134]. Different CEs models are trained via Eq. (2.67) against a training set and their predictive power is tested against a validation set, yielding a cross-validation score

$$CV = \frac{1}{n}\sum_{i=1}^{n}\left(E_i - \bar{E}_i\right)^2, \tag{2.68}$$

where E_i are the reference energies of the testing sets and $\bar{E}_i$ are the energies predicted by the CE model. This protocol selects the CE model with the highest predictive power (best CV score) rather than the lowest deviation from the training set (best fit).

2.2.3 Monte Carlo Simulations

The idea behind the vast class of Monte Carlo methods is to use random numbers to obtain numerical results. Most of the time, in physics, Monte Carlo is associated with the Metropolis algorithm and the purpose of sampling the Boltzmann distribution of a system without relying on any knowledge of the partition function. Monte Carlo simulations are used to sample Boltzmann distributions defined by the CE Hamiltonian on the lattice model describing the alloy system.

The simulations are carried out in the semi-grand canonical ensemble: total energy E and atom species concentration x on the fixed N lattice sites vary during the evolution, while temperature T and chemical potential μ are kept fix. This ensemble has the advantage of sampling only pure phases of the system: as the concentration is free to change, no grain boundaries and phase coexistence can form in the system. Thus, the behaviour of the properties considered arises from pure phases, without any signal from interfaces. The evolution of the system is controlled by the following thermodynamic potential [138]:

$$\phi(\beta, \mu) = -\frac{1}{\beta N}\log\left(\sum_i e^{-\beta N(E_i - \mu x_i)}\right), \tag{2.69}$$

where $\beta = 1/k_{\mathrm{B}}T$, E_i and x_i are, respectively, the energy and concentration associated with micro-state i. The system properties are studied by carrying out equilibrations on a grid of μ and T values. Observables can be estimated by averaging over equilibrated configurations. For example, by looking at the concentration itself, one can obtain the stability window of different phases as a function of the temperature.

Simulations on the grid can be concatenated in two different ways, as sketched in Fig. 2.5, and the initial grand potential is obtained from either high- or low-temperature expansions [138]. In the high-temperature limit, the starting point is $T = \infty$, where the behaviour is well approximated as an ideal solid solution with entropy $\beta S(x) = -x\log x$ and concentration $x = 1/2$. The system is started from a random configuration at this concentration and cooled down at a fixed μ mimicking an annealing process. Conversely,

in the low-temperature limit, the temperature is kept fixed, and μ is varied. The energy and entropy costs are estimated in the single-spin-flip approximation, which is justified by the low thermal energy available to the system. The limit of this approximation must be determined case by case.

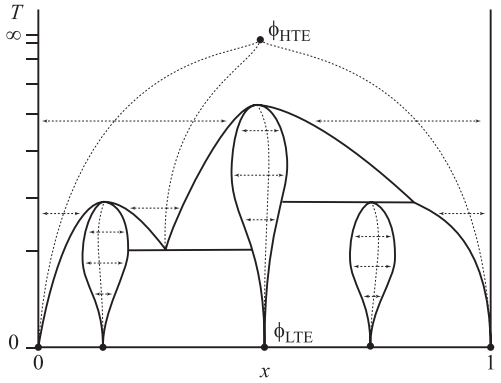

Figure 2.5: Example of paths of integration during a MC simulation in the $\mu - T$ space. Adapted from [138].

2.3 Classical Molecular Dynamics

Classical MD or Molecular Mechanics (MM) uses a classical approach to simulate atoms and molecules. Atoms are considered to be a point-like object interacting with one another. The total potential energy of the system of N atoms is expanded in many-body terms [139]:

$$U(\boldsymbol{r}_1, \ldots, \boldsymbol{r}_N) = \sum_i U_1(\boldsymbol{r}_i) + \sum_{i,j} U_2(\boldsymbol{r}_i, \boldsymbol{r}_j) \sum_{i,j,k} + U_3(\boldsymbol{r}_i, \boldsymbol{r}_j, \boldsymbol{r}_k) + \ldots, \tag{2.70}$$

where $\mathbf{r}$ the Cartesian position and V_is are one-body, pair, triplet interactions.

Force Fields

FF is a functional description approximation of the atom interactions comprising the potential energy in Eq. (2.70). The FF entails a set of parameters that is system dependent and defines the behaviour of the functional form. These parameters are benchmarked on experiments or more precise DFT calculations. In the most general sense, there are two types of particle interactions, bonded and non-bonded [139, 140]. The bonded interactions represent the covalent bonds between atoms. Three components usually approximate these interactions: stretching of the bonds, the angle from bending of the bonds and the dihedral from torsion of the bonds. The functional forms of these are [139]:

$$U_{\text{stretching}}(\boldsymbol{r}_i, \boldsymbol{r}_k) = k_b(r_{ij} - r_0)^2 \tag{2.71}$$

$$U_{\text{bending}}(\boldsymbol{r}_i, \boldsymbol{r}_j, \boldsymbol{r}_k) = k_\theta(\theta_{ijk} - \theta_0)^2 \tag{2.72}$$

$$U_{\text{torsion}}(\boldsymbol{r}_i, \boldsymbol{r}_j, \boldsymbol{r}_k, \boldsymbol{r}_l) = \frac{V_n}{2}[1 + cos(\tau_{ijkl} - \tau_0)], \tag{2.73}$$

where $r_{ij} = |\boldsymbol{r}_i - \boldsymbol{r}_j|$, k_b is the harmonic constant for the bonds, r_0 is the equilibrium bond length, k_θ is the harmonic constant for the bending, θ_0 is the equilibrium bond angle, V_n is the torsion constant, and τ_0 is the equilibrium dihedral angle. θ_{ijk} identifies the angle between the three atoms i, j, k and τ_{ijkl} is the dihedral angle between the four atoms i, j, k, l.

The non-bonded interactions represent the van der Waals and electrostatic interactions[140, 139]. A common choice to represent van der Waals contribution is the Lennard-Jones (LJ) potential, which has a short-range repulsive and long-range attractive character:

$$U_{\mathrm{LJ}}(\boldsymbol{r}_i, \boldsymbol{r}_j) = 4\epsilon_{ij}\left[\left(\frac{\sigma_{ij}}{r_{ij}}\right)^{12} - \left(\frac{\sigma_{ij}}{r_{ij}}\right)^{6}\right], \tag{2.74}$$

where σ_{ij} controls the equilibrium distance and ϵ_{ij} the strength of the interaction between the atoms ij. A Coulomb potential represents the electrostatic term:

$$U_{\mathrm{C}}(\boldsymbol{r}_i, \boldsymbol{r}_j) = \frac{q_i q_j}{\epsilon r_{ij}}, \tag{2.75}$$

where ϵ_{ij} and σ_{ij} are empirical coefficients, r_{ij} is inter-particle distance, q_i and q_j the partial charges, and ϵ the permittivity.

Computer Experiments

Using the FF described above, one can determine the instantaneous energy of a system. However, almost always one would like to find the minimum energy configuration of a system or perform some sort of dynamics on the system. Using the FF and Newtonian dynamics (or a minimization algorithm), MD can simulate the conformation landscape and simulate the system evolution. This evolution is assumed to resemble a real experiment closely. Once the system is equilibrated, the "in-silico" experiment can start, and any observable of interest A can be measured from its expression in terms of atom positions and velocities.

The basic working scheme of an MD simulation is as follows[140]. In the first step, t_0, the system is initialized, providing the positions of all atoms. Velocities of all atoms are assigned according to the Boltzmann distribution at the given temperature. Next follows the central part of the program, the calculation of the forces, which scales with the number of particles. In the case of Newton dynamics, the positions evolve according to [139, 140]

$$F_i = -\nabla_{\boldsymbol{r}_i} U = m_i \cdot \frac{d\boldsymbol{r}_i^2}{dt^2}. \tag{2.76}$$

The equation above is, in general, not solvable analytically and is integrated numerically, e.g. with the Verlet algorithm [141]. Finally, the observable $A(t_0)$ is measured, the position updated, and the system advanced to t_1.

The expectation value of the observable A is obtained by thermodynamic sampling

along the MD trajectory

$$\langle A \rangle_{t_\mathrm{s}} = \int_{-\infty}^{+\infty} dt A(t) \approx \frac{1}{t_\mathrm{s} - t_\mathrm{eq}} \sum_{t_i = t_\mathrm{eq}}^{t_\mathrm{s} - t_\mathrm{eq}} A(t_i), \tag{2.77}$$

where t_s is the total simulation time and t_eq is the equilibration time. This average is taken to be representative of the true behaviour of the system under the ergodic assumption and, thus, the time average is equivalent to the phase space average [142], i.e.

$$\lim_{t_\mathrm{s} \to \infty} \langle A \rangle_t \equiv \langle A \rangle_\Gamma \int \int d\boldsymbol{p} d\boldsymbol{q} A(\boldsymbol{q}, \boldsymbol{p}), \tag{2.78}$$

where Γ is the volume phase space of the system generated by the conjugate variable $\boldsymbol{q}, \boldsymbol{p}$. The finite time t_s after which the limit in Eq. (2.78) can be considered satisfied needs to be carefully tested for each system to avoid under-sampling of the phase space. Moreover, the initial condition of the system must be chosen carefully, as the system could get trapped in subtle local minima in the potential energy manifold. To benchmark against this problem, equivalent MD simulations with slightly different initial condition are computed and compared.

2.4 Materials Descriptors

2.4.1 Equation of State

The first descriptor useful when dealing with phase stability of materials is the Equation of State (EoS) of a crystalline phase, that is the energy of cohesion as a function of the volume. The EoS describes the energy paid by shifting a crystalline system away from its equilibrium volume, e.g. by applying pressure on a sample. Many empirical models describe the relationship between thermodynamic quantities at varying pressure [143]. In particular, the Birch-Murnaghan (BM) EoS equation is adopted [144, 145], which is based on a third-order approximation of the free energy F in the strain component and a linear approximation of the bulk modulus as a function of pressure in isothermal processes [145]

$$B(P) = -V \left. \frac{\partial P}{\partial V} \right|_T \tag{2.79}$$

$$= B(0) + \left. \frac{\partial B}{\partial P} \right|_{P=0} P = B_0 + B_0' P, \tag{2.80}$$

where the bulk modulus at zero pressure $B_0 = -V \left. \frac{\partial P}{\partial V} \right|_{P=0,T}$ was defined, along with its derivative with respect to pressure $B_0 = \left. \frac{\partial B}{\partial P} \right|'_{P=0}$. At zero temperature, the energy-volume relation as a function of the reduced volume $\eta = (V_0/V)^{2/3}$ is given by [145]

$$E(\eta) = E_0 + \frac{9}{16} B_0 V_0 (\eta - 1)^2 (2 + (B_0' - 4)(\eta - 1)), \tag{2.81}$$

where E_0 is an arbitrary shift and V_0 is the equilibrium volume. The model is expected to be accurate only at moderate compression, as it is based on a linear expansion of the bulk modulus [145]. The quantities appearing in Eq. (2.81) can be computed from experiments or DFT calculations or, provided a set of energy-volume pairs, they can be regarded as free parameters in a fitting procedure, as shown in Fig. 2.6.

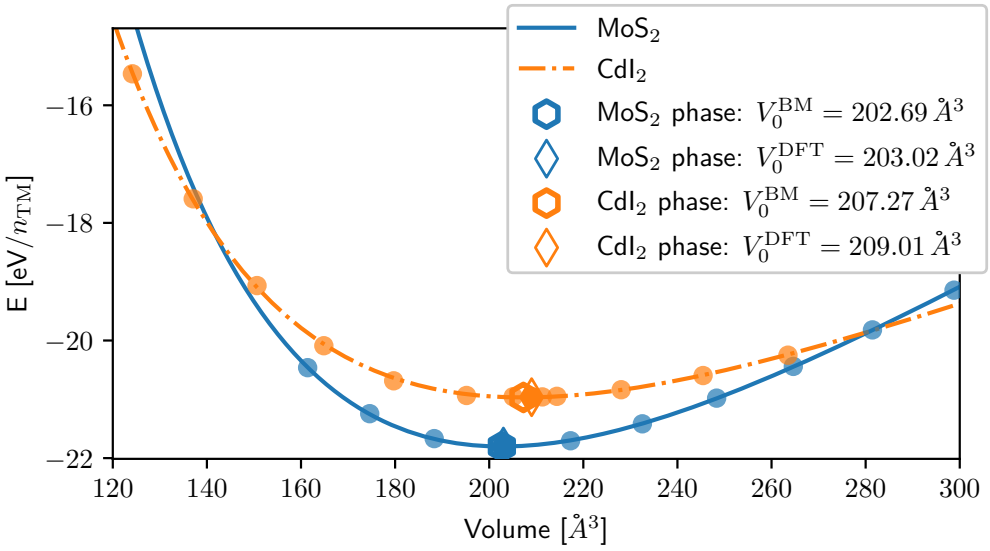

Figure 2.6: EoS for MoS_2 in its stable trigonal prismatic phase, termed MoS_2 prototype, and in the unstable octahedral phase, CdI_2 prototype. The coloured circles report DFT calculations while the lines refer to BM fit of Eq. (2.81).

2.4.2 Crystal Field Theory

The Crystal Field (CF) Theory is a simple electrostatic model that describes the effect of charged ions on the energy levels of a TM. The model assumes a complete ionization of the TM and the negatively charged ligands are regarded as point-like charges, i.e. purely ionic bonding. While this is a drastic simplification, and CF is not adequate to describe properties of real materials quantitatively, its physical interpretation is clear, and it can lead to a qualitative understanding of phase stabilization mechanisms.

Atomic Orbitals

The single-electron atomic orbitals, i.e. the hydrogen atom energy levels, are used to evaluate the CF Hamiltonian matrix elements. The starting point is the Schrödinger equation for a single electron in the electric field generated by the nucleus, which in atomic units reads

$$\left(-\frac{1}{2}\nabla^2 + V(\boldsymbol{r})\right)\psi_\lambda(\boldsymbol{r}) = E_\lambda \psi_\lambda(\boldsymbol{r}), \tag{2.82}$$

where λ labels the eigenvalues E_λ and eigenfunctions $\psi_\lambda(\boldsymbol{r})$. The potential $V(r)$ created by the nuclei charge at the origin of the reference frame is

$$V(\boldsymbol{r}) = -\frac{qZ}{r}, \tag{2.83}$$

where q is the unit charge and Z is the atomic number.

Because of the central potential Eq. (2.83) in the Schrödinger equation, Eq. (2.82) factorises in a angular part and a radial part and, thus, the eigenfunctions $\psi_\lambda(\boldsymbol{r})$ are:

$$\psi_\lambda(\boldsymbol{r}) = \psi_{nlm}(\boldsymbol{r}) = R_{nl}(r)Y_l^m(\theta,\phi), \tag{2.84}$$

in spherical coordinates $r \in [0,\infty)$, inclination $\theta \in [0,\pi]$, and azimuth $\phi \in [0,2\pi)$. The index λ has been decomposed into three quantum numbers: n is the energy level, emerging from the conditions that the radial part R_{nl} needs to satisfy [146], i.e. $n = 1,2,3,4,\ldots;$ l and m are the eigenvalues of the angular momentum operator $\hat{L}^2$, $l = 0,1,\ldots,n-1$ and $m = -l,;-1,0,1,\ldots,l$.

The angular part of Eq. (2.82) is a Laplace-type equation, and its eigenfunctions are the spherical harmonics [146][3]:

$$Y_l^m(\theta,\phi) = (-1)^m\sqrt{\frac{(2l+1)}{4\pi}\frac{(l-m)!}{(l+m)!}}P_{lm}(\cos\theta)e^{im\phi} \tag{2.85}$$

where $P_{lm}(x)$ are associated Legendre polynomials. The spherical harmonics are orthogonal under the following inner product [146]

$$\langle Y_l^m|Y_{l'}^{m'}\rangle = \int_0^{2\pi}\int_0^{\pi} Y_l^m(\theta,\phi)Y_{l'}^{m'} * (\theta,\phi)\sin\theta d\theta d\phi = \delta_{l,l'}\delta_{m,m'}. \tag{2.86}$$

The family of Y_l^m function is a basis for the space of functions defined on the sphere and, thus, any function in this space might be represented in terms of series of harmonics:

$$f(\theta,\phi) = \sum_{ml} c_{ml}Y_l^m(\theta,\phi). \tag{2.87}$$

The solution of the radial equation is the family of functions:

$$R_{nl}(r) = \sqrt{\left(\frac{2Z}{n}\right)^3\frac{(n-l-1)!}{2n(n+l)!}}e^{-Zr/n}\left(\frac{2Zr}{n}\right)^l L_{n-l-1}^{2l+1}\left(\frac{2Zr}{n}\right)$$

where L_i^α are the generalized Laguerre polynomials. The behaviour of R_{nl} is characterized by its n nodes. As $|\psi_{nlm}^2|$ represent the probability density of finding the particle of at a given position, the nodes in R_{nl} represent points in space where the probability of finding

[2]Because $[\hat{H},\hat{L}] = 0$, there is a complete set of eigenvalues that diagonalises both simultaneously.

[3]Following the usual definition for the spherical harmonics adopted in physics and chemistry, which includes the Condon–Shortley $(-1)^m$ phase factor

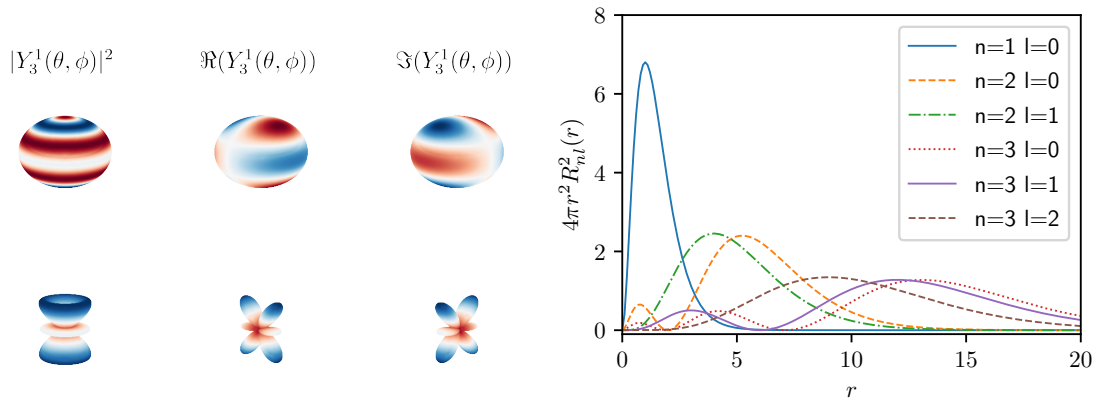

(a) **(b)**

Figure 2.7: (a) Representation of the spherical harmonic for $l = 3$, $m = 1$. The upper row shows the value of $|Y_1^3|^2$, $\Re(Y_1^3)$ and $\Im(Y_1^3)$ as coloured regions on the unitary sphere. To better appreciate the spatial variation of the harmonics, the bottom row shows the surface defined by the same quantities, i.e. $r = |Y_1^3|^2$, $r = \Re(Y_1^3)$, and $\Im(Y_1^3)$, respectively. (b) Radial distribution function $g(r) = 4\pi r^2 R_{nl}(r)$ for $1 \leq n \leq 3$ and corresponding allowed values of l.

an electron vanishes. Moreover, as the angular part $Y_l^m(\theta, \phi)$ is normalized, integration over the solid angle $\Omega = 4\pi$ yields the radial function, which thus represents the radial distribution function $g(r)$ of the system:

$$g(r) = \int_\Omega \psi(r, \theta, \phi) r^2 \sin\theta d\theta d\phi = 4\pi r^2 R_{nl}(r).$$

The radial distribution function, reported in Fig. 2.7b for a set of n, l values, has a direct physical interpretation: the probability of finding a particle at a distance r from the nucleus at any possible angle.

Crystal Field Potential

The electrostatic potential acting on a charge at position $\boldsymbol{r}$ generated by the set of ions at positions $\underline{R}$ is

$$V_{\underline{R}}(\boldsymbol{r}) = \sum_j \frac{q_j}{|\boldsymbol{r} - \boldsymbol{R}_j|}, \tag{2.88}$$

where R_j are the positions of the ions and q_j the corresponding charges. Since the crystal potential in Eq. (2.88) is a sum of central potentials centred on $\boldsymbol{R}_j$, it can be decomposed in a radial and angular part, and the latter expressed in terms of spherical harmonics in the form Eq. (2.87) [147]. Thus, the crystal potential can be written in the form [147, 146]:

$$V_{\underline{R}}(r, \theta, \phi) = \sum_{k=0}^{\infty} \sum_{q=-k}^{k} r^k \gamma_{kq} Y_k^q(\theta, \phi) \tag{2.89}$$

where the information about the ion lattice is embedded in

$$\gamma_{kq} = \sum_j^{\text{ions}} \frac{4\pi}{2k+1} \frac{q_j}{R_j^{k+1}} (-1)^q Y_k^{-q}(\theta_j, \phi_j). \tag{2.90}$$

The symmetry of atomic orbitals and orthogonality of spherical harmonics reduces the number of components in the infinite sum. For a fixed angular manifold l, the elements of the CF Hamiltonian are

$$\langle \psi_{nlm} | V_{\underline{R}} | \psi_{nlm'} \rangle \propto \langle Y_l^m | Y_k^q | Y_l^{m'} \rangle. \tag{2.91}$$

Because of the orthogonality of spherical harmonics in Eq. (2.86), $\langle Y_l^m | Y_k^q | Y_l^{m'} \rangle = 0$ if $k > 2l$. Thus, for p orbitals $k \leq 2$, $k \leq 4$ for d orbitals and $k \leq 6$ for f orbitals.

Octahedral Coordination As an example, consider the case of a transition metal of the d group in the six-fold octahedral coordination, i.e. cations of charge q_{C} positioned at the centre of the faces of a cube of side $2a$ centred on the TM, as shown in Fig. 2.8a. In this case, the expansion in Eq. (2.89) yields [147]

$$V_{\mathrm{oct}}(\boldsymbol{r}) = \frac{7\sqrt{\pi}}{3} \frac{q}{a^5} r^4 \left(Y_0^4(\theta, \phi) + \sqrt{\frac{5}{14}} \left(Y_4^4(\theta, \phi) + Y_{-4}^4(\theta, \phi) \right) \right). \tag{2.92}$$

By evaluating $\langle \psi_{nlm} | V_{\mathrm{oct}}(\boldsymbol{r}) | \psi_{nlm} \rangle$ one obtains the split of the d-orbitals manifold. The angular and radial parts factorize. The former describes *how* the manifold splits, while the latter the *magnitude* of such splitting, Dq:

$$Dq = -q_{\mathrm{C}} \frac{\langle r^4 \rangle_{R_{nl}}}{6a^5}, \tag{2.93}$$

where $\langle r^4 \rangle_{R_{nl}}$ indicates the average of the crystal field according to the radial part of the wavefunction.

The angular part $V_{\mathrm{oct}}(r_0, \theta, \phi)$ in Eq. (2.92) is reported in Fig. 2.8b. High energy regions (blue) point toward the ions: Coulomb interaction penalize electrons occupying this region. Lower energy regions (red), point in between the ions. The angular integrals evaluated on the d manifold via the orthogonality relation Eq. (2.86) yields the 5×5 matrix [146]

$$\langle \psi_{32m} | V_{\mathrm{oct}}(\boldsymbol{r}) | \psi_{32m'} \rangle = 10Dq \begin{pmatrix} 1 & 0 & 0 & 0 & 5 \\ 0 & -4 & 0 & 0 & 0 \\ 0 & 0 & 6 & 0 & 0 \\ 0 & 0 & 0 & -4 & 0 \\ 5 & 0 & 0 & 0 & 1 \end{pmatrix}. \tag{2.94}$$

The spectrum of Eq. (2.94) is composed of two degenerate eigenvalues [146, 148]: triple-degenerate low-energy $E_{t_{2g}} = -4Dq$ level and the double-degenerate high-energy $E_{e_g} = 6Dq$ level. As one might see from the angular behaviour shown in Fig. 2.8b, the low-energy orbitals are a linear combination of d_{xy}, d_{xz}, d_{yz}, that point in-between the negatively charged ions, while the high-energy orbitals are a combination of the remaining $d_{3z^2-r^2}$ and $d_{x^2-y^2}$ orbitals, which point towards the ions.

The CF theory thus provides an energy level structure. These energy levels are then

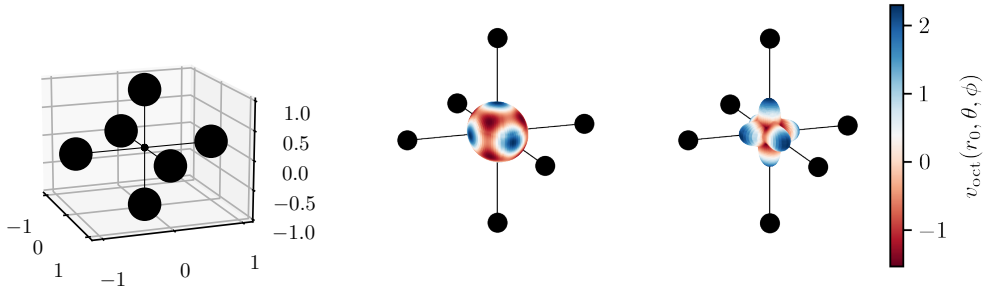

(a) **(b)**

Figure 2.8: (a) Octahedral coordination of the TM site, placed at the origin of the reference frame. (b) Angular dependence of the CF generated by the octahedral crystals. The left plots report the value of the potential on a sphere. The right plots highlight the angular dependence by drawing the surface defined by $r = V_{\mathrm{oct}}(r_0, \theta, \phi)$.

populated according to Hund's rules by the electrons retained on the TM site in a fully ionic picture.

2.4.3 Sliding Potential Energy Surface

In a nanocontact between two layers, the sliding behaviour is determined by the shape of the PES, which describes the interaction between two parts of the contact as a function of the relative position of the two. PES has been shown to regulate the frictional behaviour of several atomistic contacts [93, 149]. In the case of crystalline system, the PES can be evaluated by directly sampling translated configurations within the primitive cell of the system. Moreover, the underlying symmetry of each part can help reduce the number of expensive quantum mechanical calculations needed to sample the PES. Finally, a suitable interpolation protocol is developed, to allow evaluation of the PES at any given point.

Definition

Let S be a bilayer crystal defined in the unit cell $(\boldsymbol{a}, \boldsymbol{b}, \boldsymbol{c})$ and the collection of N atomic positions

$$\underline{S} = \{\boldsymbol{r}_{i,\nu_i}\},$$

where $\boldsymbol{r}_{i,\nu_i}$ is the position of atom i of type ν_i, amongst the set $\underline{\nu} = (\nu_0, \ldots, \nu_{n_\nu})$ of atom species in the system. Because the bilayer system is periodic only in two directions, it is always possible to arrange the unit cell so that $\boldsymbol{a}, \boldsymbol{b}$ lie in only the xy plane and $\boldsymbol{c}$ is along z. Defined by a cutting plane at height c_{cut} along the $\boldsymbol{c}$ axis, the system is divided into a top layer $\underline{t}$ of m atoms and bottom $\underline{b}$ one of n atoms:

$$\underline{b} = \{r^{\alpha}_{j,\mu_j} \in \underline{S} : r^{3}_{j,\mu_j} \leq c_{\mathrm{cut}}\}, \tag{2.95}$$

$$\underline{t} = \{r^{\alpha}_{j,\mu_j} \in \underline{S} : r^{3}_{j,\mu_j} > c_{\mathrm{cut}}\}, \tag{2.96}$$

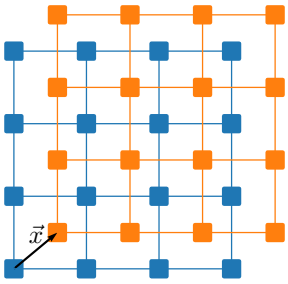

Figure 2.9: Example of point in the sliding PES. The top layer (orange grid) is translated with respect to the bottom one (blue grid) of a vector $\boldsymbol{x} = (0.6,\ 0.5)$.

where index α runs over the 3 spatial components. The PES $\mathcal{P}(\boldsymbol{x})$, is then defined as

$$\mathcal{P}(\boldsymbol{x}) = \frac{E(\{\underline{t} + \boldsymbol{x}, \underline{b}\}) - E_0}{A} \tag{2.97}$$

where A is the area of the unit cell, E_0 is the energy of the bilayer at equilibrium and $E(\{\boldsymbol{r}_i\})$ denotes the total energy of a configuration of atoms at position $\{\underline{t} + \boldsymbol{x}, \underline{b}\}$. The argument of the energy function $\{\underline{t} + \boldsymbol{x}, \underline{b}\}$ is a shorthand denoting a bilayer geometry with the top layer translated by $\boldsymbol{x}$, i.e. $\{\boldsymbol{t}_{0\mu_0} + \boldsymbol{x}, \ldots, \boldsymbol{t}_{m\mu_m} + \boldsymbol{x}\}$. Note it is assumed that translation obeys the minimum image convention: atoms translated out of the unit cell are mapped back to an equivalent position.

The PES $\mathcal{P}(\boldsymbol{x})$ is evaluated over a grid $\underline{g} = \{\boldsymbol{x}\}$ of translation vectors inside the unit cell. The translations of the top layer only break the symmetry of the bilayer system. On the other hand, the symmetry of each separate ML is left unchanged: the translated top layer $\underline{t}$ retains the symmetry of its non-shifted, isolated counterpart, as global translation. Thus, one cannot identify equivalent points in the translation grid $\underline{g}$ by applying the space group symmetry operations of the bilayer crystal, e.g. as is done for k point sampling in electronic structure calculations. A different definition of equivalency must be defined.

Symmetric equivalent sites

Two translation vectors in the grid $(\boldsymbol{x}, \boldsymbol{x}') \in \underline{g}$ are equivalent if the geometry with the top layer $\underline{t}$ translated at position $\boldsymbol{x}$ can be mapped onto the geometry with top layer translated at $\boldsymbol{x}'$ and the stacking relative to the bottom layer is preserved. This mapping is done via an operation O related to the space group of the top layer Ω_t, as top layer geometries translated at different positions need to be equivalent, while the bottom layer is a spectator. Since the translation grid $\underline{g}$ is purely 2D, symmetry operations must be constrained to the xy plane, e.g. reflections along the c axis are not allowed. Defining the projector onto ab sub-space and the identity along c as

$$P_{ab} = \begin{pmatrix} 1 & 0 & 0 \\ 0 & 1 & 0 \\ 0 & 0 & 0 \end{pmatrix} \qquad \mathbb{I}_c = \begin{pmatrix} 0 & 0 & 0 \\ 0 & 0 & 0 \\ 0 & 0 & 1 \end{pmatrix}. \tag{2.98}$$

Any operation O can be restricted to the (ab) plane by

$$\tilde{O} = P_{ab} O P_{ab}^{\dagger} + \mathbb{I}_c,$$

This leads to the following definition: any two points $(\boldsymbol{x}, \boldsymbol{x}') \in \underline{g}$ are equivalent $\boldsymbol{x} \equiv \boldsymbol{x}'$ if there exists an operation $O \in \Omega_t$ such that

$$\begin{aligned} \underline{t} + \boldsymbol{x} &= \tilde{O}(\underline{t} + \boldsymbol{x}') \\ \underline{b} &= \tilde{O}(\underline{b}), \end{aligned} \tag{2.99}$$

Finally, atoms of the same type μ lead to the same interaction and, thus, the energy is invariant under same-species permutation of atoms in the system $\pi_\nu(\{r_{i,\nu_i}\})$. While this is implicit in the energy, it needs to be explicitly included in the definition of equivalency. The operation O is thus accompanied by a pair of permutation p_t, p_b acting separately on the bottom $\underline{b}$ and top $\underline{t}$ layer. The condition in Eq. (2.99) becomes

$$\begin{aligned} &(\boldsymbol{x}, \boldsymbol{x}') \in \underline{g},\ \boldsymbol{x} \equiv \boldsymbol{x}' \iff \exists O \in \Omega_t, p_t \in \pi_\nu(\underline{t}), p_b \in \pi_\nu(\underline{b}) : \\ &\begin{cases} p_t(\underline{t}) + \boldsymbol{x} &= \tilde{O}(p_t(\underline{t}) + \boldsymbol{x}') \\ p_t(\underline{b}) &= \tilde{O}(p_b(\underline{b})). \end{cases} \end{aligned} \tag{2.100}$$

An example of this protocol applied to a MoS_2 bilayer is reported in Fig. 2.10. Due to rounding errors, the protocol is subject to false-positive errors, i.e. equivalent sites labelled as distinct. This type of error is benign: it increases the number of calculations needed but the PES shape and overall symmetry is described correctly.

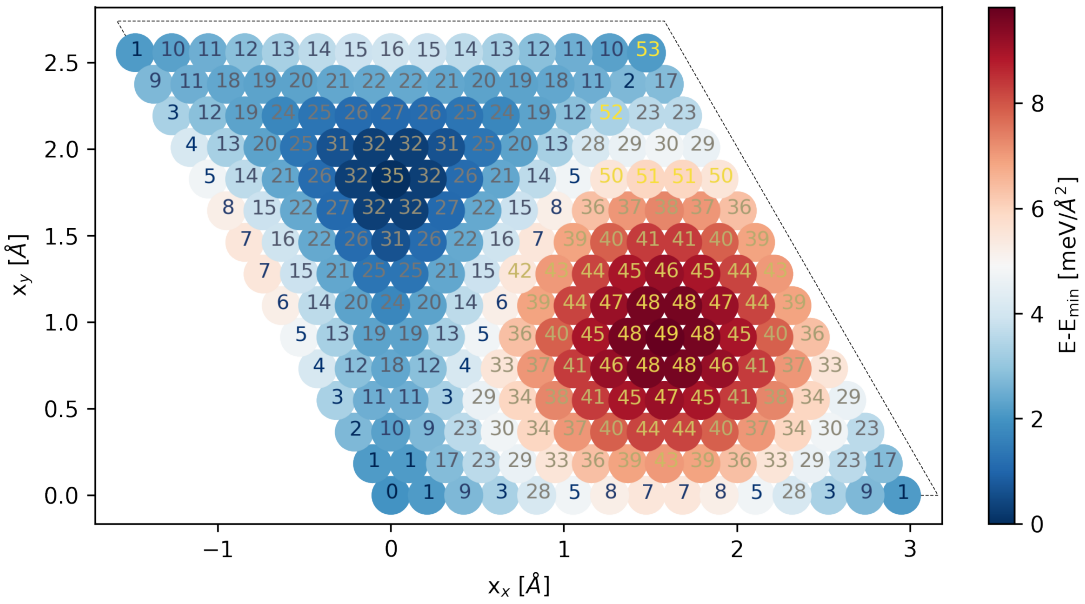

Figure 2.10: PES $\mathcal{P}(\boldsymbol{x})$ of MoS_2 bilayer system evaluated over a 15×15 grid within the unit cell, shown as dotted line. The colour-code of each point shows the energy per area with respect to the stable configuration. Each point is the results of a DFT relaxation with the bottom layer fix in xyz and the top layer fixed in xy. The label sorts each point into the symmetrically distinct sites. The font colour is a guide to the eye. Misplaced labels 52 (instead of 3) and 53 (instead of 1) are false positives.

Interpolation

In order to obtain a smooth surface to evaluate, PES $\mathcal{P}(\boldsymbol{x})$ evaluated on discrete grids with DFT calculations are interpolated using radial basis functions:

$$\mathcal{P}(\boldsymbol{x}) = \sum_i w_i \phi(|\boldsymbol{x} - \boldsymbol{c}_i|), \tag{2.101}$$

where the centres $\boldsymbol{c}_i$ are the input points, i.e. DFT-computed grid, $\phi(r)$ is the chosen functional form of the radial basis function and w_i the weight of the radial function centreed on c_i, computed via a least-square fit. The analytical form of the radial function chosen is the multi-quadratic:

$$\phi(r) = \sqrt{1 + \left(\frac{r}{\epsilon}\right)^2}, \tag{2.102}$$

where ϵ is a shape factor regulating how localized the basis function is. Here, $\epsilon = \Delta c$, i.e. the distance between input points.

The gradient of the PES governs the rigid sliding of the layers. This can be evaluated directly from the expansion using the linearity of the gradient operator:

$$\nabla\mathcal{P}(\boldsymbol{x}) = \sum_i w_i \nabla\phi(|\boldsymbol{x} - \boldsymbol{c}_i|) = \sum_i w_i \phi'(r_i)\frac{\boldsymbol{r}_i}{r_i} \tag{2.103}$$

$$= \sum_i w_i \frac{\boldsymbol{x} - \boldsymbol{c}_i}{\epsilon^2\sqrt{1 + \left(\frac{|\boldsymbol{x}-\boldsymbol{c}_i|}{\epsilon}\right)^2}}, \tag{2.104}$$

where $\boldsymbol{r}_i = \boldsymbol{x} - \boldsymbol{c}_i$. Fig. 2.11 reports the expansion of $\mathcal{P}(\boldsymbol{x})$ along with $\nabla\mathcal{P}(\boldsymbol{x})$ for the same MoS_2 bilayer shown in the previous section.

2.4.4 Phonons

The normal modes of a crystal, or phonons, provide a convenient formalism to describe the response of a crystal system near its equilibrium configuration. The process developed now is valid for any crystal, and it shall be adapted to 2D materials later on. Here a classical description of vibrations in a crystal is given. Consider a crystal of N sites and a basis set of n atoms. The configuration of the crystal is given by the set of nN_0 vectors

$$\boldsymbol{r}_{\nu l} = \boldsymbol{R}_{\nu l} + \boldsymbol{u}_{\nu l}, \tag{2.105}$$

where l labels unit cells in the Bravais lattice and ν atoms inside the unit cell. Thus, $\boldsymbol{u}_{\nu l}$ is the displacement vector, from equilibrium site $\boldsymbol{R}_{\nu l}$. Fig. 2.12 shows lattice with $N = 4$ and a basis with $n = 2$. The Bravais lattice points $\boldsymbol{R}_l$ are shown in light blue, while atom equilibrium positions within the cell $\boldsymbol{R}_\nu$ are shown in blue. Following Eq. (2.105), the position of the atom $\boldsymbol{r}_{\nu l}$ is marked by a pink arrow, the sum of the displacement vector $\boldsymbol{u}_{\nu l}$ by a purple arrow The equilibrium lattice position are $\boldsymbol{R}_{\nu l} = \boldsymbol{R}_l + \boldsymbol{R}_\nu$.

The internal energy of a crystal is $U(\boldsymbol{r}_{00} \dots \boldsymbol{r}_{nN_0})$, i.e. a mapping from the coordinate space to the real numbers $\mathbb{R}^{3nN_0} \to \mathbb{R}$. The internal energy around the equilibrium

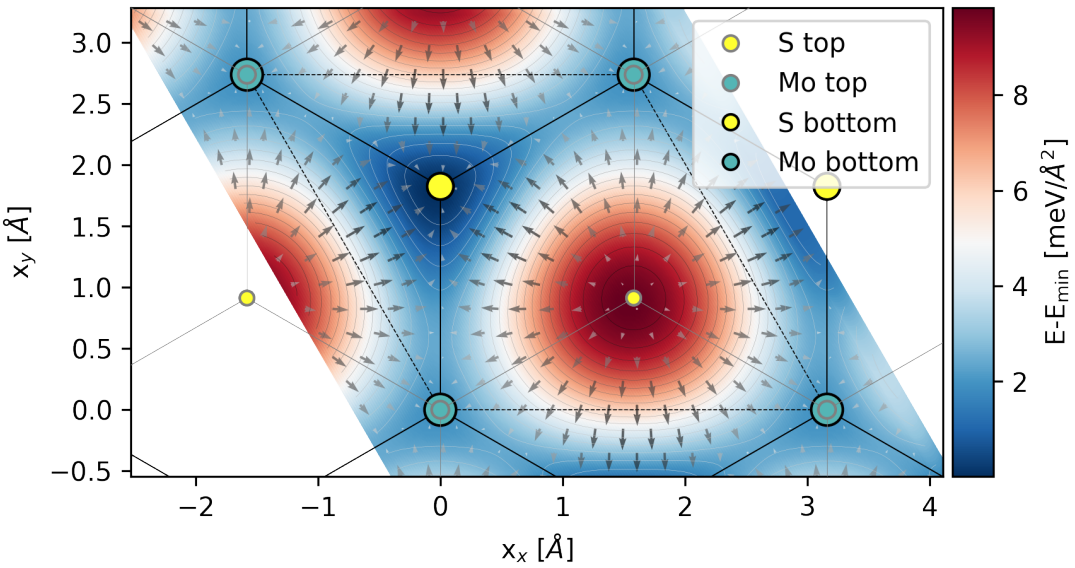

Figure 2.11: Radial basis function interpolated PES $\mathcal{P}(\boldsymbol{x})$ for MoS_2 bilayer evaluated over a 200×200 grid within the unit cell, shown as dotted line. The 15×15 grid in Fig. 2.10 was used for interpolation. The colour-code of each point shows the energy per area with respect to the stable configuration. Gray-scale arrows show the gradient evaluated from the interpolation using Eq. (2.104) on a 20×20 grid . The legend reports the colour-code for different atom types. Larger circles and black bond lines refer to the bottom layer, while smaller circles and dashed grey bonds refer to the top layer.

configuration $\underline{R} = \{\boldsymbol{R}_{\nu l}\}$ can be expanded using a multivariate Taylor expansion of the form [150, 143]

$$U(\underline{r}) = U(\underline{R}) + \sum_{l,\nu} \left.\frac{\partial U}{\partial r^{\alpha}_{\nu l}}\right|_{\underline{R}} u^{\alpha}_{\nu l} + \frac{1}{2} \sum_{\substack{l,l' \\ \nu,\mu}} u^{\alpha}_{\nu l} \phi_{\alpha\beta}(\nu l, \mu l') u^{\beta}_{\mu l'} + O(u^3_{\nu l}), \tag{2.106}$$

where α, β refer to Cartesian coordinates. The Einstein convention applies for Cartesian indices: repeated indices imply summation, that is $v^{\alpha} w^{\alpha} = \sum_{\alpha} v^{\alpha} w^{\alpha} = \boldsymbol{v} \cdot \boldsymbol{w}$. To strike a balance between clarity and overwhelming notation, the Einstein convention is applied to Cartesian indices only, always labelled with Greek letters. The constant U($\underline{\mathrm{R}}$) represents the cohesive energy of the crystal. The linear term in Eq. (2.106) vanishes because of the choice of expansion point: $\frac{\partial U}{\partial r^{\alpha}_{\nu l}}$ is the force acting on the (νl) atom of the crystal, which must be zero by definition at the equilibrium position $R_{\nu l}$. The matrix of force constants $\phi_{\alpha\beta}(\nu, l, \mu, l')$ is defined as

$$\phi_{\alpha\beta}(\nu l, \mu l') = \left.\frac{\partial^2 U}{\partial r^{\alpha}_{\nu l} \partial r^{\beta}_{\mu l'}}\right|_{\underline{R}}. \tag{2.107}$$

Retaining only terms quadratic in the displacement, the internal energy in Eq. (2.106)

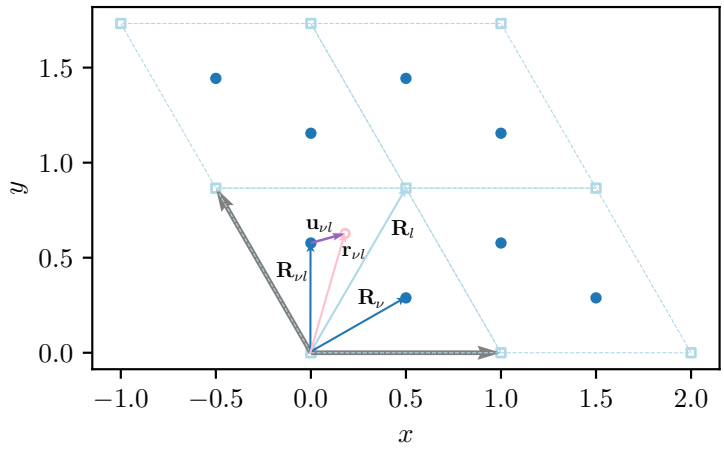

Figure 2.12: Definition of the atom position vectors in Eq. (2.105).

becomes

$$U(\underline{r}) - U(\underline{R}) \approx \frac{1}{2} \sum_{\substack{l,l' \\ \nu,\mu}} u^{\alpha}_{\nu,l} \phi_{\alpha\beta}(\nu, l, \mu, l') u^{\beta}_{\mu,l'}. \tag{2.108}$$

The equations of motion induced by the quadratic form in Eq. (2.106) are solved in reciprocal space $(\boldsymbol{k}, \omega)$ by defining the dynamical matrix as [151, 143]

$$D_{\alpha\beta}(\nu\mu, \boldsymbol{k}) = \frac{1}{\sqrt{m_\nu m_\mu}} \sum_{l} \phi_{\alpha\beta}(\nu, 0, \mu, l) e^{i\boldsymbol{k}\cdot(R_{\mu l} - R_{\nu 0})}, \tag{2.109}$$

where m_ν is the mass of the atom ν in the unit cell. The sum in Eq. (2.109) runs over a single supercell index l because the system is treated in PBC. For fixed ν and μ, $D_{xy}(\boldsymbol{k})$ records the force along $\alpha = x$ acting on the atom $r_{\nu 0}$ due to the displacement along y of atoms μ in all N_0 unit cells; the amplitude (and phase) of this displacement varies between different unit cells with wavelength $\lambda = 1/|\boldsymbol{k}|$ and along the direction $\hat{k}$. By definition D is Hermitian, $D(\boldsymbol{k})^\dagger = D(\boldsymbol{k})$, implying real eigenvalues, and, moreover, the following properties hold

$$D^*(\boldsymbol{k}) = D(-\boldsymbol{k}). \tag{2.110}$$

The intrinsic vibrations of the system are found by diagonalising D:

$$\sum_{s,s'} (\epsilon^{\alpha}_{s}(\nu, \boldsymbol{k}))^* D_{\alpha\beta}(\nu\mu, \boldsymbol{k}) \epsilon^{\beta}_{s'}(\mu, \boldsymbol{k}) = \omega^2_s(\boldsymbol{k}) \delta_{s,s'}. \tag{2.111}$$

The solution of each eigenvalue problem at fixed k is a set of $3n$ eigenvalues $\omega_s(\boldsymbol{k})$, which represent the frequency of the normal mode. The index s labels the so-called *branches* of the dispersion curve, e.g. longitudinal and transverse acoustic branches, in which the displacement is parallel and perpendicular to the wavevector, respectively. The set of $\omega_s(\boldsymbol{k})$ characterises the response of the system to a perturbation of wave-vector $\boldsymbol{k}$. The $3n$

complex eigenvectors $\underline{\epsilon}_s(\boldsymbol{k})$ are themselves composed of n 3D vectors:

$$\underline{\epsilon}_s(\boldsymbol{k}) = \begin{pmatrix} \epsilon_s^x(0,\boldsymbol{k}) & \epsilon_s^y(0,\boldsymbol{k}) & \epsilon_s^z(0,\boldsymbol{k}) \\ \vdots & & \\ \epsilon_s^x(n,\boldsymbol{k}) & \epsilon_s^y(n,\boldsymbol{k}) & \epsilon_s^z(n,\boldsymbol{k}) \end{pmatrix}. \tag{2.112}$$

Each of them represents the direction (real part) and phase (imaginary part) of the displacement of the atom ν in the unit cell. Because D is Hermitian and from Eq. (2.110), it follows that [143]:

$$(\epsilon_s^\alpha(\nu,\boldsymbol{k}))^* = \epsilon_s^\alpha(\nu,-\boldsymbol{k}). \tag{2.113}$$

The set of vectors $\underline{\epsilon}_s(\boldsymbol{k})$ is an orthogonal basis set. Thus, they satisfy the following relations [143, 150]:

$$\boldsymbol{\epsilon}_s^*(\boldsymbol{k'}) \cdot \boldsymbol{\epsilon}_{s'}(\boldsymbol{k})) = 0 \tag{2.114}$$

$$\boldsymbol{\epsilon}_s^*(\nu,\boldsymbol{k}) \cdot \boldsymbol{\epsilon}_{s'}(\nu,\boldsymbol{k})) = \delta_{s,s'} \tag{2.115}$$

$$\sum_s \sqrt{m_\mu}(\epsilon_s^\alpha(\mu,\boldsymbol{k}))^* \epsilon_s^\beta(\mu,\boldsymbol{k}))\sqrt{m_\nu} = \delta_{\alpha,\beta}\delta_{\nu,\mu}. \tag{2.116}$$

Any configuration of the crystal can be written in terms of $\underline{\epsilon}_s(\boldsymbol{k})$:

$$u_{\nu l}^\alpha = \frac{1}{\sqrt{N_0 m_\nu}} \sum_{\boldsymbol{k},s} \gamma_{\boldsymbol{k}s} \epsilon_s^\alpha(\nu,\boldsymbol{k}) e^{i\boldsymbol{k}\cdot R_{\nu l}}, \tag{2.117}$$

where each coefficient of the linear expansion is defined as

$$\gamma_{\boldsymbol{k}s} = \frac{1}{\sqrt{N_0}} \sum_{\nu,l} \sqrt{m_\nu} \boldsymbol{u}_{\nu l} \cdot \boldsymbol{\epsilon}_s(\nu,-\boldsymbol{k}) e^{-i\boldsymbol{k}\cdot R_{\nu l}}. \tag{2.118}$$

The complex numbers $\gamma_{\boldsymbol{k}s}$ are termed phonon [143] or normal [152] coordinates. From Eq. (2.113) it follows that:

$$\gamma_{\boldsymbol{k}s}^* = \gamma_{-\boldsymbol{k}s} \tag{2.119}$$

Substituting in Eq. (2.108) the expansion of $u_{\nu,l}^\alpha$ in Eq. (2.117) and using the definition of D in Eq. (2.109), the internal energy of the crystal is approximated as

$$U(\underline{r}) = \frac{1}{2} \sum_{\substack{\boldsymbol{k} \\ s,s'}} \gamma_{\boldsymbol{k}s}\gamma_{-\boldsymbol{k}s'} \sum_{\nu,\mu} \epsilon_s^\alpha(\nu,\boldsymbol{k}) D_{\alpha\beta}(\nu\mu,\boldsymbol{k}) \epsilon_{s'}^\beta(\mu,-\boldsymbol{k}) \tag{2.120}$$

$$= \frac{1}{2} \sum_{\boldsymbol{k},s} \omega_s^2(\boldsymbol{k}) |\gamma_{\boldsymbol{k}s}|^2, \tag{2.121}$$

where between the second and third lines Eq. (2.111) was used. Thus, if the small displacement approximation in Eq. (2.108) holds, the energy of a configuration $\underline{r}$ of the system can be approximated by the energy of each phonon mode, weighted by the projection of the current displacement on that mode.

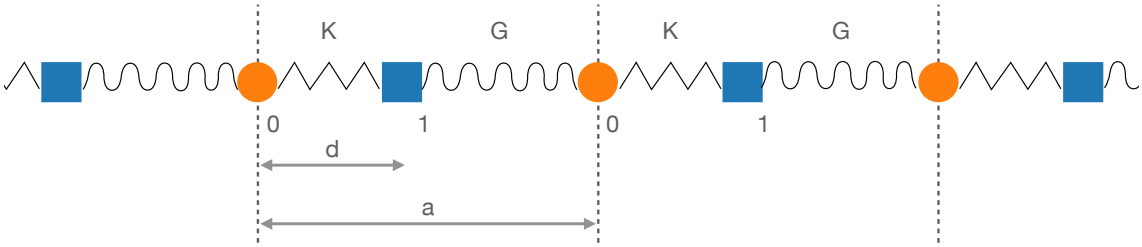

Figure 2.13: Sketch of the diatomic chain in Eq. (2.122).

1D Example

Consider a mono-atomic 1D chain like the one sketched in Fig. 2.13. The chain has a spacing a and two atoms of mass m_0 and m_1 per unit cell at positions $R_{0n} = na$, $R_{1n} = na + d$. Atoms within and outside the unit cell are connected via springs of different elastic constant, yielding the energy

$$U = \frac{1}{2}K\sum_n [u_{0n} - u_{1n}]^2 + \frac{1}{2}G\sum_n [u_{0n} - u_{1(n-1)}]^2 \tag{2.122}$$

$$= \sum_{\substack{n,l\\ \mu,\nu}} u_{\mu n} D^{\nu m}_{\mu n} u_{\nu m}, \tag{2.123}$$

with spring constant $K = \phi''(d)$, if $\phi(x)$ is the potential energy between two atoms at distance x, and $G = \phi''(a-d)$. In Eq. (2.123), the interaction potential is cast into the general kernel form $v_i M_{ij} u_j$ reported in the definition of dynamical matrix Eq. (2.109), and the kernel $D^{\nu m}_{\mu n}$ has the form

$$D^{\nu m}_{\mu n} = \delta_{n,m}\delta_{\nu,\mu}\sum_{r,\pi}\left(\varphi^{r,\pi}_{n,\mu}\right) - \varphi^{m,\nu}_{n,\mu} \tag{2.124}$$

and $\varphi^{m,\nu}_{n,\mu} = K\delta_{n,m} + G\delta_{n-m,1}\delta_{\nu-\mu,1}$. Inserting the interaction in Eq. (2.124) in the definition Eq. (2.109), for each wavevector q one obtains a 2×2 dynamical matrix $D(q)$

$$D(q) = \begin{pmatrix} \frac{K+G}{m_0} & -\frac{e^{iqd}}{\sqrt{m_0 m_1}}\left(K + Ge^{-iqa}\right) \\ -\frac{e^{-iqd}}{\sqrt{m_0 m_1}}\left(K + Ge^{iqa}\right) & \frac{K+G}{m_1} \end{pmatrix}. \tag{2.125}$$

The eigenvalues of $D(q)$ are given by

$$\omega_s^2(q) = \frac{K+G}{\mu} \pm \frac{1}{2}\sqrt{\frac{K^2+G^2}{\mu^2} + 2KG\left(\frac{1}{\mu^2} - \frac{4}{m_1 m_0}(1-\cos(qa))\right)}, \tag{2.126}$$

where $\frac{1}{\mu} = \frac{1}{m_0} + \frac{1}{m_1}$ is often referred to as reduced mass. In the case of equal masses $m_1 = m_0 = m$ the physics become even easier to grasp, with the frequency of the system being

$$\omega_s^2(q) = \frac{K+G}{m} \pm \frac{1}{m}\sqrt{K^2 + G^2 + 2KG\cos(qa)}. \tag{2.127}$$

The dispersion relation, in this case, is illustrated in Fig. 2.14. The two solutions of the eigenvalue problem yield one acoustic ω_A and one optical ω_O branch. The former describes coherent modulation within the unit cell and is characterized by a vanishing behaviour near the centre of the BZ $q \to 0$, corresponding to long-wavelength distortions (rigid translation of the chain for $q = 0$), as shown in the lower inset in Fig. 2.14. In this region, the dispersion can be approximated with a linear relation

$$\lim_{q \to 0} \omega_A(q) = cq,$$

where $c = \sqrt{\frac{KG}{2m(K+G)}}$ is the speed of sound in the chain. The latter describes modulation within the unit cell and retain a non-zero frequency $\omega_O(\pi/a) = \sqrt{\frac{2(K+G)}{M}}$, and thus energy cost, also in the limit of $q = 0$, as atoms in all unit cells are vibrating coherently around their equilibrium position, as shown in the upper inset in Fig. 2.14. At the edge of the BZ, the modulation changes sign between neighbouring cells, the shortest wavelength possible. As a result, the displacements between neighbouring cells are in phase opposition, i.e. π phase, as shown in the insets on the left of Fig. 2.14.

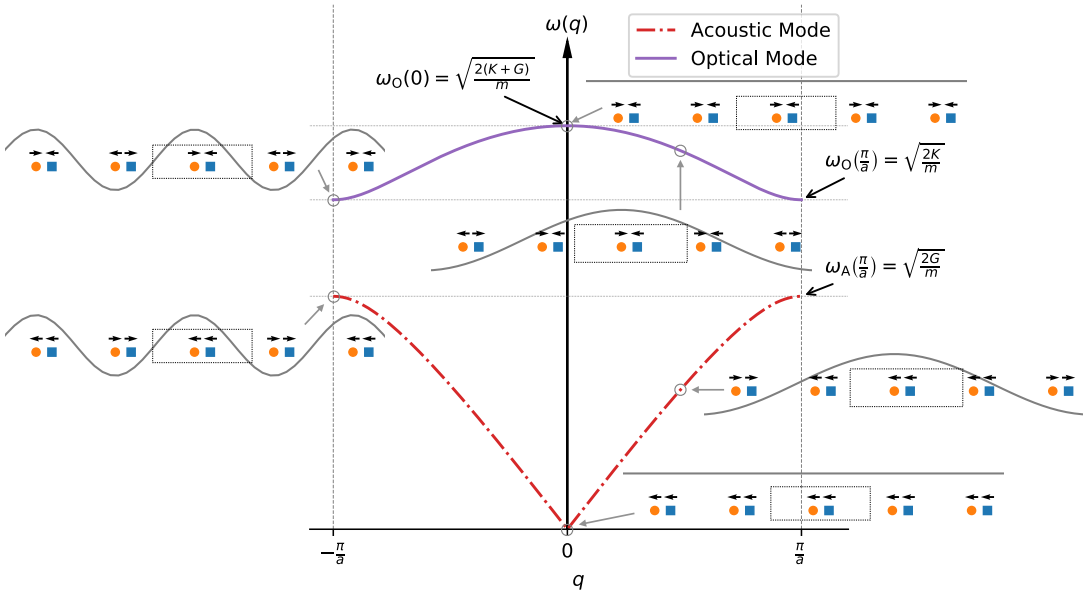

Figure 2.14: Dispersion relation of optical $\omega_O(q)$ (solid purple line) and acoustic $\omega_A(q)$ (dashed red line) versus wavevector q in a 1D chain with atoms of mass m per unit cell, orange circles and blue squares in the insets. The intra-cell K and inter-cell G interactions between atoms define the gap $\Delta(q) = \omega_O(q) - \omega_A(q)$ between acoustic and optical branches. Insets show the displacement patterns at the centre $q = 0$, edges $q = \pi/a$ and intermediate wave vector $q = 2\pi/5a$ in the unit cell, as marked by grey circles. Dashed lines highlight the unit cell of the chain and the modulation wavelength is reported in a solid grey line; at the centre, the wavelength diverges, thus the horizontal line.

To show clearly the connection between the dispersion relation in Fig. 2.14 and real-space displacements, Fig. 2.15 reports the expansion coefficients $|\gamma_{ks}|^2$ along the dispersion curve for a periodic and non-periodic displacement of the chain. Whether the energy cost associated with this expansion is meaningful depends on how well the small displacement

hypothesis is satisfied.

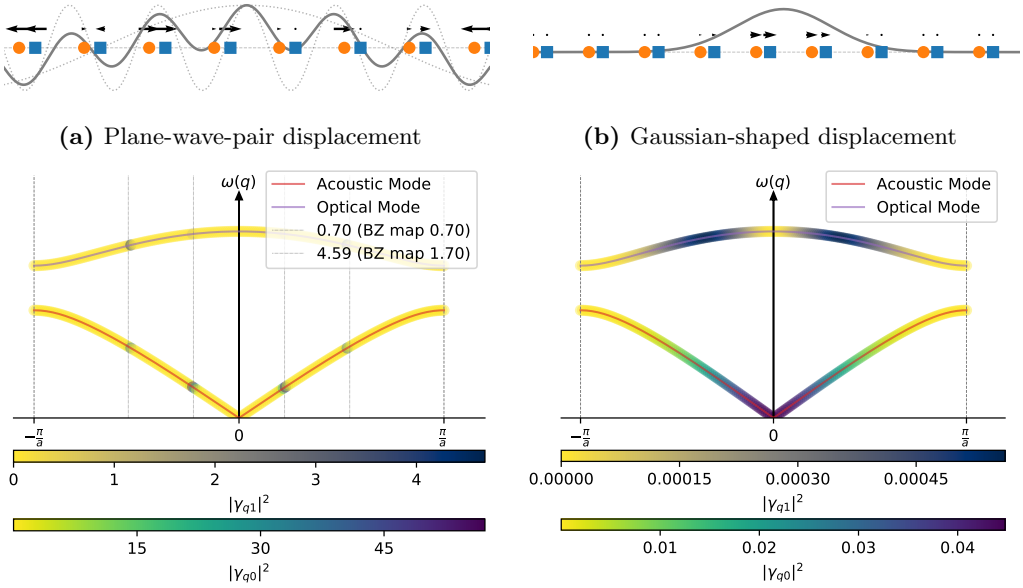

(a) Plane-wave-pair displacement

(b) Gaussian-shaped displacement

(c) Projection of plane-wave-pair displacement

(d) Projection of Gaussian displacement

Figure 2.15: Projection example. The chain with a two-atom basis is shown as orange circles and blue squares. (a) A portion of the chain with the displacement (black arrows) resulting from the superimposition (solid grey line) of two plane waves (dotted lines) at $k_0 = \frac{2\pi}{9a}$, wavelength larger than the unit cell, and $k_1 = \frac{\pi}{9a}\frac{73}{50}$, wavelength smaller than the unit cell. (c) Projection of the displacement pattern in (a) onto the phonon dispersion in Fig. 2.14. Vertical grey lines highlight the position in the BZ of the modulating wave k_0, k_1. The intra- and inter-cell character of the displacements is correctly reproduced in the dispersion. (b) A portion of the chain with the displacement (black arrows) resulting from a Gaussian-shaped displacement pattern (solid grey line) centred at $x = 2$ and of width $\sigma = 1.2a$, a little over a single unit cell. (d) Projection of the displacement pattern in (b) onto the phonon dispersion in Fig. 2.14. The projection of this localized in space is delocalized onto many wavevectors, as expected from the Fourier Transform definition.

Much of the physics shown by this simple example carries on to real crystals, where higher dimension and directional-dependent interactions yield intricate band structures with degeneracy and band-crossing points.

Phonons in layered materials

As an example of phonon dispersion in a real 3D crystal, Fig. 2.16(a) reports the phonon dispersion of bulk MoS_2. The anisotropy of the crystal structure gives rise to a characteristic structure of modes where high-energy intralayer branches are sharply separated from inter-layer low energy eigenmodes. As shown by the blue curves in Fig. 2.16(a) from K to Γ, wavevectors along in-plane lattice vectors result in high energy distortions while modulations along the interlayer axis c, shown in as red curves between the BZ centre Γ and A in Fig. 2.16(a), occur at low energy cost due to the weak inter-layer van der Waals coupling compared to strong in-plane bonds. The characteristic inter-layer modes are divided into longitudinal, *breathing* modes [153], representing the vibration of layers along the c axis around the minimum of the van der Waals potential, and transverse, *shearing* modes,

representing the onset of sliding that have been linked to the frictional response of the material [92, 154].

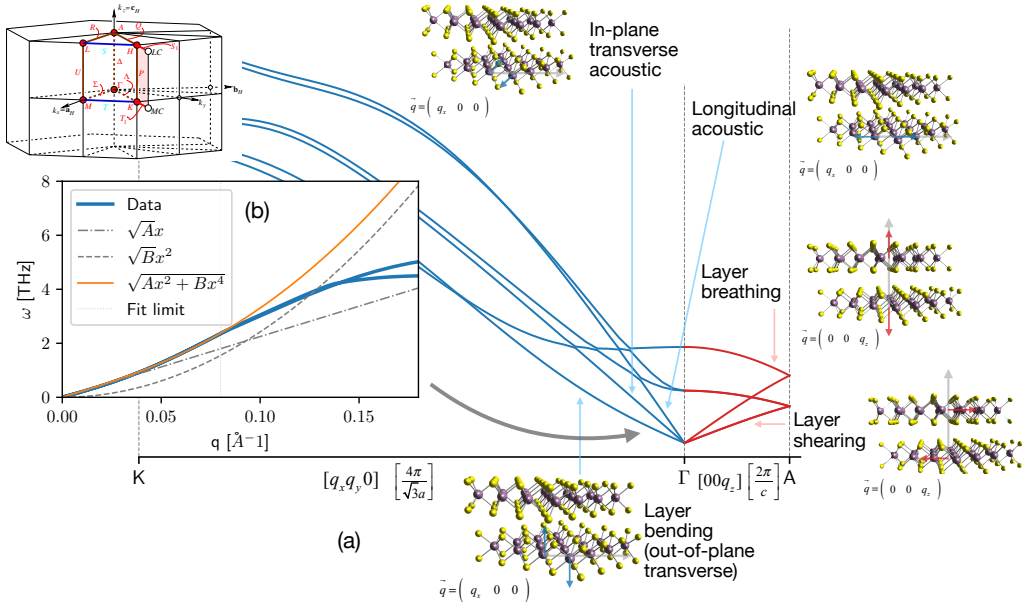

Figure 2.16: (a) Interlayer and acoustic phonon dispersion of MoS_2. Blue curves refer to the in-plane wavevector, in the xy, while red curves refer to out-of-plane wavevectors, along z. The inset in the top left reports a schematic of the Brillouin, highlighting the high-symmetry points; from Ref. [155]. Other insets sketch the displacement pattern of different branches. (b) Fitting of the dispersion relation for the bending modes according to Eq. (2.128). The dash-dotted and dotted lines report the linear and quadratic parts, respectively.

Another unique characteristic of the phonon spectrum in layered materials is the quadratic dispersion $\omega_{\mathrm{B}}(q) \propto q^2$ near Γ of the out-of-plane transverse branch, usually termed *bending* modes. This behaviour is characteristic of bending of 2D sheets in classical mechanics [153]. The dispersion is thus written as

$$\lim_{q\to\Gamma} \omega_{\mathrm{B}}(q)^2 = Aq^2 + Bq^4, \tag{2.128}$$

where the slope $\sqrt{A}$ dominates at small q and further away from Γ the parameter B, known as bending stiffness constant, expresses the energy cost of creating ripples in the material [153]. The fit of Eq. (2.128) for MoS_2 phonon dispersion is reported in the inset Fig. 2.16(b). In the case of an isolated ML, e.g. a single graphene sheet, the interlayer modes disappear, i.e. the spectrum between Γ and A in Fig. 2.16(a) is flat, while only bending, transverse and longitudinal acoustic modes are retained.

3

Structural Properties of Heterostructures

Strong intralayer covalent bonds in Van der Waals (vdW) 2D materials complement the weak vdW interlayer interactions which facilitate the lamellar structure of bulk crystals. While the attractive properties of the pure compounds are widely known, recent efforts have been focusing on the physics and properties emerging from the stacking degree of freedom offered by these lamellar materials. Despite the interesting physics that results from these relative mismatches, an often overlooked question is what determines their rotational energy landscape and thus which geometries are stable. Indeed, experimental studies are contradictory on this point, with a wide range of misfit angles found, even for the same type of system [156, 157, 158, 159]. Examples of heterostructures based on MoS_2 on G are discussed below. This system may be regarded as the prototypical 2D heterostructure, as it combines two well-known and extensively studied materials, widely reported on in the literature. Moreover, it has been reported that MoS_2/G heterostructures show interesting electronic behaviour as a function of the mismatch angle [160, 161]. Using CVD, Liu *et al.* [156] epitaxially grew triangles of MoS_2 on top of G, shown in Fig. 3.1a, about 0.135 μm in size, with the majority of them (84%) aligned to the substrate and the remainder rotated by 30°. Using the same technique, Shi *et al.* [157] found mismatch angles between MoS_2 and G, on top of a Cu foil, ranging from $-11°$ to 18°, with a hexagonal flake size of about 1 μm, as shown in Fig. 3.1b. For CVD-grown flakes of 9 μm reported in Fig. 3.1c, Lu *et al.* [158] found a mismatch with typical angles below 3°. Finally, using an exfoliation protocol, Adrian *et al.* [159] prepared multi-layered heterostructures and observed a misfit angle of 7.3° using diffraction spectroscopy, as reported in Fig. 3.1d. As well as different values for the observed mismatch angle, these studies offer different explanations for its origin. Whereas some attribute the observed (mis)alignment to the

vdW epitaxy accommodating the mismatch in lattice constants [156, 157], others use the structural features of the underlying G and the edges [158] as an explanation.

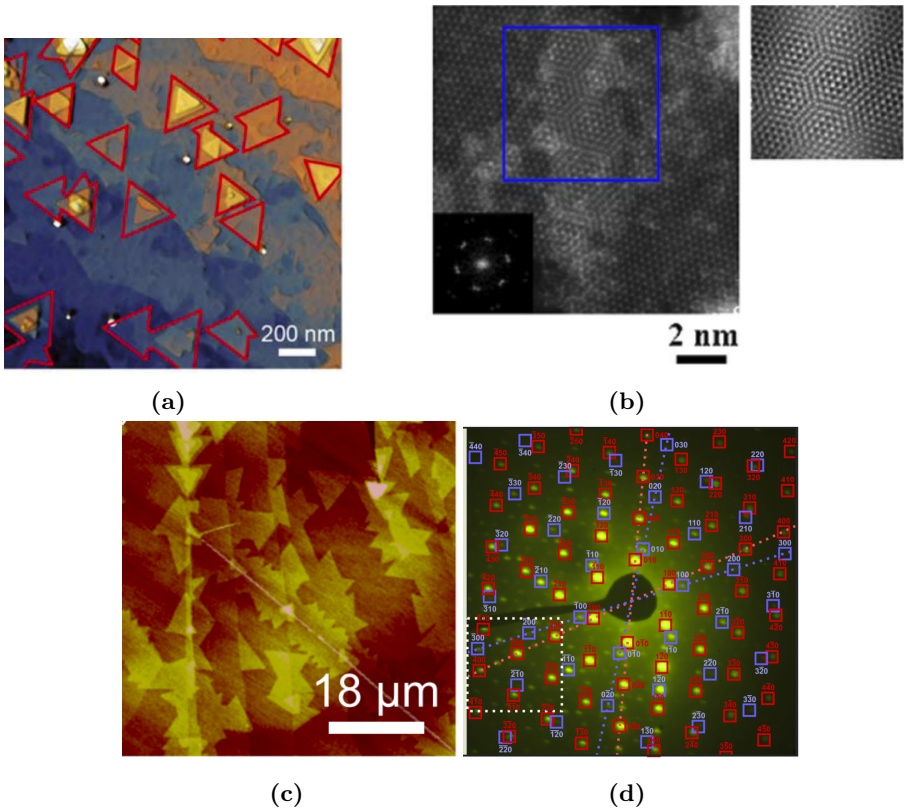

Figure 3.1: (a) CVD-grown flakes adapted from Ref. [156] (b) HRSTEM of misaligned MoS_2 flakes grown on graphene. The insets show a spacial FFT of the highlighted region. Adapted from Ref. [157]. (c) CVD-grown flakes adapted from Ref. [158] (d) Electron diffraction image of the multilayer heterostructures in Ref. [159].

In a recent theoretical work, Zhu *et al.* [54] explained the orientational ordering of finite size homostructures, e.g. MoS_2 flakes on an MoS_2 substrate, using a purely geometrical argument: the lowest energy configuration is the one obtained by the roto-translation of the rigid flake which maximizes the number of locally commensurate regions. Although this argument is solely based on geometry, it provides a satisfactory approximation for finite size systems but in the limit of infinite planes, i.e. for large enough flakes, commensurate regions equal incommensurate ones. Therefore, in the limit of extended interfaces, other theoretical frameworks are needed.

This chapter explores the energy landscape originating from the rotational degree of freedom of edge-free, complex layered heterostructures and relate its fundamental origin to incommensurability and layer deformation at imposed angles. This will provide guidance for the design of vdW heterostructures and the control of the twisting degree of freedom. In order to make a more general point about the relative importance of different contributions in determining the total energy landscape, the following analysis focuses on a specific but well-studied system, namely MoS_2/G. While previous energy analysis focused on commensurate MoS_2/MoS_2 homostructures [162] or near-commensurate 2D-crystal G/hBN heterostructures [163], the MoS_2/G BL system has a mismatch ratio $\rho = l_G/l_{MoS_2} \approx 0.8$

far away from the commensurate value $\rho = 1$ and it is composed of a mixture of 2D and 3D crystal monolayers. This selected analysis shows the practical application of the argument developed and will also allow one to comment on the apparently contradictory experimental observations regarding this particular system.

3.1 Epitaxy Theory

An approximate theory for the orientational ordering of an incommensurate interface was proposed by Novaco and McTague [164, 165]. Although developed in the context of epitaxial growth of noble gas layers on metal surfaces, it has been successfully applied to the behaviour of mesoscopic colloidal layers in optical lattices [166] and metal clusters adsorbed on G [167]. The assumption of the Novaco-McTague (NM) theory is that two ML linked via an interface may be divided into two separate components, regarded as purely 2D systems: a soft adsorbate layer, treated within the harmonic approximation, atop a rigid substrate.

The Hamiltonian of the system is decomposed into intralayer and interlayer inter-atomic interactions

$$H = H_{\mathrm{L}_1} + H_{\mathrm{L}_2} + H_{\mathrm{L}_1\mathrm{L}_2}. \tag{3.1}$$

The NM prescription means that the first intralayer term in Eq. (3.1) is substituted by its harmonic approximation, while the coordinates of the second layer are frozen at its initial values, r_0, yielding a rigid substrate potentials for the first layer:

$$H_{\mathrm{NM}} = H_{\mathrm{L}_1}|_{\mathrm{harmonic}} + H_{\mathrm{L}_2}|_{r_0} + H_{\mathrm{L}_1\mathrm{L}_2}. \tag{3.2}$$

The system is frustrated if the substrate and the adsorbate lattices are mismatched: the intralayer interactions within the adsorbate favour the intrinsic equilibrium lattice spacing, while the interactions with the substrate drive the atoms toward the minima of the potential generated by the frozen ML. The first term of Eq. (3.2) is treated within the phonon formalism described in section 2.4.4. The second term $H_{\mathrm{L}_2}|_{r_0}$ is a constant shift of the energy, the cohesive energy of the ML. The third term of Eq. (3.2), $H_{\mathrm{L}_1\mathrm{L}_2}(\underline{r})$, is the interaction between the harmonic monolayer and the rigid substrate, generated by the frozen atoms in the monolayer of lattice vectors $\boldsymbol{b}_i$. The interlayer interaction $H_{\mathrm{L}_1\mathrm{L}_2}(\underline{r})$ can be approximated in terms of monolayer geometries and harmonic response only. Here, a generalisation of the model proposed in Ref. [164, 168] is given and it is shown how the results therein are recovered within the proposed formalism.

The geometry of the ML, described in Appendix B, allows the position of the atoms to be decomposed as in-plane vectors and out-of-plane coordinates, $\boldsymbol{r}_{\nu l} = (\boldsymbol{\rho}_{\nu l} z_{\nu l})$. Considering a plane perpendicular to the z, the potential generated by the frozen atoms in the substrate is a periodic two-dimensional function, with the periodicity of the substrate lattice $V(\boldsymbol{\rho} + \boldsymbol{B}) = V(\boldsymbol{\rho})$, where $\boldsymbol{B} = l_1\boldsymbol{b}_1 + l_2\boldsymbol{b}_2$ is a vector of the Bravais lattice of the substrate. The interaction potential with rigid substrate $H_{\mathrm{L}_1\mathrm{L}_2} : \mathbb{R}^{3nN_0} \to \mathbb{R}$ is a 1-body

potential for the particles in the harmonic ML. It can be decomposed into single-atom contributions and expanded in a Fourier series over the reciprocal lattice of the frozen monolayer G:

$$H_{\mathrm{L_1L_2}}(\boldsymbol{r}_{00},\ldots,\boldsymbol{r}_{nN_0}) = \sum_{\nu,l} V(\boldsymbol{\rho}_{\nu l}, z_{\nu l}) = \sum_{\nu,l,\boldsymbol{G}} V_{\boldsymbol{G}}(z_{\nu l}) e^{i\boldsymbol{\rho}_{\nu l}\cdot\boldsymbol{G}}. \tag{3.3}$$

The coefficients appearing in Eq. (3.3) are defined as

$$V_{\boldsymbol{G}}(z_{\nu l}) = \sum_{\nu l} V(\boldsymbol{\rho}_{\nu l}, z_{\nu l}) e^{-i\boldsymbol{\rho}_{\nu l}\cdot\boldsymbol{G}}. \tag{3.4}$$

In the assumption of small displacements from the equilibrium positions, the Fourier coefficients in Eq. (3.4) can be Taylor-expanded to the first order around the equilibrium interlayer distance z_0:

$$V_{\boldsymbol{G}}(z_{\nu l}) = V_{\boldsymbol{G}}(z_0) + V'_{\boldsymbol{G}}(z_0)\delta z_{\nu l} + \mathcal{O}(u^2), \tag{3.5}$$

where $\delta z_{\nu l} = (\boldsymbol{R}_\nu + \boldsymbol{u}_{\nu l})\cdot\hat{e}_3 - z_0$ and $V'_{\boldsymbol{G}}(z_0) = \left.\frac{dV_{\boldsymbol{G}}}{dz}\right|_{z_0}$. To simplify the notation, in the following $z_0 = 0$ and $\delta z_{\nu l} = z_{\nu l}$ and the expansion point will be dropped, $V_{\boldsymbol{G}} = V_{\boldsymbol{G}}(0)$. In an incommensurate heterostructure, atoms of the harmonic crystal a are found at all possible positions in xy with respect to the substrate crystal b, i.e. the adsorbate-atoms positions, mapped into the substrate unit cell, cover it densely, as shown in Fig. 3.2. The position of any adsorbate atom can be written in terms of the substrate lattice $\boldsymbol{\rho} = \boldsymbol{\rho}\,' + \boldsymbol{B}$, where $\boldsymbol{B}$ is the appropriate lattice vector and $\boldsymbol{\rho}\,'$ is confined in the unit cell of the substrate. Using the expansion in Eq. (3.5), the sum in Eq. (3.4) may then be converted into an integral over the unit cell Ω_b of the substrate potential at fixed height

$$V_{\boldsymbol{G}} = \sum_{\nu l} V(\boldsymbol{\rho}_{\nu l}\,' + \boldsymbol{B}, z_{\nu l}) e^{-i(\boldsymbol{\rho}_{\nu l}\,' + \boldsymbol{B})\cdot\boldsymbol{G}} = \lim_{L\to\infty} \int_{\Omega_b} V(\boldsymbol{\rho}, z_0) e^{-i\boldsymbol{\rho}\cdot\boldsymbol{G}} \mathrm{d}\boldsymbol{\rho}, \tag{3.6}$$

which is independent of the position of the adsorbate atoms. The coefficients can thus be evaluated providing an analytic form for the interaction $V(\boldsymbol{r})$, without the need for the exact atoms position in an extended geometry, which is usually out of reach for accurate QM calculations. The same reasoning can be applied to $V'_{\boldsymbol{G}}$ in Eq. (3.5).

In the limit of small displacements $u \ll l_a$, the plane-wave term in Eq. (3.3) can be expanded at first order as

$$e^{i\boldsymbol{r}_{\nu l}\cdot\boldsymbol{G}} = e^{i\boldsymbol{R}_{\nu l}\cdot\boldsymbol{G}}(1 + i\boldsymbol{G}\cdot\boldsymbol{u}_{\nu l}) + \mathcal{O}(u^2). \tag{3.7}$$

By substituting Eq. (3.5) and (3.7) in Eq. (3.3) and retaining only terms linear in $\boldsymbol{u}$:

$$H_{\mathrm{L_1L_2}} \approx \sum_{\nu,l,\boldsymbol{G}} V_{\boldsymbol{G}} e^{i\boldsymbol{R}_{\nu l}\cdot\boldsymbol{G}} + \sum_{\nu,l,\boldsymbol{G}} V'_{\boldsymbol{G}}(0) z_{\nu l} e^{i\boldsymbol{R}_{\nu l}\cdot\boldsymbol{G}} + i\sum_{\nu,l,\boldsymbol{G}} V_{\boldsymbol{G}}\boldsymbol{G}\cdot\boldsymbol{u}_{\nu l} e^{i\boldsymbol{R}_{\nu l}\cdot\boldsymbol{G}}. \tag{3.8}$$

By exploiting the periodicity of the adsorbate ML as explained in Appendix B, the

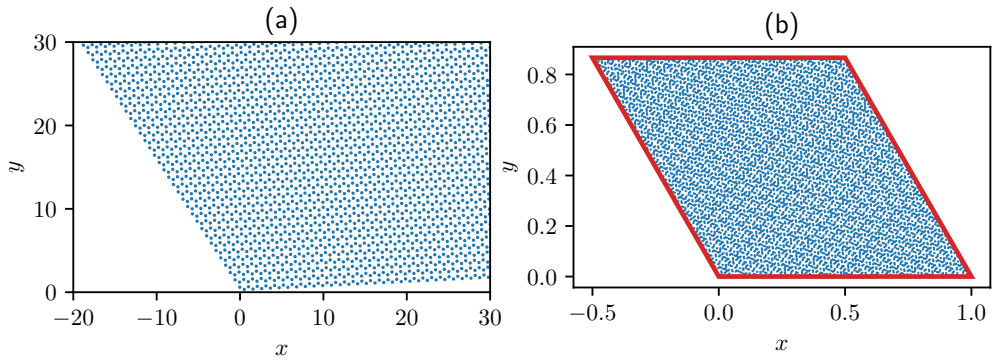

Figure 3.2: Graphical representation of the dense correspondence of lattice positions between incommensurate lattices in Eq. (3.6). Supercell with $L = 60$ of lattice $\underline{b}$ (left) mapped back in $\underline{a}$ (right).

interlayer interactions can be approximated as

$$H_{\mathrm{L_1L_2}} = nN_0 \sum_{\tau,\boldsymbol{G}} V_{\boldsymbol{G}} f_\tau \delta_{\boldsymbol{G},\boldsymbol{\tau}} \tag{3.9}$$

$$+ n\sqrt{N_0} \sum_{\substack{\boldsymbol{\tau},\boldsymbol{G},\boldsymbol{k} \\ s}} V'_{\boldsymbol{G}} \gamma_{\boldsymbol{k}s} \sum_\nu \frac{1}{\sqrt{m_\nu}} \left(\boldsymbol{\epsilon}_s(\nu,\boldsymbol{k}) \cdot \hat{u}_3\right) e^{i\boldsymbol{R}_\nu \cdot \boldsymbol{\tau}} \delta(\boldsymbol{G} + \boldsymbol{k} - \boldsymbol{\tau}) \tag{3.10}$$

$$+ in\sqrt{N_0} \sum_{\substack{\boldsymbol{\tau},\boldsymbol{G},\boldsymbol{k} \\ s}} V_{\boldsymbol{G}} \gamma_{\boldsymbol{k}s} \sum_\nu \frac{1}{\sqrt{m_\nu}} \left(\boldsymbol{\epsilon}_s(\nu,\boldsymbol{k}) \cdot \boldsymbol{G}\right) e^{i\boldsymbol{R}_\nu \cdot \boldsymbol{\tau}} \delta(\boldsymbol{G} + \boldsymbol{k} - \boldsymbol{\tau}). \tag{3.11}$$

The term in Eq. (3.9) is a *lock-in* contribution: non-null elements occur when $\boldsymbol{\tau} = \boldsymbol{G}$, i.e. substrate and adsorbate have commensurate lattice points. For aligned homostructures, this is the only contribution, as $\boldsymbol{\tau}$ and $\boldsymbol{G}$ are always the same vectors. In the presence of misalignment θ or mismatched lattice spacings, the equality is never satisfied and this contribution is null. The term in Eq. (3.10) describes the coupling between the adsorbate $\boldsymbol{\tau}$ and substrate $\boldsymbol{G}$ lattices due to an out-of-plane part of the mass density wave with wavevector $\boldsymbol{k}$. The scalar product $\boldsymbol{\epsilon}_s(\nu,\boldsymbol{k}) \cdot \hat{u}_3$ selects only the eigenvectors with a components along z and the coefficient $V'_{\boldsymbol{G}}$ is related to the force recalling the atoms towards the minimum of the binding potential between the layers, i.e. a LJ potential well. A similar effect for the in-plane-part is described by the term in Eq. (3.11): the scalar product projects the phonon eigenvectors $\boldsymbol{\epsilon}_{s\nu}$ on the xy plane and couples them with the direction (and magnitude) of the substrate lattice G, thus introducing an explicit dependence on the mismatch angle $\boldsymbol{\epsilon}_s(\nu,\boldsymbol{k}) \cdot \boldsymbol{G} = \epsilon_s G \cos\theta$.

Dirac's δ functions in Eq. (3.10) and (3.11) dictate that the three vectors $\boldsymbol{G}, \boldsymbol{\tau}, \boldsymbol{k}$, satisfy the geometry sketched in Fig. 3.3. In an incommensurate system, each density wavevector $\boldsymbol{k}$ identifies a single pair $\boldsymbol{G}(\boldsymbol{k}), \boldsymbol{\tau}(\boldsymbol{k})$ of reciprocal lattice vectors [164], i.e. each triplet of vectors is unique and the sums in Eq. (3.10) and (3.11) run over only one of these vectors.

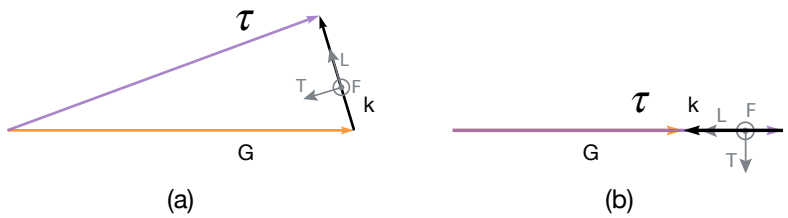

Figure 3.3: Example of geometry for the triplets appearing in Eq. (3.10) and (3.11) at (a) $\theta \neq 0$ and (b) $\theta = 0$. Orange arrows represent substrate reciprocal lattice $\boldsymbol{G}$, purple arrows represent the adsorbate reciprocal lattice $\boldsymbol{\tau}$ and black arrows are phonon excitation vectors $\boldsymbol{k}$. Grey arrows show the direction of the polarization of the phonon excitation of a branch s, described by the eigenvectors $\boldsymbol{\epsilon}_s(\boldsymbol{k})$. The flexural branch is always perpendicular to plane where $\boldsymbol{\tau}, \boldsymbol{G}, \boldsymbol{k}$ lie.

Total Energy

Adopting a second-quantisation formalism, as outlined in Appendix B, the total energy of the system is approximated by the following Hamiltonian operator

$$\hat{H} = E_c + \sum_{\boldsymbol{k},s} \hbar\omega_s^2(\boldsymbol{k}) \left(\hat{a}^\dagger_{\boldsymbol{k}s} \hat{a}_{\boldsymbol{k}s} + \frac{1}{2} \right) + nN_0 \sum_{\tau,\boldsymbol{G}} V_{\boldsymbol{G}} f_\tau \delta_{\boldsymbol{G},\boldsymbol{\tau}} \tag{3.12}$$

$$+ n\sqrt{N_0} \sum_{\boldsymbol{k},s} g_s^z(\boldsymbol{k})(\hat{a}_{\boldsymbol{k}s} + \hat{a}^\dagger_{-\boldsymbol{k}s}) + in\sqrt{N_0} \sum_{\boldsymbol{k},s} g_s^{xy}(\boldsymbol{k})(\hat{a}_{\boldsymbol{k}s} + \hat{a}^\dagger_{-\boldsymbol{k}s}). \tag{3.13}$$

The layer coupling and phonon amplitude have been grouped into

$$g_s^z(\boldsymbol{k}) = \sqrt{\frac{\hbar}{2\omega_s(\boldsymbol{k})}} \sum_{\boldsymbol{\tau},\boldsymbol{G},\nu} \frac{V'_{\boldsymbol{G}}}{\sqrt{m_\nu}} \boldsymbol{\epsilon}_s(\nu,\boldsymbol{k}) \cdot \hat{u}_3 e^{i\boldsymbol{R}_\nu \cdot \boldsymbol{\tau}} \delta_{\boldsymbol{G}+\boldsymbol{k},\boldsymbol{\tau}} = (g_s^z(-\boldsymbol{k}))^* \tag{3.14}$$

$$g_s^{xy}(\boldsymbol{k}) = \sqrt{\frac{\hbar}{2\omega_s(\boldsymbol{k})}} \sum_{\boldsymbol{\tau},\boldsymbol{G},\nu} \frac{V_{\boldsymbol{G}}}{\sqrt{m_\nu}} \boldsymbol{\epsilon}_s(\nu,\boldsymbol{k}) \cdot \boldsymbol{G} e^{i\boldsymbol{R}_\nu \cdot \boldsymbol{\tau}} \delta_{\boldsymbol{G}+\boldsymbol{k},\boldsymbol{\tau}} = -(g_s^{xy}(-\boldsymbol{k}))^*, \tag{3.15}$$

where the relation with the complex conjugate follow from $\omega(-k) = \omega(k)$, $\omega(k) \in \mathbb{R}$, phonon eigenvectors properties discussed in section 2.4.4 and the physical requirement for the energy in Eq. (3.3) to be a real number.

The Hamiltonian in Eq. (3.12) is not diagonal in $\hat{a}^\dagger_{\boldsymbol{k}s}$, $\hat{a}_{\boldsymbol{k}s}$ and the expectation value of $\hat{a}^\dagger$ and $\hat{a}$ operators on the ground state of the system is not null. Thus, the ground state of the system present a permanent phonon excitation, a mass density wave. To diagonalise the Hamiltonian in Eq. (3.12), new creation and annihilation operators are defined in terms of complex order parameters ξ:

$$\hat{a}_{\boldsymbol{k}s} = \sqrt{N_0}\xi_{\boldsymbol{k}s} + \hat{b}_{\boldsymbol{k}s} \qquad \hat{a}^\dagger_{\boldsymbol{k}s} = \sqrt{N_0}\xi^*_{\boldsymbol{k}s} + \hat{b}^\dagger_{\boldsymbol{k}s}. \tag{3.16}$$

The Hamiltonian in terms of the new operators reads

$$H = E_c + \sum_{\boldsymbol{k},s} \left(\hat{b}^\dagger_{\boldsymbol{k}s} \hat{b}_{\boldsymbol{k}s} + N_0 \xi^*_{\boldsymbol{k}s} \xi_{\boldsymbol{k}s} + \frac{1}{2} \right) \omega_s^2(\boldsymbol{k}) + nN_0 \sum_{\tau,\boldsymbol{G}} V_{\boldsymbol{G}} f_\tau \tag{3.17}$$

$$+ \sqrt{N_0} \sum_{\boldsymbol{k},s} \hat{b}_{\boldsymbol{k}s} \left(\hbar\omega_s(\boldsymbol{k}) \xi^*_{\boldsymbol{k}s} + n g_s^z(\boldsymbol{k}) + i n g_s^{xy}(\boldsymbol{k}) \right) \tag{3.18}$$

$$+ \sqrt{N_0} \sum_{\boldsymbol{k},s} \hat{b}^\dagger_{\boldsymbol{k}s} \left(\hbar\omega_s(\boldsymbol{k}) \xi_{\boldsymbol{k}s} + n g_s^z(\boldsymbol{k})^* + i n g_s^{xy}(\boldsymbol{k})^* \right) \tag{3.19}$$

$$+ nN_0 \sum_{\boldsymbol{k},s} \left(\xi_{\boldsymbol{k}s} g_s^z(\boldsymbol{k}) + (\xi_{\boldsymbol{k}s} g_s^z(\boldsymbol{k}))^* \right) + inN_0 \sum_{\boldsymbol{k},s} \left(\xi_{\boldsymbol{k}s} g_s^{xy}(\boldsymbol{k}) + (\xi_{\boldsymbol{k}s} g_s^{xy}(\boldsymbol{k}))^* \right). \tag{3.20}$$

The system is diagonalised by imposing that the coefficients of the linear terms in $\hat{b}$, $\hat{b}^\dagger$, Eq. (3.18) and (3.19) are null [164]:

$$\xi^*_{\boldsymbol{k}s} = -\frac{n}{\hbar\omega_s(\boldsymbol{k})} \left(g_s^z(\boldsymbol{k}) + i g_s^{xy}(\boldsymbol{k}) \right) = \xi_{-\boldsymbol{k}s}. \tag{3.21}$$

Finally, substituting Eq. (3.21) back into Eq. (3.17) yields

$$H = E_c + \sum_{\boldsymbol{k},s} \hbar\omega_s^2(\boldsymbol{k}) \left(\hat{b}^\dagger_{\boldsymbol{k}s} \hat{b}_{\boldsymbol{k}s} + \frac{1}{2} \right) + nN_0 \sum_{\tau,\boldsymbol{G}} V_{\boldsymbol{G}} f_\tau \tag{3.22}$$

$$- n^2 N_0 \sum_{\boldsymbol{k},s} \frac{1}{\hbar\omega_s(\boldsymbol{k})} \left[|g_s^z(\boldsymbol{k})|^2 + |g_s^{xy}(\boldsymbol{k})|^2 - 2\mathrm{Im}\left(g_s^z(\boldsymbol{k})^* g_s^{xy}(\boldsymbol{k}) \right) \right]. \tag{3.23}$$

Equations (3.22) and (3.23) represent a generalisation of eq. 13 in Ref. [168]: while the original work by NM assumes simple Bravais crystals and a purely 2D system, this result applies to real crystal systems, including distortions perpendicular to the ML surface. The last term in Eq. (3.23) represents the coupling between in- and out-of-plane distortions. While the first two terms in Eq. (3.23) always lower the energy of the system, the sign of the coupling contribution is not fixed and its effect must be determined case by case. Finally, equation Eq. (3.22) and (3.23) can be evaluated from pristine ML crystals and coupling potentials. This characterisation is cheaper than running MD simulations on extended systems and does not required a parametrisation of a material-specific force field. This would allow the exploration of the rotational landscape of a large set of heterostructures in a HT fashion, offering a way to tailor the energy landscape for twistronic application or nano-scale devices. This would, for example, ensure that the desired rotational configuration is thermodynamically stable.

3.1.1 Simple Crystal in the Long-wavelength Limit

From the result in Eq. (3.22) and (3.23), the NM approximation (eq. 21 in Ref. [168]) can be recovered. When considering a simple Bravais crystal, i.e. a single $n = 1$ atom of mass m per unit cell, the sum over ν disappears and the system presents only acoustic phonon branches. The eigenvector geometry neatly resembles the ML nature of the system: $\epsilon_{L,T}$ lie in the G plane and $\epsilon_F \perp G$. This yields the geometrical relations $\epsilon_T \cdot G = (R(\pi/2)\epsilon_L) \cdot G = G\tau \sin\theta/k$

and $k^2 = |G - \tau|^2 = G^2 + \tau^2 - 2G\tau\cos\theta$). Moreover, the coupling term $\mathrm{Im}(g^z g^{xy})$ is identically null: only one of the scalar products in Eq. (3.14) and (3.15), $\boldsymbol{\epsilon}_s(\nu, \boldsymbol{k}) \cdot \hat{u}_3$ or $\boldsymbol{\epsilon}_s(\nu, \boldsymbol{k}) \cdot \boldsymbol{G}$, respectively, can be non-null. In the long-wave limit, the phonon dispersion relations can be approximated as

$$\omega_L^2(\boldsymbol{k}) \approx c_{\mathrm{L}} k \tag{3.24}$$

$$\omega_T^2(\boldsymbol{k}) \approx c_{\mathrm{T}} k \tag{3.25}$$

$$\omega_F^2(\boldsymbol{k}) \approx A k^2, \tag{3.26}$$

where $c_{L,T}$ are the longitudinal and transverse sound velocities, respectively, and A is the bending rigidity of the layer [153]. Starting from Eq. (3.22) and (3.23), the energy gain per atom granted by the GS density wave compared to the isolated adsorbate ML equilibrium geometry reads

$$\Delta E = \frac{\langle \hat{H} \rangle_0 - E_c}{N_0} \tag{3.27}$$

$$= -\frac{1}{2m} \sum_{\boldsymbol{k}} \left[V_{\boldsymbol{G}}'^2 \frac{1}{A^2 k^4} + V_{\boldsymbol{G}}^2 \frac{G^2}{c_{\mathrm{L}}^2 k^2} + V_{\boldsymbol{G}}^2 \frac{G^2 \tau^2 \sin^2\theta}{c_{\mathrm{L}}^2 k^4} \left(\frac{c_{\mathrm{L}}^2}{c_{\mathrm{T}}^2} - 1 \right) \right]. \tag{3.28}$$

The definition of $g_s(\boldsymbol{k})$ in Eq. (3.14) and (3.15) were used. The delta functions in $g_s(\boldsymbol{k})$ reduce the sum to a single vector, $\boldsymbol{k}$; the dependency on this vector $\boldsymbol{\tau} = \boldsymbol{\tau}(\boldsymbol{k})$ and $\boldsymbol{G} = \boldsymbol{G}(\boldsymbol{k})$ is implicit.

The energy minima as a function of the misalignment angle is found by setting the derivative of Eq. (3.27) with respect to θ to be null

$$\frac{\partial \Delta E}{\partial \theta} = 0 = \sum_{\boldsymbol{k}} \frac{V_G^2}{c_{\mathrm{L}}^2} G^2 \left[\frac{G\tau\sin\theta}{k^4} + \tau^2 \sigma \left(\frac{\sin\theta\cos\theta}{k^4} - \frac{2G\tau\sin^3\theta}{k^6} \right) \right] - \left(\frac{V_{\boldsymbol{G}}' \epsilon_F^z(\boldsymbol{k})}{A} \right)^2 \frac{G\tau\sin\theta}{k^6}, \tag{3.29}$$

where $\sigma = ((c_{\mathrm{L}}/c_{\mathrm{T}})^2 - 1)$ and an implicit dependence on θ is contained in k^n at the denominators.

Dividing Eq. (3.29) by $\sin\theta$, $\theta = 0$ emerges as a solution. From the physical point of view, $\theta = 0$ must be a solution: the energy cannot depend on the sign of the misalignment and, thus, $\theta = 0$ must be an extrema point, either maximum or minimum. The energy scales of in-plane and out-of-plane contributions to the position of the energy minima are separated in Eq. (3.29). The in-plane deformations are scaled by the prefactors $\frac{V_G^2}{c_{\mathrm{L}}^2} G^2$, which is the ratio between the energy gain from matching the substrate periodicity ($V_G G$) and the cost of elastic deformation (c_{L}), and $\tau^2((c_{\mathrm{L}}/c_{\mathrm{T}})^2 - 1)$, which expresses the lower energy cost of transverse phonon branch compared to longitudinal one. The contribution of out-of-plane deformation is governed by $\left(\frac{V_{\boldsymbol{G}}' \epsilon_F^z(\boldsymbol{k})}{A} \right)^2$, which is the ratio between out-of-plane interlayer coupling ($V_G' \epsilon_F^z(\boldsymbol{k})$) and cost of layer bending (A). In contrast with the 2D case presented in the following section, Eq. (3.29) retains a dependency from the

reciprocal lattice vectors $\boldsymbol{\tau}$ and $\boldsymbol{G}$. This is rooted in the different dependence from $\boldsymbol{G}$ of the in- and out-of-plane contributions: the energy contribution related to the flexural phonons couples with the z axis rather than with the Bravais lattice of the adsorbate. No simple analytical solution is found for the limiting case in Eq. (3.29) and while it could be evaluated numerically, the non-approximated model in Eq. (3.22) and (3.23) would yield a better description of the system.

Purely 2D Monolayer

To recover eq. 21a in [168], the adsorbate ML is regarded as a 2D object, i.e. only L and T phonon branches are present. Moreover, it is assumed that by symmetry there are p equivalent triplets $\boldsymbol{\tau}, \boldsymbol{G}, \boldsymbol{k}$ that satisfy the construction in Fig. 3.3 [164, 168]. Equation (3.29) becomes

$$\Delta E_{\mathrm{2D}} = -\frac{pV_{\boldsymbol{G}}^2 G^2}{2mc_{\mathrm{L}}^2}\left[\frac{1}{k^2} + \frac{\tau^2 \sin^2\theta}{k^4}\sigma\right], \tag{3.30}$$

Solving $\partial \Delta E_{\mathrm{2D}}/\partial\theta = 0$ for θ yields eq. (21a) in Ref. [168]

$$\cos\theta_{\mathrm{NM}} = \frac{1+\rho^2(1+2\sigma)}{\rho[2+\sigma(1+\rho^2)]}, \tag{3.31}$$

where $\rho = \tau/G$. The trigonometric function imposes the following limits on the parameters in Eq. (3.31):

$$0 < \rho < 1 \vee \rho > 1 \tag{3.32}$$

$$c_{\mathrm{L}} \geq \sqrt{1+\rho^{-1}}c_{\mathrm{T}}. \tag{3.33}$$

The first condition correctly implies that for commensurate bilayers ($\rho = 1$) the minimum-energy angle is always $\theta = 0$, i.e. aligned lattices. The second condition states that the transverse branch must be lower enough in energy compared to the longitudinal one to justify the shift from $\theta = 0$ which coincides with the shortest k value and thus lower frequency ω. In ref. [168], ignoring the out-of-plane displacements in Eq. (3.29) is justified by the experimental observation that $V' \approx 0$.

To summarise the physics of the NM model, a computational result from the following analysis of MoS_2/G system is anticipated here. As illustrated in Fig. 3.3, as function of the misalignment angle θ the relative alignment of the the substrate lattice G (blue arrow) and the phonon acoustic eigenvectors (gray arrows) changes. Since flexural phonons are perpendicular to the xy plane, and thus to $\boldsymbol{G}$, they can never participate to this energy term. As Fig. 3.3(b) show, at $\theta = 0$ $\boldsymbol{G} \perp \epsilon_T$ and thus only longitudinal phonon modes contribute to the in-plane interaction with the substrate. Instead, when $\theta \neq 0$ like Fig. 3.3(a) both transverse and longitudinal eigenvectors have a non-null projection on $\boldsymbol{G}$. The macroscopic effect of the different excited branches at different angles is shown in the displacement maps in Fig. 3.4. In the aligned case $\theta = 0°$ only compression and

extension of the bonds are found and all displacements lie along the lattice parameters. In the misaligned case $\theta \neq 0°$ displacements have components along and perpendicular to the bonds, signalling the excitation of the transverse band as well. According to NM approximation [164, 168] in Eq. (3.31), the non-null amplitude of the transverse branch can lead to a lower total energy of the system, despite $\theta \neq 0$ implies a larger $|\boldsymbol{k}|$, thus larger energy penalty proportional to $\omega(k)$; this is because the transverse branch lies lower in energy than the longitudinal one. This model does not take into account the complex structure of the unit cell crystal and the out-of-plane deformation, whose effect is analysed in the remainder of this chapter.

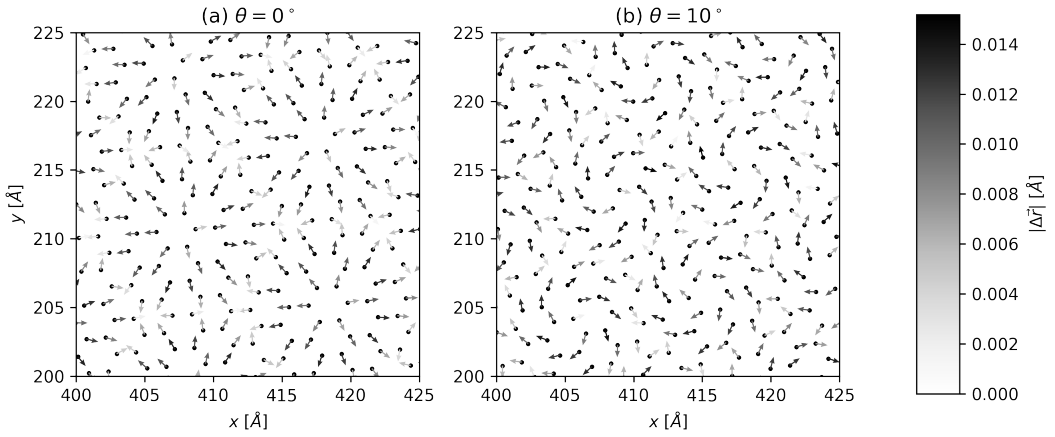

Figure 3.4: In plane relaxation of graphene layer in the potential generated by MoS_2. In (a) $\theta = 0$ and the two Bravais lattices are aligned: the only contribution to the distortion comes from $\epsilon_L \cdot G$, parallel to Bravais lattice vectors. In (b) $\theta \neq 0$ and the two Bravais lattices are misaligned: both $\epsilon_L \cdot G \neq 0$ and $\epsilon_T \cdot G \neq 0$ and displacements are both along and perpendicular to Bravais lattice vectors. To enhance visibility, arrows report the direction of the displacement of each C atom, while the colour-code reports the length.

3.2 Computational Methods

This section introduces the computational protocols and methods used to study the system of MoS_2/G heterostructure, taken as a case study for the epitaxy theory outlined in section 3.1. In order to avoid finite-size effects and harvest information solely from the relaxation of the atoms in the layers, edge-free geometries are adopted. The resulting supercells are simultaneously compatible with the lattice mismatch and a relative imposed angle between the lattices. As a result, periodic boundary conditions (PBC) can be applied to such cells. The starting interface geometry is described by a pair of 2D lattices defined by vectors $(l_{\mathrm{a}}\hat{\mathbf{a}}_1, l_{\mathrm{a}}\hat{\mathbf{a}}_2)$ and $(l_{\mathrm{b}}\hat{\mathbf{b}}_1, l_{\mathrm{b}}\hat{\mathbf{b}}_2)$, where l_{a} and l_{b} represent the lattice constants and the $\hat{b}_i$ vectors are rotated by an angle θ with respect to $\hat{a}_i$. Two layers will be compatible if they satisfy the matching condition

$$l_{\mathrm{a}}(n_1\hat{\mathbf{a}}_1 + n_2\hat{\mathbf{a}}_2) = l_{\mathrm{b}}(m_1\hat{\mathbf{b}}_1 + m_2\hat{\mathbf{b}}_2), \tag{3.34}$$

where the integer numbers n_1, n_2, m_1, m_2 are supercell indices representing the repetition along each lattice vector. In practice, for incommensurate lattice constants, the matching condition yielding PBC-compliant supercells can only be satisfied approximately, i.e. the lattice spacing l' of one of the two components needs to deviate from its equilibrium value l . Here, in order to obtain suitable structures with imposed angles between 0° and 60°, only supercells satisfying $|l' - l| < 5 \times 10^{-7}$ Å are accepted. The strain is applied to the MoS_2 layer, which leads to a maximum strain $\epsilon = \frac{l'-l}{l}$ within the same order of magnitude, four orders less than reported strains in other computational studies [169, 170, 171]. This protocol yields a set of supercells, each of which has a different number of atoms up to 343893, created according to the four supercell indices resulting in an unique twisting angle, satisfying the matching condition. Details of this protocol and all the parameters of the supercells used are reported in Appendix C.

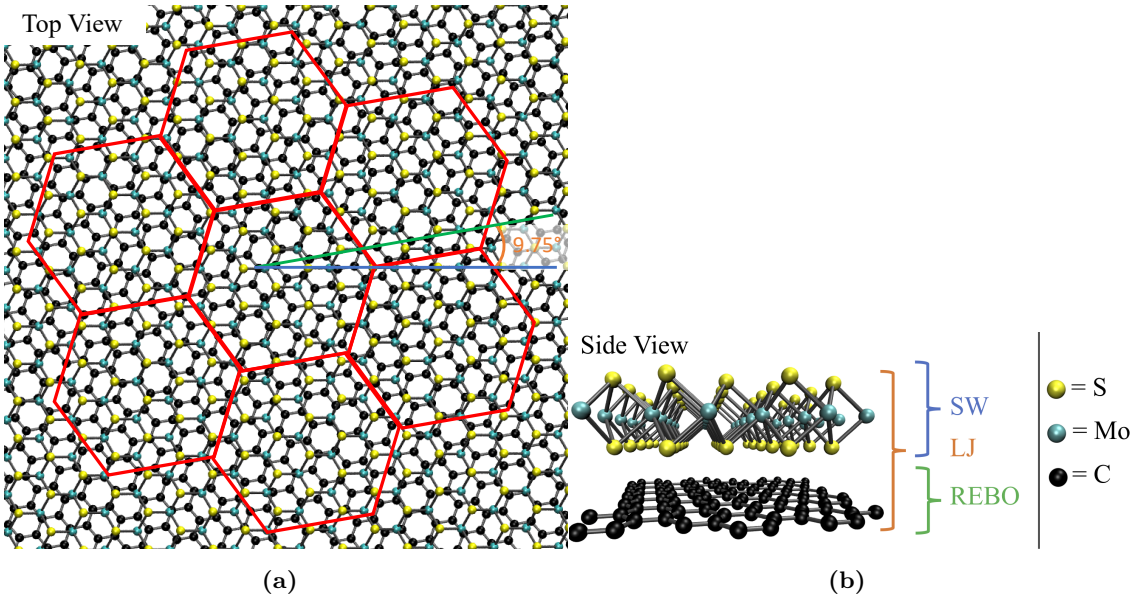

Figure 3.5: Schematic overview of computational setup displayed for a mismatch angle of 9.75°. (a) Top view, including a sketch of moiré tiling resulting from the geometrical interference between the two lattices. The mismatch angle between the lattice direction of MoS_2 (blue line) and G (green line) lattices is reported as well. (b) Side view, including the corresponding force fields that have been used.

The bilayer system is described using the force field reported in Appendix D: G layer is modelled using Reactive empirical bond order (REBO) potential [172], MoS_2 layer is modelled using Stilling-Weber (SW) potential [171], and the interlayer interactions are modelled with LJ dispersion term, whose parametrisation is reported in Appendix D. This yields the following Hamiltonian for the bilayer system:

$$H = H_{\mathrm{C}}^{(\mathrm{REBO})} + H_{\mathrm{MoS_2}}^{(\mathrm{SW})} + H_{\mathrm{C-MO,C-S}}^{(\mathrm{LJ})}. \tag{3.35}$$

Energy minimizations of Eq. (3.35) for large supercell geometries were performed using the conjugate gradient algorithm available within the LAMMPS package [173], with the convergence tolerance on the total energy value set to 1×10^{-15}. An overview of the

computational setup can be found in Figures 3.5a and 3.5b. Appendix D reports a benchmark of the intralayer part of the FF, comparing lattice parameter and phonon dispersion with DFT calculations, and a refinement of the interlayer part, since the parametrisation found in literature was not deemed satisfactory.

Sound Velocity Estimation The NM approximation in Eq. (3.31) requires an estimation of the linear dispersion regime $\lim_{k\to 0}\omega_i(k) = v_i k$, where $i = \mathrm{L}, \mathrm{T}$ labels either the transverse (T) or longitudinal (L) branch and $v_i = \frac{\partial\omega(k)}{\partial k}\Big|_\Gamma$ is the speed of sound of corresponding branch. Fig. 3.6 shows the longitudinal and transverse branches close to Γ of G and MoS_2, extracted from the phonon dispersion reported in Appendix D. The plot also

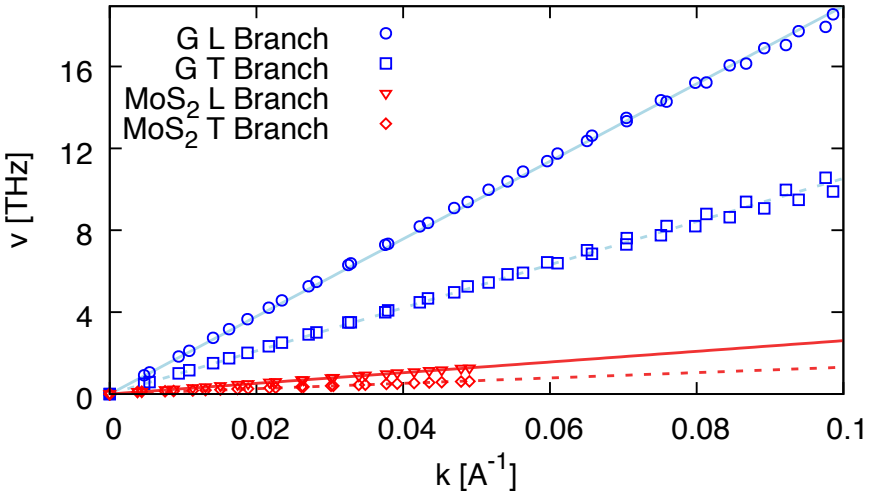

Figure 3.6: Sound velocity fits from the phonon dispersion in G (shades-of-blue symbols) and in MoS_2 monolayer (shades-of-red symbols). The y axis reports the frequency ν in THz and the x axis the distance from Γ in Å^{-1}. The colour-matching lines report the linear fit of that branch, i.e. $\nu_i = v_i k$.

shows the linear fits obtained from the points, including their fitted slopes representing the sound velocities, as reported in Table 3.1. This leads to the values $\sigma_{\mathrm{G}} = 2.235$ and $\sigma_{\mathrm{MoS_2}} = 2.968$ used to evaluate Eq. (3.31).

Material	v_{L}[km/s]	v_{L}[km/s]
G	18.9403 ± 0.0005	10.5298 ± 0.0005
MoS_2	0.2608 ± 0.0005	0.131 ± 0.002

Table 3.1: Sound velocity of transverse and longitudinal phonon branches in G and monolayer MoS_2 extracted from Fig. 3.6. The uncertainty arises from the linear fitting procedure.

3.3 Results

The reminder of the chapter tests the NM model and long-wavelength limit on the prototypical complex heterostructure: MoS_2 ML on G. The analysis will highlight the limit of the NM approximation and the direction in which an advanced model should go.

3.3.1 Constrained 2D Simulations

In this section, MoS_2/G system is constrained to meet the assumption of the NM limit in section 3.1.1. Following the model presented in section 3.1.1, the intralayer term in Eq. (3.1) is substituted by its harmonic approximation, while the coordinates of the second layer are frozen at its initial values, r_0. The theoretical misalignment angle minimising the energy is given by Eq. (3.31). There are two possible scenarios covered by NM theory: G can be treated as the rigid substrate, while MoS_2 acts as a soft adsorbate, or vice versa. In the first case, the theory predicts $\theta_{\mathrm{NM}}^{\mathrm{MoS_2}} = 8.0°$, while if G is the adsorbate, the minimum-energy angle is $\theta_{\mathrm{NM}}^{\mathrm{G}} = 8.6°$. The prediction of the NM model can be verified by minimizing the total energy of the twisted geometries described above under suitable constraints. The atoms of the heterostructures are constrained in the direction perpendicular to the surface, i.e. the z axis, effectively reducing the dimensionality of the system to 2D. Furthermore, the atoms of the substrate layer are frozen in the in-plane directions x and y, enforcing a fully rigid substrate. As mentioned at the beginning of this chapter and explained in detail in the Appendix C, the edge-free geometries used in this work inevitably retain a degree of stress resulting from the matching condition for the two lattices in order to be able to apply PBC. The slightly different strains applied to each geometry result in different offsets in the starting energies. It was found that this offset is comparable with the energy gain arising from in-plane movements of the atoms, even in the biggest supercell within computational limits. This artifact leads to a significant noise in the signal of the energy as a function of the imposed angle. To overcome this problem and to obtain a clear signal in these simulations, the LJ-coupling strength between the MoS_2 and G layers was enhanced. During the geometry optimization, the LJ-parameters ϵ_{ij} in Eq. (D.1) are set to $\epsilon'_{ij} = 100 \cdot \epsilon_{ij}$. Next, the resulting energy profile is scaled back, as if simulated with the original value $\epsilon'_{ij} = \epsilon_{ij}$. As is shown in the Figures 3.7a and 3.7b, this computational trick reduces the noise without affecting the actual physics of the problem. The LJ-coupling between the layers of MoS_2 and G was enhanced during the constraint simulations as mentioned in the main text. This was done because the strain posed on the MoS_2 lattice, in order to create a supercell suitable for the application of PBC, results in a noise significantly affecting the energy profile upon rotating the lattices. Fig. 3.7a reports the energy profile $E(\theta)$ for different values of the scaling factor f in $\epsilon' = f\epsilon$. It can be seen that this computational trick does not alter the physics but purely amplifies the energy trends that otherwise get progressively hidden by the noise. Fig. 3.7b reports the scaling relation at $\theta = 30°$, showing an almost quadratic behaviour. In order to make comparison between Fig. 3.8 and Fig. 3.9 easier, the values computed at $\epsilon'_{LJ} = 100\epsilon_{LJ}$ are scaled back, according to $E^{100}(30°)/E^{1}(30°) = 1751.57$. In other words, both the minima and maxima remain located at the same angle, however, their absolute energy value is scaled according to the LJ-coupling.

Fig. 3.8 shows the optimized energy per atom, $E(\theta)$, of the bilayer system as a function of the angle, θ, with respect to the energy of the aligned structures, $E(0)$. The two curves refer to the following models: 2D-adsorbed G atop rigid MoS_2 (red) and 2D-adsorbed MoS_2

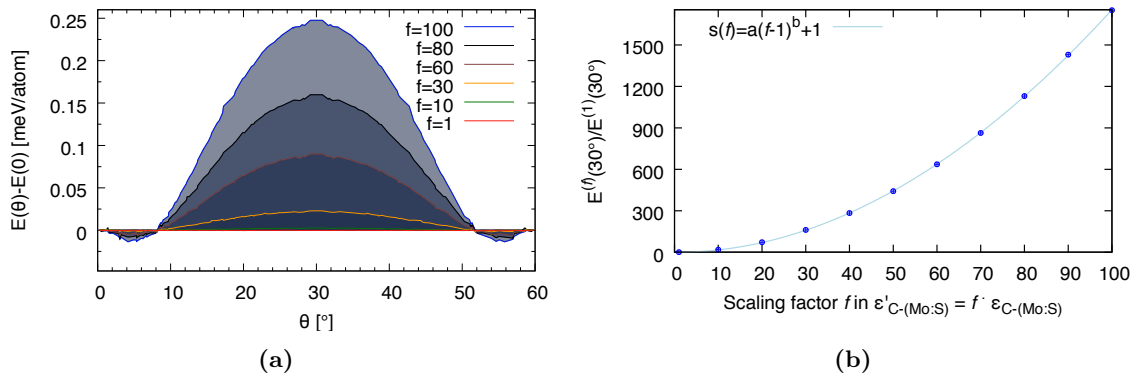

(a) **(b)**

Figure 3.7: (a) Enhancement of the LJ-coupling. The plot reports the energy $E(\theta)$ in meV/atom versus angle θ for rigid MoS_2 and soft G for increasing values of LJ coupling f, as reported in the legend. (b) Scaling relation between the maximum energy ratio and the LJ coupling parameter ϵ. Blue circles represent the energy at $\theta = 30°$ computed at a given enhancement factor f, with respect to $f = 1$, versus the scaling factor f. The light-blue line shows the fitted power law reported in the legend with parameters $a = 0.217837$ and $b = 1.9572$.

atop rigid G (blue). Both cases reveal a minimum at a non-zero angle: for the adsorbed G case, the minimum is found at $\theta^{\mathrm{G}}_{\mathrm{min}} = 4.2°$ while for the adsorbed MoS_2 case it is at $\theta^{\mathrm{MoS_2}}_{\mathrm{min}} = 12.3°$. The simulations show that the physics described by the approximation of Eq. (3.31) is still valid, i.e. a non-zero minimum angle is observed for both cases. However, the absolute values of the predicted and observed angles are not in agreement, yielding a discrepancy of $\theta^{\mathrm{G}}_{\mathrm{min}} - \theta^{\mathrm{G}}_{\mathrm{NM}} = -4.4°$ in the case of 2D-adsorbed G and $\theta^{\mathrm{MoS_2}}_{\mathrm{min}} - \theta^{\mathrm{MoS_2}}_{\mathrm{NM}} = 4.3°$ in the case of 2D-adsorbed MoS_2.

A previous study [163], dealing with G and h-BN, showed that the NM model quantitatively describes the relaxation of the constrained system of these purely 2D materials. Here, the NM theory captures the basics of the physics, i.e. non-zero minimum-energy misalignment, but is not able to describe satisfactorily the complex geometry of the bilayer system, especially in the case of the flexible MoS_2 layer. The poor prediction of the theory in this case is attributed to the internal 3D structure of the MoS_2 monolayer, which indeed is unaccounted for in the NM model. This suggests that the NM theory is generally of limited utility for any bilayer comprising TMDs or other systems with a multi-atom thick single layer. Another difference between the results here and the ones found for G/hBN heterostructures [163] is the quantitative difference in the energy values. In fact, the results here report energy differences of one order of magnitude less. This difference is explained by the earlier mentioned MoS_2/G BL system mismatch ratio $\rho = l/l \approx 0.8$. Due to this significant incommensurability between the MoS_2 and G, present for all rotations, the atom displacements and energy difference is expected to be less pronounced. In fact, a similar observation has been done experimentally by Diaz *et al.* [160] and Pierucci *et al.* [161]. For example, Diaz *et al.* found that the moiré pattern obtained from AFM measurements from MoS_2/G was less pronounced compared to the one of hBN/G. Finally, a BL system with constraints between the pure NM theory and free system was considered: atoms in each MoS_2/G ML are free to move in the equilibrium xy plane but constrained along z. This corresponds to lifting the rigid substrate assumption of the NM theory, while enforcing

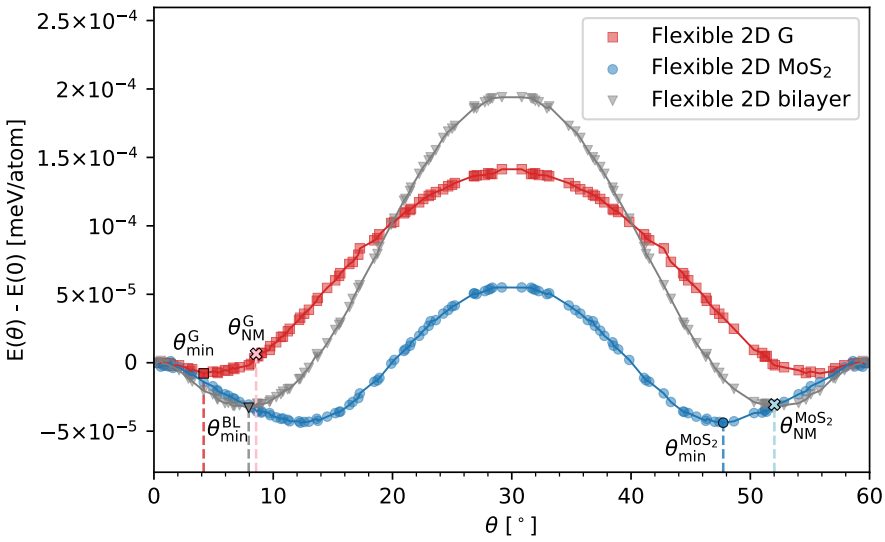

Figure 3.8: Energy per atom $E(\theta)$, in meV, as a function of the imposed angle θ in degrees for different 2D models: red squares refer to flexible G on top of rigid MoS_2, blue circles refer to flexible MoS_2 on top of rigid G and gray triangles refer to flexible MoS_2 on top of flexible G. The label in the legend indicate the flexible ML. The reference value of the energy scale is set to $E(0)$. The minimum-energy point along each curve is highlighted by a dashed line and a label. Red and blue crosses (accompanied by a label) mark the minimum angle predicted by the NM theory for the first and second case, respectively. The minimum-energy and NM-predicted angles for flexible MoS_2 are reported starting from 60° for ease of reading.

a constant interlayer distance. The black symbols in Fig. 3.8 report the results of this case. As a result, the two layers can mutually influence and distort each other, reaching configurations not included in the NM model. A minimum at $\theta = 7.94°$ is clearly visible in Fig. 3.8, midway between the two rigid substrate approximations. Note that the the model does not describe the mutual interaction between the layers and does not provide a prediction for the minimum-energy angle in this case. The behaviour of the system is thus qualitatively different from the h-BN/G heterostructures studied by Guerra et al [163]. In that case the NM theory was found to explain quantitatively the energetics of the rigid and z-frozen scenario, i.e. blue and red lines in Fig. 3.8, but removing the rigid substrate constraint changed the behaviour qualitatively: the minimum-energy angle predicted by NM disappeared from the energy profile of the system. From this observation, one can conclude that relaxing the constraint of a rigid substrate in this system with a 3-dimensional single layer does not contradict the physics described by the NM model.

3.3.2 Free bilayer 3D

Indeed, the NM theory is even qualitatively inadequate if all degrees of freedom are considered, i.e. all atoms are free to move in the 3D space. Fig. 3.9 shows the energy per atom as a function of the angle of the system with no rigid substrate, but two soft, interacting layers. Naturally, the LJ-coupling between the two layers has been restored to the values obtained from fitting against the DFT data to correctly reproduce interlayer forces. The behaviour is both quantitatively and qualitatively different from the constrained

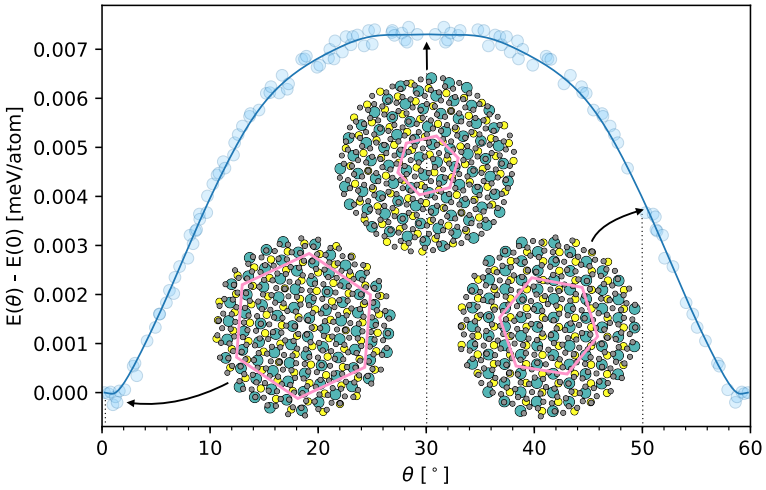

Figure 3.9: Energy per atom $E(\theta)$, in meV, as a function of the imposed angle θ. Each point in the energy landscape represents a distinct geometry at a different imposed angle and the blue line is a Bézier fit. The small oscillations at $\theta = 0°, 60°$ are due to numerical noise in the energy simulations. The circular insets show a top views within a distance $d = 15\,\text{Å}$ from the origin of relaxed geometries at $\theta \approx 0°$ (bottom left), $\theta \approx 50° \equiv 10°$ (bottom right) and $\theta \approx 30°$ (top centre). The atoms are coloured according to the scheme in Fig. 3.5. The pink hexagons sketch the moiré tile in each configuration.

system presented previously. The introduction of the out-of-plane dimension (z) changes the response qualitatively. The energy minima at non-zero angles have disappeared and $E(\theta)$ rises symmetrically from the global minima at the aligned cases (0°,60°) towards the global maximum at the mismatch angle of 30°. From Fig. 3.9, one can thus deduce that at 0 K, the fully flexible bilayer system will be stable when aligned at 0° or 60°. The energy profile around the mis-alignment of 30° is flat and the misaligned geometry at this angle could therefore be characterized as metastable, as a vanishing force $F = -\mathrm{d}E(\theta)/\mathrm{d}\theta$ drives the system toward the global minima at 0° or 60°. In the thermodynamic limit this orientation should not occur, considering its maximum character. The fact that it is observed experimentally [156] can be explained by the fact that this geometry can be stabilized by a small internal friction, e.g. due to defects.

The NM theory does not hold when structural distortions perpendicular to the interface are allowed. Results indicate that these are important for MoS_2/G heterostructures and there is reason to believe that this is more widely the case. The core of the NM argument is that the collective misalignment arises from the excitation of the transverse phonon branch in the xy plane, which lies lower in energy than the longitudinal one. This static distortion, which raises the internal energy of the adsorbate layer, is counterbalanced by a better interdigitation of the two lattices, that is, the displaced atoms are shifted to more favourable stacking with respect to the interlayer potential [164, 165]. If out-of-plane distortions, unaccounted for in NM theory, lead to a better interplay between the two layers, i.e. a gain in the interlayer coupling energy that is larger than the intralayer energy penalty from the modulation itself, the system will lower its total energy. Differently from the NM theory, the lowest-energy distortion in this scenario would not result in a

misalignment between the components but in the formation of ripples keeping the locally commensurate zones at the equilibrium distance and pushing away incommensurate ones.

3.4 Discussion

Out-of-plane displacements magnitude This section compares the out-of-plane displacement of G layer with the MoS_2 one. The thickness of a ML is defined as $\tau(\theta) = z_{\max} - z_{\min}$ in the relaxed geometry. Since MoS_2 comprises three atomic layers, the analysis has been carried out on the separate components: bottom S layer, Mo layer and top S layer, as reported in Fig. 3.10. The thickness of the bottom S layer, shown as an orange dashed line in Fig. 3.10, shows the larger displacements amongst the atomic layers comprising MoS_2 and the trend mirroring G displacement (blue solid line in Fig. 3.10. This behaviour can be explained as the bottom S layer is the closest atomic layer of MoS_2 to G and, thus, is the most affected by the interlayer potential. As the misalignment angle θ grows, the less convenient it becomes for G to modulate and the more important the contribution from MoS_2 modulation becomes, albeit still small compared to G signal. The Mo layer shows a level of modulation only after $\theta = 20°$, when G starts to flatten. Finally, the top S layer, furthest from the interface with G, remains essentially flat throughout the spectrum and the small fluctuation can be regarded as numerical noise.

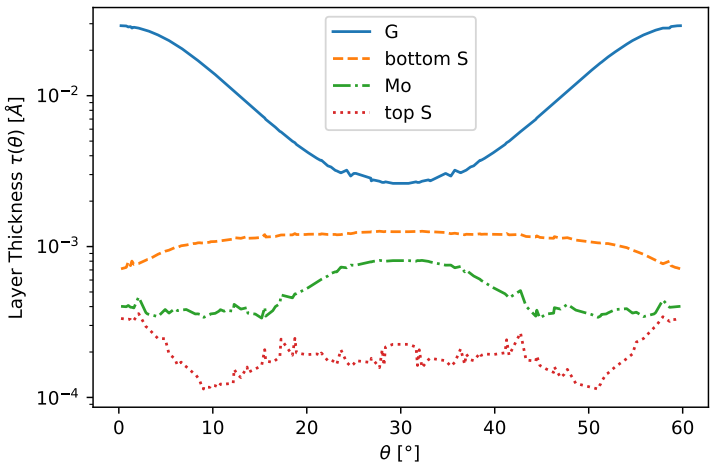

Figure 3.10: Thickness $\tau(\theta)$ of the atomic layers as a function of the mismatch angle θ. The y axis is in logarithmic scale for better comparison.

The total variation Δ between all values θ are reported in Table 3.2. The last column reports the variation with respect to the one occurring in G (Δ_G): the modulation in MoS_2 is at least 2 orders of magnitude less than in G. The structural distortion representing the leading order in the system energy economy occurs mostly in the G layer. Thus the following discussion will focus on this part of the system only.

Phonon dispersion in G The out-of-plane deformations disregarded in NM theory are characterized here in terms of the flexural phonon branch, which described excitation

Atom layer	$\min_\theta(\tau)$ [Å]	$\max_\theta(\tau)$ [Å]	Δ [Å]	Δ/Δ_G
G	0.0026	0.0291	0.0265	1
Bottom S	0.0007	0.0013	0.0006	0.021
Mo	0.0003	0.0008	0.0005	0.018
Top s	0.0001	0.0004	0.0002	0.009

Table 3.2: Minimum and maximum thickness across θ. Variation of thickness $\Delta = \max_\theta(\tau) - \min_\theta(\tau)$. Variation relative to the one occurring in G.

perpendicular to the ML plane. In line with the edge-free geometries adopted, the phonon picture is independent of size of sample and since the phonon eigenvectors represent a complete basis set [143], any distortion in the crystal may be expressed as a linear combination of phonons. Moreover, treating the distortions of a layer in terms of its phonon spectrum decouples the intralayer energetics from interlayer interaction. As shown by the blue solid line in Fig. 3.11, the flexural band is flat near the centre of the BZ (Γ point), i.e. the long-wave modulations perpendicular to the basal plane can occur essentially without an energy penalty. Transverse (dashed grey in Fig. 3.11) and longitudinal (dash-dotted gray in Fig. 3.11) bands, at the base of the argument given by NM theory, are higher in energy, resulting in more expensive modulations of the G layer.

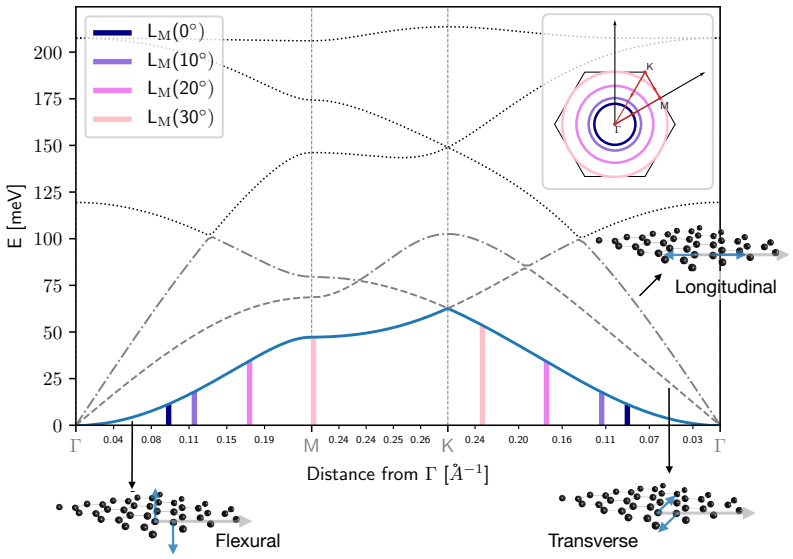

Figure 3.11: Phonon band structure of the G monolayer. The y axis reports the phonon energy, while the x axis marks the distance from the origin along the path $\Gamma \to M \to K \to \Gamma$, shown in the top right inset and marked along the x axis by gray dashed lines. The flexural branch is reported by a solid blue line, transverse branch by dashed gray line and longitudinal branch by dash-dotted grey line while other branches are shown in dotted black lines. Coloured segments along x raising from $y = 0$ to the flexural branch mark wavevectors matching the moiré spacing $L_M(\theta)$ for the geometries in the insets of Fig. 3.12, as highlighted by the colour-code. The moiré wavevector k_M corresponding to real-space wavelength L_M is shown in the top-right inset following the colour-code in the legend in top left.

Moiré pattern While the phonon spectrum describes the energy penalty compared to an isolated ML at equilibrium, the energy gain from interlayer interactions can be

quantified in terms of moiré patterns. The moiré superlattice is a geometrical construction describing the interference between two lattices and can be used to identify geometrical correspondence between lattices, i.e. zones of local commensuration versus incoherent stacking. The symmetry of the moiré superlattice reflects the one underlying Bravais lattices and its lattice parameter L_{M} is given by [112]

$$L_{\mathrm{M}}(\theta) = \frac{l_{\mathrm{G}}}{\sqrt{1+\rho^{-2}-2\rho^{-1}\cos\theta}}. \tag{3.36}$$

Fig. 3.12 shows the correlation between out-of-plane modulations in the G sheet, i.e.

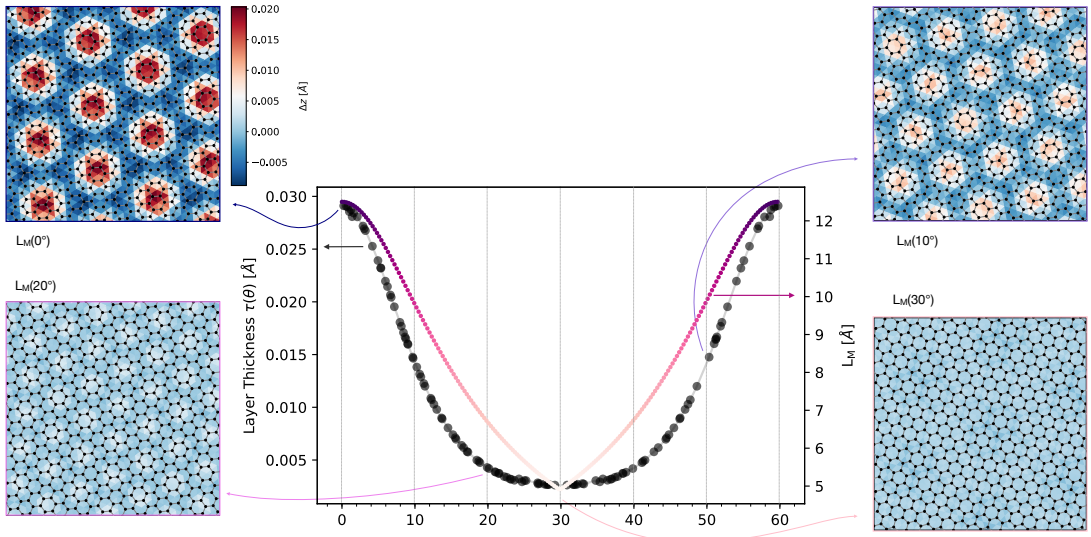

Figure 3.12: Thickness of G layer $\tau(\theta)$ resulting from the displacement of C atoms (black circles, left axis) and spacing of the moiré pattern $L_{\mathrm{M}}(\theta)$ (coloured dotted line, right axis) as a function of θ for equivalent configurations at 0° and 60° rotating towards 30°. The insets show the local distortion following the moiré lattice in a square of sides 60 Å at the nearest configuration having approximately an angle of $\theta = 0°$ (0.23°, dark purple), 10° (9.75°, purple), 20° (19.89°, dark pink), 30° (29.17°, pink). The colour of each triangle reports change in height $\Delta z = z - z_{\mathrm{eq}}$ coordinate of the corresponding C atom (black points) following the colour code reported in top left. For example, the moiré pattern can be seen in the inset for $\mathrm{L_M}(0°)$ as the lattice defined by the red regions.

rippling in the z dimension quantified by the layer thickness $\tau(\theta)$, and the moiré pattern. The thickness of the G layer $\tau(\theta)$ originates from local ripples of the carbon sheet. This thickness is, therefore, a global descriptor defined for each misaligned geometry and represents a useful tool to quantify the behaviour of the system. At $\theta = 0$, the moiré spacing and the thickness $\tau(\theta)$ are at a maximum and they both decrease as the misalignment increases. As θ increases, the length of the pattern shrinks with the displacement along z: at $\theta = 30°$ the moiré shrinks to a couple of unit cells and the monolayer remains basically flat. The ripple patterns, i.e. local geometry, follow perfectly the moiré superlattice, as shown in the insets of Fig. 3.12 for selected values of θ.

Moiré-Phonon interplay Combining the geometrical construction shown in Fig. 3.12 and the G phonon dispersion in Fig. 3.11, the energy profile in Fig. 3.9 can be explained. The moiré spacing $L_{\mathrm{M}}(\theta)$ can be mapped to wavevectors into the BZ by $k_{\mathrm{M}}(\theta) = \frac{2}{\sqrt{3}L_{\mathrm{M}}(\theta)}$. The wavevectors k_{M} corresponding to the spacing L_{M} of the geometries in the insets of Fig. 3.12 are highlighted, following the same colour-code, in Fig. 3.11 by vertical segments along the path and as circles in the inset, showing all wave-vectors in the BZ at the moiré spacing. A modulation of the G sheet with wavelength $L_{\mathrm{M}}(\theta)$ can be represented as a combination of phonon modes of matching wavevectors $k_{\mathrm{M}}(\theta)$. Since the modulation of G layer takes place essentially in the z direction only, the major contribution in the decomposition onto phonon modes arises from the flexural branch, which point in this direction, and, to a lesser extent, from the high-energy optical branches. Within small displacements from the equilibrium positions, the energy price of such modulations can be estimated by the corresponding phonon energy. As θ varies from 0° to 30° and the moiré shrinks as shown in Fig. 3.12, the associated wavevector $k_{\mathrm{M}}(\theta)$ assumes the values between $k_M(0°) = 0.09\,\text{Å}^{-1}$ (dark-purple lines in Fig. 3.11) and $k_M(30°) = 0.24\,\text{Å}^{-1}$ (pink lines in Fig. 3.11), at increasing flexural-phonon energies. These limiting cases are the most instructive. At $\theta = 0°$, the spacing of the moiré is $L_{\mathrm{M}} = 12.5\,\text{Å}$, which is the distance between the locally commensurate patches, and the red regions in Fig. 3.12. As signaled by the dark-purple line in Fig. 3.11, flexural phonon modes of this length in G are close enough to the flat region around Γ and are therefore energetically inexpensive. This allows commensurate regions to stay at the equilibrium interlayer position while incommensurate ones are pushed away from MoS_2 ML perpendicular to the basal planes. As θ increases to 30°, L_{M} decreases and thus the distance between locally commensurate areas reduces, something which is also observed experimentally [58]. As a result, the deformation needs to occur over a shorter distance and its energy cost therefore increases. At $\theta = 30°$, $L_M = 4.88\,\text{Å}$, which is about 2 G unit cells. As shown by the pink line in Fig. 3.11, deformations of this length scale are described by phonons at the edges of the BZ and are energetically more expensive than the gain coming from the interdigitation with the substrate. Therefore the G sheet remains flat, at the expense of the interlayer coupling, resulting in a higher total energy of the heterostructure compared to the aligned case. The flattening of the flexural branch near the edges of the BZ, as shown by the solid blue line between M and K in Fig. 3.11, is mirrored by the plateau in the energy profile in Fig. 3.9 around $\theta = 30°$: in the whole region moiré modulations are too expensive and the system cannot obtain any energy gain.

To sum up, the unconstrained 3D heterostructure lowers its energy by out-of-plane distortions according to the moiré pattern. This is particularly convenient at $\theta = 0$, where $L_{\mathrm{M}} = 12.5\,\text{Å}$: here the flexural distortion is almost without any energy penalty and the system lowers its energy by improving the interdigitation between the G and the MoS_2 layer. As θ increases, L_{M} decreases and the cost of the ripples overtakes the gain in energy due to local commensuration, yielding flat G and an increased total energy. Finally, the region of the BZ spanned by the moiré spacing as a function of θ (the region between

purple and pink segments in Fig. 3.11) shows that the approximation of long-wavelength used to derive Eq. (3.31) is unsuited in the large-mismatched heterostructures. As even phonon excitations near the border of the BZ are involved in the energy economy of the system, a modified epitaxy theory is needed in these cases to predict and understand the phase stability of imposed twist angles.

3.5 Final Remarks

Although often overlooked, the stability of twisted vdW heterostructures is of particular importance in the emerging field of twistronics, as it can be a decisive factor in the real-life application of such systems. The energy as a function of imposed angle determines whether a device is at risk of rotating away from a prepared angle even if it can be prepared in a metastable state. The analysis of MoS_2/G heterostructures helps to clarify the scattered experimental data. A single global minimum is found at $\theta = 0°$ and 60°: i.e. only epitaxial stacking is expected for the system at 0 K. However, experiments always present defects or intrinsic friction that might result in the emergence of activation energies, potentially trapping a system in a metastable (or even unstable) state. In the limit where such effects become negligible, i.e. activation energy approaching zero, one would mostly observe aligned at $\theta = 0°$ and 60° and few 30°-rotated heterostructures, in agreement with the results of Liu *et al.* [156]. A possible experiment to test the validity of these results would be a systematic repetition of the aforementioned experiments, focused upon reducing deviations resulting from working conditions, e.g. annealing temperature. Hopefully, the results of such an effort will confirm these findings: with a high enough annealing temperature and large enough flakes of significant quality, the bilayer system should be found in the aligned configuration, with possibly some outlier around 30°. The relevance of the results presented here becomes clear when considering the fact that interesting physics is observed at certain unstable mismatch angles [161]. Our findings show that care must be taken when designing nanodevices as properties observed in studies at a specific angle might fade out due to the system spontaneously rotating toward the real thermodynamic equilibrium. In fact, others [55] also suggest that commensurate structures are most suitable.

Finally, the origin of the observed energy economy is explained in terms of the interplay between flexural phonon modes of the pristine compounds and the moiré superlattice. This insight is general in nature and can be applied to all layered materials and heterostructures, serving as a design tool for twistronic devices. Stiffness in the out-of-plane direction should be considered a critical property in the design of such devices. It is for example known that rippling can affect the Schottky junctions, which are directly related to the performance of optoelectronic devices such as photodetectors and solar cells [174]. Soft flexural phonon modes might be a lower energy route out of frustration than twisting, hindering the possibility of stable rotated configurations. Furthermore, the observed behaviour shows the need for a novel theory of epitaxy for layered materials, incorporating the flexural branches ignored in the NM theory and taking into account all phonon wavelengths. The insights

presented here can serve as a starting point for developing such a theory of the epitaxial growth for vdW heterostructures.

4

High-throughput Alloy Design

Since the discovery of graphene, 2D materials have been at the forefront of materials science discovery. Aside from fundamental research, recently their unique properties and reduced dimensionality have sparked an interest for nanoscale engineering application and ideas for 2D-materials-based devices can be found in tribology [175], electronics [9, 176, 177] and catalysis [178, 179, 180]. In this relatively new field, there have been so far only limited attempts to exploit the vast chemical space to optimise properties. Up to now, most research effort has focused on identifying 2D unaries and binaries both theoretically [21, 22] and experimentally [23, 63]. However, little is known about their thermodynamic behaviour. The structures and ordering of possible alloys are virgin territories [181]. Only a handful of 2D ternaries have been reported by experiments [182, 183, 184, 185] and, while a handful of binary alloys have been studied [186, 113, 187, 188, 189], no systematic analysis has been carried out. Knowledge of thermodynamic behaviour is fundamental in developing the engineering application of 2D materials. When properties such as bandgap and electronic transport need to be tuned to desired values by chemical doping, the presence of miscibility gaps and competing ternaries is fundamental [190]. In tribology, one can imagine designing mismatched heterostructures via single-layer alloying. Consider a BL like the one reported in Fig. 4.1, composed of a hypothetical single-TM CS_2 layer, dotted-edge blue circles, and an alloyed layer (A:B)S_2, dashed-edge red circles and solid-edge grey ones. The single-TM CS_2 layer acts as substrate with lattice constant l_C. Over this substrate is grown or transferred a second alloyed layer $A_xB_{1-x}S_2$. The lattice parameter can be tuned between extremal values $l_{\mathrm{AB}}(x) = xl_{\mathrm{A}} + (1-x)l_{\mathrm{b}}$, assuming a linear dependency of lattice parameter on concentration, for the sake of argument. Ideally, A and B should mix well but not mix with C, to allow maximum control of the lattice parameter. A device of this kind would

allow study of the effect of the lattice mismatch in real nanoscale contacts systematicly, whereas this has only been done in toy systems as of now, like colloids or cold ions in optical lattices [191].

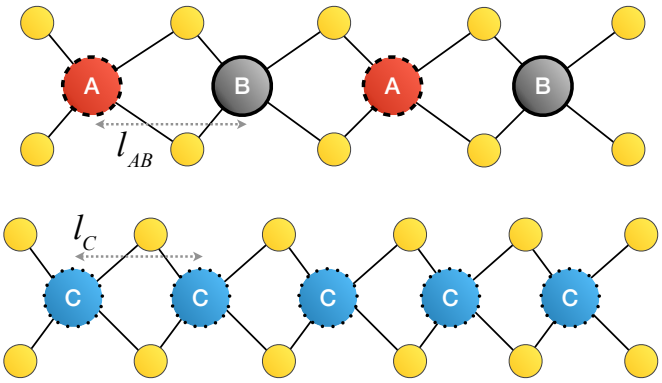

Figure 4.1: Sketch of a mismatched alloyed heterostructure.

The vast crystallographic and chemical spaces cannot be explored by experiments alone. Computational tools can provide guidelines to experimental synthesis, reducing the number of possible candidates by orders of magnitude. As an example, Mounet *et al.* [21] reduced a dataset of 1×10^5 bulk geometries from experimental databases to 256 easily exfoliable ML candidates. As a comparison, large-scale experimental studies usually deal with dozens of candidates [23, 63]. Here, a framework is developed to explore alloy possibilities and to compile a dataset for the TMD family, the most widely studied 2D material family for engineering application. The first section defines the chemical and coordination spaces considered. Secondly, a hierarchy of approximate descriptions of the structure and thermodynamics of doped systems is developed. Finally, the formalism outlined in section 2.2 is used to explore ordering in a select number of TMD-allowed binaries.

4.1 Chemical and Coordination Spaces Definition

The starting point to build the space of possible compounds is the 2D-materials database compiled by Mounet and coworkers [21]. The database comprises 258 mechanically stable ML structures identifies from experimental bulk compounds. Thus, the following phase stability study is conducted on ML geometries only. From these, one can extrapolate to bulk structures, assuming that the phase behaviour of each layer is independent. Extrapolating from monolayer formation energies to bulk without information on interlayer interactions yields errors in the prediction of the order of stacking fault energies. Stacking fault energies are typically around 10 meV/atom for TMDs [192, 97] and other 2D sheets bounded by vdW dispersion [193, 93] and 50 meV/atom for layered transition metal oxides [194].

The selection of the possible prototypes and the elements to mix into them must be guided by chemical and geometrical intuition, e.g. one can assume with confidence that metallic Mo is unstable in the graphene prototype and the same holds for N atoms in place of a TM in the MoS_2 prototype. Thus, the original database is filtered according to the class of materials of interest. While the Mounet database spans the whole periodic table,

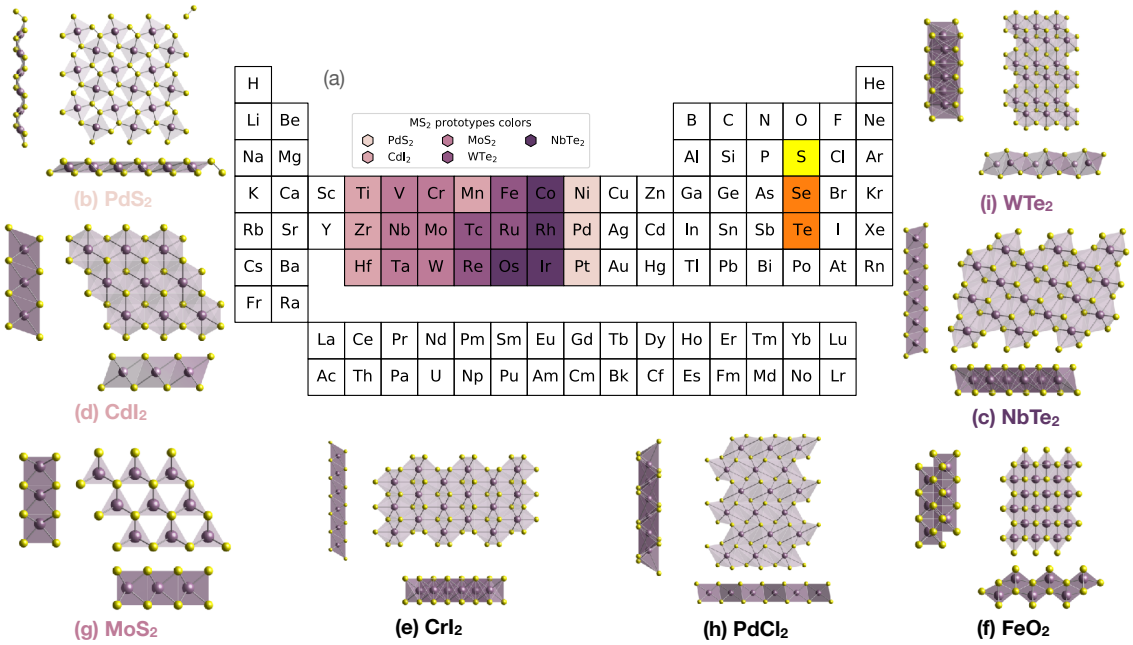

Figure 4.2: (a) Periodic table showing the elements selected. TM boxes are coloured according to the MX_2 GS prototype, as reported in Fig. 4.3. (b-i) The sides and top views of the eight MX_2 prototypes.

this search focuses on TMDs. The database is scanned for compounds of the form M_nA_m, where M is a TM cation, and A is the anion oxidising the TM. The search is not limited to chalcogenide anions, as there are relevant prototype geometries not expressed in the database, e.g. NbTe2 prototype is expressed by the $CrBr_2$ compound. This search yields the 13 prototypes reported in Table 4.1. The selection of TM to consider in the exploration is based on the review by Chhowalla *et al.* [4] (reported in Fig. 1.6). Most pristine materials in this group have been synthesised in their ML form in the works in Ref. [63] and Ref. [23], including CrS_2 and CoS_2. Intermediate TMs (Cr, Mn, Fe, Ru, Os) are added to this selection. While these do not form layered materials on their own, they might form alloys in combination with other TMs, e.g. Fe-doped MoS_2 ML [38, 195]. Late transition metals from group XI onward are excluded as they do not bind with chalcogenide to form layered materials [63, 196]. This yields the 21 TMs highlighted in Fig. 4.2 as possible cations in the M_nA_m stochiometry; the anion site can be occupied by a chalcogenide S, Se, Te, highlighted in yellow and orange in Fig. 4.2.

Stochiometry	Prototypes
M_3X_2	Hf_3Te_2
MX	ZrCl, FeSe
M_2X_3	W_2N_3
MX_2	CrI_2, $PdCl_2$, MoS_2, WTe_2
	CdI_2, $NbTe_2$, PdS_2, FeO_2
MX_4	SnF_4

Table 4.1: Prototypes of the form M_nA_m identified in Mounet database [21]. The 13 prototypes are grouped according to the stoichiometry and displayed for decreasing metal fraction, i.e. decreasing n/m ratio.

This selection results in TM × prototypes × chalcogenides = 21 × 13 × 3 = 819 compounds as a starting point for TM_1 × TM_2 × prototypes × chalcogenides = 17 199 possible combinations for TM-site substitutional alloys. While the methodology outlined below is valid for any stochiometry and anion, this section will focus on MS_2 compounds, as an illustrative example. Sulphides are the easiest to synthesise, and most studied compounds of the family and the MS_2 stochiometry represents eight of the 13 prototypes, which are sketched in Fig. 4.2b-i. This further selection yields 168 binaries as a starting point for 3528 substitutional alloys on the TM site, allowing for an exhaustive analysis rather than relying on approximate methods based on a statistical sampling of configurational space.

Lattice Stability The formation energy of each compound MS_2 in all prototypes p, i.e. pairs (M, p) is obtained from the EoS calculations, as outlined in section 2.4.1. *First principles* calculations of the total energy are carried out with the Vienna *ab initio* Software Package (VASP) [197, 119, 198, 199], within the PAW framework for pseudopotentials [124, 200]. As benchmarked in Appendix E, the electron density is described with a cutoff of $E_{\text{cutoff}} = 650\,\text{eV}$ and the BZ is sampled with a $17 \times 17 \times 1$ mesh.

Direct calculation of the EoS is necessary as benchmark calculations showed that minimisation with VASP cannot locate the minimum-energy volume of the 2D material and might drive the system away from the prototype coordination considered. The volume range considered in the EoS is determined using the notion of covalent radius $r_{\text{c,i}}$ of the element E_i. The bond length between two elements E_1, E_2, i.e. a TM and the chalcogenide, is estimated as

$$\Delta_{1,2} = r_{\text{c},1} + r_{\text{c},2}. \tag{4.1}$$

Values for the covalent radius are tabulated in the Mendeleev package [201] according to Bragg [202] r_{B}, Coredo [203] r_{C}, Pyykko [204] r_{P} and Slater [205] r_{S} models. The minimum and maximum values among these models, plus a buffer $\epsilon = 0.05$, are chosen as bounds for the EoS.

In building the geometries for the EoS calculations, the anisotropic geometry of the ML is enforced by the following transformation matrix of the unit cell:

$$M = \begin{bmatrix} f & 0 & 0 \\ 0 & f & 0 \\ 0 & 0 & 1 \end{bmatrix}. \tag{4.2}$$

Isotropic stretching of the cell would needlessly increase the vacuum in the unit cell, reducing the accuracy of the DFT calculation. In order to span the right range of bond distances, f must be chosen appropriately. Using the shortest bond vector $\boldsymbol{\Delta}$ in a prototype structure, the stretch factor f of the unit cell is chosen according to

$$f = \sqrt{\frac{\Delta'^2 - \Delta_z^2}{\Delta_x^2 + \Delta_z^2}}, \tag{4.3}$$

in order to scale the bond length $|\Delta| = \Delta_{1,2} \to \Delta'_{1,2}$.

The formation energy of each MS_2 compound in a given prototype p, also known as *lattice stability* [206], is given by the energy per site with respect to the ground state (GS) prototype, i.e.

$$E_{\mathrm{F}}(M,p) = \frac{E(M,p)}{n} - \frac{1}{n}\min_{p} E(M,p), \tag{4.4}$$

where $E(M,P)$ is the minimum-volume energy of MS_2 compound in prototype p and n is the number of the TM site in the unit cell.

Fig. 4.3 reports the formation energy defined in Eq. (4.4) for the selection of TM and prototypes shown in Fig. 4.2. The ground state of known compounds are labelled by green squares: d^2-metal TMDs (TiS_2, ZrS_2 and HfS_2) show octahedral CdI_2 coordination, Fig. 4.2d. The MoS_2 tetragonal prototype, Fig. 4.2(g), is the preferred GS of d^4 TMDs and the d^{10} metals Ni, Pd and Pt are found in the PdS_2 prototype, Fig. 4.2b. Moreover, the larger steric hindrance of heavier TM in the same group raises the formation energy of the unstable prototype. This can be observed by following in Fig. 4.3 the rows of PdS_2, $E_{\mathrm{F}}(\mathrm{Ti}, PdS_2) = 2.47\,\mathrm{eV}$, $E_{\mathrm{F}}(\mathrm{Zr}, PdS_2) = 2.99\,\mathrm{eV}$ and $E_{\mathrm{F}}(\mathrm{Hf}, PdS_2) = 3.26\,\mathrm{eV}$, and CdI_2, $E_{\mathrm{F}}(\mathrm{Cr}, CdI_2) = 0.42\,\mathrm{eV}$, $E_{\mathrm{F}}(\mathrm{Mo}, CdI_2) = 0.84\,\mathrm{eV}$ and $E_{\mathrm{F}}(\mathrm{W}, CdI_2) = 0.99\,\mathrm{eV}$.

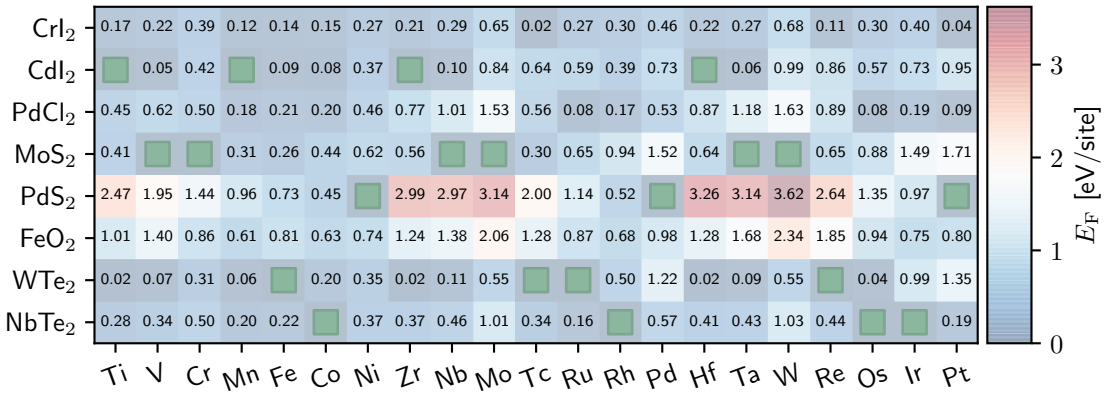

Figure 4.3: Formation energy of MS_2 compound in the prototypes according to Eq. (4.4). Green squares mark GS prototypes, defined by $E_F = 0$.

4.2 Ideal Solid Solution Limit

Starting from the stability matrix in Fig. 4.3, a question arises naturally: do different metals mix in a given prototype? The most straightforward approach to explore this question is the ideal solid solution limit, a non-interacting model based on the formation energies of pristine TMDs defined in Eq. (4.4). Given a binary alloy prototype p, $M_xN_{1-x}S_2|_p$, in the ideal solution model represents a model with negligible interactions between the fraction x of sites occupied by M and the remaining $1-x$ N sites. In the energy-composition space, the system behaviour is represented by the line connecting the formation energy of NS_2 in prototype p, i.e. the element M,p of the formation energy matrix Fig. 4.3, at $x = 0$

with the formation energy for M at $x = 1$. Thus, in the ideal solid solution model, the formation energy of a mixed configuration at concentration x is given by:

$$E^0_{N,M,p}(x) = xE_{\mathrm{F}}(M,p) + (1-x)E_{\mathrm{F}}(N,p). \tag{4.5}$$

By construction, this energy is exactly zero everywhere if M and N share the same ground state structure and thus $E_{\mathrm{F}}(M,p) = E_{\mathrm{F}}(M,p) = 0$. In any other case the formation energy will be positive: suppose the metal N has a ground state geometry $p' \neq p$, the fraction $1-x$ of material $NS_2|_p$ would transform into p' to reach equilibrium. Even though this model cannot predict stable orderings, it offers a first step in discriminating possible mixing materials from the ones most likely to phase-separate: the higher the energy of the solid solution model, the more substantial any entropic or chemical stabilising mechanisms must be. In the solid solution limit, the substitutional entropy of a binary alloy is a function of the concentration x only, and not of the composition:

$$S(x) = -(x\log x + (1-x)\log(1-x)), \tag{4.6}$$

which counts possible arrangements of the two atom types on the metal sub-lattice [207]. Therefore, it cancels, and the simpler linear energy model in Eq. (4.5) can be used.

In order to make this discrimination quantitative, a metric in the composition-energy space is needed to compare different combinations.

Solubility Metric

Given a prototype p and two metals M and N, the solubility window of the (p, N, M) triplet is defined as the range of concentration x where the mixing energy in Eq. (4.5) within the prototype p is lower or equal to the mixing energy within the ground-state structures of MS_2 and NS_2, as shown in Figures 4.4a and 4.4c.

Fig. 4.4a reports an example of a possible large miscibility window in the $Tc_{1-x}Pt_xS_2$ system: formation energy in the CrI_2 prototype lies lower in energy than the formation energy within either GS prototypes, WTe_2 and PdS_2, over most of the concentration range. The stability window might not exist for a given triplet, as shown in Fig. 4.4b: the formation energy within the FeO_2 prototype lies higher than the one in either ground state prototypes for the whole concentration range. In this case, the formation of an alloy within this prototype is unlikely. When the prototype p is the ground-state for one of the metals, then the stability window extends from the extremal concentration $x = 0$ or $x = 1$ up the intercept with the other prototype solid solution, as shown in Fig. 4.4c. Finally, when the two TMDs share the same prototype ground state, the formation energy in that prototype is zero everywhere, like in Fig. 4.4d. This case indicates that the solid solution can occur at no energy cost.

Applying the construction depicted in Fig. 4.4 yields a $n \times n$ symmetric matrix, for each prototype p. Each entry of this *solubility matrix* is a 2×2 matrix with the bounds of the solubility window and the formation energy in Eq. (4.5) evaluated there, i.e. minimum

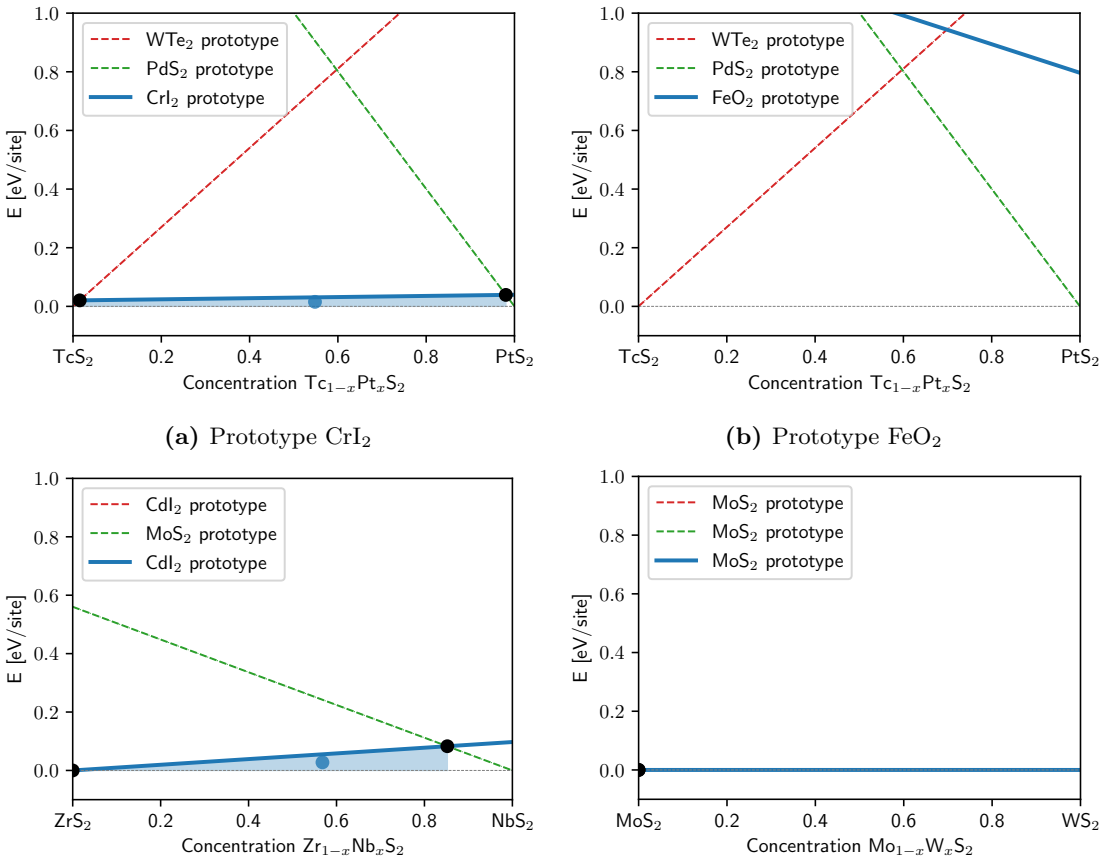

(a) Prototype CrI_2 **(b)** Prototype FeO_2

(c) Prototype CdI_2 **(d)** Prototype MoS_2

Figure 4.4: Solubility metric construction (blue lines) for (Tc:Pt)S_2 in (a) CrI_2 and (b) FeO_2 prototypes, (c) (Zr:Nb)S_2 in CdI_2 prototype, and (d) (Mo:W)S_2 in MoS_2 prototype. A blue-shaded area highlights the extent of the solubility window. A blue circle marks the centroid of the area below the solid solution energy within the solubility window. Red dashed lines show the energy in the prototype of the left end-member, $x = 0$. Green dashed lines show the energy in the prototype of the right end-member, $x = 1$.

and maximum energy cost of the window. The matrices associated with each prototype are reported in Appendix A. As an example, Fig. 4.5 reports the solubility matrix within the MoS_2 host, where the marker size shows the width of the solubility window and the colour-code in upper and lower triangles shows the minimum and maximum energy penalty, respectively.

Groups of favourable solubility windows (large blue marks) can be seen around group V and group VI elements, which according to Fig. 4.3 prefer this coordination. This observation is in agreement with the experimental realisation of a few alloys of this type [189, 208]. A large energy penalty (red marks) is associated with group VI and group X transition metal mixtures, e.g. $Mo_xPd_{1-x}S_2|_{MoS_2}$, indicating MoS_2 prototype as a poor candidate for mixing. Indeed, only Ni-doped MoS_2 MLs with isolated impurities are reported by experiments [180], and Ni shows the lowest mixing energy with MoS_2 among group X elements. Finally, a narrow solubility window (small marks) suggest that other prototypes are preferred for the corresponding mixture, even when MoS_2 is the prototype of one TM; an example of this is $Ti_xV_{1-x}S_2|_{MoS_2}$, which favours the CdI_2 prototype, as

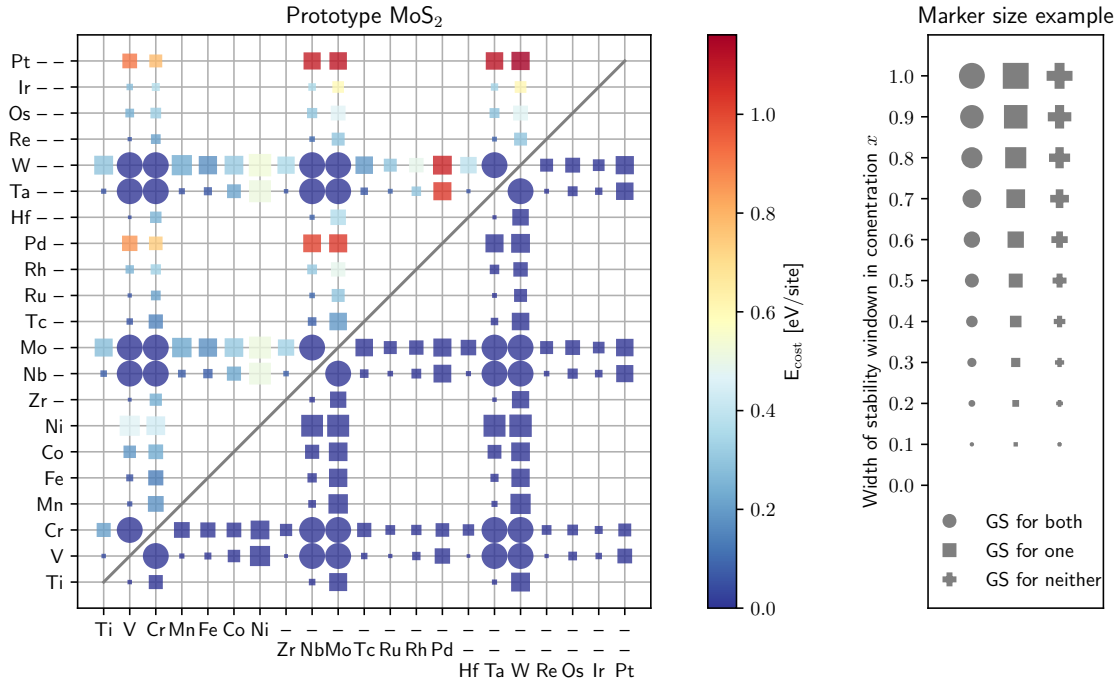

Figure 4.5: Stability metric in MoS_2 prototype. The colour-code shown by the colour-bar on the right marks the energy cost, in eV, of the stability window. The upper triangle of the matrix reports the upper limit of the energy cost in the stable window, while the lower triangle, the lower one. The size of the marker encodes the stability window size, as reported by the legend on the right. Circles mark metal pairs whose GS prototype is MoS_2, square pairs in which only one metal has MoS_2 as GS.

shown below.

Goal Function

The most promising candidates for alloys can be identified by comparing the solubility windows reported in Appendix A. To rank candidates, a function to associate a score to each solubility window needs to be defined. This ranking needs to assign a single value to the solubility windows of TM_1-TM_2-prototype triplets. The following parametric function is chosen as the goal function

$$f_\zeta(w,\epsilon) = \zeta^2 \frac{\sqrt{w}}{\zeta^2+\epsilon^2}, \tag{4.7}$$

where w is the width of the solubility window and the energy penalty ϵ is the height of the centroid defined by the stable window in energy-concentration space, e.g. blue points in Fig. 4.4. Thus, the function encourages large solubility windows w and discourages large energy penalties ϵ. This goal function $f_\zeta(w,\epsilon) : w \in [0,1]\, \epsilon \in [0,\infty] \to [0,1]$ associates zero to "bad" candidates and one to "good" candidate. In detail, all zero-width windows are mapped to zero, $f_\zeta(0,\epsilon) = 0\ \forall\epsilon$. Moreover, as shown in section 4.2b, f_ζ is a monotonically decreasing function of the energy penalty ϵ. Finally, $f_\zeta(1,0) = 1$, i.e. the highest score is assigned to the combination of maximum width and lowest energy penalty.

The parameter ζ, measured in the same unit as the energy penalty ϵ (here eV), sets the

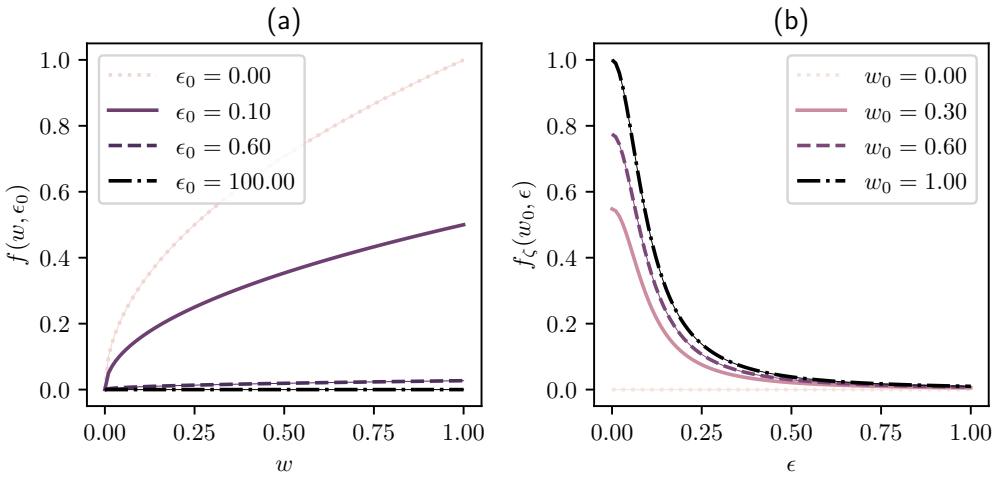

Figure 4.6: Sections of the surface in Eq. (4.7): (a) f at fixed energy penalty ϵ_0 and (b) f at fixed solubility window width w_0. The examples are computed at $\zeta = 0.1$.

relative importance of the two arguments. Its effect is evident by the limiting behaviours. For small ζ, $\lim_{\zeta \to 0} \approx \zeta^2 \frac{\sqrt{w}}{\epsilon^2}$, a large energy penalty lowers the score, within the upper-limit given by the window size $\sqrt{w}$. On the other hand, for large ζ, $\lim_{\zeta \to \infty} \approx \sqrt{w}$ the largest window is always selected regardless of the energy price. The parameters ζ must be tuned according to the dataset studied in order to achieve the right sensitivity, achieving a trade-off between large, but costly windows and low energy solutions defined on a narrow concentration range.

4.2.1 Optimal Host Matrix

Using the goal function defined in Eq. (4.7), the solubility windows in the matrices in Appendix A can be ranked, yielding an optimal prototype for each metal pair. The first step is to tune the ζ parameter in the goal function $f_\zeta(w, \epsilon)$ in Eq. (4.7) for the dataset at hand. Left plots in Fig. 4.7 place all the solubility windows in all the matrices in Appendix A in the w, ϵ space. Each point in Figures 4.7a to 4.7c is colour according to increasing values of ζ in Eq. (4.7), while coloured lines report isolines of $f_\zeta(w, \epsilon)$. The two limiting behaviours mention in the previous section are well pictured. For small $\zeta = 1 \times 10^{-3}$ eV, Fig. 4.7a, all windows with non-zero energy penalty are assigned a low score, dark element on the right plots, while only TM pairs with $(w, \epsilon) = (1, 0)$ show the maximum scores, yellow entries on the right plots. On the other hand, for $\zeta = 1 \times 10^{2}$ eV, Fig. 4.7c, the isolines of f divide the data points in vertical stripes. Thus, only the window width determines the score, resulting in the largest windows being picked as optimal prototypes, as shown in the right plots. The value adopted in this work is $\zeta = 0.080$ eV, which achieves a balance between low energy cost and wide solubility window, as shown in Fig. 4.7b. Somewhat surprisingly, the ranking is quite robust against the value of ζ: going from $\zeta = 1 \times 10^{-3}$ eV to $\zeta = 1 \times 10^{2}$ eV only 12% of prototypes change.

The optimal prototype for each pair of transition metals, selected by f_ζ with $\zeta = 0.080$ eV, are shown in Fig. 4.8. The symbol assigned to each entry refers to the optimal

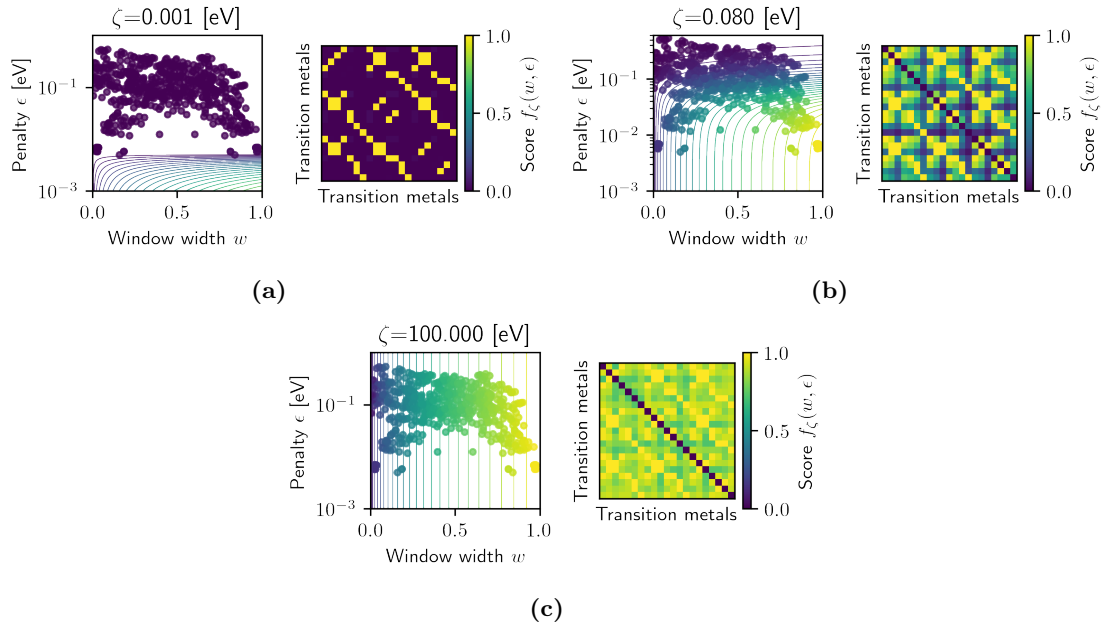

Figure 4.7: Behaviour of the goal function within the solubility windows dataset for (a) $\zeta = 1 \times 10^{-3}\,\mathrm{eV}$, (b) $\zeta = 8 \times 10^{-2}\,\mathrm{eV}$, and (c) $\zeta = 1 \times 10^{2}\,\mathrm{eV}$. Left plots, scatter plot of solubility windows in width w and energy cost ϵ space. Marker colours are assigned by $f_\zeta(w,\epsilon)$. Coloured lines are isolines of $f_\zeta(w,\epsilon)$. Right plots show the value of f for the highest-scoring prototype for each TM pair.

prototype, as shown in the lower legend; symbols on the diagonal refer to the stable prototype for that transition metal. The size of each marker shows the width of the stability window associated with that metal pair in that prototype. The colour code of the upper and lower triangles follows the one in Fig. 4.5.

Fig. 4.8 provides a visual tool to navigate the possible mixings of transition metals in sulphur planes and highlights trends across the periodic table. Broad, large blue marks in Fig. 4.8 indicate a favourable mixing and therefore a large miscibility is likely. For example, MoS_2 and WS_2 share the same prototype GS, prismatic MoS_2. Thus, Fig. 4.8 indicates the solid solution can occur at no cost throughout the whole concentration range. In the case of TiS_2, GS prototype octahedral CdI_2, and NbS_2, GS prototype prismatic MoS_2, Fig. 4.8 indicates that a good miscibility in the CdI_2 prototype, that can be traced back to the relatively low formation energy of NbS_2 in TiS_2 native prototype, $E_F(\mathrm{Nb}, \mathrm{CdI_2}) = 0.1\,\mathrm{eV/site}$, in Fig. 4.3. On the other hand, a high mixing energy is likely to result in narrow miscibility regions and a phase separating system, like group X TMs with any group IV, e.g. $\mathrm{Pd}_x\mathrm{Zr}_{1-x}\mathrm{S}_2|_{\mathrm{CdI_2}}$, whose optimal energy cost is still 0.6 eV/site.

As a first benchmark, the information in Fig. 4.8 can be compared with alloys reported in the literature. Zhou and coworkers [23] recently reported synthesis of ML of (Mo:W)Te_2, (Nb:Mo)S_2, (W:Nb)S_2, which are all shown as likely to mix in Fig. 4.8. On the other hand, the same work reports a $MoReS_2$ ML alloy, while the stability window of this TM pair is small and high in energy in Fig. 4.8. Another recent work reports the experimental characterisation of (V:Mo)S_2 ML, which is also a highly mixable TM pair according to our analysis. Many alloys have been suggested by computational works as well. Rama-

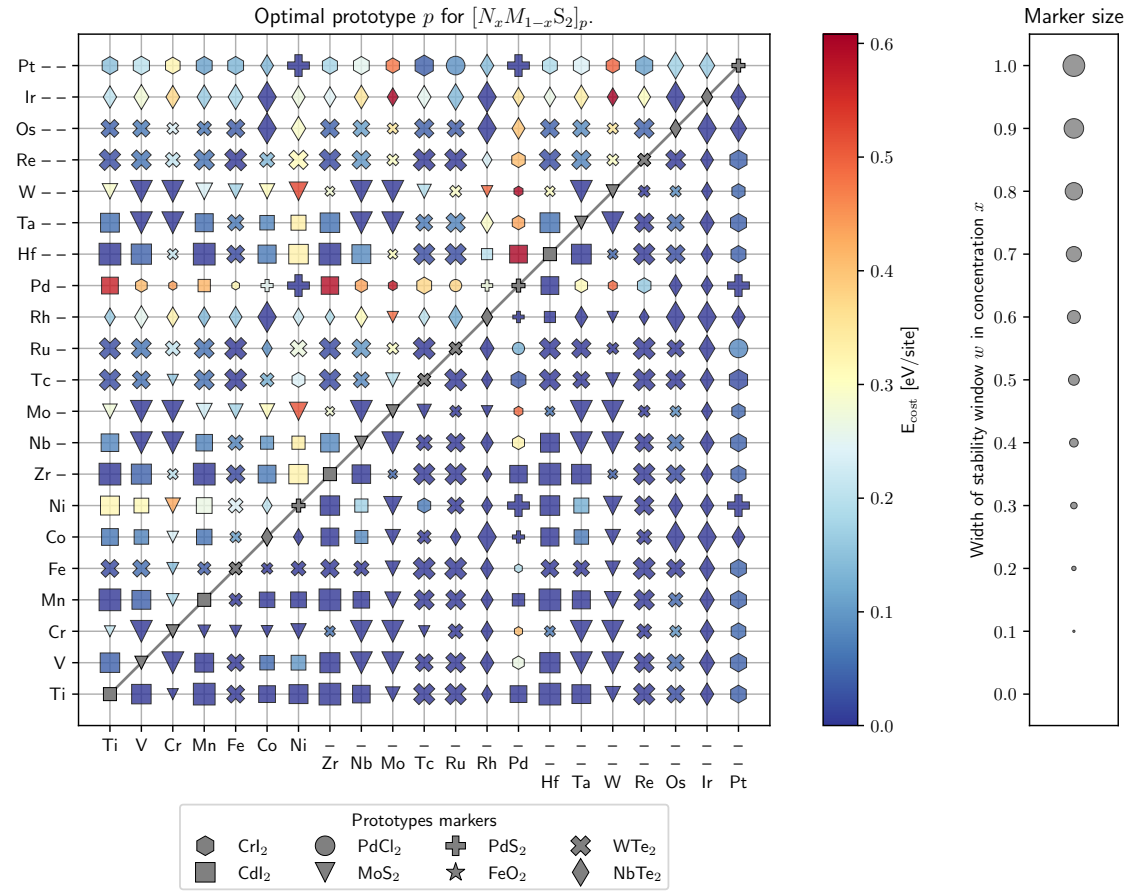

Figure 4.8: Optimal prototype for TM pairs. The colour-code and size of the markers follow convention in Fig. 4.5, as reported by the legends on the right. Marker-prototype correspondence is reported in the legend at the bottom. Markers on the diagonal report the GS prototype.

subramaniam *et al.* [38] proposed Mn-doped MoS_2 ML as a possible diluted magnetic superconductor. The authors report study configurations at concentration $x = 0.06$ and $x = 0.12$ in 1H-$Mo_{1-x}Mn_xS_2$. While the authors report these configurations to be mechanically stable within the DFT framework, they would separate into elemental compounds if not thermodynamically stable. According to the stability metric reported in Fig. 4.8, the upper formation energy is 0.2 eV, which suggests that some miscibility is possible but the possibility of high concentration ordering, like reported in Ref. [38], should be investigated in more detail. In another computational study, Onofrio and coworkers [209] compile possible substitutional alloys of 1H-MoS_2 ML throughout the whole periodic table, on both metal and chalcogenide site. According to the authors' analysis, based on substitution in the smallest possible unit cell (roughly $x = 0.5$), all early TMs between group III and group VI have negative formation energy. These observations agree with the stability metric predictions for metals of group V and group VI, while group IV elements, i.e. Ti, Zr and Hf, show low miscibility according to Fig. 4.8.

Furthermore, using the data in Fig. 4.8 one can design the mismatched alloyed bilayer proposed in Fig. 4.1. For example, MoS_2 in MoS_2 prototype, with lattice spacing $l_{Mo} = 3.182$ Å, can be used as a substrate and coupled with an $Mn_xZr_{1-x}S_2$ alloyed ML in the

CdI_2 prototype. Given $l_{Zr} = 3.684\,\text{Å}$ and $l_{Mn} = 3.172\,\text{Å}$, the mismatch can be tuned between $l_{Mo}/l_{Zr} = 0.864$ to $l_{Mo}/l_{Mn} = 1.068$, assuming a simple linear dependence of the lattice spacing on the concentration. According to Fig. 4.8, Zr and Mn ions display high miscibility, as they share the same CdI_2 ground-state prototype. On the other hand, both Zr and Mn show poor solubility in MoS_2 crystal, and, according to Fig. 4.5, the energy prices within the MoS_2 prototype are $\epsilon = 0.23\,\text{eV/site}$, at the Mn-rich side, and $\epsilon = 0.34\,\text{eV/site}$, at the Zr-rich side. While a system of this type could be synthesized with known protocols [63, 59], they are challenging from a computational point of view. The analysis here combined with the CE methodology can provide stable orderings of the alloyed ML part of the heterostructures. However, representing the heterostructure geometries would require a large supercell, as discussed in chapter 3, beyond the possibilities of standard DFT codes, like VASP. MD simulation would also pose a problem, as no general FF for TMDs alloyed ML are available, to the best of the author's knowledge. A possible solution to study this system could come from linear-scaling DFT: considering thousands of atoms in the unit cell with the protocol outlined in Appendix C can reduce the residual strain enough to allow an accurate description of the PES of the system, as outlined in section 2.4.3.

Prototype Frequency Information in Fig. 4.8, readily answers another question as well: what is the frequency of optimal prototypes? Fig. 4.9 reports the fraction of each prototype in the optimal matrix Fig. 4.8. The distorted octahedral coordination of WTe_2 and CrI_2, shown in Fig. 4.2i,e, are the prototypes that more often yield the optimal solution. A possible explanation for this lies in the low-symmetry coordination of these. When neither of these two prototypes is the ground state of the TMD considered, the broken-symmetry coordination still allows for a favourable redistribution of the charge density, in contrast with other high-symmetry prototypes, e.g. MoS_2 and CdI_2. Moreover, the PdS_2 prototype with its unique 'puckered' 2D layers depicted in Fig. 4.2a is supported almost only by group X elements and few high-energy solutions. Finally, no metal pair exhibits the binary FeO_2 as the preferred prototype, which can thus be excluded from any further analysis.

Polymorphism The information in Fig. 4.8 can help understand the tendency of TMDs to form metastable polymorphs in ML synthesis. Purple shaded marks in Fig. 4.10 reports, for each TM_1-p pair, the minimum centroid energy across all possible combinations TM_1-TM_2-p. For example, for group IV TMDs, TiS_2, ZrS_2, and HfS_2, whose GS is the perfect octahedral CdI_2, a low energy penalty is found for the distorted octahedral coordination of WTe_2 (light purple crosses in Fig. 4.10). For group VI TMDs, CrS_2, MoS_2, and WS_2, the first metastable prototypes are distorted WTe_2 and perfect CdI_2 octahedral, at almost degenerate energy. The WTe_2 and CdI_2 polymorphs have indeed been observed experimentally [180] and in simulations [66] in MoS_2 layers. An even lower energy penalty, WTe_2 and CdI_2 prototype is observed for group V TMDs, VS_2, NbS_2, and TaS_2, suggesting that polymorphism observed in group VI TMDs should be even stronger in this case.

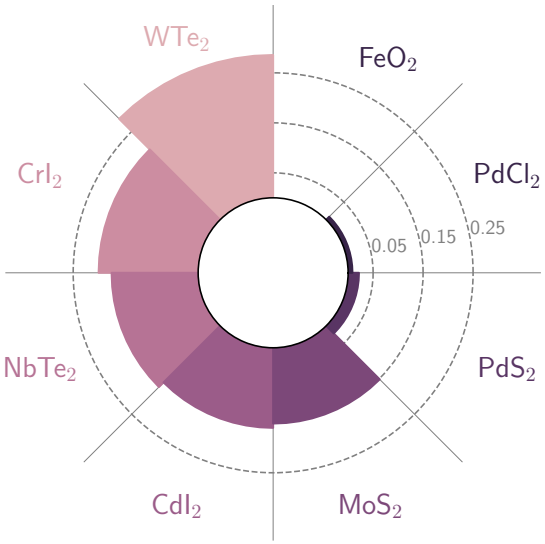

Figure 4.9: Frequency of prototypes in candidate TMDs binaries alloys in Fig. 4.8.

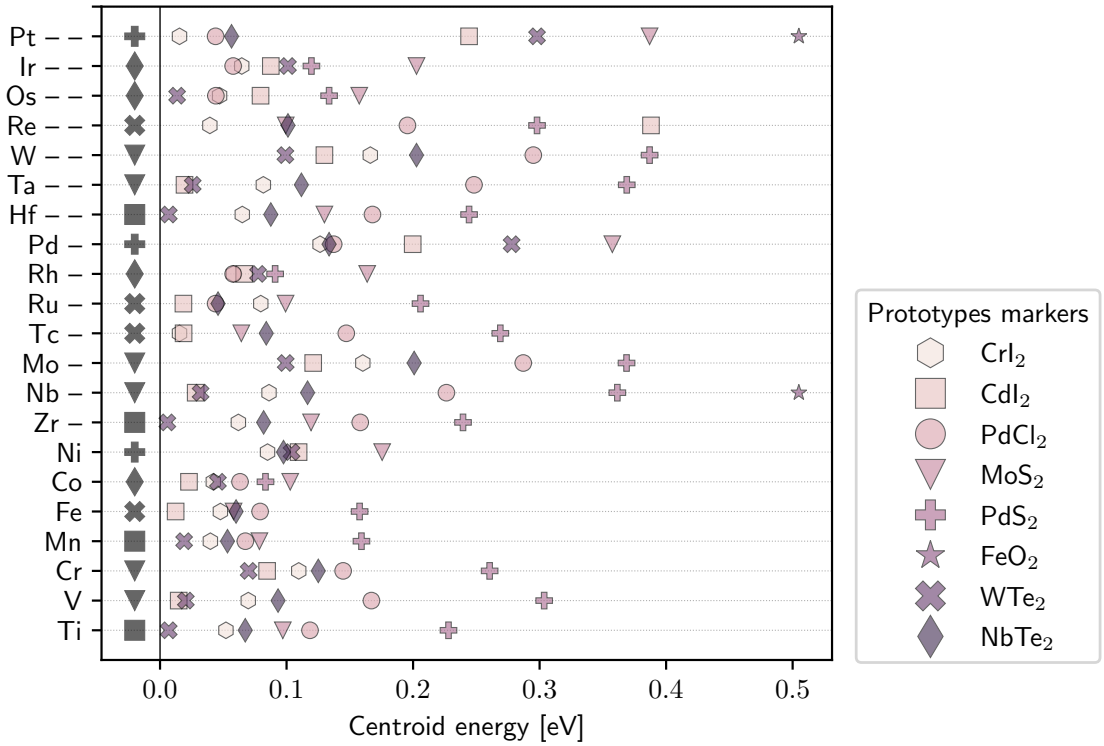

Figure 4.10: Minimum centroid energy, x axis, of all non-GS prototypes for each TM, y axis. The legend on the right reports marker and colour associated with each prototype. Black marks left of $x = 0$ line show the GS prototype of the TM.

4.3 Metal Site Orderings

Promising systems in Fig. 4.8 can be further analysed by exploring the stability of possible orderings and miscibility regions across the concentration range. The formation energy of the pseudo-binary system $M_xN_{1-x}S_2$ considered is modelled with the CE formalism presented in section 2.2. The interaction between different species on the TM site of the sub-lattice, like the triangular one formed by orange and blue circles in Fig. 4.11, is modelled via a set of many-body interactions, termed clusters, e.g. the pairs α and β and the triplet γ in Fig. 4.11. The sulphur atoms (yellow circles in Fig. 4.11) are spectators, i.e. they are considered in the DFT calculations but not in the CE interaction figures.

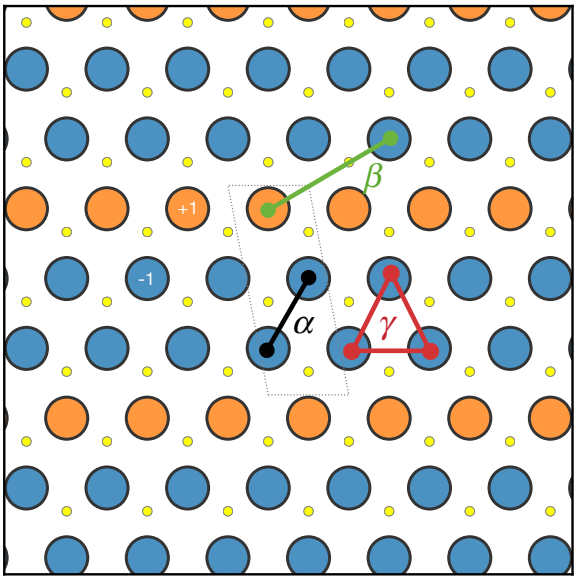

Figure 4.11: Top view sketch of a ideal TMD hexagonal lattice, e.g. MoS_2 prototype, used in the CE expansion. The TM sub-lattice comprises of the large, black-edge circles. Two different species, blue and orange circles, occupy the sub-lattice, by a two-value spin variable ± 1. The two species are here arranged in a striped pattern, whose unit cell is highlighted by grey, dashed lines. Small yellow circles show the spectator chalcogenide atoms. Coloured shapes show few cluster: nearest-neighbour (α black line), next-nearest-neighbour (β green line) and a triplet (γ red triangle).

The solid solution limit is take as reference to compute the formation energy of the interacting, ordered structures $\sigma(x)$:

$$E_{N,M,p}(x) = E(M_xN_{1-x}S_2)|_p - xE(M, p_M) - (1-x)E(N, p_N), \tag{4.8}$$

where $E(M_xN_{1-x}S_2)|_p$ is the total energy of the configuration $\sigma(x)$ in the host lattice p. $E(M, p_M)$ and $E(N, p_N)$ are the total energies of MS_2 and NS_2 in their GS prototypes, p_M and p_N, respectively. This chemical reference assures that the formation energy in Eq. (4.8) at end member concentration $x = 0$ and $x = 1$ formally corresponds to the one reported in Fig. 4.3. Moreover, no interaction between the fraction x of M sites and the remaining N sites, Eq. (4.8) corresponds to the ideal solid solution limit in Eq. (4.5).

The set of geometrically distinct orderings is generated using CASM [210, 211, 212, 213]. The geometries are then fully relaxed (including cell shape and volume) using the DFT

methodology outlined in section 4.1 and benchmarked in Appendix E. The set is used to parameterise a CE model using the framework presented in section 2.2. The dataset is updated iteratively with stable orderings suggested by the CE model until predicted and computed convex hulls coincide.

The fitting procedure is carried out within the CASM API. Each configuration σ_i is weighted according to its distance from the convex hull:

$$w(\sigma_i) = \exp\left(-\frac{E_{\mathrm{F}}(\sigma_i) - E_{\mathrm{hull}}(x_i)}{k_{\mathrm{B}}T}\right) \tag{4.9}$$

where $E_{\mathrm{F}}(i)$ is the formation energy of the configuration i, $E_{\mathrm{hull}}(x_i)$ is the formation energy of the convex hull at the concentration x_i of the configuration considered and $k_{\mathrm{B}}T$ is a fictitious temperature set according to the energy scale of the problem. These weights bias the fitting towards more accurate reproduction of low-energy configurations, which are the relevant ones to capture the phase behaviour of the system. Orbits included in the CE model are selected with a genetic algorithm based on the Distributed Evolutionary Algorithm in Python suite [214]. A population of 100 individuals, each starting with five randomly selected orbits, evolves for 20 generations. The best 50 models are selected from five repetitions of the evolution process. The evolution is driven by the cross-validation score of each individual, computed using the ten-split K-fold algorithm as implemented in Scikit-learn [215]. In order to favour low-complexity models with fewer orbits ϕ, a penalty $p(c) = \gamma\Sigma_c$ is added to the cross-validation score of each individual c. Σ_c denotes all the cluster functions defining the model c, i.e. all the orbits associated with non-null effective cluster interaction $J\alpha$ in Eq. (2.58). A value $\gamma = 1 \times 10^{-6}$ has been found to yield a good compromise between reducing the number of orbits in the selected models and retaining satisfying accuracy. Table 4.2 reports the details of the CE models.

System	#DFT	CE size	CV [eV/site]	ρ_2	ρ_3	ρ_4	ρ_5
$(\mathrm{Mo{:}W})\vert_{\mathrm{MoS_2}}$	304	6	7.2×10^{-5}	14.01	10.61	8.52	-
$(\mathrm{Mo{:}Nb})\vert_{\mathrm{MoS_2}}$	613	169	0.001	25.0	15.0	13.0	9.0
$(\mathrm{Mo{:}Ta})\vert_{\mathrm{MoS_2}}$	423	137	0.002	25.0	15.0	13.0	9.0
$(\mathrm{Ir{:}Ru})\vert_{\mathrm{MoS_2}}$	542	253	0.090	19.0	11.0	9.0	-
$(\mathrm{Ir{:}Ru})\vert_{\mathrm{MoS_2}}$	207	122	0.018	19.0	11.0	9.0	-

Table 4.2: Parameters of the CE models of the selected system, reported in the first column. The notation $(M{:}N)\vert_p$ is a shorthand for $M_xN_{1-x}\mathrm{S_2}\vert_p$, indicating the two species occupying the TM sub-lattice, defined by the prototype indicated in the subscript. The second column, #DFT, reports the number of *ab-initio* calculations comprising the training set. The third column, CE Size Σ_c, reports the number of orbits comprising each model, i.e. the orbits with $J_\alpha \neq 0$ in Eq. (2.58). The orbits ϕ represent interaction figures up to the maximum radii, in $\mathring{A}$, reported in the columns ρ_2, ρ_3, ρ_4, and ρ_5; the subscript indicates the number of vertices in the clusters, i.e. pairs, triples and so on.

4.3.1 Mo-W-S Binary Alloy

The first benchmark of the miscibility predicted by Fig. 4.8 is the $Mo_xW_{1-x}S_2$ system. The system has recently attracted attention as experiments showed that the value of the bandgap of an ML could be finely tuned as a function of the ratio between the two metals [189, 208].

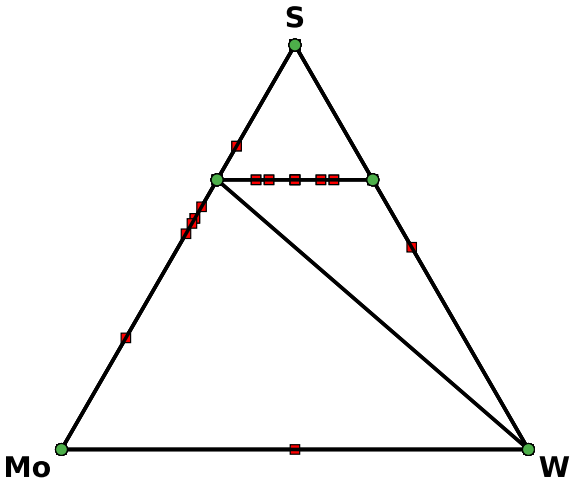

Figure 4.12: Ternary phase diagram for Mo-W-S elements. Obtained from the MP database [216, 217].

Fig. 4.12 shows the ternary phase field computed by the Materials Project (MP) [216, 217]. The only stable compounds (green circles in Fig. 4.12) are pure elements and the TMDs WS_2 and MoS_2. All alloy configurations in the tie line between the TMD MoS_2 and WS_2 are reported as unstable (red squares) in Fig. 4.12 by the MP. These calculations consider only layers of pure WS_2 and MoS_2 in different stacking orders and are not therefore related to this analysis. Moreover, the formation energy is of the order of 1 meV/atom, suggesting that the stacking order does not play a significant role in the phase stability of TMD alloys, as assumed here.

According to the optimal prototype matrix in Fig. 4.3, the end-members MoS_2 and WS_2 share the same ground-state prototype, prismatic MoS_2, which is thus the parent lattice for the CE. The details of the expansion are reported in Table 4.2. Fig. 4.13a shows, as orange crosses, the formation energies of the DFT training-set geometries. The solid orange line shows a convex hull of the *ab-initio* data. All points across the concentration range have negative formation energy, confirming the perfect solubility in Fig. 4.8, Although the system shows ordered ground states, the formation energy is considerably lower than k_BT room temperature $E_F \approx 1\,\text{meV} \ll k_BT_{\text{room}} \approx 25\,\text{meV}$. Thus, at room temperature, the entropic term in the free energy of the system $F = E - TS$ represents the dominant contribution and an ideal solid-solution behaviour should be observed, with Mo and W ions occupying lattice sites at random.

Fig. 4.13a reports the formation of energy for the same DFT structures (orange crosses) as predicted by the CE model (blue circles). Moreover, light blue crosses show the formation energy predicted by the CE for geometries, and not in the DFT training-set. The computed

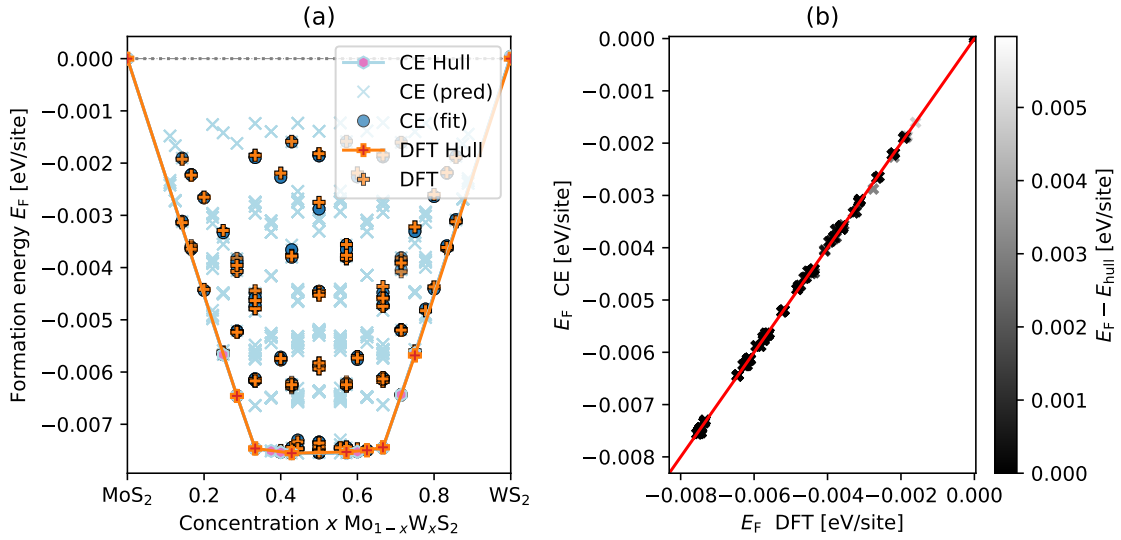

Figure 4.13: (a) Formation energy E_F, in eV/site, versus concentration x of the $Mo_{1-x}W_xS_2$ system. Orange symbols and lines refer to DFT-computed energies, while blue-shaded ones refer to CE-predicted energies, as reported in the legend on the top right. (b) Correlation plot of DFT-training-set and CE-fitted energies. The red line marks $x = y$, i.e. perfect correspondence between the two sets. The shade of grey of each marker shows the distance from the DFT hull (orange line in (a) panel).

(orange line) and predicted (light-blue line) convex hulls in Fig. 4.13a match: no new ground states are predicted by the CE, which is, thus, a reliable description of the phase behaviour of the system. The correlation plot in Fig. 4.13b shows remarkable agreement between DFT energies and CE-predicted ones, meaning that the CE formalism accurately describes the system. Finally, one can note from Table 4.2 that only six clusters are needed to describe the behaviour of the system, as no subtle electronic effects (W and Mo have the same electronic configuration) or long-range elastic interactions are present (MoS_2 and WS_2 have the same lattice parameter).

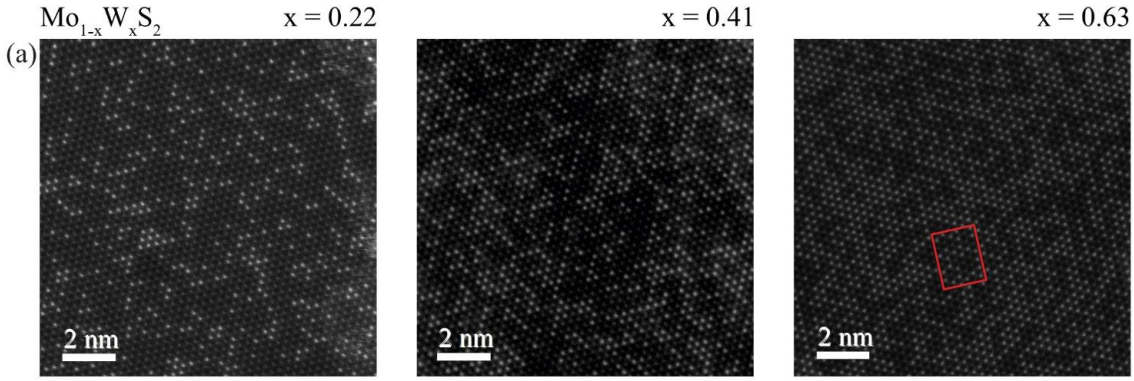

Figure 4.14: STM images of $W_xMo_{1-x}S_2$ ML alloys at concentration reported in the top right corner of each plot. Bright dots represent W atoms, dim dots Mo atoms. Adapted from Ref. [208]

The result of this analysis is in line with experimental synthesis, where the bandgap varies between 1.82 eV and 1.99 eV for increasing W concentration x in $Mo_{1-x}W_xS_2$ [189]. Another recent study focused on spintronic applications of $Mo_{1-x}W_xS_2$, showing how the

spin-orbit splitting of the valence band varies with the W content. The work by Xia and coworkers [208] confirms the solid-solution behaviour and shows the ability of experiments to produce high-quality samples with CVD deposition at any alloy concentration, as shown in Fig. 4.14. The trained CE model presented here can be used as Hamiltonian in MC simulations to generate realistic, finite-temperature configurations that could serve as a starting point for theoretical characterisation of the system.

From a tribology point of view, this system offers an interesting possibility to explore the effect of disorder on the sliding interface. It has been shown in a toy model [218] that dopants at low concentration act as defects and worsen frictional response, as they act as pinning centres during the sliding. As concentration approaches $x = 0.5$, this argument may lose validity, as the alloying element is no longer a localised defect but a considerable fraction of the sliding layer. In light of this, it would be interesting to study the possible coupling between different solid-solution arrangements in two adjacent layers and how this affects dissipation.

4.3.2 Mo-group V-S Binary Alloy

The similar electronic structure of group V elements make them an interesting alloy possibility for MoS_2-based devices. In particular, (Nb:Mo)S_2 alloys have been indicated as a viable p-doping solution for MoS_2 ML transistors [176, 186]. On the other hand, Ta has been used to enhance electrical conductivity in SnO_2-based catalytic supports [190], while Nb doping fails to deliver the same results. Ta-doped MoS_2 composite coatings have been identified as a promising fatigue-resistant material for tribological applications [75]. Moreover, Ta-based TMDs attracted attention for the peculiar CDW behaviour [219, 220], which is also associated with unusual non-contact frictional dissipation [221]. One would expect similar behaviour from Nb and Ta dopants, as the two have the same covalent radii, electronic configuration [201] and the same lattice parameter in TMD compounds [1]. A good understanding of the phase behaviour of these systems is needed, especially as the doping concentration needed in p-doped devices may reach 20% [186] and the competition with ternary phases might make synthesis problematic.

Fig. 4.15a shows the ternary phase fields for Mo-Nb-S and Fig. 4.15b the corresponding one for Mo-Ta-S, computed from MP [216, 217]. No stable compound is reported in the Mo-Nb-S except Mo_nS_m and Nb_nS_m binaries. Apart from the binaries, the ternary 2H-Ta_4MoS_{10}, shown in Fig. 4.15b, is reported as stable in the Mo-Ta-S phase field. 2H-Ta_4MoS_{10} is a ground state in the $Mo_xTa_{1-x}S_2$ bulk alloy, with formation energy $E_F = -5 \times 10^{-3}$ eV/atom in the reference frame of the end members, within the MP dataset [216, 217]. As shown in Fig. 4.15b, each layer is composed of single rows of Mo alternated by four rows of Ta, for a concentration of $x = 0.8$. To the best of our knowledge, the only experimentally reported ternary in the pseudo-binary alloy is $MoTaS_4$ [184], for which no structure is reported.

[1] Spin-orbit coupling differs between Nb and Ta, but it is not included here and rarely influences the phase behaviour of the material.

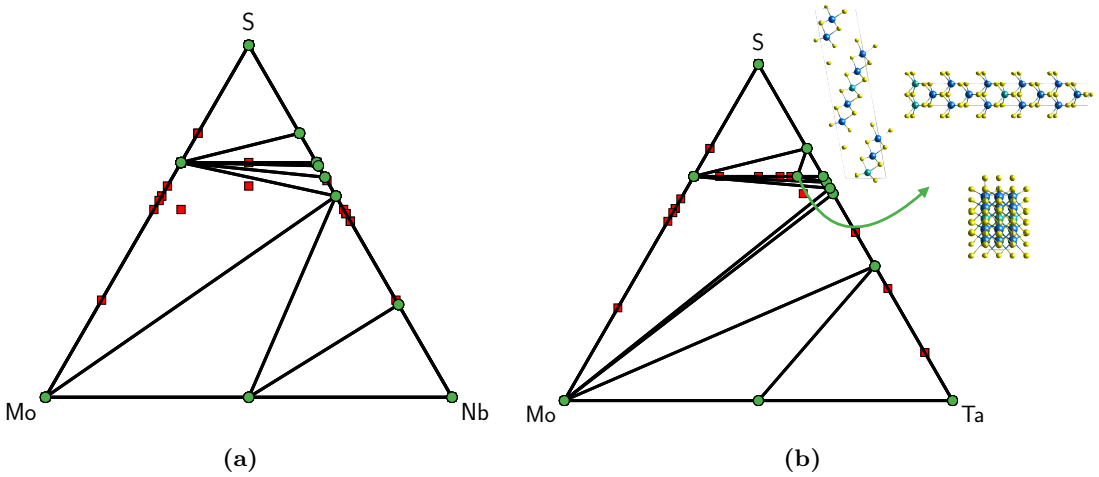

Figure 4.15: Ternary phase diagram for (a) Mo-Nb-S and (b) Mo-Ta-S elements. The structure on the top right in (b) is the ordering in the tie line MoS_2-TaS_2 reported as stable. Obtained from the MP database [216, 217].

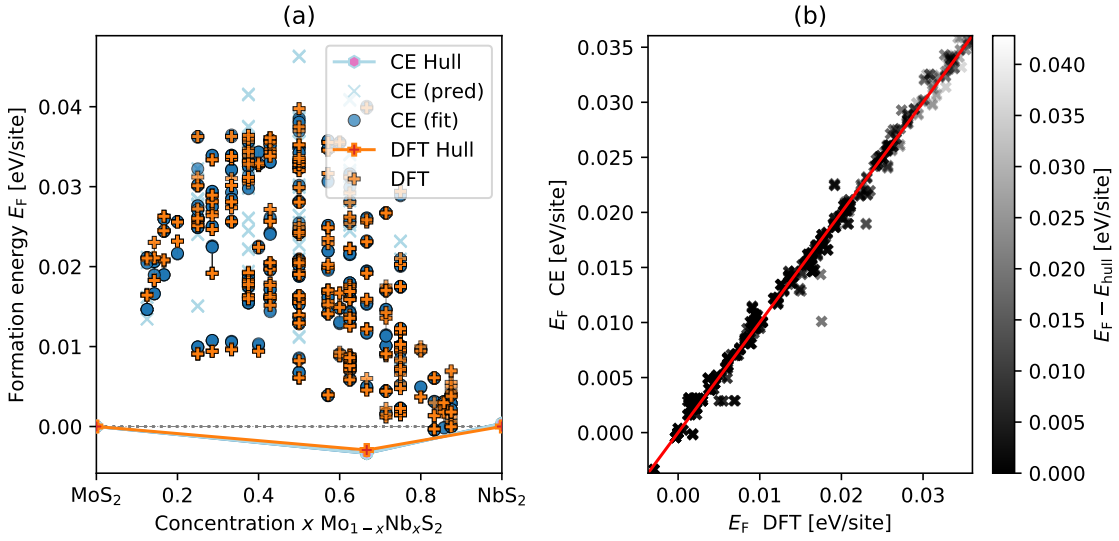

Figure 4.16: (a) Formation energy E_F, in eV/site, versus concentration x of the $Mo_{1-x}Nb_xS_2$ system and (b) CE model correlation plot. Colours and symbols as in Fig. 4.13.

$Mo_{1-x}Nb_xS_2$ pseudo-binary According to Fig. 4.3 the end members MoS_2 and NbS_2 share the same ground state prototype, prismatic MoS_2, which is the parent lattice for the CE. The details of the expansion are reported in Table 4.2. Fig. 4.16a shows, as orange crosses, the formation energies of the DFT training-set geometries. The solid orange line shows a convex hull of the *ab-initio* data. The simple SS hull (dashed gray line at $E_F = 0$) is broken by a GS at $x = 0.66$, with formation energy $E_F = -3\,\text{meV/site}$. Blue circles in Fig. 4.16a show the formation energy for the DFT set (orange crosses) as predicted by the CE model. Light-blue crosses show the CE-predicted formation energy for geometries not in the DFT training-set. The computed (orange line) and predicted (light-blue line) convex hulls in Fig. 4.16a match: CE provides a reliable description of the phase behaviour of the system. The correlation plot in Fig. 4.16b shows good agreement between DFT energies and CE-predicted ones. The slight spread around the $x = y$ red line in Fig. 4.16b

compared to Fig. 4.13b is a signal of the more complex chemical and mechanical interactions underpinning the phase behaviour in Fig. 4.16a. More quantitatively, 169 five-vertex orbits are needed to achieve a good description of the $Mo_{1-x}Nb_xS_2$ system, whereas the W-based alloys only required six, as shown in Table 4.2.

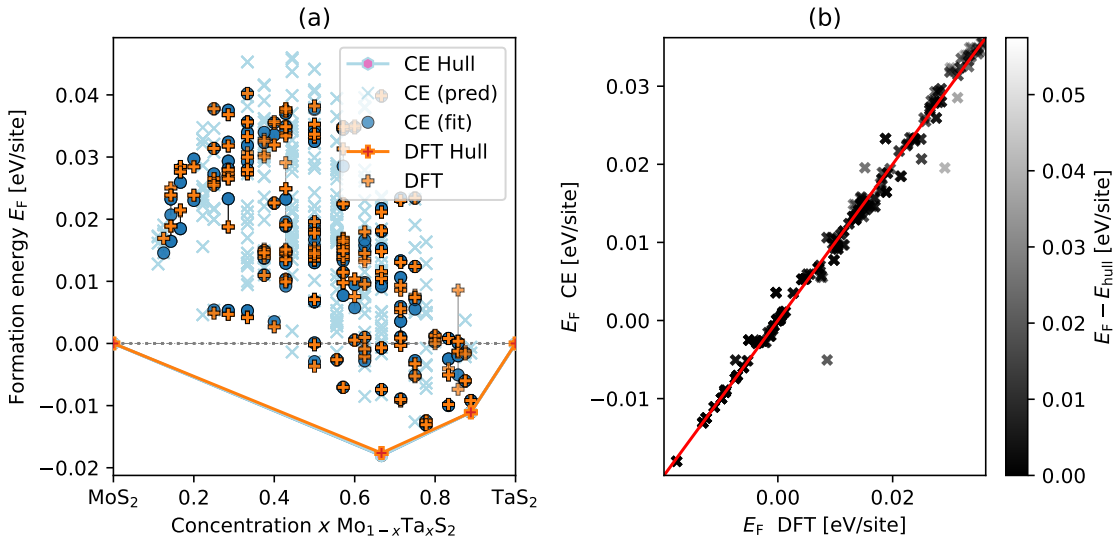

Figure 4.17: (a) Formation energy E_F, in eV/site, versus concentration x of the $Mo_{1-x}Ta_xS_2$ system and (b) CE model correlation plot. Colours and symbols as in Fig. 4.13.

$Mo_{1-x}Ta_xS_2$ pseudo-binary According to Fig. 4.3 the end members MoS_2 and TaS_2 share the same ground state prototype, prismatic MoS_2, which is the parent lattice for the CE expansion. The details of the expansion are reported in Table 4.2. Fig. 4.17a reports the convex hull of DFT-computed orderings (orange crosses) for the $Mo_xTa_{1-x}S_2$ pesudo-binary alloys. The hull is dominated by the ground-state orderings at $x = 0.667$, with $E_F = 18\,\text{meV/site}$ and at $x = 0.889$, $E_F = 11\,\text{meV/site}$. The system shows two stable ternaries, with formation energy comparable with room temperature, which should therefore be within experimental synthesis capabilities. The ground state at $x = 0.667$ identified by the CE-DFT tandem search comprises of two Ta rows and one Mo row; the one at $x = 0.889$ comprises of two Ta rows alternated by Mo-Ta sequenced rows. The correlation plot in Fig. 4.17b shows a degree of spreading around the ideal behaviour (red line $y = x$) and few outliers, as expected from the more complex behaviour displayed by the system. Nonetheless, since predicted and computed hull (yellow and blue lines in Fig. 4.17a) match, the description of the system is still well-captured by the CE model.

Discussion A more detailed analysis of the ground state is warranted to understand the origin of the phase behaviour. Figures 4.18a and 4.18b shows the geometries of the GS at $x = 0.66$ for $Mo_{1/3}Nb_{2/3}S_2$ and $Mo_{1/3}Ta_{2/3}S_2$, respectively; Fig. 4.18c shows the geometry for $Mo_{1/9}Ta_{8/9}S_2$. The arrows show the displacement of the TM sites, with starting position marked by smaller grey circles and final position by larger pink circles. The displacement of the S ions follows the direction of the closest TM and is negligible in magnitude; hence

they are not shown here. In all cases, the cell expands, increasing the distance between Nb or Ta ions, approaching their equilibrium lattice parameter, $l_{\mathrm{Ta}} = l_{\mathrm{Nb}} = 3.33\,\text{Å}$, larger than the MoS_2 lattice spacing, $l_{\mathrm{Mo}} = 3.18\,\text{Å}$, which is the starting point for the CASM-generated geometries.

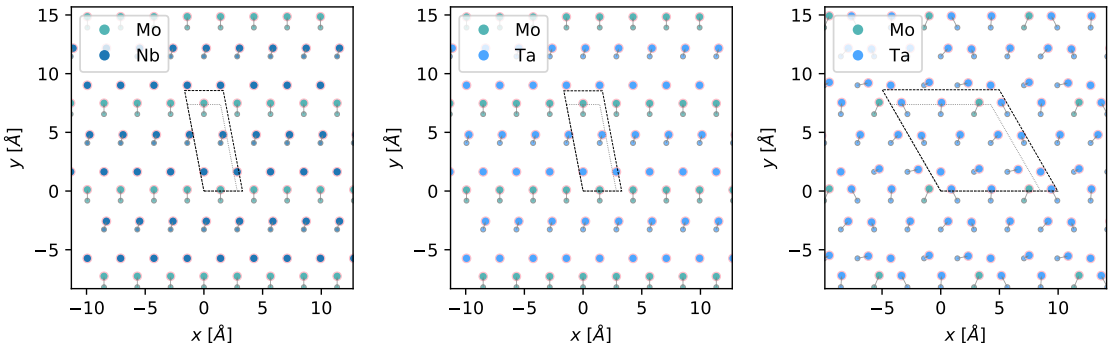

(a) $Mo_{1/3}Nb_{2/3}S_2$ **(b)** $Mo_{1/3}Ta_{2/3}S_2$ **(c)** $Mo_{1/9}Ta_{8/9}S_2$

Figure 4.18: Geometry and relaxation displacement (magnified by a factor 1.1) of the ground-states in (a) Fig. 4.18a and (b,c) Fig. 4.18b. Atom types are reported in the legend; S atoms are not shown. The starting geometry, perfect MoS_2 prototype, is reported with small, grey-edged circles, and the relaxed position is reported with larger, pink-edged circles. Dotted grey lines show the starting supercell and black dashed ones the final cell.

Modelling these alloys presents a double challenge. One needs to capture, at the same time, the many-body, non-local character of phase stability, and the long-range elastic interactions due to lattice mismatch. The CE formalism is well suited to efficiently handle the first task, while the description of elasticity is problematic [136]. Since the sum in Eq. (2.58) is a complete representation of the energy landscape of the lattice model, the CE can describe such elastic effects, at the cost of increased complexity and features included. Indeed, to appropriately describe the convex hull in Figures 4.16 and 4.17 more than a hundred orbits must be included in the model, up to five-vertex clusters, far more than for the (Mo:W)S_2 case, as reported in Table 4.2.

A possible way to efficiently describe this behaviour might arise from a toy-model suggested by Frechette *et al.* [222, 223, 224]. TMs are placed on a flexible lattice, whose spacing is a function of the local composition [222]. Each lattice site $\boldsymbol{R}$ can be occupied by the metal M, $\sigma_R = 1$, or the other metal N, $\sigma_R = -1$. The elastic energy penalty in terms of the displacements $\boldsymbol{u}_i$ of the flexible-lattice sites is described by the Hamiltonian [222]

$$\mathcal{H} = \frac{K}{4} \sum_{\langle \boldsymbol{R}, \boldsymbol{R}' \rangle} \left[|\boldsymbol{R} - \boldsymbol{R}' + \boldsymbol{u}_R - \boldsymbol{u}_{R'}| - l(\sigma_R, \sigma_{R'}) \right]^2 , \tag{4.10}$$

where the sum is over nearest neighbour sites $\boldsymbol{R}$, $\boldsymbol{R}'$. K is a positive constant representing the stiffness of the lattice. The term $l(\sigma_R, \sigma_{R'})$ in Eq. (4.10) encodes the different equilibrium

lattice spacing of the two elements

$$l(\sigma_R, \sigma_{R'}) = \begin{cases} l_{MM},\ \sigma_R = \sigma_{R'} = 1 \\ l_{MN},\ \sigma_R \neq \sigma_{R'} \\ l_{NN},\ \sigma_R = \sigma_{R'} = -1, \end{cases} \tag{4.11}$$

where a simple mixing rule is used for $l_{MN} = |l_{MM} - l_{NN}|/2$. The core idea of Eq. (4.10) is that the displacements $\boldsymbol{u}_R, \boldsymbol{u}_{R'}$ distort lattice bond-vector $\boldsymbol{R} - \boldsymbol{R}'$ to match the equilibrium lattice spacings $l(\sigma_R, \sigma_{R'})$ and, thus, minimise the difference in square brackets. In this frustrated system, the end-members $x = 0, 1$ are the only ground states, while intermediate compositions at low temperature favour same-type strips and clusters that release local stress via underlying lattice distortions [222]. Hence, one could think of an extended CE formalism that includes this elastic contribution explicitly. This extended theory could result in a two-fold improvement. On a physical ground, decoupling the elastic contribution could make it easier to understand the remaining effects determining the phase behaviour of the system. Moreover, from a modelling point of view, the stiffness K and equilibrium spacings l_{ij} in Eq. (4.10) could be easily obtained from DFT. Hypothetically, subtracting the elastic contribution from Figures 4.16 and 4.17 could reduce the spread of the points, resulting in a more accurate fit and less complex CE model.

The argument at the base of this model helps to understand the displacements of Ta and Nb ions in Figures 4.18, 4.18b and 4.18c, but since any displacement from the end-members lattice parameter results in an energy penalty, it cannot explain the origin of the negative formation energy of these orderings. Quantifying this electronic effect is a challenging task, but a simple qualitative argument can be made in terms of the interaction between the TMs. Figures 4.19a and 4.19b report the atom-projected electronic band-structure of $Mo_{1/3}Nb_{2/3}S_2$ and $Mo_{1/3}Ta_{2/3}S_2$, respectively. Point colour represents the overlap between the Mo and Nb, or the Ta character of each band eigenvalue. A non-zero overlap is an indicator of a level of bonding between the two atoms. As shown in Fig. 4.19, this overlap is larger where the bands are curved and therefore the electron density is more de-localised, consistent with a possible bond between Mo and the group V metal. The delocalisation of the extra electron of Mo ions lowers the total energy of the system, compared to the separate Mo_2 and Ta_2. Finally, the more negative formation energy of Mo-Ta alloys arises from the fact that the overlapping d manifold lies slightly lower in energy compared to the Mo-Nb case, consistently with similar observation in Nb- and Ta-doped SnO_2.

4.3.3 Ir-Ru-S Binary Alloy

The last case study shows the limit of the CE formalism. The system considered combines two chalcogenides interesting for ammonia catalysis applications: IrS_2 and RuS_2. No ternary is reported in the phase-field within the MP database.

Dark-blue hexagons and red crosses show the DFT-computed convex hull for the $Ir1 - xRu_xS_2$ alloys in the $NbTe_2$ and WTe_2 prototype, which, as in Fig. 4.3 are the

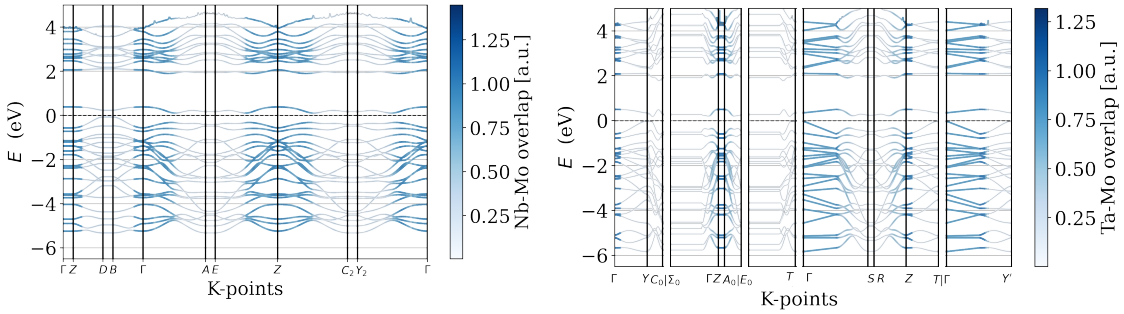

(a) $Mo_{1/3}Nb_{2/3}S_2$ **(b)** $Mo_{1/3}Ta_{2/3}S_2$

Figure 4.19: Atom-projected band structure of GS at $x = 0.66$ of Nb- and Ta-MoS_2 alloys. The colour-code reports the product of the projection onto the TM atoms, i.e. (a) $p_{s,\mathrm{Mo}}(\boldsymbol{k})p_{s,\mathrm{Nb}}(\boldsymbol{k})$ and (b) $p_{s,\mathrm{Mo}}(\boldsymbol{k})p_{s,\mathrm{Ta}}(\boldsymbol{k})$, where s is the band index and $\boldsymbol{k}$ a vector in the BZ. The high-symmetry path is generated with the SeeK-path suite [225], and each line is interpolated over 60 points.

low-energy ML configuration of IrS_2 and RuS_2, respectively. The reference energies are given by the pyrite RuS_2, $x = 0$, and non-layered IrS_2, $x = 1$, shown by figures with black edges at the left and right of the plot respectively. As shown in Fig. 4.20, the CE formalism fails to capture the energy landscape of the system even with the extensive training set and basis size reported in Table 4.2. The predicted convex hulls (light blue and orange dashed lines) differ significantly from the DFT-computed one (blue and solid red lines). Moreover, as shown in Fig. 4.21, the fitted and computed energies display low correlation. The poor performance of the CE model is rooted in the large relaxation undergone by many structures. Different orderings relax to the same final structure, breaking mapping between geometrical ordering on a fixed lattice and energies underpinning the CE formalism [136].

This system is a reminder that coarse-graining is a delicate process, and special attention must be paid to structures displaying large relaxation when deploying the CE formalism.

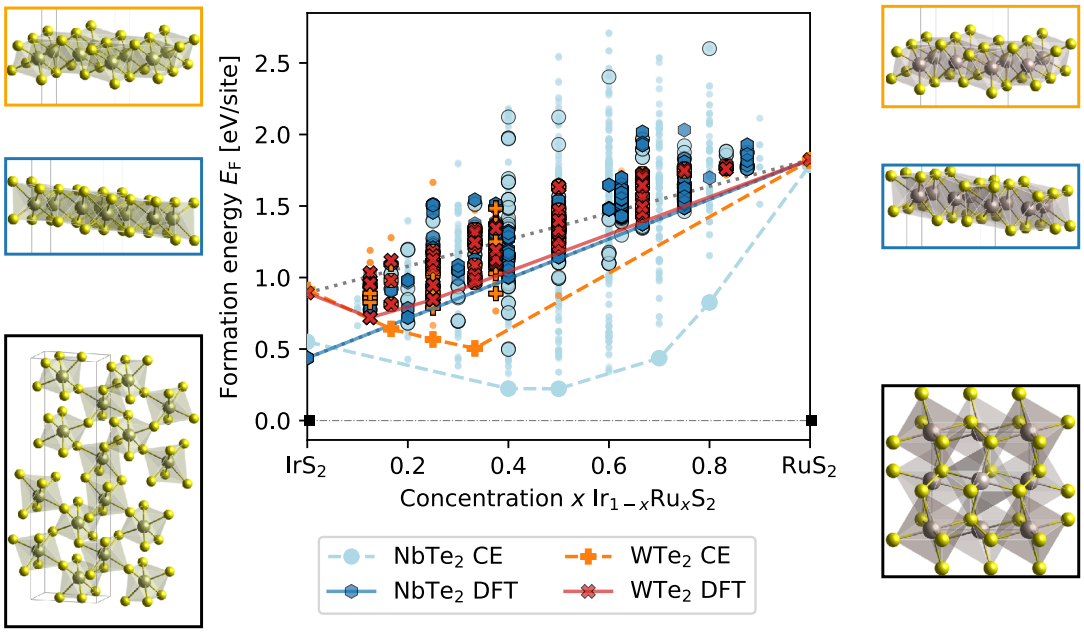

Figure 4.20: (a) Formation energy E_F, in eV/site, versus concentration x of the $Ir_{1-x}Ru_xS_2$ system in the $NbTe_2$ (blue-shaded symbols) and WTe_2 (red-shaded symbols) prototypes. Colour-mathced solid lines show the DFT convex-hull within each host and dashed lines the one predicted by CE. Insets on the left of the plot show IrS_2 polymorphs: GS non-layered geometry (black-edge inset), $NbTe_2$ ML (blue-edge inset) and WTe_2 ML (orange-edge inset). Insets on the right show RuS_2 polymorphs following the same colour-code.

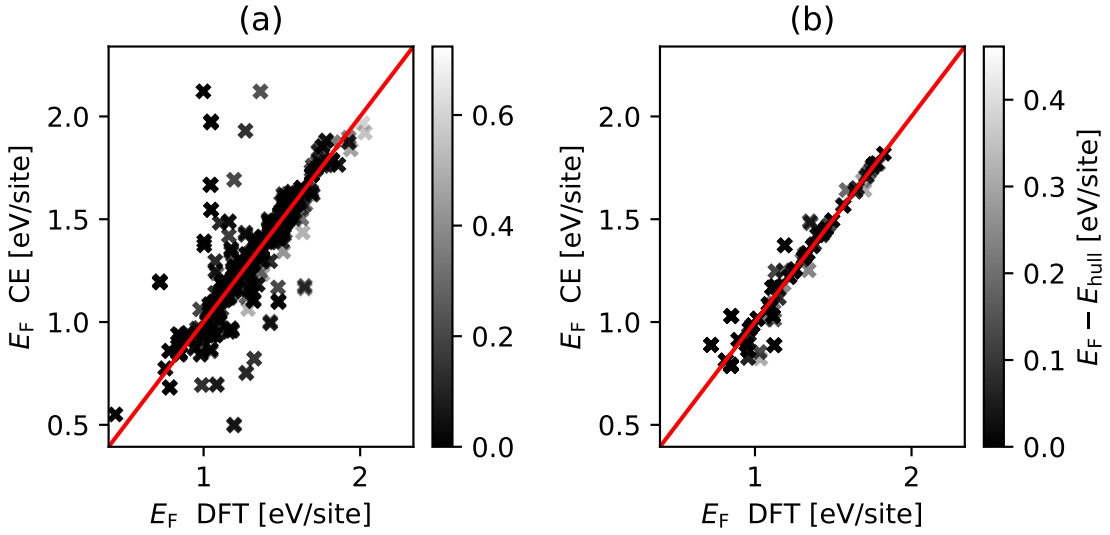

Figure 4.21: Correlation plot of the DFT-training-set and CE-fitted energies. The red line marks $x = y$, i.e. perfect correspondence between the two sets. The grey-scale of each marker shows the distance from the DFT hull (solid lines in Fig. 4.20).

4.4 Final Remarks

This chapter represents a systematic analysis of possibilities to alloy in TMD families. The ideal solution limit provides the first guideline for in-depth computational studies and experimental synthesis. Comparison between the ideal solid solution results and the literature suggests the description is a reliable starting point. Moreover, ordering on the metal site of promising candidates identified from the ISS data has been explored with CE formalism for a few case studies. The CE analysis agrees in (Mo:W)S_2, (Nb:Mo)S_2 and (Ta:Mo)S_2 cases with the ISS prediction, which predicts maximum solubility in these cases. In the case of (Nb:Mo)S_2 and (Ta:Mo)S_2, the ISS predicts the same behaviour for both systems. Conversely, the CE analysis can capture the different behaviour of the two alloys systems, which show quantitative different formation energies and a different shape of the convex hull. Nonetheless, the ISS correctly predicts the qualitative character of the systems, as both Nb and Ta show good miscibility with Mo within the MoS_2 prototype. These results show that the ISS model and CE analysis can be a good guideline for CVD synthesis and the search for new alloys and ternary in the TMD chemical space.

A more in-depth analysis will be carried out on the (Mo:Ti)S_2 alloys. This family of compounds has captured the interest of the tribology community, as both experimental [74] and computational studies [80] suggest it as a promising candidate for solid lubrication. In the following chapter, the CE model will be developed to describe the phase behaviour of the system. This model, coupled with MC simulation, will be used to predict the system high-temperature behaviour and compare the results with available literature.

5

Phase Stability of (Mo:Ti)S_2 Alloys

Building on the protocol outlined in chapter 4, an in-depth analysis is reported here of the phase behaviour of a compound that has captured the interest of the tribology community. (Mo:Ti)S_2 alloys have been identified as a promising material with enhanced tribological properties both by experimental and computational investigations. Experiments on a mesoscale report that Ti-doped composite coatings show better resistance to oxidation compared to pristine MoS_2 while preserving low friction coefficients [74]. Recent computational work [80, 226] has put forward an argument to rationalise the good frictional behaviour in terms of the vibrational properties: the low frequency optical phonon modes taken to be associated with the perfect shear of two layers are extrapolated along the sliding path and taken as an indication of low energy barriers for *sliding modes*. By studying this descriptor across the transition-metal dichalcogenide (TMD) chemical space, the authors identified layered 2H-$Ti_{1/4}Mo_{3/4}S_2$, shown in Fig. 5.1a where a quarter of TM sites within the TM-S_2 layers are occupied by Ti, as a candidate material with enhanced frictional properties compared with other analysed TMDs. Despite the interest attracted by this compound, the exact structure and chemistry is still debated. In order to experimentally realise this computationally engineered chemistry, it would be advantageous for $Ti_{1/4}Mo_{3/4}S_2$ to be thermodynamically stable within the Ti-Mo-S chemical space. However, the reported mechanically stability in DFT calculations [80] is by itself insufficient to assess the thermodynamic viability. Experiments do not provide a definite answer either. On the one hand, studies on thin films synthesised via magneto-sputtering suggest Ti is not fully integrated within the TM-S_2 planes [74, 227]. On the grounds of the measured ratio between chemical composition and film hardness, the authors conclude that if Ti were fully incorporated into the layered structure, the resulting properties of the material, including hardness, should

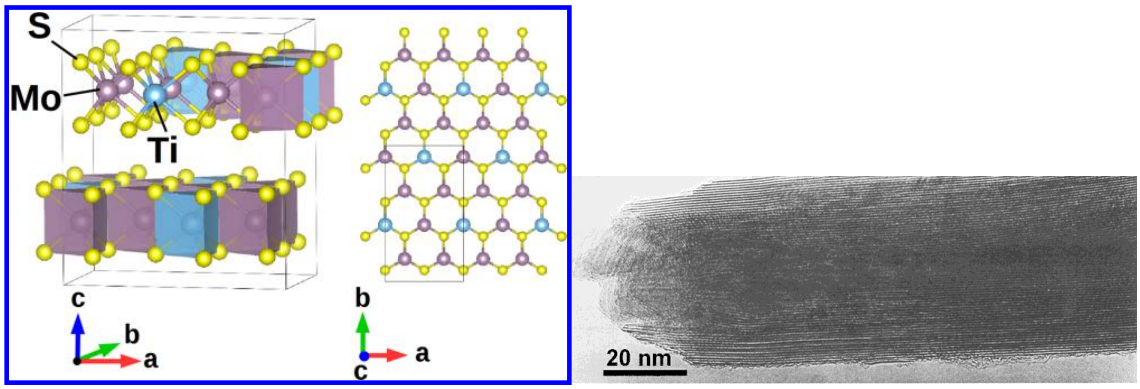

(a) (b)

Figure 5.1: (a) Tribological-enhanced compound proposed in Ref. [80]. (b) HRTEM image of a Ti doped MoS_2 nanostructure from Ref. [228]. The layering structure of TMDs compound is clearly visible.

deviate more from pristine MoS_2 than is observed. On the other hand, a separate study of Ti doped MoS_2 nanostructures, reported in Fig. 5.1b, concluded that Ti is incorporated within the TM-S_2 planes. The authors disregarded a possible intercalation between the layers due to the absence of distortion along the interlayer c axis, suggesting that Ti is embedded in the planes.

In an attempt to elucidate the thermodynamic viability of layered (Mo:Ti)S_2 compounds including 2H-$Ti_{1/4}Mo_{3/4}S_2$, the energetics and thermodynamics of metal-site substitutions are investigated with computational techniques to identify ordered phases and solubility limits along the full (Mo:Ti)S_2 pseudo-binary line within the Mo-Ti-S phase space.

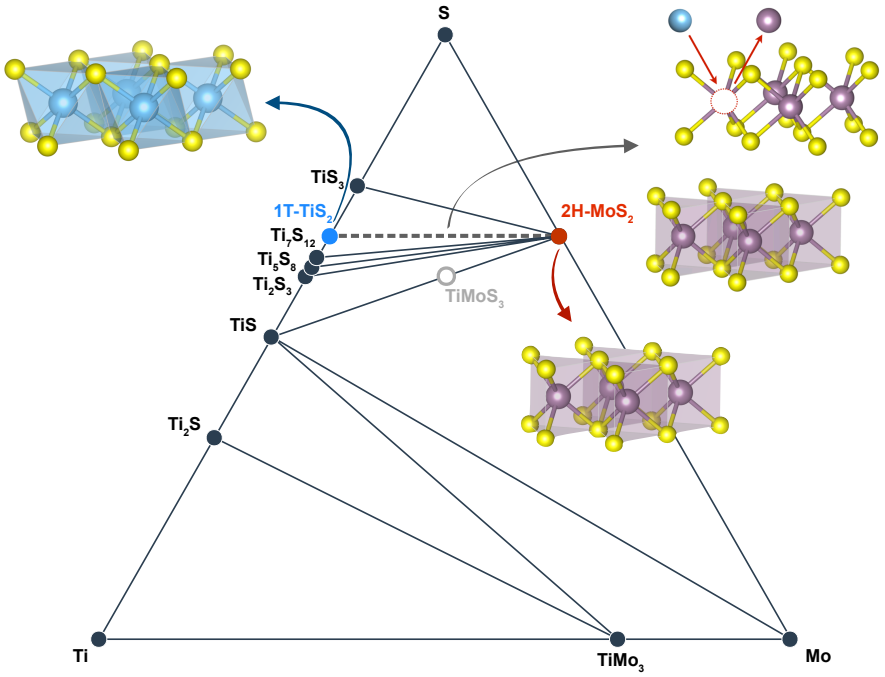

Figure 5.2: Ternary space of the Mo-Ti-S system. Insets on the left and right show the coordination of the pristine compounds, 1T-TiS_2 and 2H-MoS_2, respectively. The binary alloy system studied here is represented by the dashed line and the substitutional process is sketched at the bottom.

Fig. 5.2 visualises the considered part of the ternary phase space. Only compounds $Ti_xMo_{1-x}S_2$ within the two end members prototypes are considered. The ternary plot in Fig. 5.2 reports stable configurations and tie lines in the chemical space according to the Materials Project Database [216, 217]. The only ternary compound reported, $TiMoS_3$, is an unstable non-layered structure, with a formation energy of $E_F = 0.04\,\text{eV}$ above the convex Hull. To the best of our knowledge, there are no stable ternaries reported in the phase field MoS_2-TiS_2-Ti_7S_12 relevant here, and no attempt was made to computationally search for unknown ternaries in this region of the chemical space.

The two end-members are:

1. 1T-TiS_2 is a semi-metal that crystallises in a layered compound with space group $P\bar{3}m1$. The structure is depicted on the left side in Fig. 5.2. Each layer shows CdI_2 prototype: triangular Ti layers are sandwiched by triangular chalcogenide planes, mutually rotated by 60°, resulting in octahedrally coordinated Ti. The 1T prefix indicates that TiS_2 planes are stacked in an AA fashion [35].

2. 2H-MoS_2 is a semiconductor with an indirect bandgap of 1.3 eV and crystallises in a layered structure with space group $P6_3/mmc$. Each layer presents the coordination of the MoS_2 prototype: Mo planes are sandwiched by S planes that are not rotated relative to each other, resulting in a prismatic coordination of Mo, as sketched on the right side in Fig. 5.2. The 2H prefix designates an AB stacking order of MoS_2 layers [35].

In order to explore the effects of system dimensionality on the phase stability, the systems are also studied in purely ML form, as done in chapter 4. No stacking order is present in the ML case and the pristine compounds are referred to as 1T-TiS_2 and 1H-MoS_2.

5.1 Methodology

Cluster Expansion method The combinatorial problem of cation ordering within a crystal structure is addressed using the CE formalism [41], described in detail in section 2.2. The Alloy Theory Automated Toolkit (ATAT) [136] has been used to construct cluster expansions. The series Eq. (2.58) is truncated at figures of four vertices and cross-validation is used to select the most predictive model over a training set. The expansion is considered converged once the ground states predicted by the CE agree with DFT calculations and the error on predicted energies is deemed negligible.

First-principles calculations Total energy calculations of geometries along the $Ti_xMo_{1-x}S_2$ tie-line are performed using DFT within the PAW framework [124] as implemented in the VASP software [198, 199]. Exchange-correlation effects are modelled using the SCAN functional [128]. The subtle van der Waals interactions coupling the layers in bulk systems are described using the non-local kernel correction rVV10 [229]. This combination has

proven to accurately describe layered materials and complex geometries [129] and is further benchmarked in Appendix E.

A plane wave cut-off of 800 eV was adopted for all DFT calculations; the Brillouin zone of the pristine compounds in their primitive cell was sampled using a $11 \times 11 \times 11$ mesh and the number of k points per reciprocal atom was kept constant for larger supercells. These parameters were evaluated via a convergence study for the current DFT setup in Appendix E. For the ML geometries, layers of TMD are separated by 20 Å, ensuring there is no interaction between periodic images. In order to obtain accurate total energies, cell vectors and atomic positions were relaxed until the energy between iterations is less than 0.5 meV/atom.

Monte Carlo simulations To investigate the effect of temperature and configurational entropy on the system, Monte Carlo simulations were performed using the CE Hamiltonians and the EMC routine of the ATAT package [138]. The simulations are carried out in the semi grand-canonical ensemble, where the chemical potential μ, number of lattice sites N and temperature T are fixed while concentration x and energy E can fluctuate.

The supercells used in the calculations are reported in Table 5.1. All ground states of the system are stabilized within the chosen chemical potential range, spanned in steps of $\Delta\mu = 0.01\,\text{eV}$. Temperature is varied as function of its inverse $\beta = 1/T$ between $\beta_1 = 1/100\,\text{K}$ and $\beta_1 = 1/8000\,\text{K}$ in steps $\Delta\beta = 1 \times 10^{-4}$. This ensures a high sampling density at low temperatures while conveniently enabling the ideal solid solution case as a high temperature starting point. Each MC simulation is considered converged once concentration fluctuations are less than the threshold of $\Delta x = 5 \cdot 10^{-3}$.

Host	Training set size	Clusters Φ_α	CV [eV]	MC cell size
2H bulk	57	19	0.009	37x37x8
1T bulk	113	31	0.052	21x21x11
1H ML	39	8	0.016	-
1T ML	46	37	0.083	-

Table 5.1: Training set and convergence of the CE in the trigonal prismatic 2H and octahedral 1T hosts, for bulk and ML geometries.

5.2 Results

5.2.1 Crystallography and Cluster Expansion

The DFT-SCAN with rVV10 correction describes the in-plane bonding accurately and stacking lattice constants are in good agreement with experiment, which indicates that the rVV10 kernel accurately captures the cohesive inter-layer interactions. The lattice parameters of the pristine compounds 2H-MoS_2 and 1T-TiS_2 as obtained from calculations are reported in Table 5.2 and are compared with experimental crystallographic data.

Separate CE Hamiltonians were built for the trigonal-prismatic (H) and the octahedral (T) hosts. Two datasets of total energy calculations, one per host, were used to train

Compound	a[Å]	c[Å]	Method	Reference
2H-MoS_2	3.168	12.5	DFT-SCAN	This work
	3.161	12.3	experimental	[230]
1T-TiS_2	3.409	5.75	DFT-SCAN	This work
	3.410	5.70	experimental	[231]

Table 5.2: Intralayer a and interlayer c lattice parameters from simulations and experiments. Bulk lattice parameter a is within 0.03% and 0.2% of the experimental measured value, while the interlayer one c is within 0.7% and 1.8% for TiS_2 and MoS_2, respectively.

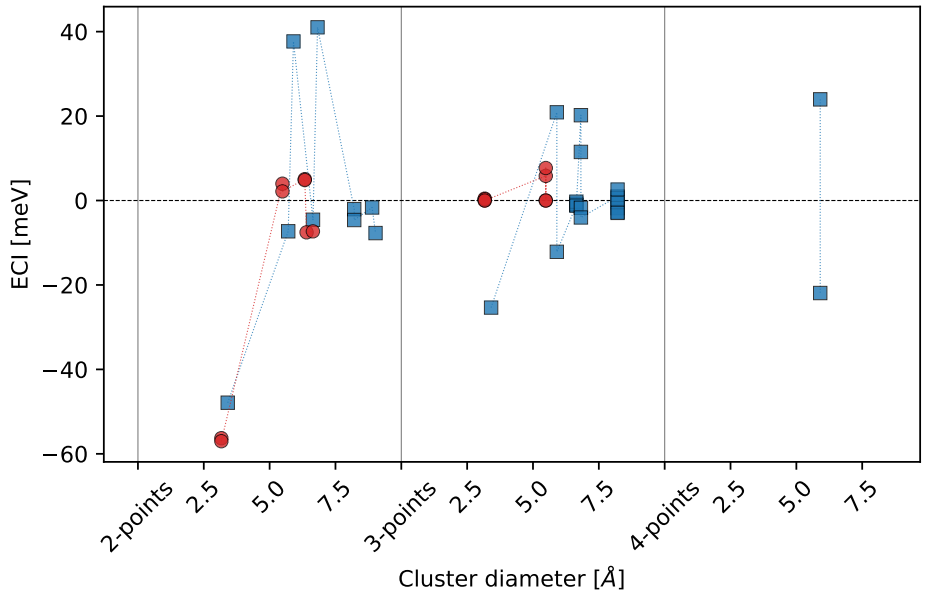

Figure 5.3: ECI in prismatic 2H host (red circles) and octahedral hosts (blue squares) as defined in Eq. (2.58). The dashed lines connecting the points are a guide to the eye.

the ECIs, which are reported in Fig. 5.3. A dataset comprising around 50 structures was sufficient to bring CE and DFT into agreement for the trigonal-prismatic host, while a little over a hundred configurations were needed for the octahedral host as reported in Table 5.1. While the CE for the trigonal-prismatic host was built using the full concentration range $x \in [0, 1]$, within the octahedral host, it was decided to bias the CE model to accurately reproduce the ground-states only in $x \in [0, 0.6]$ as explained in section 5.2.2. As reported in Fig. 5.4, energies predicted by CE models agree well with the DFT-computed ones: average error is 0.8 ± 6.9 meV/site for the 2H host and -2 ± 24 meV/site for 1T host. Considering that the energy landscape is dominated by the formation energy of end-members in the non-native host, which is of the order of 0.5 eV, this error is negligible in the description of the energetics in most of the phase diagram. The error in 1T host is in the order of thermal energy at room temperature $k_B T_{\text{room}} = 25\,\text{meV}$, making it relevant for low-temperature simulations at low concentration x, near the 1T-TiS_2 end-member. In turn, in the high-temperature portion of the phase diagram, which is the one of interest here, this error becomes negligible.

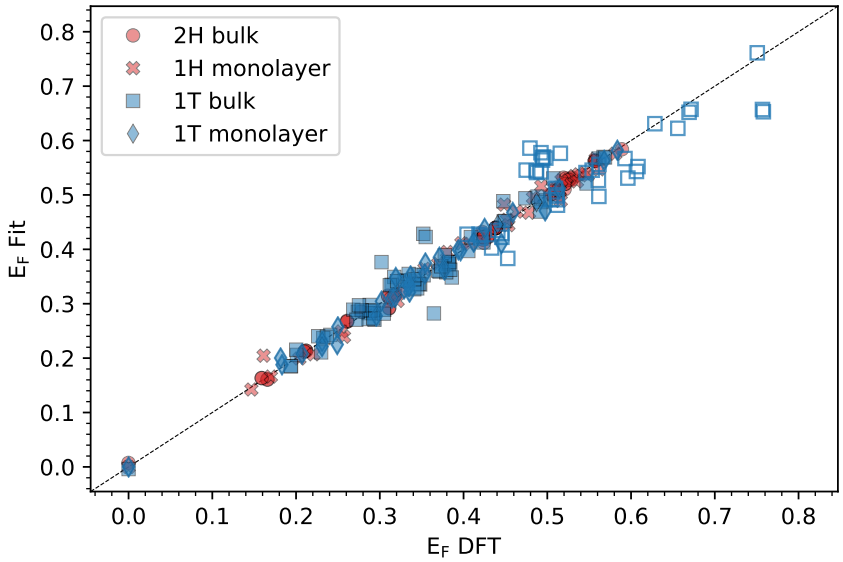

Figure 5.4: Fitted versus DFT-computed formation energies in both hosts. In a perfect fit all points would lie on the bisector, shown as a dashed black line. Empty squares refer to configuration $x > 0.6$, which have a different weight in the fit as explained in section 5.2.2.

5.2.2 Convex Hull

In order to understand stability across the two hosts p, the formation energy defined in Eq. (4.8) is adopted and, for this system, reads

$$E_{\mathrm{Mo,Ti},p}(x) = E(\mathrm{Mo}_x\mathrm{Ti}_{1-x}\mathrm{S}_2)|_p - xE(\mathrm{Mo}, p_{\mathrm{Mo}}) - (1-x)E(\mathrm{Ti}, p_{\mathrm{Ti}}) = E_{\mathrm{F}}^p(x), \tag{5.1}$$

where $E(\mathrm{Mo}_x\mathrm{Ti}_{1-x}\mathrm{S}_2)|_p$ is the energy per TM site of the configuration $\sigma(x)$ at concentration x, and remaining terms are the total energy of the pristine compound in the ground-state hosts, i.e. p_{Mo} is prismatic MoS_2 and p_{Ti} is octahedral CdI_2. $E_{\mathrm{F}}^p(x)$ is introduced as a short-hand, as in the remaining of the chapter the TM will not change. Formation energies from Eq. (5.1) are reported in Fig. 5.5 for bulk and ML in both octahedral 1T and trigonal prismatic 1H and 2H hosts. The line connecting the end-member in each host (solid red for H host and dashed grey for T host in Fig. 5.5) represents the energy of the ideal solid-solution limit with negligible interactions between the fraction x of sites occupied by Mo and the remaining Ti sites. Points lying below this line represent stable configurations in the given host while points over it mark energetically unfavourable regions, where Mo-rich and Ti-rich parts are segregated within the same host geometry. Finally, stable structures across both hosts would show negative formation energies, lying below the black dotted line in Fig. 5.5, but no such configuration has been found.

The prismatic host is not receptive to alloying. All training set configurations lie above the line connecting the end-members (red symbols in Fig. 5.5), indicating a high energy penalty for Ti in prismatic coordination. Since no ordered arrangement of the two

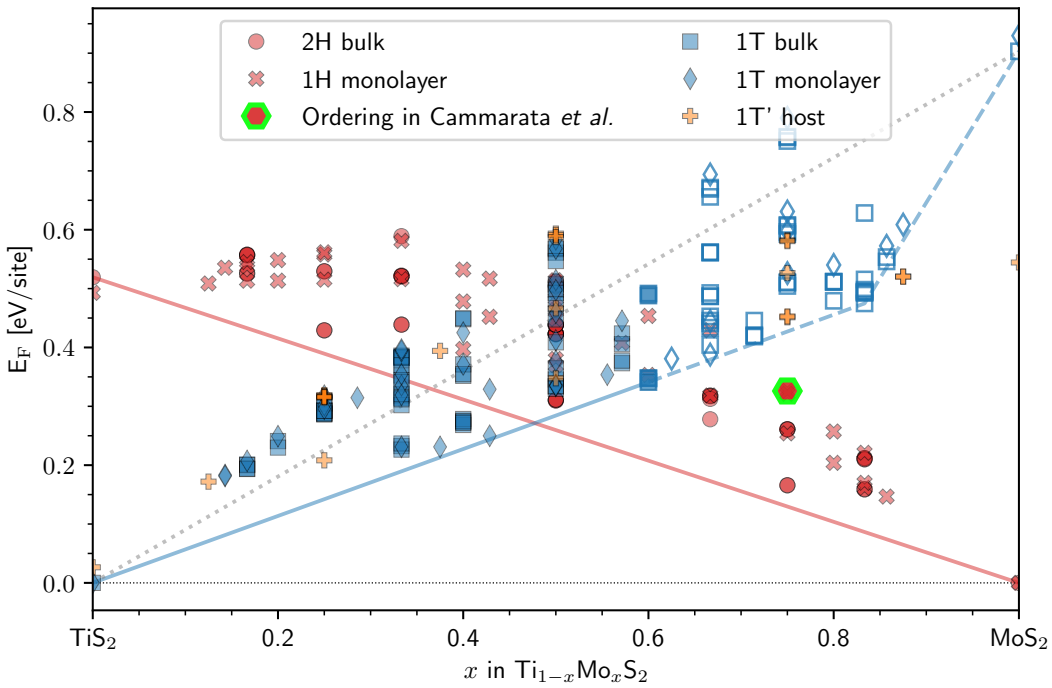

Figure 5.5: DFT-computed energies for the H host in bulk (red circles) and ML form (red crosses) and T host in bulk (blue squares) and ML (blue diamonds). Hollow symbols mark the 1T configuration at $x > 0.6$, where the CE model is not required to reproduce the right ground state. The dashed gray line connects the end-members formation energies of the T host. Red and blue solid lines show the convex hull within the H and T hosts, respectively. The black dotted line marks the zero-formation energy limit.

species yield an energy gain, at 0 K Mo and Ti ions within the 2H host are segregated into separate regions. Conversely, energy favourable orderings are found within the octahedral host. Several training set configurations lie below the ideal solid-solution line, as shown by blue marks below the gray dotted line in Fig. 5.5. In particular the CE iterative search identifies ground-state orderings at $x = 0.60$ ($Mo_{3/5}Ti_{2/5}S_2$) and at $x = 0.83$ ($Mo_{5/6}Ti_{1/6}S_2$). According to the convex hull in Fig. 5.5, the octahedral T host is favourable until $x \approx 0.5$, after which the prismatic H host becomes more stable. This concentration-dependant stability between the two hosts at 0 K and the large distortions occurring in the T host for $x > 0.6$ motivated the decision to constrain the selection of the 1T model: CE Hamiltonians are required to correctly reproduce the 1T ground-state only within the range $x \in [0, 0.6]$. This is in light of the fact that at higher concentrations the system will prefer the H host and the CE cannot reproduce large lattice distortions [136], as shown in section 4.3.3. Fig. 5.6 reports the distortion from the native geometry occurring upon relaxation as a function of concentration x. The host distortion is defined as the strain needed to transform the original cell into the relaxed one, apart from isotropic scaling and rotations. Values larger than 0.1 are usually considered too large for the CE formalism to be applied [136], as the mapping of the relaxed configuration to the perfect lattice breaks down.

The 1T' host observed in other TMD compounds, e.g. WTe_2, has been considered but is not relevant for the present system. The formation energy of several orderings within

this host is reported as orange crosses in Fig. 5.5 along with the convex hull of the 2H and 1T hosts. The formation energy within 1T' host is comparable with the results obtained within the 1T host. Within 1T' host, relaxed geometries in the Ti-rich portion of the composition axis revert to perfect-octahedral 1T coordination while Mo-rich configurations reach distorted geometries similar to the ones obtained within the 1T host (blue hollow symbols in Fig. 5.5). Thus, the phase behaviour of the system is unchanged, as the relaxed configuration from 1T' and 1T are equivalent in the range $x \in [0, 0.6]$ and the 2H host lies lower in energy for higher concentrations of Mo.

Since no part of either convex hulls lies below the zero-formation energy line of the composite-host system (black dotted line in Fig. 5.5), the system is deemed phase-separating at 0 K: the lowest-energy configuration at any concentration comprises two separate regions of 1T-TiS_2 and 2H-MoS_2. Only at finite temperature can entropic effects stabilise the presence of a mixed-concentration configuration within a single host.

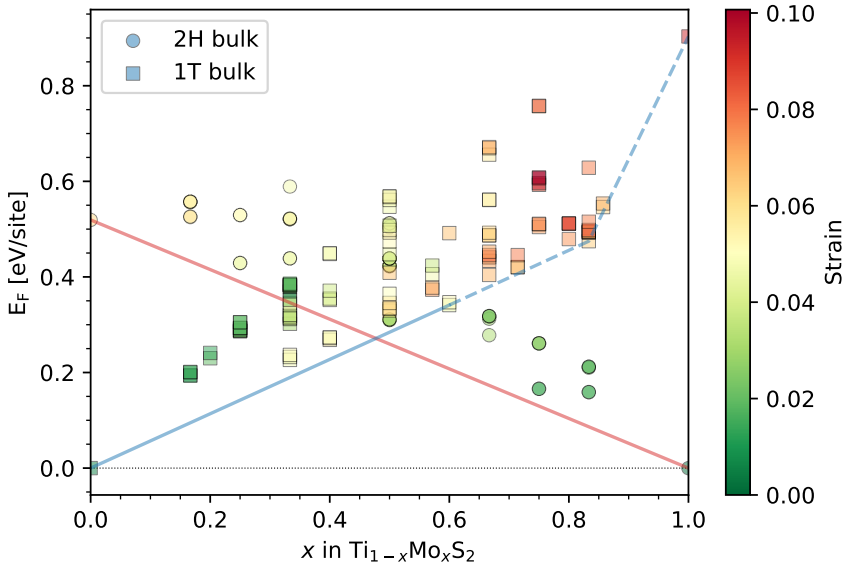

Figure 5.6: Distortion of all computed structure in 2H (circles) and 1T (squares) bulk systems. The y axis reports the formation energy per site versus the concentration x, like in Fig. 5.5. The colour of each point shows the distortion value, increasing from no distortion (green) to the maximum distortion observed (red).

5.2.3 Miscibility at High Temperature

The CE Hamiltonians for the 2H and 1T bulk system trained with the data-points in Fig. 5.5 was used to run finite-temperature MC simulations. Free-energy curves for each host are built from MC simulations, allowing the understanding of the stability of the system once temperature and configurational entropy are introduced. Since the MC simulations are carried out in a semi grand-canonical ensemble, only single phase regions of the phase diagram are directly explored by the simulations and two-phase equilibrium regions are inferred. Then the multi-host free-energy surface is obtained by a double

tangent construction: at fixed temperature, the free energy surface of each host is built with the two-tangent construction and the convex hull of the resulting two surface yields the total free energy $F(x, T)$.

The phase diagram of the system across 2H and 1T hosts is thus divided in phase separating and solid-solution regions. The colour scheme in Fig. 5.7 shows the value of the multi-host Helmholtz free-energy $F(x, T)$ as function of concentration x and temperature T. The T host shows solid-solution behaviour already at room temperature, while in the 2H system a phase-separation of Ti and Mo within the prismatic host dominates the diagram up to $T = 3000\,\mathrm{K}$ at $x = 0.5$. The solid black lines in Fig. 5.7 show the phase boundaries between multi-host phase separation (central region) and solid solution in a single host (left-most and right-most regions). In a realistic temperature range the system is completely phase separating, with configurational entropy stabilizing only small-percentage doping around the two end-members.

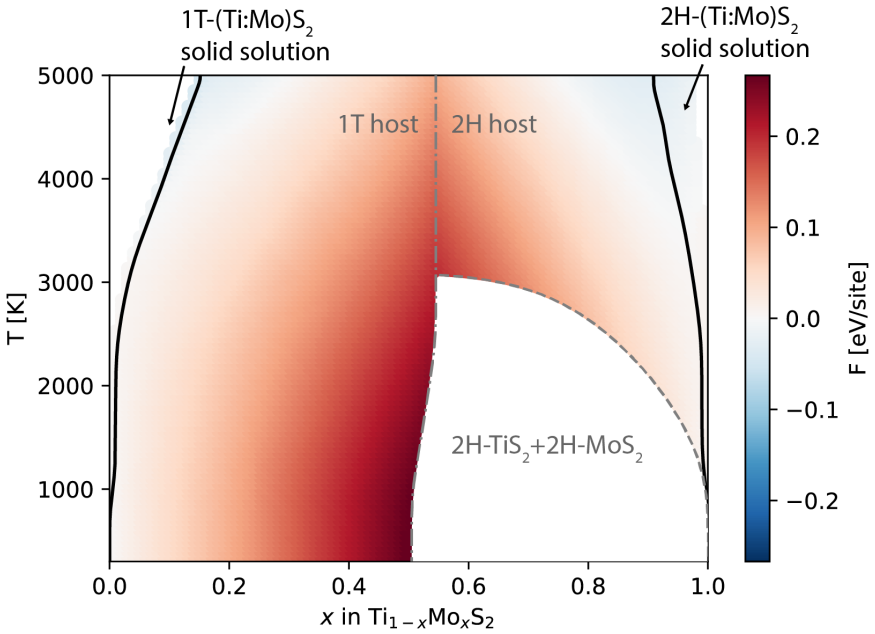

Figure 5.7: Phase diagram of the combined-host system showing temperature T versus equilibrium concentration x in MC simulations. The colours report the value of the free energy $F(x, T)$, linearly interpolated between the MC points. The solid black line highlights the phase boundary between solid solution in T and H hosts from phase separation into 2H-MoS_2 and 1T-TiS_2. The dash-dotted gray line indicates the separation between the 1T-host stability and 2H-host stability, as indicated by the gray labels. The white region between dash-dotted and dashed gray lines indicates a two-phase equilibrium within the 2H host not accessible by semi-grand canonical MC simulation.

5.3 Discussion

Stabilisation mechanism in octahedral host Even though it does not lead to overall-stable geometries, it is interesting to understand the origin of the stabilization mechanism leading to the ground state $Mo_{3/5}Ti_{2/5}S_2$ at $x = 0.6$ in the 1T host. Fig. 5.8a reports a top view of the starting geometry of this ground-state ordering. This configuration is

composed of three staggered rows of Mo and two rows of Ti. As shown by the displacement arrows in Fig. 5.8a, Ti cations retain their starting position, locally preserving octahedral CdI_2 prototype coordination, while Mo clusters distort the host, locally breaking the symmetry. This distortion around Mo ions can be understood qualitatively with the Kramer theorem [148] and the CF theory, outlined in section 2.4.2. The CF description has an intuitive physical interpretation, but only leads to a qualitative description of the present system: while the CF model assumes purely ionic bonds, the transition metal-chalcogenide bond shows a degree of covalency. According to CF theory, the degenerate five d orbitals of the isolated TM are split into two energy manifolds for CdI_2 octahedral coordination and into three manifolds for MoS_2 prismatic coordination, as reported on the left hand side of Fig. 5.8b.

Assigning Ti a formal valence of 4+, the trice-degenerate low energy t_{3g} states of the d^0 ions are empty. Hence, octahedral coordination is favoured as it provides the most efficient packing [34]. On the other hand, Mo^{4+} is a d^2 ion leading to partial occupation of the t_{2g} manifolds. According to the Kramer theorem, the system will lower its symmetry through Jahn-Teller (JT) distortion: this breaks the degeneracy of t_{2g} and lowers the total energy. The lattice is thus divided in non-JT-active sites, i.e. Ti rows, and JT-active sites, composed of the Mo triplets clustering together, as shown in Fig. 5.8a. The same mechanism cannot occur in the MoS_2 native prismatic coordination, as the d^0 configuration of Ti^{4+} ions and the low-energy CF level is non-degenerate and hence Kramer's theorem cannot be applied.

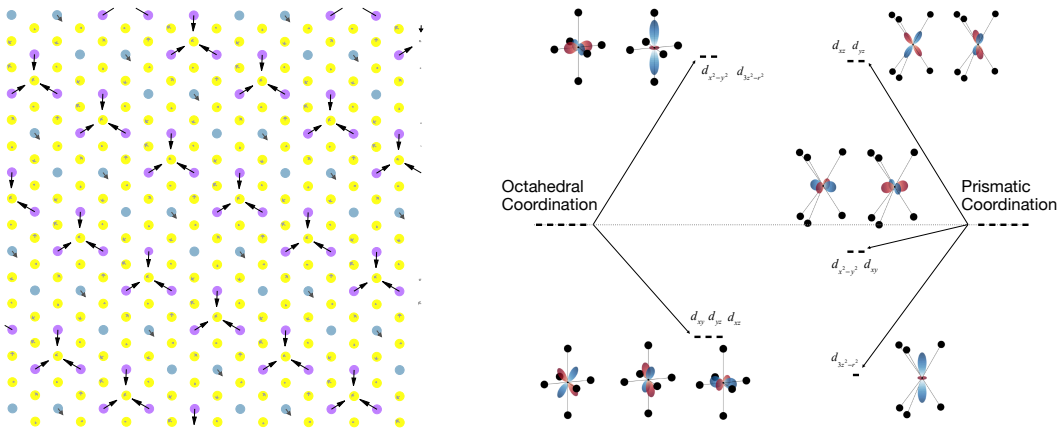

Figure 5.8: (a) Azimuthal view of the starting, perfect octahedral $Mo_{3/5}Ti_{2/5}S_2$ ordering at $x = 0.6$. Purple, blue and yellow circles represent Mo, Ti and S ions, respectively. The distortion stabilising the geometry is shown with arrows, whose length and shade are proportional to the magnitude of the displacement. (b) Sketch of the octahedral (left) and prismatic (right) energy levels in the CF splitting picture. Insets beside energy levels depict the corresponding hydrogen-like orbitals on the transition metal sites, surrounded by sulfur ions in the respective coordination.

Generalised principle for 2D TMDs design The dimensionality and vdW interactions do not affect the phase stability of the alloy system. As Fig. 5.5 reports, in both hosts, the convex hull of the bulk system and their ML counterpart present the same character.

This result validates the assumption in chapter 4: since the phase behaviour is unchanged from the bulk case, one could extrapolate from ML phase diagrams to the bulk.

Moreover, the electron-lattice stabilisation mechanism presented in section 5.3 could occur in other TMD-based compounds and must be taken into account when designing similar alloys. The JT-based distortion lowers the energy of the ground-state configurations at $x = 0.60$ in Fig. 5.5 by about 100 meV compared to the ideal solid-solution limit. Even though this energy gain is not enough to redefine the multi-host convex hull in the (Mo:Ti)S_2 system, it could lead to ground-state orderings in other similar alloys, if the formation energy of the end-members in both host is low enough or zero, when end-members share the same ground-state host [190].

Comparison with experimental data The phase diagram in Fig. 5.7 contains useful information from a synthesis point of view, allowing estimation of the maximum doping fraction at a given temperature. For example, at $T = 1200$ K the maximum fraction of substituted Ti should be around 1%. Considering that the melting point of pristine MoS_2 and Mo-Ti metallic alloys are reported to be around 1700 K and 2000 K [232], respectively, it should be in principle possible to observe such doped configurations experimentally by quenching the results of a high-temperature synthesis, in order to inhibit the phase segregation mechanism shown to occur at lower temperature. This prediction is consistent with the results by Hsu *et al.* [228], where energy dispersive X-ray analysis detected the presence of a small amount of Ti in 2H-MoS_2-based nanostructures obtained by mixing Mo-Ti powder and H_2S at 1200 K, while the inter-layer lattice constant measured from the High-Resolution Transmission Electron Microscopy and X-ray diffraction fails to show an expansion, which would be indicative of Ti ions intercalated between MoS_2 sheets.

5.4 Final Remarks

The (Ti:Mo)S_2 phase diagram originating from TM substitutions within the native hosts of the pristine compounds has been computed using the methods outlined in chapter 4 and section 2.2. The model predicts full phase separation in the system across hosts and the solubility limits inferred from our MC simulations are in agreement with high-temperature synthesis of Ti-doped 2H-MoS_2 reported by Hsu and coworkers [228].

The phase behaviour of the system is understood in terms of a general electron-lattice coupling mechanism that could apply to the other members of the TMD family and, if strong enough, lead to stable ordering in other binary compounds. Comparison between 3D bulk and 2D convex hulls reveals interlayer coupling and system dimensionality, at the origin of sought-after exotic electronic behaviour, are negligible in regard to phase stability of the binary alloys. This result should be valid for most 2D materials in which phase stability is governed by the similar in-plane electron-lattice effect, while more subtle behaviour could arise in presence of magnetic or Coulombic interactions [38, 233].

6

Digital Tribology

6.1 Superlubricity in Large-Mismatch Heterostructure

The concept of superlubricity was proposed by K. Shinjo and M. Hirano in the 1990s [18], which describes the phenomenon of vanishing friction between two contact surfaces (also known as structural lubricity later). Superlubricity has been widely found in van der Waals (vdW) materials, as their crystalline structures are kept together by weak vdW forces. However, superlubricity in two dimensional (2D) homostructures shows a strong twist-angle dependence [53, 177]. Layers prefer to rotate and lock in the commensurate state when sliding occurs, leading to the disappearance of superlubricity [234, 235]. The lattice mismatch between the two contact materials in VdW heterojunctions may reduce the commensuration problem. Micro-scale superlubricity has been uncovered in the graphene/hexagonal boron nitride (h-BN) heterostructure with a significant reduction of twist-angle dependence [29, 19, 236, 175]. However, the twist-angle dependence is still present in graphene/h-BN heterostructure, perhaps due to the small lattice mismatch. Therefore, it is crucial to explore the lattice mismatch influence on the superlubricity of 2D heterostructures. Furthermore, the effect of widespread domain edges on the superlubricity of the finite-size 2D interfaces is largely unexplored [175].

Two-dimensional heterojunctions with different lattice mismatches were characterized with Lateral Force Atomic Force Microscope (LF-AFM) and simulations. Experiments presented here show that the coefficient of friction of the large lattice mismatch heterojunction interfaces is below 1×10^{-6}, and twist-angle dependence is suppressed. Friction forces of these large-mismatch heterojunctions are dominated by pinned edges effects rather than resistance to interface sliding, e.g. from potential energy corrugation, while interface sliding

resistance dominates the friction process in sliding of small mismatch lattices. Classical MD simulations indicate that atoms near the edges of the flake play a distinctive role during the sliding dynamics, presenting enhanced structural distortions with respect to the rest of the flake.

Experiments reported in this chapter were performed by Prof. Guangyu Zhang group at Beijing National Laboratory for Condensed Matter Physics and Institute of Physics (Beijing, China) and the simulations were performed in collaboration with Prof. Tomas Polcar group at Czech Technical University in Prague (Prague, Czech Republic). The main contributions carried out in Southampton were the design of the MD simulation, the FF benchmark and the analysis of electronic effects at the edges.

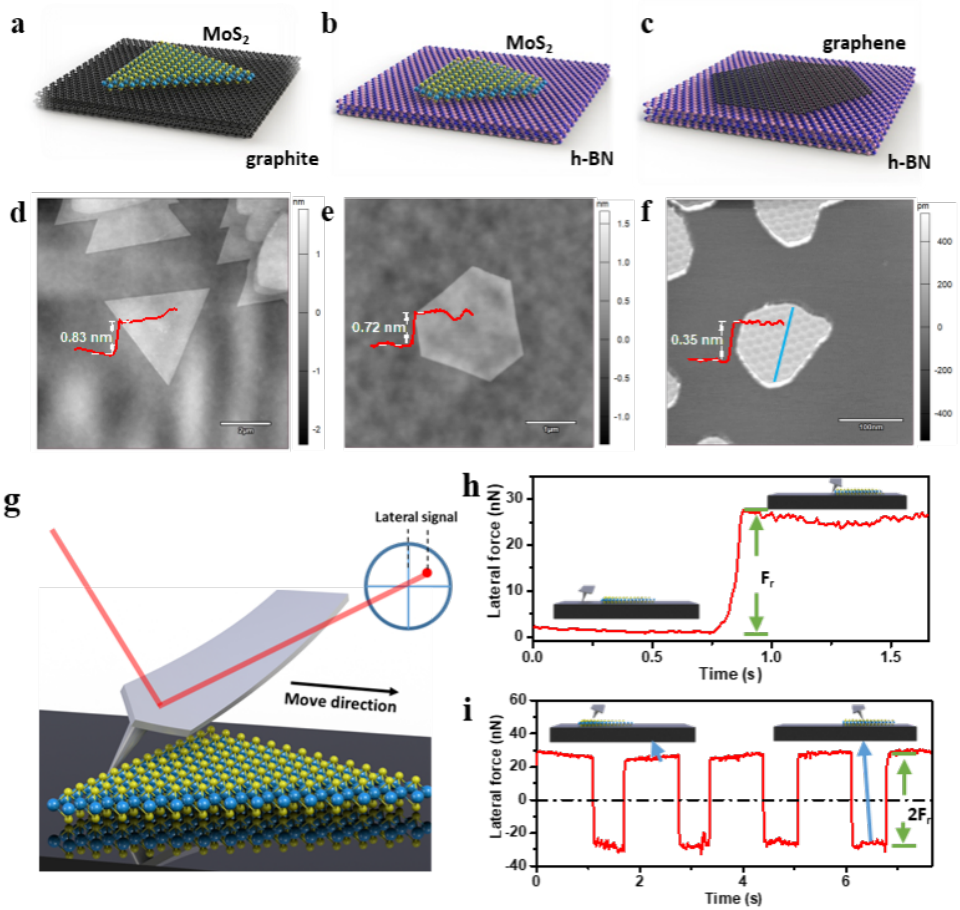

Figure 6.1: (a-c) Sketches of the heterostructures considered: MoS_2/graphite, MoS_2/h-BN, and graphene/h-BN, respectively. (d-f) AFM images of the corresponding heterostructures. (g) Working principle of the lateral-force AFM. Two manipulation techniques adopted and corresponding force signal: edge-pushing method (h) and top-dragging method.

6.1.1 Experimental Results

The VdW heterostructures experimentally investigated are: MoS_2/graphite, MoS_2/h-BN, and graphene/h-BN, with lattice mismatches of 26.8%, 24.6%, and 1.8%, respectively. Fig. 6.1a-c show the structures of these three heterostructures, prepared by a CVD epitaxial growth technique [25, 237] and characterised by AFM topography as shown in Fig. 6.1d–f.

In Fig. 6.1f a faint moiré superlattice of $\approx 16\,\mathrm{nm}$ can be seen, suggesting a 0° twist angle between G and h-BN. Electron diffraction images confirm the flakes and substrate lattices are aligned. AFM topography finds lattice parameters in line with the literature and confirm that the flakes in Fig. 6.1a-c are composed of a single layer while Raman and photo-luminescence demonstrate a high sample quality.

Friction force measurements were performed by AFM in dry N_2 atmosphere to reduce airborne contaminations. Fig. 6.1g shows a schematic of the measurement process. Manipulation techniques [236, 59] allow to slide atop epitaxial domains on the substrate by using an AFM tip and monitor the lateral force during the sliding simultaneously. Two approaches to slide on-top domains over substrates by using AFM tips are deployed. The first is illustrated in Fig. 6.1h, where the edge of the top domain is pushed laterally and the difference of lateral force before and after on-top domain sliding is detected. The second way is shown in Fig. 6.1i, where the domain is anchored to the tip end and dragged over the substrate. For MoS_2/graphite and MoS_2/h-BN heterostructures, the top domains could slide back and forth laterally by engaging the tip onto the centre of the domain, with a load from 0.4 to 5μN, since the adhesion and the friction force between the tip and MoS_2 is greater than that between MoS_2 and graphite (or h-BN).

Superlubric Behaviour

As outlined in section 1.2, the AC model prescribes that the dependence of the dynamic friction force F_r on the load L is expressed by

$$F_d = \mu_\mathrm{d} \cdot L, \tag{6.1}$$

where μ_d is the dynamic CoF. Combining the edge-pushing and top-dragging methods, the applied tip load L_tip can be varied from zero to a few μN (near zero tip load achieved by pushing the edge). The normal force experienced by the flake can be decomposed into two contributions

$$L = L_0 + L_\mathrm{tip}, \tag{6.2}$$

with L_0 being the adhesion between the flake and the substrate and L_tip the load applied to the tip. It follows that:

$$F_d = \mu_\mathrm{d} \cdot (L_0 + L_\mathrm{tip}) = \mu_\mathrm{d} \cdot L_0 + \mu_\mathrm{d} \cdot L_\mathrm{tip} = F_{\mathrm{r}0} + \mu_\mathrm{d} \cdot L_\mathrm{tip}. \tag{6.3}$$

As shown in Fig. 6.2a and b, under N_2, the friction forces of MoS_2/graphite and MoS_2/h-BN heterostructures are almost the same for different values of L_tip, which indicates constant F_{r_0} and ultra-low CoF. As shown in Fig. 6.2, the coefficient of friction of both MoS_2/graphite and MoS_2/h-BN heterostructure interfaces is well below 1×10^{-3}, which is considered the threshold for superlubricity [89]. To calculate the friction coefficient precisely from the slope in Fig. 6.2a and b, a much higher resolution and noise reduction of the AFM signal would be needed.

Nevertheless, an alternative approach can be used to estimate the CoF. The adhesive force between MoS_2 domains and graphite or h-BN represents the major contribution to the load L [238]. Thus, we can estimate the magnitude of the CoF, μ_{d}, by using:

$$\mu_{\mathrm{d}} = \frac{F_{\mathrm{r0}}}{L_0} \tag{6.4}$$

$$L_0 = G \cdot A \tag{6.5}$$

where $G = 1.130(14)$ GPa is the adhesive pressure between graphite and MoS_2 sheets [239] and A is the area of the domain. The area of the largest MoS_2 domain on graphite is $A = 15.00\,\mu\mathrm{m}^2$ and the friction force is $F_{r_0} = 44.15\,\mathrm{nN}$ giving the adhesive force $L_0 = 16.97\,\mathrm{mN}$ and the CoF of the MoS_2/graphite heterostructure interfaces as $\mu_{d\mathrm{MG}} = 2.60 \times 10^{-6}$. This value is almost two orders of magnitude smaller than those reported in previous studies [238, 240, 241]. For the MoS_2/h-BN heterostructure the CoF value is around $\mu_{d\mathrm{MG}} = 2.29 \times 10^{-6}$, similar to MoS_2/graphite.

To further explore the twist-angle dependence of superlubricity in large lattice mismatch heterostructures, anisotropy friction test are conducted on the MoS_2/graphite heterostructure. As shown in Fig. 6.2c, the measured friction forces from MoS_2/graphite heterostructures show no dependence from the twist angle can be detected within experimental resolution. This phenomenon is attributed to the fact that the in-plane interface friction force is almost zero even at 0° due to incommensurability, and the influence of the twist angle on the friction force has a negligible contribution to the total friction force.

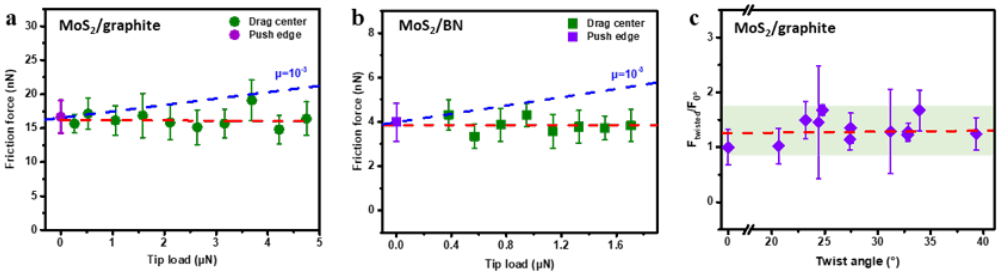

Figure 6.2: Superlubricity of MoS_2/graphite and MoS_2/h-BN heterostructure interfaces. (a) and (b) Friction force under N_2 gas environment as a function of the tip load of MoS_2/graphite and MoS_2/h-BN heterostructures. (c) The ratio of friction forces between twisted F_{Twisted} and aligned F_{0° MoS_2/graphite heterostructure. The red dashed lines are the fit. Error bars are standard deviation of data points.

Although the interface CoFs of MoS_2/graphite and MoS_2/h-BN heterostructure interfaces are small, there is still a constant friction force F_{r0} independent of load. Previous results pointed out that the friction force could be affected by many parameters, such as edges, interface steps, and contaminations [242, 243, 244]. The origin of this constant friction force is rationalised in terms of two descriptors, the shear strength S and the domain edge pinning strength E. Considering the finite size of the samples, S and E are

defined as follows:

$$S = F_d/A \tag{6.6}$$

$$E = F_d/P, \tag{6.7}$$

where A and P are the area and the perimeter of domains, respectively. Three situations are expected:

1. the in-plane interface sliding resistance predominantly contributes to the friction force and S is thus constant.

2. The in-plane interface friction is negligible and the edge pinning effect dominates the friction process and E is constant.

3. if both effects contribute significantly to the friction force, then both S and E cannot be constant.

Friction force of different samples are measured using various contact areas under a dry N_2 atmosphere. The results are consistent even though different tips were used, suggesting good consistency and repeatability of the calibration method. Fig. 6.3a shows a plot of the shear strength (S) of the MoS_2/graphite heterostructure as a function of domain area (A), clearly revealing a non-constant S. In contrast, when E vs. P is plotted, as shown in Fig. 6.3b, the edge pinning strength E is constant, with $E = 1.99(30)\,\mathrm{nN}/\mu\mathrm{m}$. These results indicate that the interface (in-plane) friction within MoS_2/graphite is negligible, and the edges of the MoS_2 domains are pinned to the surface of graphite. MoS_2/h-BN exhibits similar behaviour, as shown in Fig. 6.3c,d, where $E = 1.94(80)\,\mathrm{nN}/\mu\mathrm{m}$, close to that of MoS_2/graphite. Note that all edges of MoS_2 domains in our experiment have the same zig-zag direction. Thus, the E reported is actually the zig-zag edge pinning strength, as edges with different directions may have different edge pinning strength. As described above, the friction force of large lattice mismatch MoS_2/graphite and MoS_2/h-BN heterostructures mainly comes from the pinned edges. Therefore, the friction coefficient of infinite interfaces should be significantly lower than 1×10^{-6}.

The behaviour of the aligned graphene/h-BN heterostructure, which has a small lattice mismatch (1.8%), is different from the large-mismatch heterostructures. As shown in Fig. 6.3e,f, the shear strength of the graphene/h-BN heterostructure is constant and equal to $S = 2.20(39)\,\mathrm{MPa}$, suggesting that the in-plane interface friction is dominant. The dominance of in-plane friction in graphene/h-BN can be understood considering its near-commensurate nature at small twist angles. The period of moiré superlattice is larger than in the MoS_2-based heterostructures and, while the centre of mass moves smoothly, the dissipation arises from internal degrees of freedom of the flake [237, 245, 246, 19].

6.1.2 Electronic Structure of the MoS_2 Flake Edges

This section reports an analysis of the electron density at the MoS_2 edge sites. The study of non-periodic geometries, like edges, requires a careful balance between simulation cost

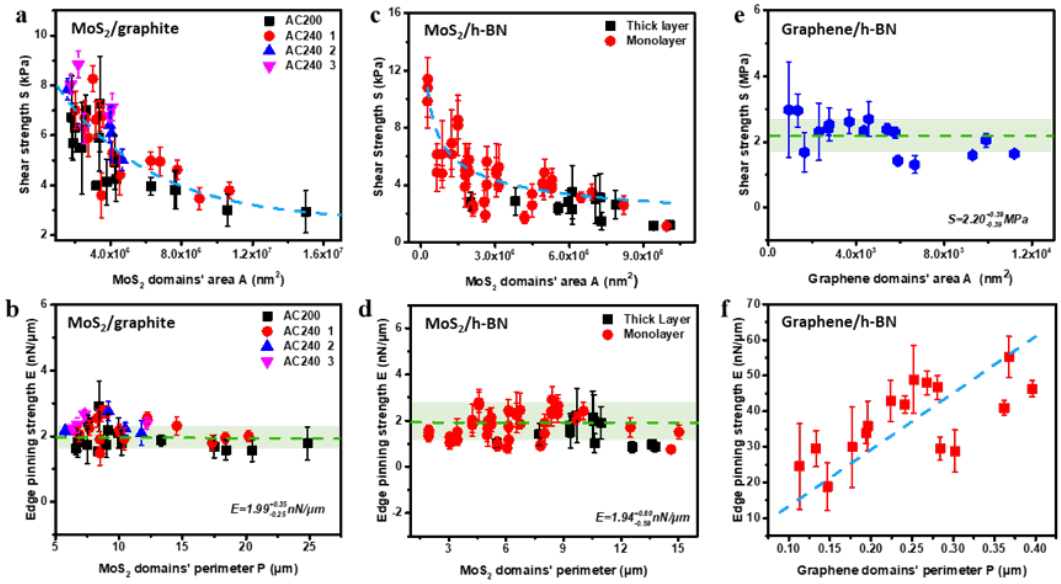

Figure 6.3: Source of friction for three different heterostructure interfaces. (a) and (b) are plots of friction characterization of MoS_2/graphite as a function of domain area A and perimeter P, respectively. (c) and (d) are similar plots for MoS_2/h-BN. (e) and (f) Friction characterization of graphene/h-BN as a function of A and P. Dash lines are the fits. Error bars are standard deviation of data points.

and geometries in DFT to ensure negligible self-interaction between periodic images is present. This balance is obtained here using the ribbon geometry reported in Fig. 6.4, where dashed a line shows the unit cell of the heterostructure system. The starting system is a bilayer system comprising of a 7x7 MoS_2 supercell epitaxially stacked on a 9x9 G supercell, for a total of 309 atoms. As explained in Appendix C, to apply periodic boundary conditions, the residual strain of 0.49% is applied to the MoS_2 layer. Removing three rows of MoS_2, S-terminated zig-zag are obtained, termed here ZZ-S1, top edge in Fig. 6.4, and ZZ-S2, bottom edge in Fig. 6.4. The edges are more than 8 Å apart, ensuring no chemical interaction between them. The zig-zag edges are the only ones observed in our CVD-synthesized samples. Moreover, analysis on MoS_2 2D flakes reported in Ref. [247] reports the lowest formation energy for ZZ-S1 and a slightly higher formation energy for ZZ-S2 edge, while armchair and Mo-terminated edges show higher formation energy. The geometry proposed here can be thought of as a portion of the side of the larger experimental or MD-simulated flakes, which exhibits only ZZ-S2 edges. No edge in the carbon plane was studied here as the flake slides above larger, high-quality G substrates. The electron density is obtained from DFT calculation using the parameters reported in Appendix D.

To investigate chemical interaction between the two subsystems, we compute the charge density along the $\boldsymbol{c}$ lattice vector, parallel z. The geometry along this direction is reported in Fig. 6.4a. The charge along the lattice direction is obtained by direct integration along the other lattice directions:

$$\rho_z(z) = \int_0^a \int_0^b \rho(x, y, z) \mathrm{d}x \mathrm{d}y. \tag{6.8}$$

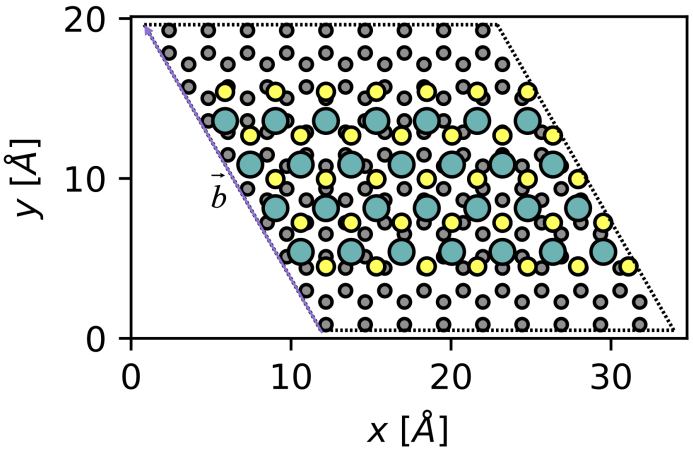

Figure 6.4: Top view of the MoS_2-stripe/G heterostructure. Carbon, molybdenum and sulfur atoms are reported in gray, cyan and yellow respectively.

Fig. 6.5b shows the electron distribution in the MoS_2 stripe (cyan thin line), G substrate (gray thin line) and heterostructure (black thick line). The vertical lines show position along z of each C (gray), Mo (cyan), and S (yellow) atom, respectively. Fig. 6.5c shows the difference between the distribution in the heterostructure and the subsystems, namely $\Delta\rho_z = \rho_z^{\text{het}} - (\rho_z^{\text{MoS}_2} + \rho_z^{\text{G}})$. Confirming our assumption that no strong chemical interaction occurs between the edges and G, the heterostructure electronic distribution in Fig. 6.5b is almost a perfect superposition of that of the isolated subsystems. No charge accumulation is seen in the interlayer space suggesting no covalent bonds are forming. The charge difference in Fig. 6.5c supports this observation, showing in-plane polarization in the G layer, with in-plane accumulation and depletion from the out-of-plane p_z manifolds. Charge also accumulates on the lower S atoms. The positive-defined profile in MoS_2 space in Fig. 6.5c indicates a level of charge transfer from G to MoS_2. To obtain a quantitative estimation of the electrons transferred per atom, the $\Delta\rho_z$ is integrated in the two hemispaces defined by the interface ζ (orange dash-dotted line in Fig. 6.5b,c):

$$\Delta\rho_z^{\text{MoS}_2} = \int_{\zeta}^{\infty} \Delta\rho_z \mathrm{d}z \tag{6.9}$$

and

$$\Delta\rho_z^{\text{G}} = \int_{-\infty}^{\zeta} \Delta\rho_z \mathrm{d}z. \tag{6.10}$$

This yields $\frac{\Delta\rho_z^{\text{MoS}_2}}{N_{\text{MoS}_2}} = 0.012\,\text{e}^-/\text{atom}$ and $\frac{\Delta\rho_z^{\text{G}}}{N_C} = -0.0071\,\text{e}^-/\text{atom}$. This minimal electronic transfer rules out the formation of covalent bonds between MoS_2 stripe and the G substrate. Instead, the slight charge transfer is ascribed to the necessary alignment of Fermi level between the two subsystems. Note that the interface height ζ is chosen to maximize the computed charge transfer between the upper (MoS_2) and lower (G) hemispaces.

To further characterize the electronic behaviour of the edges, Fig. 6.6a,c show the

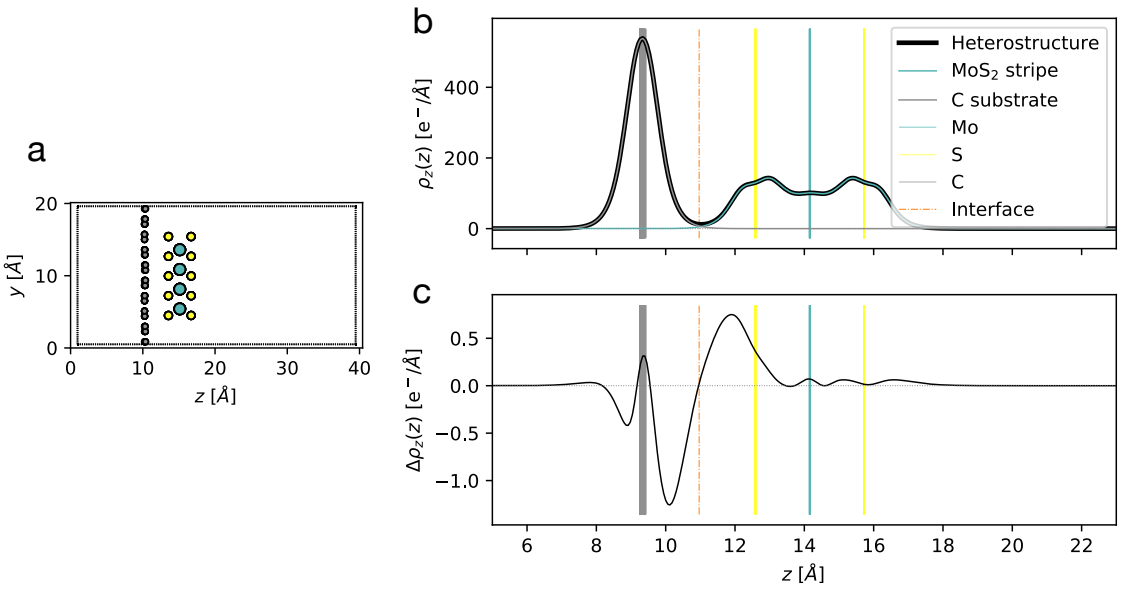

Figure 6.5: (a) Side view of the MoS_2-strip/G heterostructure. (b) Electronic distribution along z in heterostructure, MoS_2 stripe and G substrate, as reported in the legend. (c) Difference between the distributions reported in (b). The vertical lines mark atom positions, as reported in the legend. The orange dash-dotted line is the position of the ideal interface height ζ.

in-plane electron density of the heterostructure obtained by integration along z

$$\rho_\zeta^{\mathrm{C}}(x,y) = \int_{-\infty}^{\zeta} \rho(x,y,z)\mathrm{d}z \tag{6.11}$$

$$\rho_\zeta^{\mathrm{MoS_2}}(x,y) = \int_{\zeta}^{\infty} \rho(x,y,z)\mathrm{d}z. \tag{6.12}$$

As shown in Fig. 6.6a, charge outside the MoS_2 stripe vanishes, confirming that no spurious self-interaction or charge sloshing are present. Fig. 6.6b,d report the charge difference as defined above. The effect of the stacking on the G substrate is seen in Fig. 6.6b, as charge is depleted in correspondence of the MoS_2 stripe edges. The different nature of the two S-edges is reflected in the charge reconstruction promoted by the G substrate. As shown in Fig. 6.6b, charge depletion is stronger in the Mo atoms of the upper ZZ-S1 edge, while the lower ZZ-S2 edge presents a double-lobed reconstruction and less pronounced charge depletion on the metal ion.

The localized effect of the G on the MoS_2 edges is well summarized in Fig. 6.7, which shows the charge in Fig. 6.6 projected on the $\boldsymbol{b}$ axis, i.e integrated along x. Compared to the isolated MoS_2 stripe, a fractional charge is transferred to the terminating S atoms from the underlying C atoms, while the rest of the system is unaffected.

To sum up, the main effect occurring at the MoS_2 strip/G interface is a polarization of the G layer and bottom S atoms. The negligible charge transfer across the interface rules out any covalent bonding between the two subsystems and confirms the validity of the classical, non-reactive approach used in MD simulations.

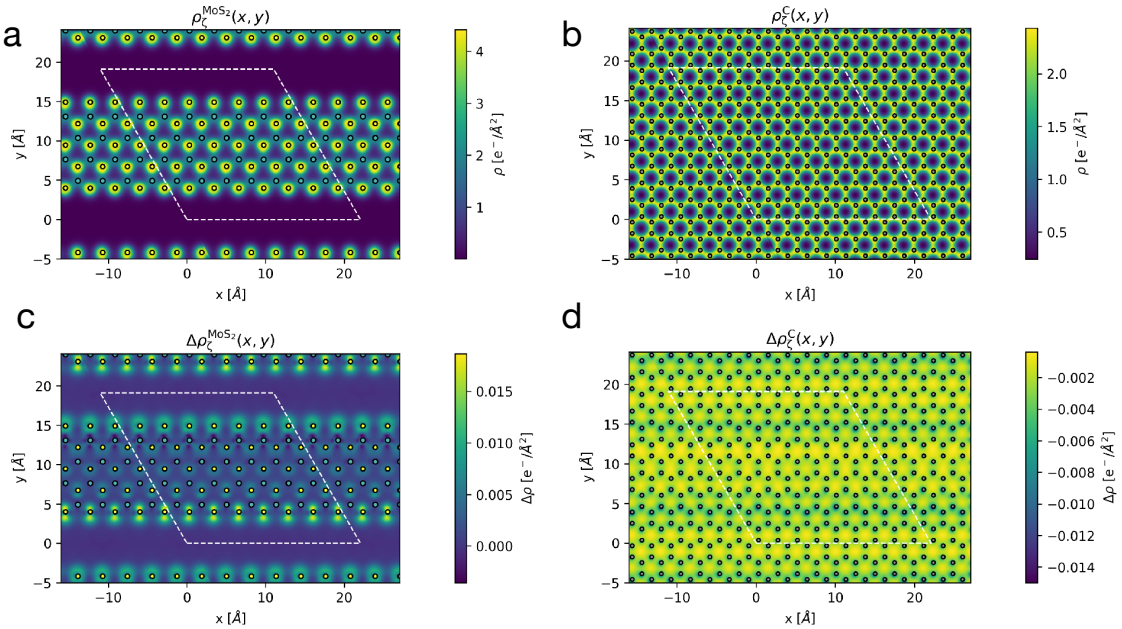

Figure 6.6: In-plane electronic distribution of (a) MoS_2 hemispace and (c) G hemispace. (c) and (d) report the difference of in-plane distribution between heterostructures and subsystems in respective hemispaces. White dashed lines show the unit cell of the heterostructure.

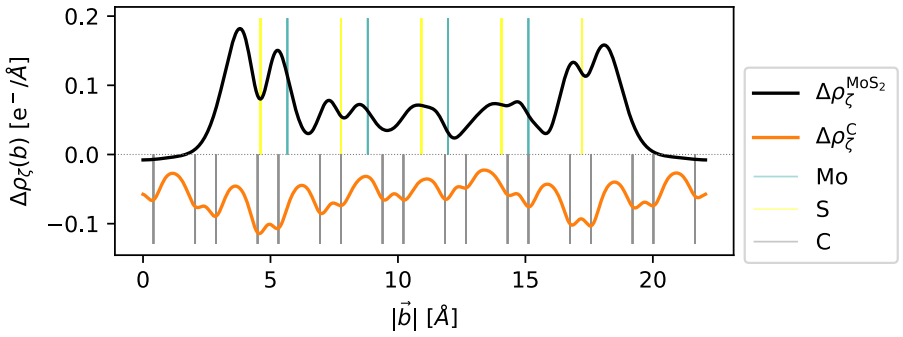

Figure 6.7: Electronic distribution difference along the ***b*** lattice direction, shown as purple arrow in Fig. 6.4. Vertical lines mark the position of atoms, according to the legend, along ***b***.

6.1.3 Sliding Barrier Force Field Benchmark

The benchmark in the previous section justifies the use of non-reactive FF and the simulations are expected to correctly reproduce the trends found in experiments. As reported in Appendix D, the intralayer interactions are described by means of Stillinger-Weber [171] and AIREBO [172] potentials for MoS_2 and graphene, respectively. The interlayer interactions are modeled via a Lennard-Jones potential, parameterised in Appendix D against DFT data. In order to test the performance of classical FF to describe sliding events in the heterostructures, MD-computed PES are compared with DFT-level data. Since the computational cost of computing PES at DFT level in large heterostructures is prohibitive, a commensurate supercell comprising 4x4 MoS_2 unit cells over 5x5 G unit cells is used. The residual strain of 2.6% resulting from lattice mismatch is applied to MoS_2. In computing the PES, the G substrate is constrained in xyz and the top S layer in xy. This protocol

prevents the system from relaxing back to minima geometries while allowing relaxation along z, mimicking the constant load experimental setup.

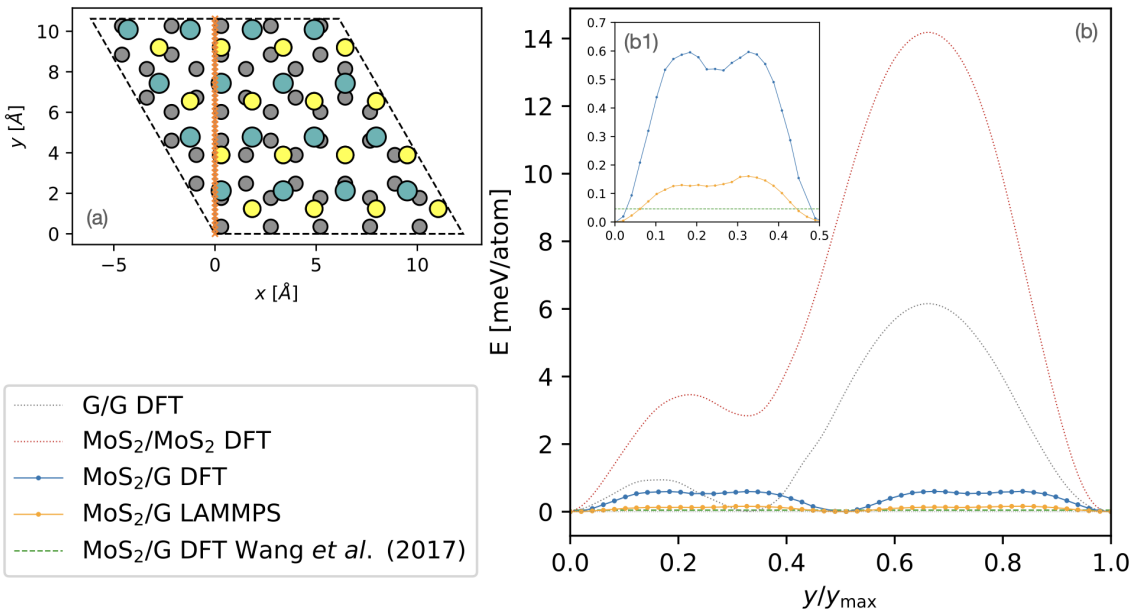

Figure 6.8: (a) Top view of the MoS_2/G heterostructure (same colouring as in Fig. 6.4). The orange crosses represent the points considered in the heterostructure PES calculations. (b) PE as a function of the dimensionless displacement $y/y_{\max}$. (b1) Magnification of the plot in (b).

The PES is sampled over 50 points along the path following the y direction in the geometry shown in Fig. 6.8a by orange crosses. The resulting PES from DFT and MD are shown in Fig. 6.8b, as blue and orange lines, respectively. For comparison, the plot reports DFT-computed PES for MoS_2/MoS_2 and G/G contacts, as red and gray dotted curves, respectively. The inset is a zoom on the energy scale showing the heterostructure PES in the first half of the path. Sliding barriers in the heterostructures are in the order of fraction of meV/atom, one order of magnitude lower than in homo contacts. The DFT-MD comparison reported in the inset in Fig. 6.8b1 shows that the "double-humped" shape of the PES is correctly reproduced by the LJ FF, but the DFT barrier is underestimated by a factor of $\frac{\Delta E_{DFT}}{\Delta E_{LJ}} = 3.7$.

Interestingly, this agreement is far better than what is reported in the literature for LJ-based FF: Fig. 6.9a from Ref. [93] reports for G/G contact an underestimation of $\frac{\Delta E_{DFT}}{\Delta E_{LJ}} = 10$ and Fig. 6.9b in Ref. [94] shows that the shapes of the PES in MoS_2/MoS_2 contact is not reproduced correctly even qualitatively. The good performance of LJ interlayer coupling here is not a coincidence: interlayer interactions are substantially different in this heterostructure system compared to pristine compounds. As shown in Fig. 6.10 in Ref. [93], in bilayer graphene charge is accumulated in the interface region, compared to isolated G layers. Thus, p_z orbitals of C atoms are more populated. The repulsion between these orbitals is the fundamental idea underpinning the anisotropic term in Kolmogorov-Crespi (KC) interlayer potentials and the failure of LJ ones in this system. As shown in Fig. 6.5 in the previous section, the main effect of the interaction between

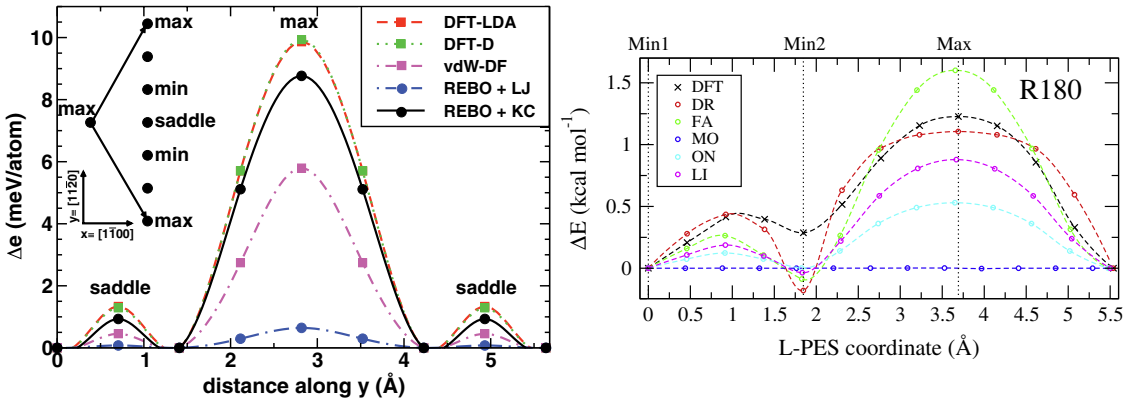

(a) **(b)**

Figure 6.9: Lateral potential energy surfaces obtained translating a graphene (a) or MoS_2 (b) layer above a fixed one along the long diagonal of the hexagonal unit cell. In each figure diffent curves refer to different models, as reported in the legends. In (b), the relevant comparison is between DFT curve (black crosses) and LI curve (pink circles). Adapted from Ref. [93] (a) and from Ref. [94] (b).

MoS_2 and G on electronic density is to move charge from the interlayer region into the C plane. Thus, p_z orbitals are depopulated and the anisotropic contribution motivating KC is weakened. Moreover, exact quantitative agreement between DFT and classical FF cannot be expected as the energy scale observed here is at the accuracy limit of ab initio methods as well. The green dashed line in Fig. 6.8b shows the sliding barrier reported in Ref. [248], based on a DFT protocol similar to the one deployed here. The nominal value the authors report is 0.046 meV/atom, putting the FF PES between the two DFT results. To sum up, a level of discrepancy between experiments and MD simulations is expected, but this should be limited to a scaling factor, while qualitative trends should be reproduced truthfully.

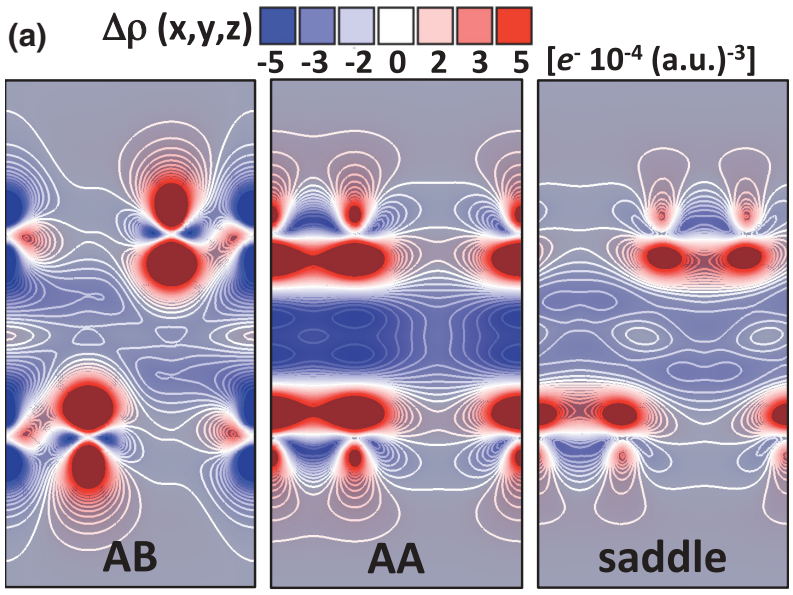

Figure 6.10: Charge difference between BLG and isolated G layers. Adapted from Ref. [93].

6.1.4 Simulation of Edge Pinning Effect

The origin of the edge pinning effect in the MoS_2/G heterostructure is unveiled by performing a set of MD simulations. The computational setup is illustrated in Fig. 6.11a and b. Triangular MoS_2 flakes are considered, with side lengths ranging from 2 to 20 nm. The adhesive pressure between MoS_2 and graphite is $G = 1.20$ GPa, which is in good agreement with both experiment and *ab-initio* calculations [239]. All systems have been equilibrated at room temperature, after which non-equilibrium simulations have been performed by applying a constant speed protocol and calculating the lateral force acting on the flake.

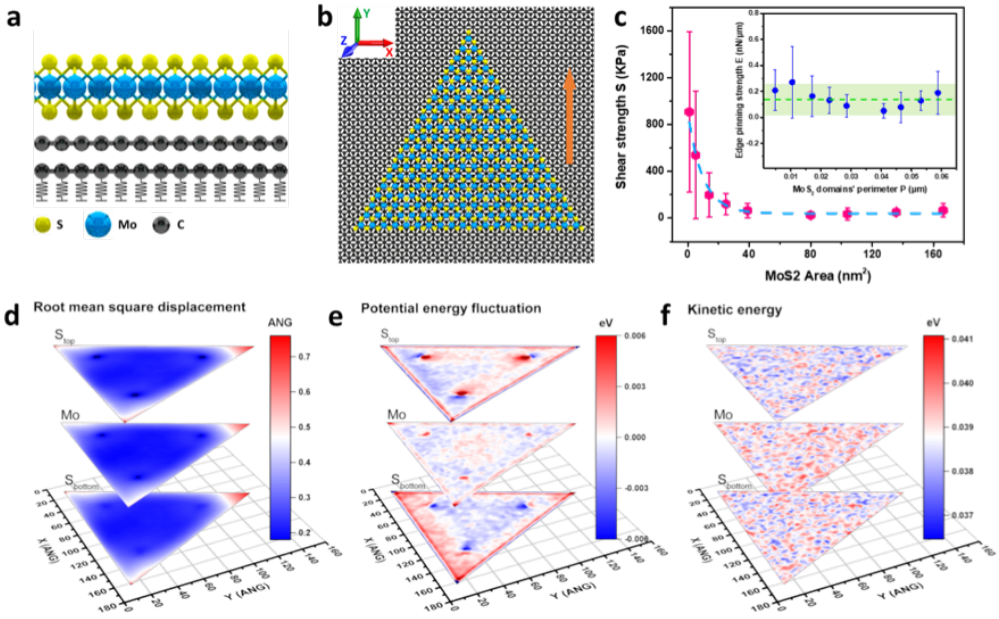

Figure 6.11: MD simulation results of a MoS_2 flake sliding on graphite. (a) and (b) Side and top views of the MD computational setup, respectively. (c) Calculated shear strength as a function of MoS_2 flake area; the inset shows the calculated edge pinning strength as a function of MoS_2 flakes' perimeter. Dash lines are the fits. Error bars are standard deviation of data points. (d) Root mean square displacement maps of different atomic layers in the MoS_2 flake calculated with respect to the optimized geometry for a typical trajectory (flake size ≈ 16 nm). (e) and (f) Per-atom average potential energy fluctuation and kinetic energy maps of different atomic layers in the MoS_2 flake, respectively. For the potential energy, values are reported as the difference with respect to the optimized system.

Fig. 6.11 summarizes the simulation results. The shear strength (S) and the edge pinning strength (E) are reported as a function of MoS_2 domain area (A) and perimeter (P), respectively. As shown in Fig. 6.11c, S presents a decreasing profile as a function of A, while E is almost constant, resembling the experimental results in Fig. 6.3. We also calculate the shear strength of an infinite heterostructure, $S_{\text{infinite}} = 4.95$ kPa, which is at least one order of magnitude smaller than that of our finite heterostructures. Despite this scaling, the trends are consistent with the experimental observations.

To get a more in-depth insight into the underlying mechanisms, Fig. 6.11d reports the map of the atomic root mean square displacement with respect to the equilibrium positions for different atomic layers of MoS_2, and averaged over the MD trajectory. The

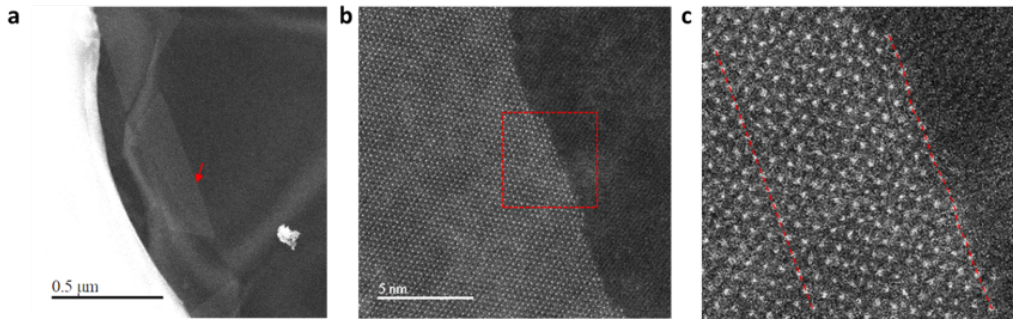

Figure 6.12: Scanning Transmission Electron Microscopy (STEM) image of MoS_2 domain edge at various zoom levels. Red dash line in c outlines the arrangement of molybdenum atoms in the body and at the edge, highlighting the distortion of the latter.

mean displacement of edge atoms is significantly larger than for centre atoms. Potential energy maps of different atom types within the MoS_2 layer (Fig. 6.11e) show that the edge S atoms have a higher potential energy than S centre atoms. For the kinetic energy maps in Fig. 6.11f, there is no apparent difference between edge atoms and centre atoms. The MD simulations indicate that, during sliding, the edge atoms are more "active" and present more energetic distortions, absorbing and dissipating more energy than the centre atoms, providing the greatest contribution to the friction force. Indeed, in Fig. 6.12, high-resolution transmission electron microscopy analysis shows more pronounced lattice distortions at the edges, which supports the simulation results.

This behaviour is rationalised in terms of a different scaling of the properties between the two system. While in the near-commensurate system friction arises from surface effect, i.e. magnitude of dissipation scales with the area of the flakes, in the large-mismatch system frictional events occur at localised regions on the edges of the flakes, i.e. friction is determined by pinning at the edges sites. The generality of the result is confirmed by the experimental observation of the same behaviour for MoS_2/hBN heterostructures.

6.1.5 Final Remarks

In conclusion, large lattice mismatch MoS_2/graphite and MoS_2/h-BN heterojunction interfaces provide ultra-low coefficients of friction, $\approx 1 \times 10^{-6}$, without any twist angle dependence. Both experiments and molecular dynamics calculations indicated that pinned edges dominate the friction process, whereas in small lattice mismatch, e.g. graphene/h-BN, a significant contribution to the interface friction arises from surface-wise effects. These results show that the large lattice mismatch of two contact surfaces is a promising route to designing a near-frictionless sliding pair.

6.2 Multi-scale Prandtl-Tomlinson Model

Friction results in significant energy losses and system failures in a wide range of technologies [70]. The design of optimised surfaces for friction in a systematic way relies on a predictive model of friction, scalable from the nano-scale up to micro/macro-scales.

Challenges for a complete description of friction include non-linearity, the complexity of the many processes, and the different scales involved [81]. Attempts to model microscopic friction include *First principle* calculations, Molecular Dynamics, and low-order models. *First principle* calculations and Molecular dynamics modelling are highly accurate, but limited to time and length scales smaller than those in experiments of friction. On the other hand, low-order models, such as the PT model [96, 106, 102, 249], approximate atomistic interactions by simple potential energy surfaces, thus allowing to access time and length scales in the nano-scale that match those of experiments using Lateral-Force Atomic Force Microscope (LF-AFM), at the cost of losing quantitative correlation with real materials. Such low order models are able to describe the stick-slip behaviour of nano-scale friction, and capture the velocity, load, and temperature dependencies observed in experiments [250, 251, 102, 252, 253], which are not included in the standard Coulomb model [83, 84].

The multi-scale model of nano-scale friction presented comprises of a modified PT model and electronic structure calculations, linked via a controlled set of approximations to achieve a more realistic description of friction between a single asperity-tip and a substrate, as measured in LF-AFM. This novel approach addresses the qualitative nature of the standard PT-based approaches found in literature [90, 91]. Atomic scale contacts in these models are approximated with an analytical function resembling the symmetry of the crystal under study. DFT is used to model the energy of interaction between a coated tip and a substrate of the same material, e.g. MoS_2 on MoS_2. The computed energy surface is used as a parameter in the two-dimensional PT model of friction. The frictional behaviour arising from their respective electronic structure is compared between a set of different crystals. In addition, the framework of stochastic thermodynamics [109, 254, 77] allows insights to be gained in the non-equilibrium thermodynamics during friction for the different crystals and for different sliding directions.

The Prandtl-Tomlinson Model

The PT model of friction describes a point-like object, the AFM tip, connected by a spring to a much larger slider moving at a constant speed in one direction, the AFM cantilever, on a static substrate, the atomic corrugation of the substrate. The model is defined by the general potential energy:

$$U(\boldsymbol{r}, t) = U_{\mathrm{s}}(\boldsymbol{r}) + \frac{C}{2}(\boldsymbol{r} - \boldsymbol{v}t)^2 \tag{6.13}$$

where the variable $\boldsymbol{r}$ is the position of the tip, U_{s} the static potential generated by the substrate, C the elasticity constant of the spring, $\boldsymbol{v}$ the velocity of the slider, and $\boldsymbol{v}t$ the position of the slider. The potential $U_{\mathrm{s}}(\boldsymbol{r})$ produced by the interaction of specific substrate material and the coated tip is modelled at DFT level as described in section 6.2.1.

To better grasp the physics behind this model, consider, as an example, the following

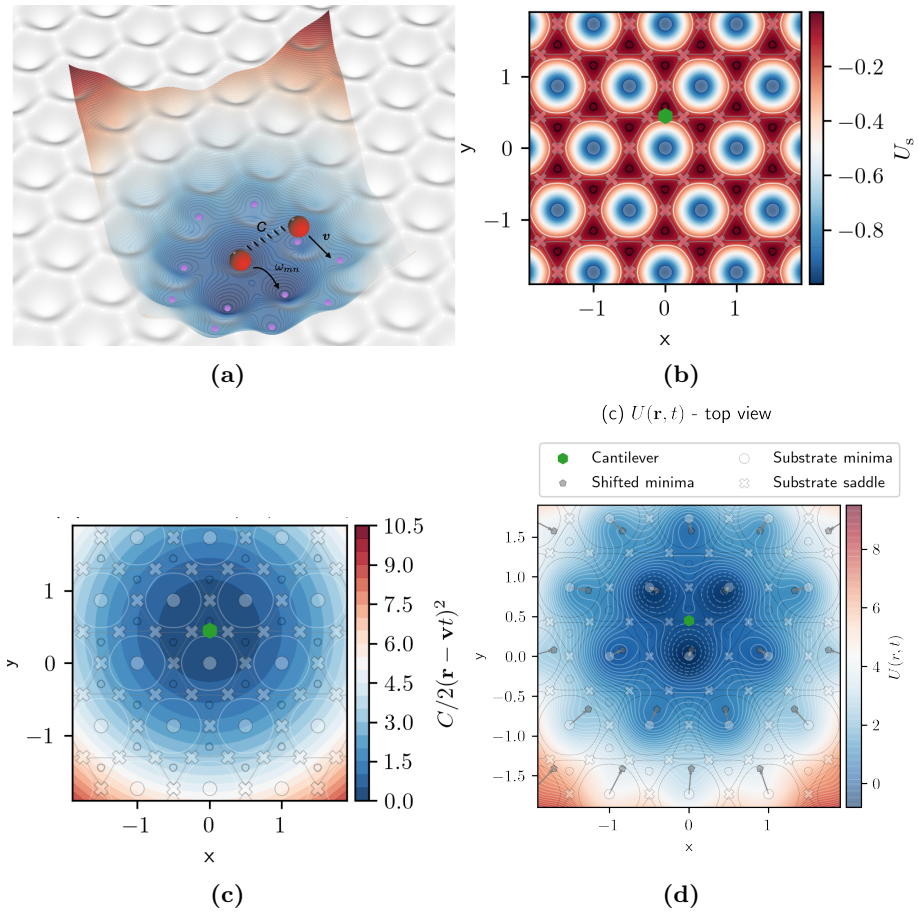

Figure 6.13: (a) Cartoon of the PT model. The total energy U in Eq. (6.13) is shown in red and blue, with $C = 1$, and substrate potential described in Eq. (6.14) is shown in black and white, with $l = 1$ and $U_0 = 1$ and The position of the cantilever (higher red sphere) is $\boldsymbol{v}t_0 = (0,\ 1/2)$. The tip, lower red sphere, sits at the global minimum and local minima by pink circles. (b) Substrate potential in Eq. (6.14) with $l = 1$. Three isolines are shown: within the minimum well $U_s = -2/9$ (white)), around the maxima $U_s = -1/90$ (black) and along the saddle energy $U_s = -1/9$ (gray). Crosses mark the saddle points, as in Eq. (6.16), and circles mark the substrate minima, as in Eq. (6.15) (c) Cantilever elastic energy with $C = 1$ overlaid over substrate isolines defined in (a). (d) Total energy in Eq. (6.13). Gray hexagons show the shift at the linear order of the substrate minima, as in Eq. (6.17). (d) Three-dimensional representation of the surface energy in (b). BW surface shows the substrate potential in Eq. (6.14). The global minimum is marked by an orange circle and local minima by purple circles. The green hexagon marks the slider position $\boldsymbol{v}t_0 = (0,\ 1/2)$.

analytical form for the substrate U_s [255]

$$U_s(\mathbf{r}) = -\frac{1}{9}\left[3 + \ 4\cos\left(\frac{2\pi}{\sqrt{3}l}r_y\right)\cos\left(\frac{2\pi}{l}r_x\right) \ + 2\cos\left(\frac{4\pi}{\sqrt{3}l}r_y\right)\right]. \tag{6.14}$$

Since $U_s(\mathbf{r}) \in [0, 1]$, the spring constant C defines the energy scale of the system. The energy landscape comprises of minima, arranged in a triangular lattice, each surrounded by six maxima, similar to the graphene on graphene potential surface [91]. The minima lie on the Bravais lattice $\boldsymbol{G} = n_1\mathbf{A}_1 + n_2\mathbf{A}_2$ generated by the vectors

$$\mathbf{a}_1 = l\begin{pmatrix} 1 & 0 \end{pmatrix} \qquad \mathbf{a}_2 = l\begin{pmatrix} -\frac{1}{2} & \frac{\sqrt{3}}{2} \end{pmatrix}. \tag{6.15}$$

In terms of the lattice in Eq. (6.15), saddle points of U_s are located at

$$\mathbf{s}_1 = \frac{\mathbf{a}_1}{2} \qquad \mathbf{s}_2 = \frac{\mathbf{a}_2}{2} \qquad \mathbf{s}_3 = \frac{\mathbf{a}_1 + \mathbf{a}_2}{2}, \tag{6.16}$$

which forms the honeycomb lattice marked by gray crosses in Fig. 6.13. This potential depends explicitly on time, and the position and depth of minima and saddle points evolve as the slider translates in space, as shown by the synthetic snapshot reported in Fig. 6.14.

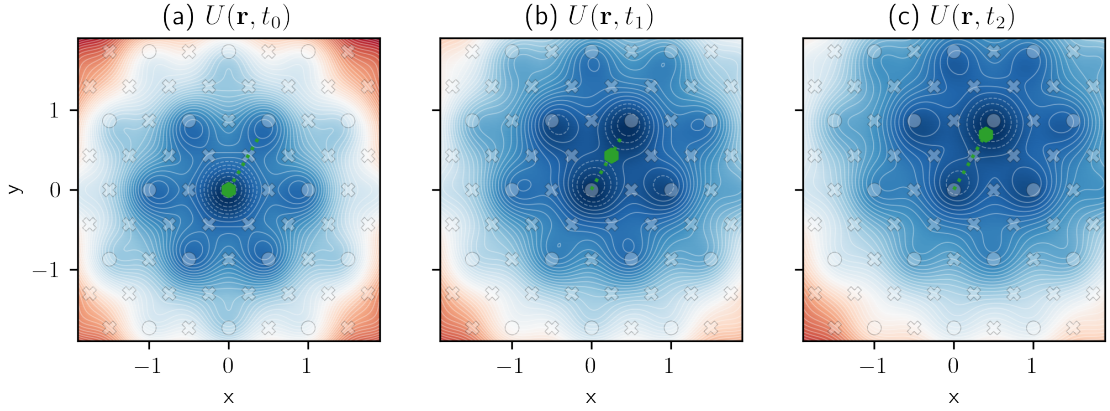

Figure 6.14: Time evolution of the total potential in Eq. (6.13).

The effect of the cantilever parabolic potential in Eq. (6.13) in the main text on the substrate, can be qualitatively understood by linearising the problem around the substrate minima, which form a Bravais lattice $\mathbf{A} = \mathbf{a}_1 n + \mathbf{a}_2$, where $\mathbf{a}_i$ are the vectors in Eq. (6.15). In the limit of small displacement $\mathbf{u}$, the total energy can be approximated to the linear order as

$$U(\mathbf{A} + \mathbf{u}, t) = U_\mathrm{s}(\mathbf{u}) + \frac{C}{2}(\mathbf{A} + \mathbf{u} - \mathbf{v}t)^2 \tag{6.17}$$

$$\approx \left(\frac{C}{2} + \left(\frac{2\pi}{l}\right)^2\right) u^2 - 2\frac{C}{2} u\gamma \cos(\theta_{u\gamma}) + \frac{C}{2}\gamma^2 - 1, \tag{6.18}$$

where trigonometric functions in Eq. (6.14) were expanded to the lowest order and $U_\mathrm{s}(\mathbf{A} + \mathbf{u}) = U_\mathrm{s}(\mathbf{u})$ is implied by symmetry. The vector $\boldsymbol{\gamma} = \mathbf{v}t - \mathbf{A}$ points from the lattice point $\mathbf{A}$ to the position of the cantilever $\mathbf{v}t$. Thus, the minimum always lies in the direction γ connecting the lattice point $\mathbf{A}$ with $\mathbf{v}t$, as shown by the arrows in Fig. 6.13c. The minimum is shifted along this direction of the quantity

$$u_\mathrm{min} = \frac{\frac{C}{2}\gamma}{\frac{C}{2} + \left(\frac{2\pi}{l}\right)^2}. \tag{6.19}$$

In the limit of soft spring $\frac{C}{2} \ll 1$, $u_\mathrm{min} \approx \frac{\gamma l^2}{(2\pi)^2}\frac{C}{2} \to 0$, i.e.the minimum is located at the substrate lattice point. In the limit of a hard spring $\frac{C}{2} \gg 1$, the position of the minima is given by $u_\mathrm{min} \approx \gamma(1 - \frac{8\pi^2}{Cl^2})$, i.e. the minimum is almost at the cantilever position.

Minimisation of the energy in Eq. (6.13) yields the stable states m of the system,

accommodating the tip in the absence of external driving forces and thermal fluctuations, but also in the presence of external driving forces in the over-damped limit. The over-damped limit refers to the case of fast dissipation of the kinetic energy of tip compared to the sliding velocity such that the tip is found, in practice, always in a minima of the energy. The energy at a minimum is $E_m = U(\boldsymbol{r}_m, t)$, where $\boldsymbol{r}_m = \boldsymbol{r}_m(t)$ is the position of the minimum.

The position, energy, as well as the number of states, are time-dependent quantities, due to the relative motion of the tip. In the over-damped limit, the tip follows a stick-slip motion, if the energy has more than one minimum [250, 256, 102]. The stick-slip movement of the tip consists of a periodic alternation of the tip sitting on a minimum of the energy for a relatively long time time (stick) and a consecutive fast movement to a new position (slip). At finite temperature, slips to a new state can also occur due to thermal activation, which is modelled here by using transition state theory as described in section 6.2.2. In this framework, the over-damped dynamics of frictional processes is viewed as a Markovian random hopping process over energy barriers separating the different states m promoted by thermal fluctuations [249].

6.2.1 Atomistic Contact Model

First principles calculations. At the DFT level, the atomic scale corrugation is modelled as two flat crystalline surfaces sliding adiabatically. Thus, the PES is obtained from a set of translated geometries as explained in detail in section 2.4.3. Each grid point is obtained from a DFT calculation of a bilayer system of the given crystal, e.g. MoS_2 on MoS_2, where the top layer has been translated by a vector $\mathbf{x}$ with respect to the bottom layer. The geometry is relaxed keeping the bottom layer fixed in xyz and letting the top layer relax in z only, to avoid it sliding back to the minimum position. From a thermodynamic point of view, allowing relaxation along z corresponds to the sliding interface at constant zero pressure.

First principles calculations were carried out using DFT as implemented in VASP [198, 199] within the PAW framework [124]. The exchange-correlation potential is approximated using the PBE functional [127] and the vdW dispersion is described by DFT-TS method, a local-geometry-corrected empirical model developed by Tkatchenko and Scheffler [257]. A plane wave cut-off of 650 eV is adopted and the Brillouin zone was sampled using a $17 \times 17 \times 1$ mesh.

Finite tip model. The PT model describes a finite-size tip sliding, while the PES from DFT represents the sliding interface between infinite planes. Thus, the next step to construct the multi-scale model is to estimate the contact area between the tip and substrate. Mimicking experimental protocols [258], the system is a spherical tip, coated with a thin crystalline layer, in contact with a thin layer of the same crystalline material, deposited over a substrate. Usually both tip and substrate are silica in experiments [259].

Atomic-scale sliding interface and tip deformation determining the contact area are assumed to be decoupled. The sliding interface arises from short-range interaction and,

thus, is determined by properties of the 2D layers in contact [93, 91, 260]. On the other hand, the contact area is determined by the deformation of the large tip and the substrate and is usually modelled by continuum mechanics, which explicitly disregards the discrete nature of nanoscale contacts [260]. An accurate description of the contact area in nanoscale tribology remains subject of current debate [85, 261]. Here the Hertz model is used to estimate the contact area. For fixed load, the contact area represents a scaling factor of the DFT-computed PES and is independent of the coating ML crystal. Its value cannot change the relative amplitude and geometry of corrugation between different materials. Thus, while the Hertz model may not describe the contact area exactly, with deviation of up to 20% [260, 86], it is suitable for the phenomena studied here.

In the Hertz model, the radius a of the contact area is expressed in terms of the applied load L and mechanical properties of the tip [262] by

$$a = \left(\frac{3LR}{4E^*}\right)^{1/3}, \tag{6.20}$$

where R is the curvature radius of the tip and the effective elastic modulus is given by

$$\frac{1}{E^*} = \frac{1-\nu_1^2}{E_1} + \frac{1-\nu_2^2}{E_2},$$

The quantities E_1, E_2 are the elastic moduli and ν_1, ν_2 the Poisson's ratios associated with each body. The quantities appearing in Eq. (6.20) are evaluated for silicon, a common material for tip and substrates. Thus, $E_1 = E_2 = E$ and $\nu_1 = \nu_2 = \nu$. The parameters $E = 151.34\,\text{GPa}$ and $\nu = 0.19732$ are obtained from DFT calculations, tabulated in the Materials Project [217].The radius $R = 10\,\text{nm}$ of the AFM tip is taken from experiments [100].

6.2.2 Dynamics and Thermodynamic Evolution

The dynamics of the PT system is modelled based on transition state theory as a Markovian random hopping process over energy barriers separating the different stable states m of the total energy U in Eq. (6.13). The rate of the transition from a state n to a state m is given by the Arrhenius law:

$$\omega_{mn} = f_0 \exp\Big(-\beta \Delta u_{mn}\Big) \tag{6.21}$$

where Δu_{mn} denotes the energy barrier for the transition from state n to state m, and f_0 is the attempt frequency setting the characteristic timescale of thermal relaxation processes, $\beta = 1/k_B T$, T is the temperature, and k_B the Boltzmann constant. The energy barriers Δu_{mn} as well as the rates ω_{mn} are time-dependent.

Single- and multi-lattice hops are considered, so m and n do not necessarily refer to nearest-neighbour sites. The energy barrier for a transition from state n to another state m is here defined as follows. A sketch in Fig. 6.15 shows the calculated path of the tip in

transitioning from an arbitrary state n to a different state m, and how the energy barrier along this path is calculated. This is done first, by using the string method [263] to find the least energy path between state n and m over the two-dimensional total energy U defined in Eq. (6.13). Second, all local maxima and local minima are found along the path using a peak detection algorithm [264]. Next, the energy at the local maxima are summed, and the energy at the local minima subtracted. This quantity is referred to as u_B. Finally, the energy barrier Δu_{mn} for the transition is defined as $u_B - u_n$, where $u_n = u(\boldsymbol{r}_n, t)$ is the energy of state n. Similarly, the energy barrier for the reverse transition, i.e. from state m to state n is $\Delta u_{nm} = u_B - u_m$. In other words, the total energy barrier is defined as the sum of partial energy barriers in the path separating the two states, which naturally implies higher energy barriers between further away states than between nearest neighbour states. Note that u_B is time dependent, as well as the energy of the states.

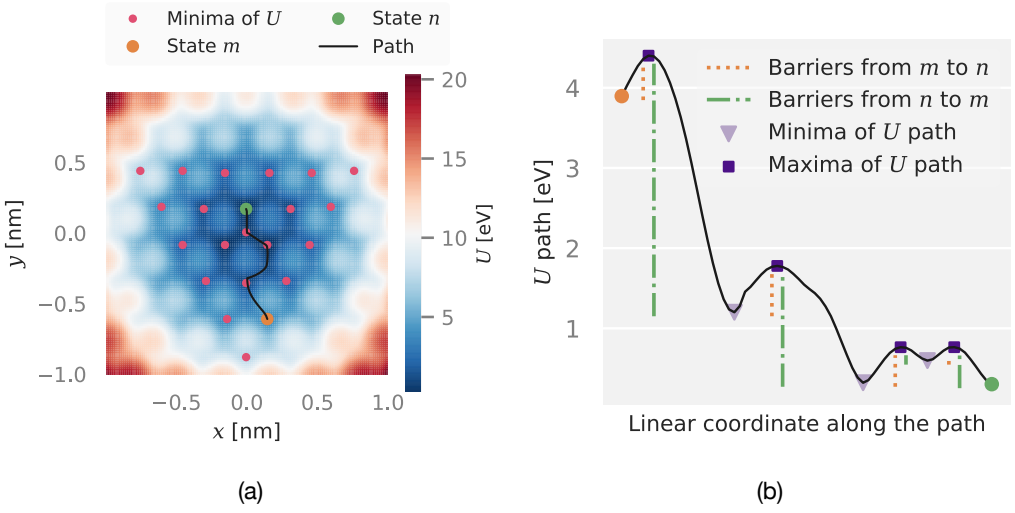

Figure 6.15: Example of energy barrier between two states in MoS_2 at time $t_0 = 0$. (a) The least energy path for the transition between two states m (orange circle) and n (green circle) is found using the string method. (b) Partial energy barriers along the path are defined by the orange dotted lines and green dot-dashed ones. The energy barrier from m to n is calculated as the sum of the partial energy barriers along the path (dotted, orange). Equivalently, the energy barrier from n to m is the sum of barriers in the opposite direction (dot-dashed, green).

Each state m has an associated probability of occupation p_m, the evolution of which is given by the Master equation for Markovian dynamics:

$$\frac{dp_m}{dt} = \sum_n \omega_{mn} p_n - \omega_{nm} p_m \tag{6.22}$$

The stochastic trajectories followed by the tip given a specific energy of the form of Eq. (6.13) and an initial condition can be found from Monte Carlo sampling of discrete states. The evolution of the PT system can be described alternatively with Langevin dynamics, by integrating Newton's equation of movement over the whole energy surface, instead of Monte Carlo sampling over the stable points of the energy.

The thermodynamic evolution of the system for single stochastic trajectories can be evaluated by applying stochastic thermodynamics. The field of stochastic thermodynamics extends the concepts of macroscopic thermodynamics to the level of single stochastic trajectories in microscopic out-of-equilibrium systems [109, 265, 266]. Stochastic thermodynamics has been applied to microscopic systems such as elastic molecular systems [267, 268, 269, 109], nanomotors [270, 271, 109], colloidal particles in non-harmonic potentials [272], and to AFM in vertical harmonic oscillator mode [273]. Only recently has stochastic thermodynamics been applied to nanoscale friction, such as in a recent study investigating the validity of the Jarzynski equality in Friction Force Microscopy trajectories [274].

Explicit expressions for the entropy are given within the stochastic thermodynamics framework and applied to the trajectories $n(t)$ followed by the tip for the Hamiltonian in Eq. (6.13), found from Monte Carlo sampling. The starting point for the derivation of such expressions is the derivative of the energy in Eq. (6.13) evaluated on a given stochastic trajectory followed by the system. It has been shown that the derivative can be split into work and heat in the same way as by the first law of thermodynamics for macroscopic closed systems [275]. In the derivative of the energy in Eq. (6.13) two terms arise, that are then associated to the work of the cantilever and to the heat transferred to the surroundings during the stick-slip friction process. The work w is the term with the explicit time dependence of the energy, and the heat q the term with the hopping between states. A term for the entropy s along a trajectory is defined in stochastic thermodynamics [276]. The derivative of the stochastic entropy can be split into two terms, entropy production s_i and entropy flow to the surroundings s_e [276], in the same way as given by non-equilibrium thermodynamics for macroscopic systems [277]. Entropy production measures irreversibly, while entropy flow is related to heat flow by $q = Ts_e$. Thermodynamic expressions applied are summarised in Table 6.1. The complete derivation of the expressions has been described in detail in [276] for general systems and, in particular, in our earlier work for time-dependent potentials [77].

6.2.3 Results

Crystalline Interfaces

Figures 6.16 and 6.17 report the PES for the BLs considered. The selection represents a collection of different geometries and chemistry within the 2D materials family, highly interesting for solid lubrication technologies. This variety allows to evaluate the impact of interface complexity on dissipation.

The first distinction in the dataset is between between purely 2D materials, GBL and h-BN, and the remaining "extended ML" compounds, whose geometry extends in 3D. As shown in Figures 6.16a and 6.16d, the former are composed of flat sheets of atoms arranged in a honeycomb lattice. Within this class, the presence of a single-component crystal, GBL, and a binary, h-BN, allows to evaluate the effect of chemical composition. The

Stochastic thermodynamics in the PT model		
Variable	**Expression**	**Notes**
Entropy s	$s(n,t) = -k_B \ln p_{n(t)}(t)$	From definition in [278, 276].
Entropy change ds	$\frac{ds}{dt} = \frac{đ_e s}{dt} + \frac{đ_i s}{dt}$	From non-equilibrium thermodynamics [277].
Entropy production $đ_i s$	$\frac{đ_i s}{dt} = \frac{\partial s}{\partial t} + k_B \sum_j \delta(t-t_j) \ln \frac{p_{n_j^-}(t_j)\omega_{n_j^- n_j^+}(t_j)}{p_{n_j^+}(t_j)\omega_{n_j^+ n_j^-}(t_j)}$	As defined in [279] for systems governed by a Master equation.
Entropy flow $đ_e s$	$\frac{đ_e s}{dt} = k_B \sum_j \delta(t-t_j) \ln \frac{\omega_{n_j^+ n_j^-}(t_j)}{\omega_{n_j^- n_j^+}(t_j)}$	Defined as $ds/dt - đ_i s/dt$.
Energy u	$u = U(\boldsymbol{r}_{n(t)}, t)$	Energy in Eq. 1 in the main text evaluated over trajectory $n(t)$.
Energy change du	$\frac{du}{dt} = \frac{đw}{dt} + \frac{đq}{dt}$	First law of thermodynamics for stochastic trajectories and close systems [275].
Work w	$\frac{đw}{dt} = \frac{\partial u}{\partial t} = -C\boldsymbol{v} \cdot (\boldsymbol{r}_{n(t)} - \boldsymbol{t})$	Where $\boldsymbol{r}_{n(t)}$ is the position of the tip along the trajectory and $f = -C(\boldsymbol{r}_{n(t)} - \boldsymbol{v}t)$ the force of the spring.
Heat q	$\frac{đq}{dt} = \frac{\partial u}{\partial n}\frac{dn}{dt} = k_B T \sum_j \delta(t-t_j) \ln \frac{\omega_{n_j^+ n_j^-}(t_j)}{\omega_{n_j^- n_j^+}(t_j)}$	Derived from from non-equilibrium thermodynamics $đq/dt = T đ_e s/dt$ [277].

Table 6.1: Stochastic thermodynamic along trajectory $n(t)$ in the PT model in the transition state theory limit. The special notation in Table 6.1 using the $đ$ symbol is to emphasise that work and heat are not state variables and depend on the path connecting the starting and the end states associated with the trajectory. The notation for the heat, entropy flow, and entropy production are defined in [109], which is $n_j^- = n(t_j)$ and $n_j^+ = n(t_j + dt)$.

extended ML compounds include two binaries from the TMD family, MoS_2 in Fig. 6.16b and WTe_2 in Fig. 6.16c, and the single component black phosphorous in Fig. 6.16e, recently indicated as a promising solid lubricant [193]. On the other hand, as shown in Fig. 6.16e, black P comprises of staggered rows of three-fold coordinated P atoms, with two in-plane neighbours and one in the neighbouring plane. Lastly, a bilayer composed of two slabs of NaCl, shown in Fig. 6.17b, is considered as an example of non-lubricant material. This crystal has been used in AFM experiments to acquire high-contrast frictional maps [280].

The simplest energy landscape is found for GBL, where the 2D nature and single composition of the layer result in a global maximum and a global minimum divided by a saddle point, as shown in Fig. 6.16a. Increasing the complexity by including different species in the unit cell, like in h-BN shown in Fig. 6.16d, results in the appearance of a local minimum in place of a single global one. The same structures is found in MoS_2 PES, albeit with a higher barrier around 10 meV compared to ≈ 3 meV in h-BN. The two systems characterised by an orthorhombic cell, WTe_2 and black P, show the most complex PES, with a local minimum and a local maximum accompanying the global ones. The PES respect the symmetry of the unit cell, giving rise to triangular lattices of maxima and minima for hexagonal crystals, Figures 6.16a, 6.16b and 6.16d, and rectangular lattices for orthorhombic cells, Figures 6.16c and 6.16e. Finally, note that the energy barrier for

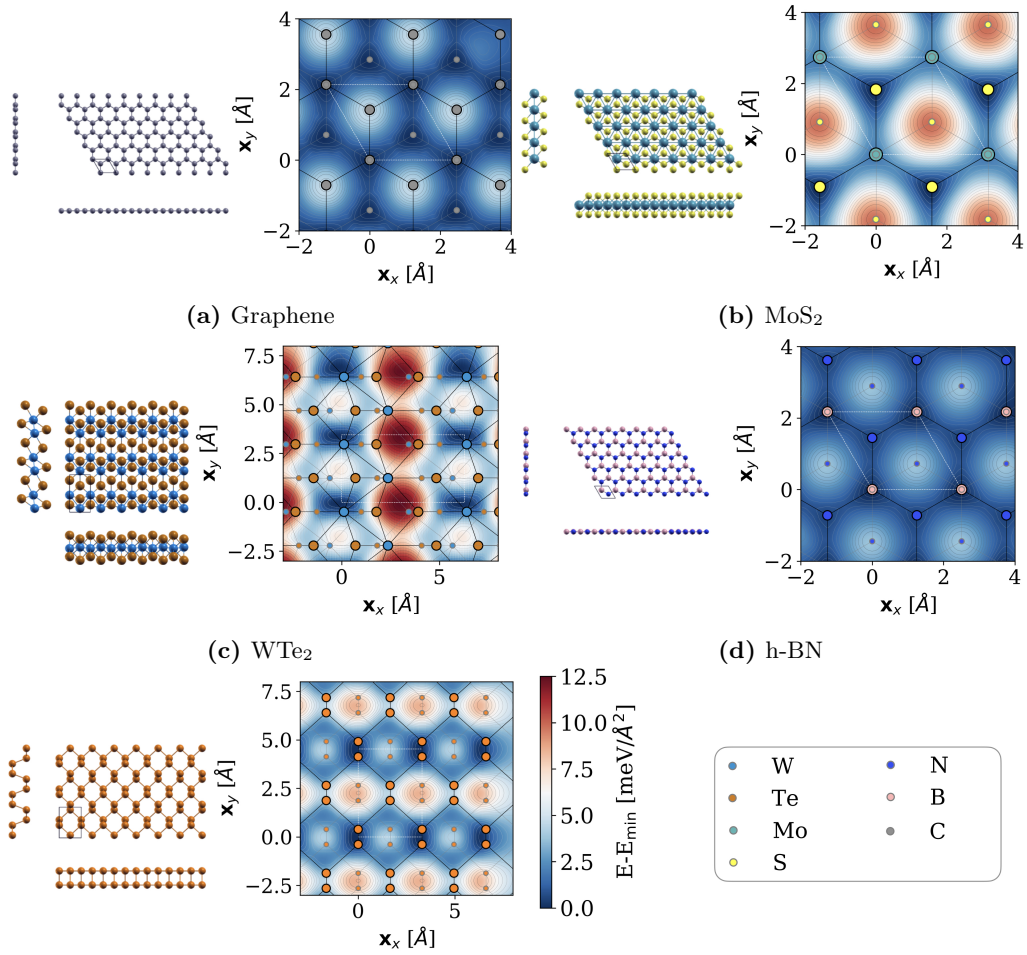

(a) Graphene **(b)** MoS_2

(c) WTe_2 **(d)** h-BN

(e) P-black

Figure 6.16: PES for the selected lubricant systems evaluated over a 15x15 grid at DFT level and interpolated over 200x200 points, with the protocol outlined in section 2.4.3. Ball-and-stick images on the right of each plot report the crystal structure of each ML system. On the right of each plot, the PES for the BL system is reported. Smaller, gray-edged circles represent atoms in the bottom layer, while larger, black-edged circles represent atoms in the top layer.

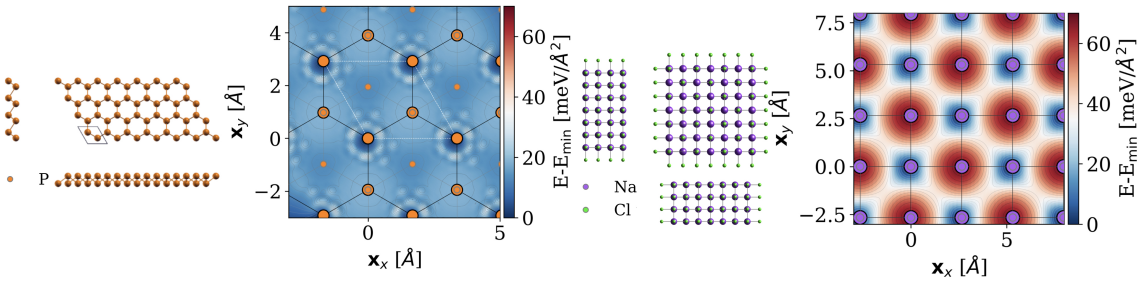

(a) P As-type **(b)** NaCl

Figure 6.17: PES for the selected non-lubricant systems evaluated over a 15x15 grid at DFT level and interpolated over 200x200 points, with the protocol outlined in section 2.4.3. Ball-and-stick images on the right of each plot report the crystal structure of each ML system. On the right of each plot, the PES for the BL system is reported.

the non-lubricant example, square lattice of NaCL bilayer in Fig. 6.17b, shows an energy barrier one order of magnitude higher than the layered materials, linked to higher friction

as seen in experiments [280]. Note that the PES reported in Figures 6.16 and 6.17 refer to the relative sliding of two infinite crystal planes; thus, they are measured in energy per area, meV/$\mathring{A}^2$. These will be transformed to the substrate corrugation U_s, energy per tip, as outlined in section 6.2.1.

Thermodynamics and Anisotropy

The thermodynamic variables described in section 6.2.2 are evaluated using the definitions reported in Table 6.1 on single stochastic trajectories for the seven potential energy surfaces, as obtained from *First principle* calculations shown in section 6.2.3.

The friction system is described for each substrate energy by a PT model with the corresponding energy surface and fixed parameters $C = 3\,\mathrm{N/m}$, $v = 10\,\mathrm{nm/s}$, $T = 300\,\mathrm{K}$, $f_0 = 10\,\mathrm{kHz}$, in the range of typical values for LF-AFM [281]. The load is fixed at $L = 10\,\mathrm{nN}$, yielding a contact area of $\pi a^2 = 3.04\,\mathrm{nm}^2$, according to the protocol outlined in section 6.2.1. The sliding distance is set between $10 - 20\,\mathrm{nm}$, to ensure that the steady state is reached.

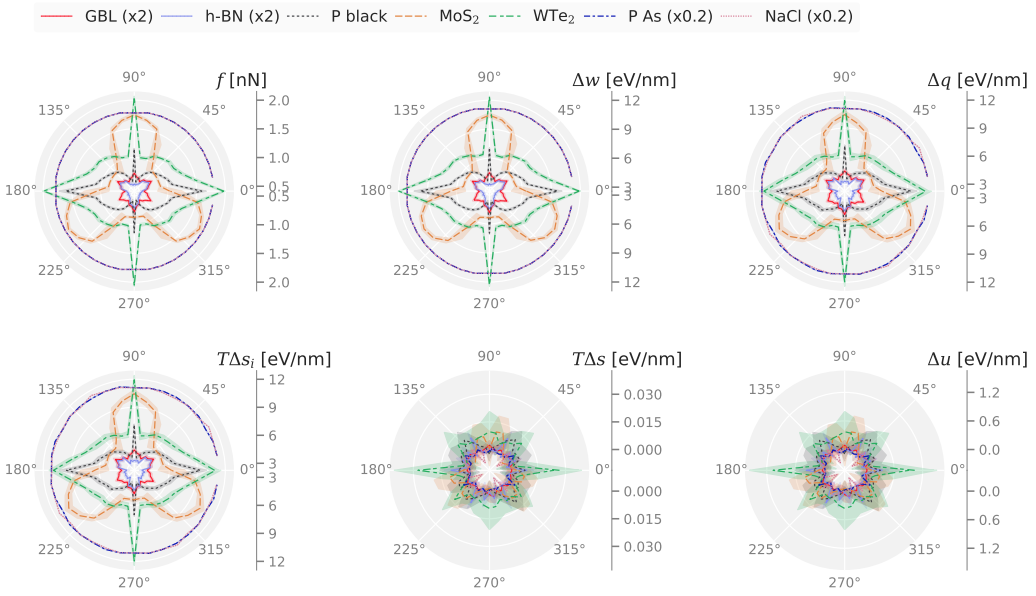

Figure 6.18: Angular dependence of the thermodynamic behaviour for different materials. The quantities shown are the time average of the lateral force after the first stick-slip event (f), the work of the lateral force (Δw), heat flow into the heat bath (Δq), entropy production (Δs_i), entropy change (Δs), and energy change (Δu). All quantities, except f are integrated over enough sliding length ($10 - 20\,\mathrm{nm}$) and then normalised in units of eV/nm. The two entropies are given multiplied by temperature. All quantities are averaged over 50 trajectories.

The polar plots of Fig. 6.18 report friction f, work Δw, heat transferred to the surroundings Δq, entropy production Δs_i, entropy change in the system Δs, and energy change Δs during sliding as a function of the sliding direction, in steps of 10°, between the lattice direction and the cantilever velocity $\mathbf{v}$. The work is the typical variable used to quantify dissipation during friction. Stochastic thermodynamics allows us to quantify a range of thermodynamic variables, providing a more detailed description of the anisotropy

and the response of each material during sliding compared to the work of the force only.

For the materials NaCl and P As-type, the simulations do not reach the steady-state of consecutive stick-slip events for reasonable simulation times of sliding distance of up to 50 nm, while the rest of the materials reach the stick-slip regime after $10-20$ nm. Thus the results of NaCl and P As-type in Fig. 6.18 are not the actual dissipation during stick slip, but the dissipation after sliding a distance of 20 nm, corresponding to a lower bound of static friction. This is because the ratio between the recall force of the cantilever spring C and the energy barrier in Eq. (6.13) is too low: the tip is stuck at the first minimum and the spring elongates as the cantilever translates away.

6.2.4 Discussion

Integrating the profiles in Fig. 6.18 over the angles, the lubrication character of the crystal considered can be ranked as in Table 6.2 by the average value of the lateral force, yielding h-BN and GBL as the bests solid lubricants, followed by P black, WTe_2, and MoS_2. Consistently with the theoretical expectation and experimental observation [280], NaCl is identified as the worst lubricant of the selection, as well as P As-type.

One possible application of the thermodynamic framework is the calculation of temperature gradient due to heating during sliding. The quantity Δq in Fig. 6.18 is the heat leaving the system which can be used to calculate the increase in temperature in the surroundings. For instance, the temperature gradient as ∇T caused by the heat transferred to the silicon in the core of the tip and in the under-layers substrate can be computed. Using the thermal conductivity of silicon of $\lambda = 8.11 \times 10^{11}\,\mathrm{eV \cdot nm/(s \cdot K)}$ through an area of $1\mathrm{nm}^2$, the relation

$$\nabla T = \nabla q/\lambda, \tag{6.23}$$

where $\nabla q = \Delta q v$. The resulting gradients are shown in Table 6.2 for the seven materials.

The average friction force predicted by the model over all angles in Table 6.2 is compared to the ideal shear strength τ, an estimation of friction behaviour based only on *First Principles* quantities. In an infinite-plane geometry, τ is defined as the maximum value of the gradient along the least energy path in the potential energy surface [282], yielding a force per unit area. This quantity represents an upper bound for friction, as it is computed at 0 K and in static calculations. Here, multiplying by the contact area, yields the ideal lateral force, f_{M}, exerted on the finite tip, reported in Table 6.2. These estimations are higher than the ones found with the PT model, coherent with the absence of thermal energy. However, the estimation from the gradient does not allow us to differentiate between different sliding directions as in Fig. 6.18; neither allows to evaluate thermodynamic variables.

Two examples are helpful in understanding the anisotropy behaviour of the thermodynamic variables in Fig. 6.18 and gain insights on the relation between the crystal PES and lubricating properties. In the first example, the instantaneous thermodynamics observables are compared in MoS_2 for three different directions. In the second example, the behaviour

Material	$\langle f \rangle$ [nN]	f_{M} [nN]	∇T in Si [10^{-11}K/nm]
h-BN	0.29±0.03	1.6	2.2 ± 0.3
GBL	0.33±0.03	1.5	2.5 ± 0.2
P black	0.91±0.24	1.5	6.7 ± 1.8
WTe_2	1.30±0.31	3.4	9.4 ± 2.1
MoS_2	1.67±0.43	3.7	9.0 ± 2.5
NaCl	9.00±0.00	15.6	69.2 ± 0.7
P As-type	9.00±0.00	16.9	69.2 ± 0.4

Table 6.2: Materials ranked by average friction over all angles and temperature gradient in silicon with thermal conductivity of $\lambda = 8.11 \times 10^{11}\,\mathrm{eV \cdot nm/(s \cdot K)}$. The quantity f_{M} is the maximum lateral force obtained from the maximum shear strength in the material specific energy surface.

of three crystals are compared for a fixed sliding direction.

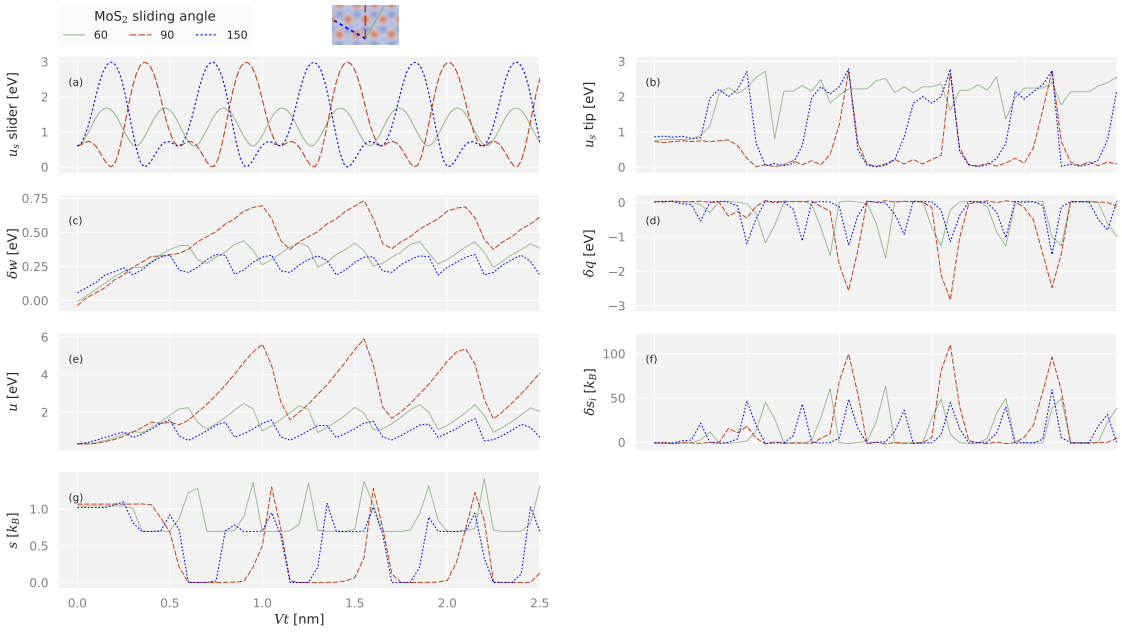

Figure 6.19: Instantaneous thermodynamics (a) substrate energy along the sliding direction, (b) work, (c) heat, (d) energy, (e) entropy production, (f) entropy, for MoS_2 sliding at 60° (green continuous), 90° (orange dashed) and 150° (blue dotted). All quantities are averaged over 50 trajectories.

For the MoS_2 PES, Fig. 6.19 shows three sliding directions, 60°, 90°, and 150°. The shape of the substrate energy along the sliding direction is shown in panel (a), and the energy of the substrate along the actual path taken by the tip on the two-dimensional energy surface is shown in (b). Panels (c)-(f) show the instantaneous behaviour of work (c), heat flow (d), energy (e), entropy production (f), and entropy of the system (g), as the cantilever slides on each of the directions.

The figure shows a clear difference between the three directions, with 90° being the worst in terms of dissipation. The large energy barriers in the substrate at 90° (dashed line in Fig. 6.19a,b) yield large spikes in the work, heat flow, and entropy production reported in Fig. 6.19c,d,f. Note that the PES energy in Fig. 6.19a along 90° and 150° are of similar shape but exhibit different thermodynamic behaviour, showing that the dissipation

is sensitive to small differences in the underlying potential surface.

Fig. 6.19e,g shows the periodic behaviour of the energy and entropy of the system, after the initial transient period. This is due to the periodicity of the energy surface and the simple modelling of the tip and substrate as constant entities with no internal degrees of freedom that would break the time periodicity of the state variables. The result are periodic state variables during sliding. The same is seen in Fig. 6.18 where work Δw, heat flow Δq, and entropy production Δs_i are very similar in Fig. 6.18. The difference between work and heat flow is the change in energy Δu (bottom right panel), and the difference between heat flow and entropy production is the entropy change of the system Δs (bottom left panel), which are both very small for all cases. The small change in internal energy and entropy observed is due to the starting and ending point of the sliding being at non-equivalent positions in the substrate energy, and it tends to zero with increasing sliding distance. However, it is not the general case that entropy and energy of system will be periodic, but a feature of the PT model assuming a point-like tip, rigid cantilever and a rigid substrate without internal degrees of freedom. On a more realistic model, entropy and energy of the system would not necessarily be periodic. Such model would include internal degrees of freedom in the tip, cantilever or substrate, which would decouple the distribution of the heat and entropy production in the different parts of the system. For example, one could imagine an explicit coupling of slider motion to the vibrational degrees of freedom of the substrate [78], allowing for a better description of how sliding energy is dissipated into the bulk.

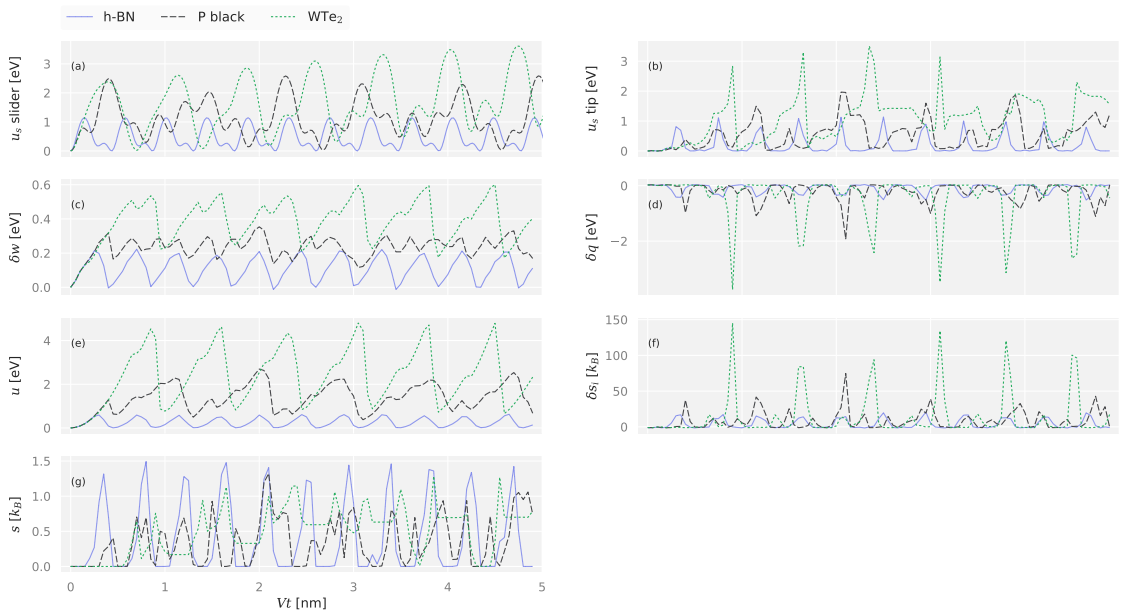

Figure 6.20: Instantaneous thermodynamics (a) substrate energy along the sliding direction, (b) work, (c) heat, (d) energy, (e) entropy production, (f) entropy, for three different substrates, h-BN (blue continuous), P black (gray dashed), and WTe_2 (green dotted) sliding at 30°. All quantities are averaged over 50 trajectories.

The next example in Fig. 6.20, shows the same thermodynamics variables as before

for three crystals h-BN, P black, and WTe_2, during sliding, at a fixed sliding angle at 30° and with the rest of the parameters as before. From the example, lower lubricating behaviour is observed for WTe_2 compared to h-BN and P black, as measured by work in Fig. 6.20c, heat flow in Fig. 6.20d, and entropy production in Fig. 6.20f. It is interesting to note the highly non-linear character of dissipation in the model. The height of the peaks in the energy landscapes along the sliding direction for P black and WTe_2 shown in Fig. 6.20a are of similar magnitude, coherent with the ideal frictional force f_M in Table 6.2 However, dissipation events for WTe_2 are approximately double than those for P black, as shown in Fig. 6.20b,c,e. This observation means that care must be taken when extrapolating from PES computed statically with DFT to dissipation in out-of-equilibrium sliding contact [193, 149]. Both magnitude and distribution of peaks in the energy landscape play a role in the dynamics and thermodynamics of the system. For instance, in the length of 'stick' events, e.g. double length stick events while equal magnitude of peaks in PES along sliding direction for 90° compared to 150° in Fig. 6.19b. The influence of the geometry of the PES on dissipation needs further analysis, left for future work.

6.2.5 Final Remarks

A multi-scale model of stick-slip friction has been developed to quantify dissipation through different thermodynamic variables on real materials in experiments of Friction Force Microscopy. The material specific response is achieved by Density Functional Theory calculations of the energy surface for the specific electronic structure. The dynamics and thermodynamics during sliding is modelled by a modified Prandtl-Tomlinson model and stochastic thermodynamics in the limit of transition state theory.

The model has been applied to a set of seven crystals, but the model can be applied to any material, provided that the material specific potential energy surface is available or can be computed from DFT. While standard DFT is able to model the PES of simple homostructures, like the ones reported here, linear scaling DFT or MD are needed in the case of mismatched heterostrcutres, whose geometry can only be approximated with supercells of thousands of atoms. The combined model allows us to link electronic structure calculations to thermodynamics models able to describe dissipation on time and length scales accessible by experiments.

The observed dissipation does not depend on the height of energy peaks on the crystal energy surface only, but also on the distribution of such peaks.

The framework adopted allows for an easy and controlled introduction of new degrees of freedom, while the stochastic thermodynamics formalism underpinning evaluation of dissipated energy would still be valid. For example, a better description of how sliding energy is dissipated into the different parts of the system could be achieved by adding to the model possible vibrations in the substrate, in the cantilever, and inside the tip [78].

The results presented here could be validated by LF-AFM with relatively little effort. A recently developed experimental protocol [258] allows to wrap flakes around AFM tips yielding the homostructure contact modelled here. By changing the orientation between

the flakes and the tip before the wrapping processes, the mismatch angle between sliding direction and crystal orientation can be varied and anisotropy maps like the ones presented in Fig. 6.18 could be measured experimentally.

7

Conclusions

This thesis shows that computational techniques can effectively describe both in-plane and interlayer phase behaviour of two-dimensional materials. Moreover, the physically rigorous models developed here can rationalise experimental results and provide a full thermodynamic description of dissipation events. The arguments developed in chapter 3 provide general insights into the physics underpinning mechanical relaxation in heterostructure systems. The general theory therein provides a starting point to make this general argument quantitative. The outlined generalised epitaxy theory can serve as a basis for a high-throughput screening of the vast space of possible twistronic devices based on different 2D materials, aiming to estimate the stability of imposed misalignment angles. Such predictions could be validated experimentally with CVD synthesis and transfer protocols already found in the literature [23, 59].

The original aim of systematicly charting the chemical space of TMDs has been addressed in chapters 4 and 5. The methodology outlined in chapter 4 is a promising way to provide starting configurations for more in-depth computational studies and inform synthesis, suggesting highly soluble TMD candidates to novel CVD-based techniques [63]. Moreover, a possible way to improve the accuracy and efficiency of alloy models is suggested in the case of long-range elastic interactions by combining the CE framework [41] and the elastic lattice model [222]. In-depth analysis of a specific system in chapter 5 shows that the finite temperature phase-behaviour, obtained within the CE framework, agrees with experiments [228].

The last chapter focuses on the characterisation of 2D materials for tribology. The relevant physics of sliding has been modelled in both heterogeneous and homogeneous nanoscale contact. In particular, sliding simulations in heterostructure systems agree

with experimental results, providing a general argument for little-studied large-mismatch heterostructures. The generalised PT model of homostructure systems provides a coherent and in-depth thermodynamic description of the sliding behaviour. The prediction of the model could be validated experimentally using LF-AFM with protocols already developed in literature [258].

The results obtained in this thesis provide a solid starting point for future analysis in both phase stability of 2D materials and their sliding behaviour. Experimental validation of in-plane phase behaviour synthesis and homostructure sliding could be carried out within the SOLUTION framework via CVD synthesis at FORTH, Greece and AFM measurements at the University of Southampton, respectively. High-throughput screening of heterostructure twisting behaviour based on the generalised epitaxy theory could be carried out soon with the SOLUTION group at CVUT, Prague, and with the Condensate Matter group at SISSA, Trieste.

A

Single Prototype Solubility Metric

All the solubility metric matrices obtained with the formalism in section 4.2.

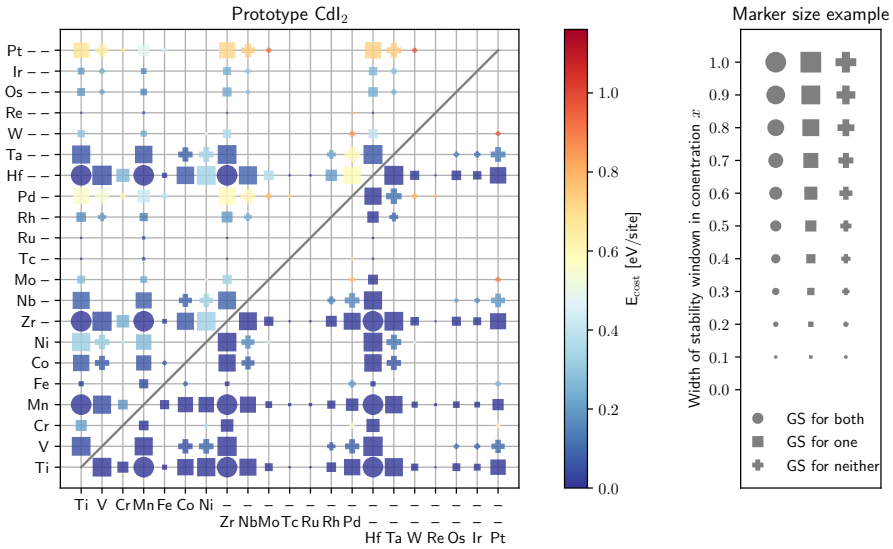
Prototype CdI_2
Pt – –
Ir – –
Os – –
Re – –
W – –
Ta – –
Hf – –
Pd –
Rh –
Ru –
Tc –
Mo –
Nb –
Zr –
Ni
Co
Fe
Mn
Cr
V
Ti
Ti V Cr Mn Fe Co Ni – – – – – – – – – – – –
Zr Nb Mo Tc Ru Rh Pd – – – – – – – – – – – –
Hf Ta W Re Os Ir Pt
E_{cost} [eV/site]
0.0
0.2
0.4
0.6
0.8
1.0
Marker size example
Width of stability windown in conentration x
0.0
0.1
0.2
0.3
0.4
0.5
0.6
0.7
0.8
0.9
1.0
GS for both
GS for one
GS for neither

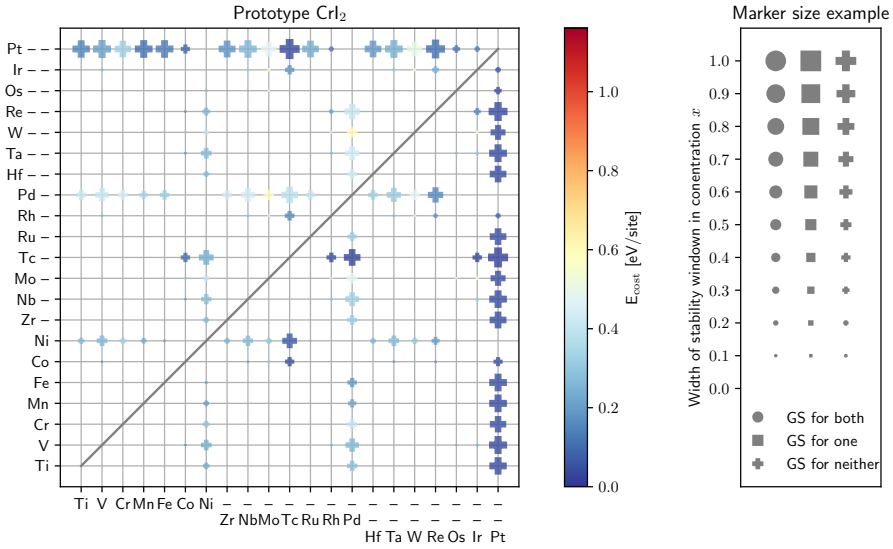
Prototype CrI_2
Pt – –
Ir – –
Os – –
Re – –
W – –
Ta – –
Hf – –
Pd –
Rh –
Ru –
Tc –
Mo –
Nb –
Zr –
Ni
Co
Fe
Mn
Cr
V
Ti
Ti V Cr Mn Fe Co Ni – – – – – – – – – – – –
Zr Nb Mo Tc Ru Rh Pd – – – – – – – – – – – –
Hf Ta W Re Os Ir Pt
E_{cost} [eV/site]
0.0
0.2
0.4
0.6
0.8
1.0
Marker size example
Width of stability windown in conentration x
0.0
0.1
0.2
0.3
0.4
0.5
0.6
0.7
0.8
0.9
1.0
GS for both
GS for one
GS for neither

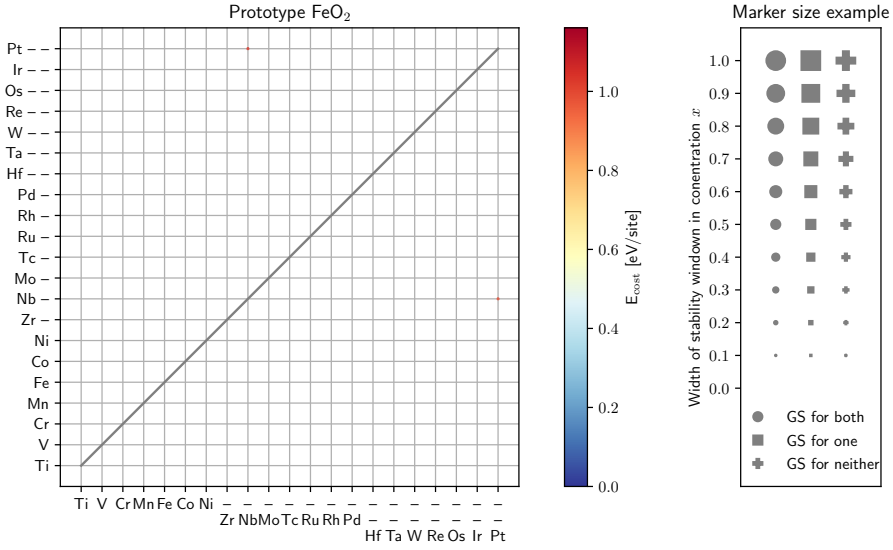
Prototype FeO_2
Pt – –
Ir – –
Os – –
Re – –
W – –
Ta – –
Hf – –
Pd –
Rh –
Ru –
Tc –
Mo –
Nb –
Zr –
Ni
Co
Fe
Mn
Cr
V
Ti
Ti V Cr Mn Fe Co Ni – – – – – – – – – – – –
Zr Nb Mo Tc Ru Rh Pd – – – – – – – – – – – –
Hf Ta W Re Os Ir Pt
E_{cost} [eV/site]
0.0
0.2
0.4
0.6
0.8
1.0
Marker size example
Width of stability windown in conentration x
0.0
0.1
0.2
0.3
0.4
0.5
0.6
0.7
0.8
0.9
1.0
GS for both
GS for one
GS for neither

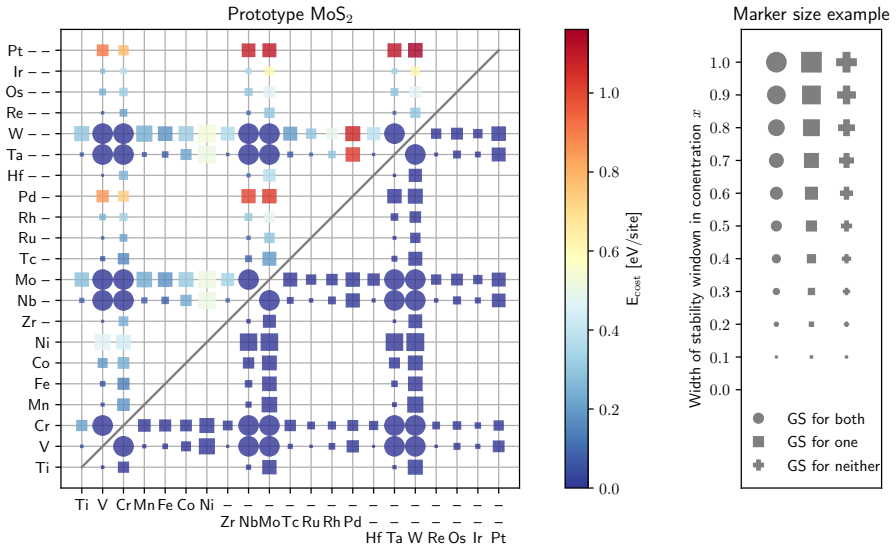
Prototype MoS2
Pt
Ir
Os
Re
W
Ta
Hf
Pd
Rh
Ru
Tc
Mo
Nb
Zr
Ni
Co
Fe
Mn
Cr
V
Ti
Ti V Cr Mn Fe Co Ni
Zr Nb Mo Tc Ru Rh Pd
Hf Ta W Re Os Ir Pt
E_cost [eV/site]
0.0
0.2
0.4
0.6
0.8
1.0
Marker size example
Width of stability windown in conentration x
GS for both
GS for one
GS for neither

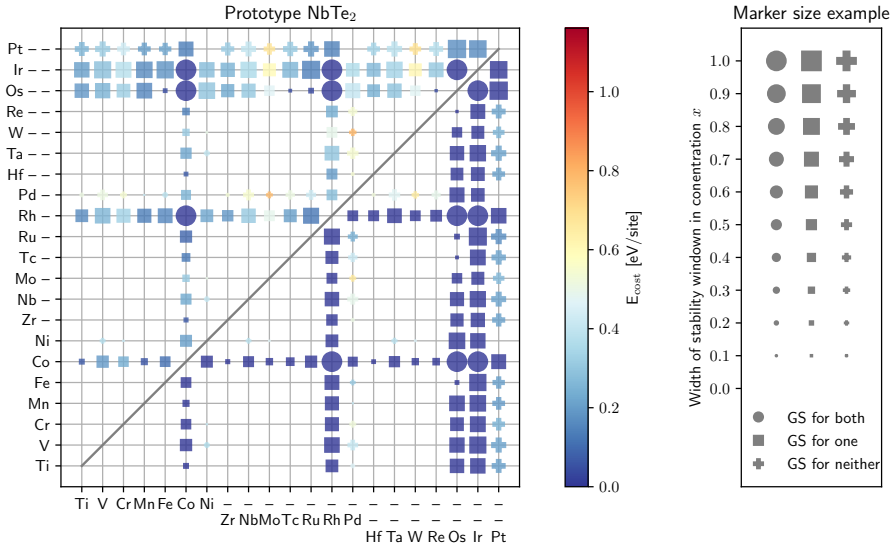
Prototype NbTe2
Pt
Ir
Os
Re
W
Ta
Hf
Pd
Rh
Ru
Tc
Mo
Nb
Zr
Ni
Co
Fe
Mn
Cr
V
Ti
Ti V Cr Mn Fe Co Ni
Zr Nb Mo Tc Ru Rh Pd
Hf Ta W Re Os Ir Pt
E_cost [eV/site]
0.0
0.2
0.4
0.6
0.8
1.0
Marker size example
Width of stability windown in conentration x
GS for both
GS for one
GS for neither

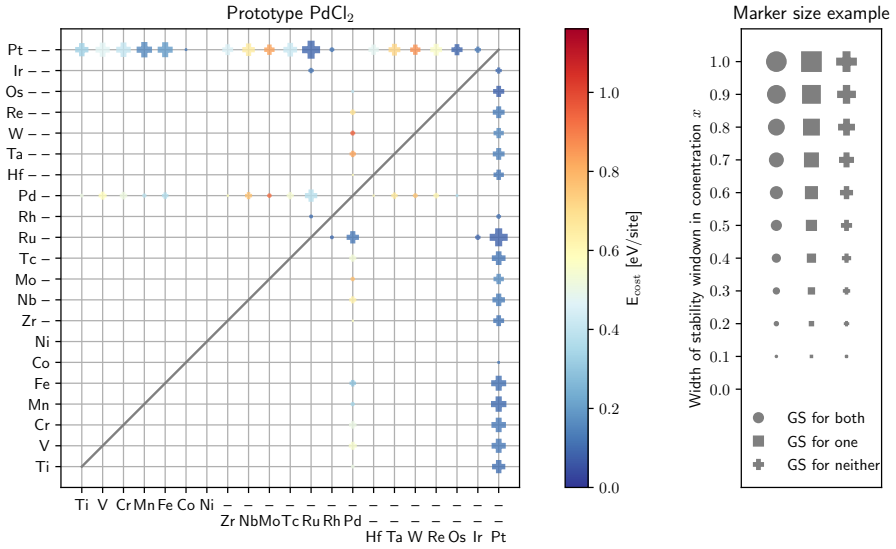
Prototype PdCl2
Pt
Ir
Os
Re
W
Ta
Hf
Pd
Rh
Ru
Tc
Mo
Nb
Zr
Ni
Co
Fe
Mn
Cr
V
Ti
Ti V Cr Mn Fe Co Ni
Zr Nb Mo Tc Ru Rh Pd
Hf Ta W Re Os Ir Pt
E_cost [eV/site]
0.0
0.2
0.4
0.6
0.8
1.0
Marker size example
Width of stability windown in conentration x
GS for both
GS for one
GS for neither

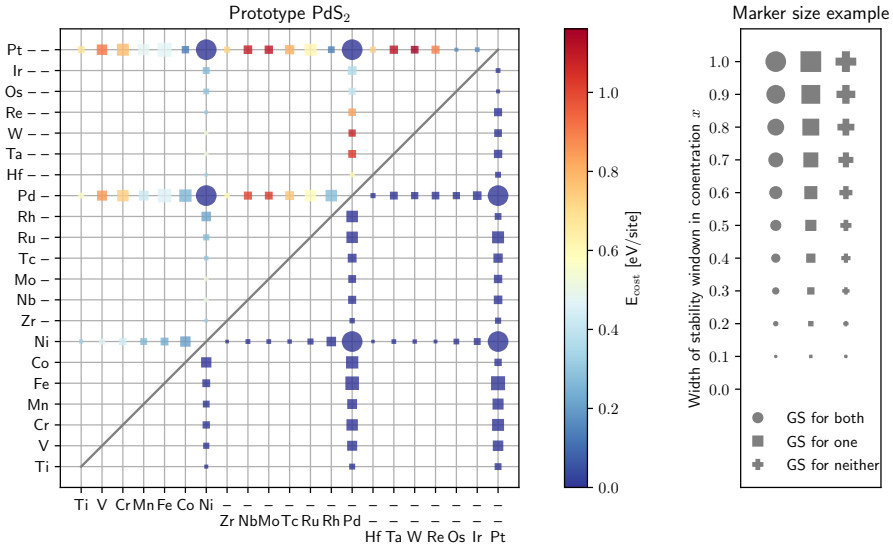
Prototype PdS2
Pt
Ir
Os
Re
W
Ta
Hf
Pd
Rh
Ru
Tc
Mo
Nb
Zr
Ni
Co
Fe
Mn
Cr
V
Ti
Ti V Cr Mn Fe Co Ni
Zr Nb Mo Tc Ru Rh Pd
Hf Ta W Re Os Ir Pt
E_cost [eV/site]
0.0
0.2
0.4
0.6
0.8
1.0
Marker size example
Width of stability windown in conentration x
GS for both
GS for one
GS for neither

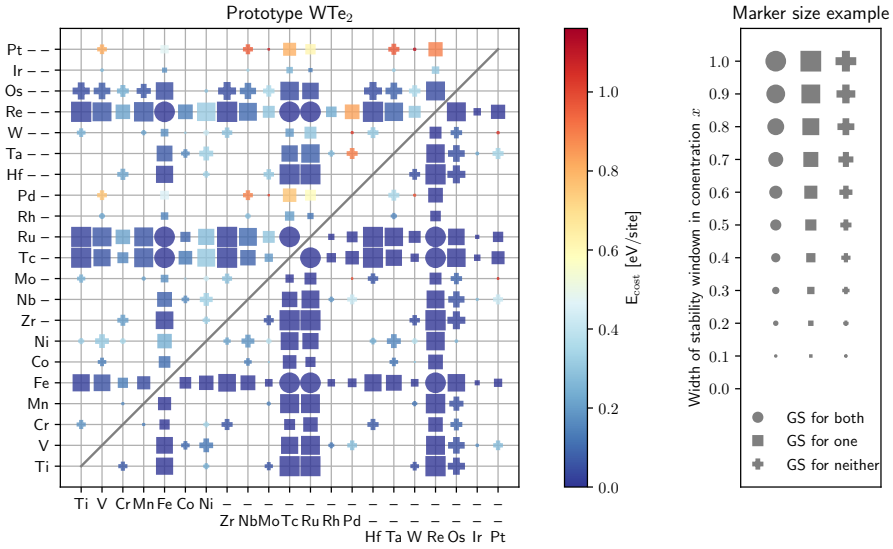
Prototype WTe2
Pt
Ir
Os
Re
W
Ta
Hf
Pd
Rh
Ru
Tc
Mo
Nb
Zr
Ni
Co
Fe
Mn
Cr
V
Ti
Ti V Cr Mn Fe Co Ni
Zr Nb Mo Tc Ru Rh Pd
Hf Ta W Re Os Ir Pt
E_cost [eV/site]
0.0
0.2
0.4
0.6
0.8
1.0
Marker size example
Width of stability windown in conentration x
GS for both
GS for one
GS for neither

B

Epitaxy Theory Details

Consider crystalline ML surrounded by vacuum. It is always possible to orient the system so that the ML is periodic in the xy plane and two lattice vectors, e.g. $\boldsymbol{a_1}$ and $\boldsymbol{a_2}$, are contained in this plane. In turn, the $\boldsymbol{a_3}$ lattice vector is parallel to z. The unit cell is thus described by vectors of the form

$$\boldsymbol{a}_1 = \begin{pmatrix} a_{1x} \\ a_{1y} \\ 0 \end{pmatrix} \quad \boldsymbol{a}_2 = \begin{pmatrix} a_{2x} \\ a_{2y} \\ 0 \end{pmatrix} \quad \boldsymbol{a}_3 = \begin{pmatrix} 0 \\ 0 \\ a_{3z} \end{pmatrix}. \tag{B.1}$$

If the ML unit cell is repeated L times along each xy-plane lattice directions, the result is a Bravais lattice of the form

$$\boldsymbol{R}_l = l_1\boldsymbol{a}_1 + l_2\boldsymbol{a}_2, \tag{B.2}$$

where the index l runs over all possible integers pairs $(l_1,\ l_2)$ in the range $-L/2, L/2$. Fig. B.1 shows examples of such a 2D lattice. The internal structure of the crystal is described by the *basis*, i.e. n vectors $\boldsymbol{R}_\nu$ describing the position of each atom in the unit cell, added to each Bravais lattice point[1]. No assumption on the dimensionality of the basis vectors is made: they may yield a 3D monolayer, like MoS_2, or be purely 2D, like in the case of graphene. An example of a 2D internal structure is shown in Fig. B.1. Basis and Bravais vectors can be combined into a single one

$$\boldsymbol{R}_{\nu l} = \boldsymbol{R}_l + \boldsymbol{R}_\nu, \tag{B.3}$$

[1]Bravais lattice vectors are indexed by Roman letters while Greek letters label degrees of freedom within the unit cell.

which describes the equilibrium position of each atom in the ML. Deviation from the equilibrium positions are described by the displacement vectors $\boldsymbol{u}_{\nu l} = \boldsymbol{r}_{\nu l} - \boldsymbol{R}_{\nu l}$, as shown in Fig. 2.12. Consider now a second ML placed on top of the first one with a misalignment

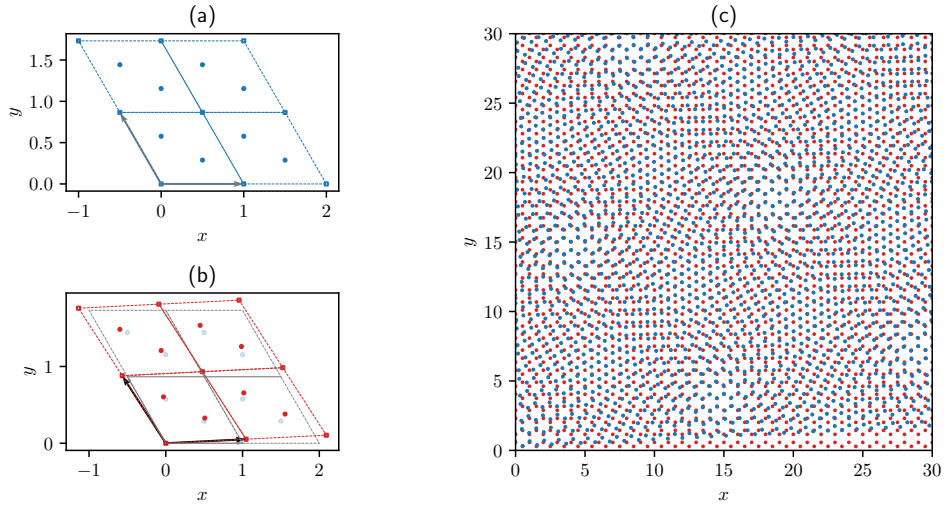

Figure B.1: (a) a lattice: hollow, blue squares mark Bravais lattice points, defined in Eq. (B.2), and filled, blue circles mark atoms. The generating vectors are $\boldsymbol{a}_1 = l_a \begin{pmatrix} 1 & 0 & 0 \end{pmatrix}$ and $\boldsymbol{a}_2 = l_a \begin{pmatrix} -1/2 & \sqrt{3}/2 & 0 \end{pmatrix}$ (gray arrows). The two atoms ($n = 2$) basis is $\boldsymbol{R}_1 = 1/3\boldsymbol{a}_1 + 2/3\boldsymbol{a}_2$ and $\boldsymbol{R}_2 = 2/3\boldsymbol{a}_1 + 1/3\boldsymbol{a}_2$. The unit cell is repeated $L = 2$ times (dotted lines). (b) b crystal lattice (red symbols), superimposed on the a one (blue symbols). The b crystal shares the same geometry as a one, but lattice spacing $l_b = l_a\pi/3$, making the resulting bilayer incommensurate. The b lattice is rotated of $\theta = 2.86°$ according to Eq. (B.4). (c) Detail of the twisted bilayer supercell ($L = 30$) showing the optical interference typical of mismatched heterostructures.

angle, to form an incommensurate heterostructure. If this second ML lattice b has the same symmetry as the first lattice a, then the vector generating its lattice can be defined in terms of the a lattice vectors:

$$\boldsymbol{b}_i = R_z(\theta) \cdot \boldsymbol{a}_i \tag{B.4}$$

$$R_z(\theta) = \begin{pmatrix} \cos\theta & -\sin\theta & 0 \\ \sin\theta & \cos\theta & 0 \\ 0 & 0 & 1 \end{pmatrix}. \tag{B.5}$$

In other words, the lattice of the second layer, b, is rotated around the z axis with respect to the first one, as shown in Fig. B.1(b,c). Finally, given the *direct* Bravais lattice a generated by Eq. (B.1), its *dual* lattice is the set of vectors $\boldsymbol{\tau}$ satisfying $e^{i\boldsymbol{R}\cdot\boldsymbol{\tau}} = 1$ for all $\boldsymbol{r}$ in Eq. (B.2), which implies

$$\boldsymbol{R} \cdot \boldsymbol{\tau} = 2\pi M, \;\; M \in \mathbb{Z}. \tag{B.6}$$

The set of vectors $\boldsymbol{\tau}$ form a Bravais lattice themselves

$$\boldsymbol{\tau} = m_1\boldsymbol{t}_1 + m_2\boldsymbol{t}_2, \tag{B.7}$$

whose primitive vectors are defined by

$$\boldsymbol{t}_i = 2\pi \frac{\boldsymbol{a}_j \times \boldsymbol{a}_k}{a_i \cdot (\boldsymbol{a}_j \times \boldsymbol{a}_k)}, \tag{B.8}$$

where i, j, k cycle through 1,2,3 [143, 150]. The same holds for the b lattice.

The geometry of the ML allows the position of the atoms to be decomposed as

$$\boldsymbol{r}_{\nu l} = \begin{pmatrix} \boldsymbol{\rho}_{\nu l} \\ z_{\nu l} \end{pmatrix} = \begin{pmatrix} \boldsymbol{R}_l + (\boldsymbol{R}_\nu + \boldsymbol{u}_{\nu l}) \cdot (\hat{e}_1 \otimes \hat{e}_2) \\ (\boldsymbol{R}_\nu + \boldsymbol{u}_{\nu l}) \cdot \hat{e}_3, \end{pmatrix} \tag{B.9}$$

where $\hat{e}_i$ is a versor along a Cartesian axis.

Interlayer Potential Expasion

The expression in Eq. (3.8) can be further simplified by taking into account the periodicity of the adsorbate ML. The plane-wave terms in Eq. (3.8) are expanded like in Eq. (3.3) in terms of the adsorbate reciprocal lattice vectors $\boldsymbol{\tau}$:

$$\sum_{\nu,l} e^{i\boldsymbol{R}_{\nu l}\cdot\boldsymbol{G}} = \frac{1}{N_0} \sum_{\tau} \left(\sum_{\nu} e^{i\boldsymbol{R}_\nu \cdot \boldsymbol{\tau}} \sum_{l} e^{i\boldsymbol{R}_l \cdot \boldsymbol{\tau}} \right) \sum_{\mu,j} e^{i\boldsymbol{R}_{\mu j}\cdot(\boldsymbol{G}-\boldsymbol{\tau})} \tag{B.10}$$

$$= \sum_{\tau} f_\tau \sum_{\mu,j} e^{i\boldsymbol{R}_{\mu j}\cdot(\boldsymbol{G}-\boldsymbol{\tau})}, \tag{B.11}$$

where $\boldsymbol{R}_{\mu l} = \boldsymbol{R}_l + \boldsymbol{R}_\mu$ and the definition of reciprocal lattice Eq. (B.6) were used. In Eq. (B.11) the *geometrical structure factors* was defined [150]:

$$f_\tau = \sum_{\nu} e^{i\boldsymbol{R}_\nu \cdot \boldsymbol{\tau}}, \tag{B.12}$$

The geometrical structure factor f_τ expresses the modulation of plane waves due to internal structure of the unit cells and in X-ray experiments of Bragg diffraction are the origin of extinction of lattice peaks [150]. Due to the parity of the lattices, the sums over μ, l of oscillatory functions in Eq. (B.11) can only be non-zero if the argument of the exponential is null for all terms, yielding

$$\sum_{\tau,\mu,j} e^{i\boldsymbol{R}_{\mu j}\cdot(\boldsymbol{G}-\boldsymbol{\tau})} = nN_0 \sum_{\tau} \delta_{\boldsymbol{G},\boldsymbol{\tau}}, \tag{B.13}$$

where $\delta(\boldsymbol{G} - \boldsymbol{\tau}) \equiv \delta_{\boldsymbol{G},\boldsymbol{\tau}}$. Substituting Eq. (B.11) and (B.13) in Eq. (3.8) yields

$$H_{\mathrm{L_1L_2}} = nN_0 \sum_{\tau,\boldsymbol{G}} V_{\boldsymbol{G}} f_\tau \delta_{\boldsymbol{G},\boldsymbol{\tau}} + \sum_{\nu,l,\boldsymbol{G}} V'_{\boldsymbol{G}} z_{\nu l} e^{i\boldsymbol{R}_{\nu l}\cdot\boldsymbol{G}} + i \sum_{\nu,l,\boldsymbol{G}} V_{\boldsymbol{G}} \boldsymbol{G} \cdot \boldsymbol{u}_{\nu l} e^{i\boldsymbol{R}_{\nu l}\cdot\boldsymbol{G}}. \tag{B.14}$$

To tackle the two right-most terms of Eq. (B.14), the displacements $\boldsymbol{u}_{\nu l}$ are written in terms of phonon eigenvalues $\boldsymbol{\epsilon}_{s\nu}$ in Eq. (2.117). The latter expansions introduces a third wave-vector $\boldsymbol{k}$ spanning the BZ of the adsorbate. The displacement perpendicular to the

monolayer plane is expanded as

$$z_{\nu,l} = \boldsymbol{u}_{\nu l} \cdot \hat{u}_3 = \frac{1}{\sqrt{N_0 m_\nu}} \sum_{\boldsymbol{k},s} \gamma_{\boldsymbol{k}s} \boldsymbol{\epsilon}_s(\nu, \boldsymbol{k}) \cdot \hat{u}_3 e^{i\boldsymbol{k}\cdot R_{\nu l}}. \tag{B.15}$$

Substituting the expansions Eq. (B.10), (B.15) and (2.117) in Eq. (B.14) and following the same reasoning leading to Eq. (B.13), one obtains the linearised substrate-adsorbate potential energy in Eq. (3.9) to (3.11) The geometrical construction obeyed by the vectors $\boldsymbol{G}$, $\boldsymbol{\tau}$, and $\boldsymbol{k}$, sketched in Fig. 3.3, is shown for extended lattices in Fig. B.2a. Moreover, Fig. B.2b shows how the allowed phonon vectors $\boldsymbol{k}$ resulting from the construction span the whole BZ.

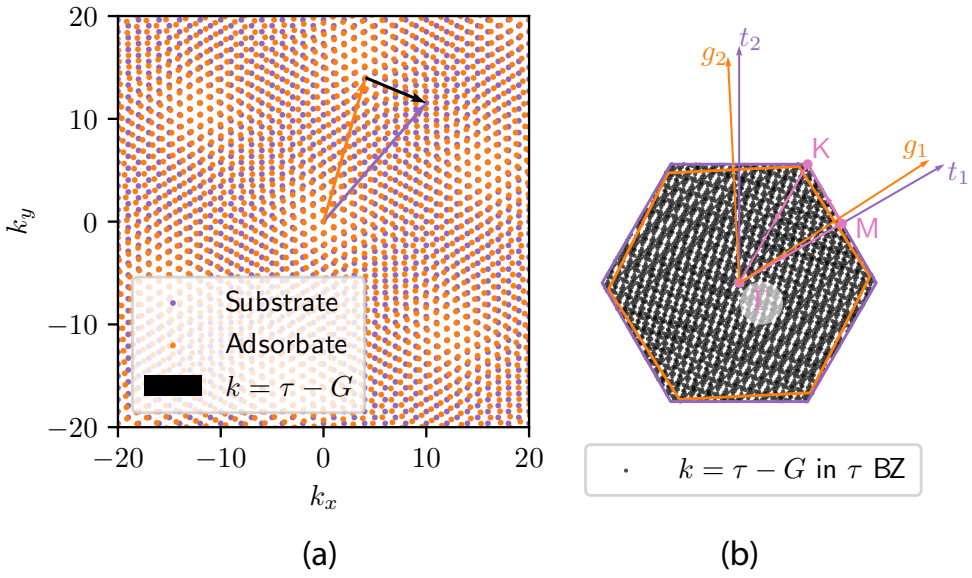

Figure B.2: Reciprocal lattices $\boldsymbol{\tau}, \boldsymbol{G}$, evaluated on a $N_0 = 60 \times 60$ grid. Arrows show an example of the construction in Fig. 3.3. (b) Allowed phonon wave-vectors $\boldsymbol{k} = \boldsymbol{\tau} - \boldsymbol{G}$ (black dots) build from all possible black arrows in (a) and mapped into the BZ of τ lattice.

Classical Total Potential Energy

Summing the internal elastic energy of the harmonic layer Eq. (2.121) and the terms comprising the interaction between this and the substrate Eq. (3.9) to (3.11), the total energy of the harmonic-substrate bilayer system in Eq. (3.2) reads:

$$E = E_c + nN_0 \sum_{\tau,\boldsymbol{G}} V_{\boldsymbol{G}} f_\tau \delta_{\boldsymbol{G},\boldsymbol{\tau}} + \sum_{\boldsymbol{k},s} \frac{1}{2} \omega_s^2(\boldsymbol{k}) |\gamma_{\boldsymbol{k}s}|^2 \tag{B.16}$$

$$+ \sum_{\boldsymbol{k},s} n\sqrt{N_0}\gamma_{\boldsymbol{k}s} \left(\sum_{\boldsymbol{\tau},\boldsymbol{G},\nu} \frac{V'_{\boldsymbol{G}}}{\sqrt{m_\nu}} \boldsymbol{\epsilon}_s(\nu, \boldsymbol{k}) \cdot \hat{u}_3 e^{i\boldsymbol{R}_\nu \cdot \boldsymbol{\tau}} \delta_{\boldsymbol{G}+\boldsymbol{k},\boldsymbol{\tau}} \right. \tag{B.17}$$

$$\left. + i \sum_{\boldsymbol{\tau},\boldsymbol{G},\nu} \frac{V_{\boldsymbol{G}}}{\sqrt{m_\nu}} \boldsymbol{\epsilon}_s(\nu, \boldsymbol{k}) \cdot \boldsymbol{G} e^{i\boldsymbol{R}_\nu \cdot \boldsymbol{\tau}} \delta_{\boldsymbol{G}+\boldsymbol{k},\boldsymbol{\tau}} \right), \tag{B.18}$$

The terms describing lattices coupling and internal structure of the unit cell in Eq. (B.17) and (B.18) depend only characteristics of the pristine layers, e.g. phonon dispersion and inter-layer coupling, and can thus be computed in a small supercell with accurate methods and plugged into this results. Note that, as expected, the interaction relative to a different wavelength is modulated by the amplitude of the corresponding phonon mode $\gamma_{\boldsymbol{k}s}$, defined in Eq. (2.118). Finally note that Eq. (B.16) to (B.18) depends on configuration of the system via γ_{sk}. Thus, it can be useful to analyse results of classical MD runs with extended geometries or regard the amplitude γ_{sk} as coefficient in a "fake-dynamics" minimisation problem.

Second Quantization Framework

In order to overcome completely the dependency on configurations in extended geometries contained in Eq. (B.16) to (B.18), the problem must be addressed according to second quantisation formalism. Following Ref. [150, 143], the total energy, sum of kinetic and potential, is transformed into an Hamiltonian operator, which needs to be diagonalised in order to study the energy spectrum of the system. Normal-modes momentum is introduced as the analogous of Eq. (2.117) for velocities [143]

$$p_{\boldsymbol{k}s} = \frac{1}{\sqrt{N_0}} \sum_{j,\nu} \sqrt{m_\nu} \dot{u}^\alpha_{\nu j} \epsilon^\alpha_s(\nu, \boldsymbol{k}) e^{i\boldsymbol{k}\cdot\boldsymbol{R}_{\nu l}} = \dot{\gamma}_{-\boldsymbol{k}s}, \tag{B.19}$$

where the dot above a quantity indicates the derivative with respect of time. The pair γ and p constitutes the conjugate variables for the system. The total energy of the isolated harmonic ML will then be the sum of kinetic and potential energy stored in the normal modes

$$E_0 = \frac{1}{2} \sum_{\boldsymbol{k}s} |p_{\boldsymbol{k}s}|^2 + \omega^2_{\boldsymbol{k}s} |\gamma_s(\boldsymbol{k})|^2. \tag{B.20}$$

In the second quantisation formalism, the Hamiltonian is written in terms of creation and annihilation operators $\hat{a}^\dagger_{\boldsymbol{k}s}$, $\hat{a}_{\boldsymbol{k}s}$. The operators $\hat{a}^\dagger_{\boldsymbol{k}s}$, $\hat{a}_{\boldsymbol{k}s}$ represent the creation and destruction of a phonon of momentum $\boldsymbol{k}$ in the branch s, respectively. Phonons are the quasi-particle equivalent of the classical normal modes. Phonons operators obey bosonic commutation rules [150]:

$$[\hat{a}_{\boldsymbol{k}s}, \hat{a}^\dagger_{\boldsymbol{k'}s'}] = \delta_{\boldsymbol{k},\boldsymbol{k'}} \delta_{s,s'} \tag{B.21}$$

$$[\hat{a}^{(\dagger)}_{\boldsymbol{k}s}, \hat{a}^{(\dagger)}_{\boldsymbol{k}s}] = 0. \tag{B.22}$$

The atomic displacements are expressed in terms of these operators as [143, 150, 151]

$$u^\alpha_{\nu j} = \frac{\hbar}{\sqrt{2N_0 m_\nu}} \sum_{j,\nu} \frac{1}{\omega_s(\boldsymbol{k})} (\hat{a}_{\boldsymbol{k}s} + \hat{a}^\dagger_{-\boldsymbol{k}s}) \epsilon^\alpha_s(\nu, \boldsymbol{k}) e^{i\boldsymbol{k}\cdot\boldsymbol{R}_{\nu l}}, \tag{B.23}$$

while the conjugate variables read [143]

$$\gamma_{\boldsymbol{k}s} = \sqrt{\frac{\hbar}{2\omega_s(\boldsymbol{k})}}(\hat{a}_{\boldsymbol{k}s} + \hat{a}^{\dagger}_{-\boldsymbol{k}s}) \tag{B.24}$$

$$p_{\boldsymbol{k}s} = i\sqrt{\frac{\hbar\omega_s(\boldsymbol{k})}{2}}(\hat{a}^{\dagger}_{\boldsymbol{k}s} - \hat{a}_{-\boldsymbol{k}s}). \tag{B.25}$$

Using Eq. (B.24) and (B.25) and the commutation rules, the energy in Eq. (B.16) to (B.18) can be transformed into the Hamiltonian operator in Eq. (3.12).

C

Supercells for Twisted Lattices

Here, we explain the procedure to obtain the twisted lattices supercells. Let l_a and l_b be the spacing of the Bravais lattices of layer a and layer b, respectively and $\hat{\boldsymbol{a}}_1 = \left(\begin{smallmatrix}1\\0\end{smallmatrix}\right)$ be one of the primitive versors of the first lattice, aligned with the x axis; the lattice with the desired periodicity is generated by a primitive vector $\boldsymbol{a}_1 = l_\mathrm{a}\hat{\boldsymbol{a}}_1$. The matrix representing the discrete rotational symmetry of the lattice by an angle $\Omega = \pi/3$ is:

$$\underline{\underline{R}}_\Omega = \begin{pmatrix} \cos\pi/3 & -\sin\pi/3 \\ \sin\pi/3 & \cos\pi/3 \end{pmatrix} = \begin{pmatrix} 1/2 & -\sqrt{3}/3 \\ \sqrt{3}/3 & 1/2 \end{pmatrix}. \tag{C.1}$$

Thus, the second versor defining the lattice is $\hat{\boldsymbol{a}}_2 = \underline{\underline{R}}_\Omega \hat{\boldsymbol{a}}_1$. Since the second lattice, b, has the same symmetry but is rotated with respect to the first one by an angle θ, versors defining it are $(\hat{\boldsymbol{b}}_1, \hat{\boldsymbol{b}}_2) = (\underline{\underline{R}}_\theta \hat{\boldsymbol{a}}_1,\ \underline{\underline{R}}_\Omega \underline{\underline{R}}_\theta \hat{\boldsymbol{a}}_1)$ where

$$\underline{\underline{R}}_\theta = \begin{pmatrix} \cos\theta & -\sin\theta \\ \sin\theta & \cos\theta \end{pmatrix} \tag{C.2}$$

describes the misalignment between the lattices. A heterostructure supercell will be compatible with both periodicities if the individual lattice cells match exactly at the edges, in other words, if the following matching condition is satisfied

$$l_\mathrm{a}(n_1\hat{\boldsymbol{a}}_1 + n_2\hat{\boldsymbol{a}}_2) = l_\mathrm{b}(m_1\hat{\boldsymbol{b}}_1 + m_2\hat{\boldsymbol{b}}_2), \tag{C.3}$$

where n_1, n_2, m_1, m_2 represent the repetition along the corresponding versor of the unit cell of the first and second lattice, respectively. An overview of the matching condition is

given in Fig. C.1. This condition can be rewritten with a matrix formalism to:

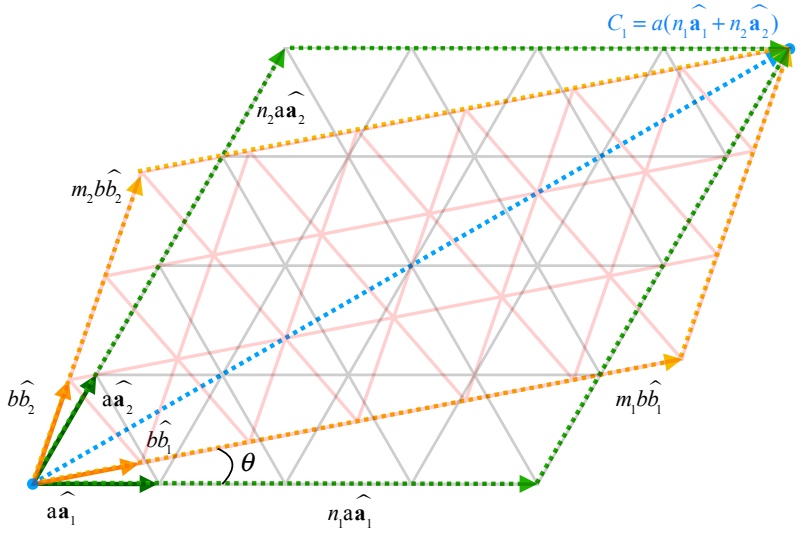

Figure C.1: Graphical overview of the matching condition Eq. (C.3) for unit cells with different lattice constant a and b at imposed angles θ. Coloured arrows refer to primitive, repeated and supercell lattices, as indicated by the labels. The low-opacity lines connect the points of the Bravais lattice described by the primitive vectors.

$$\begin{aligned} \frac{l_\mathrm{a}}{l_\mathrm{b}}(n_1\hat{\boldsymbol{a}}_1 + n_2\underline{\underline{R}}_\Omega \cdot \hat{\boldsymbol{a}}_1) &= m_1\underline{\underline{R}}_\theta \cdot \hat{\boldsymbol{a}}_1 + m_2\underline{\underline{R}}_\Omega \cdot \underline{\underline{R}}_\theta \cdot \hat{\boldsymbol{a}}_1 \\ \rho \begin{pmatrix} \mathbb{I} & \underline{\underline{R}}_\Omega \end{pmatrix} \cdot \begin{pmatrix} n_1 \\ n_2 \end{pmatrix} &= \begin{pmatrix} \mathbb{I} & \underline{\underline{R}}_\Omega \end{pmatrix} \cdot \begin{pmatrix} m_1 \\ m_2 \end{pmatrix} \cdot \underline{\underline{R}}_\theta \end{aligned} \tag{C.4}$$

where $\mathbb{I}$ is the identity matrix, we used the definition of the lattice vectors, introduced the mismatch ratio $\rho = l_\mathrm{a}/l_\mathrm{b}$, grouped the matrices and the indexes in vectors and simplified $\hat{\boldsymbol{a}}_1$ from both sides.

Albeit that the mismatch ratio of a system is fixed by the equilibrium values of the lattice parameters, it would be impractical to approximate a real number using integers, as the size of the supercells would easily exceed our computational capabilities. We follow the reverse procedure: given the four indexes $\{m_i, n_i\}_{i=1,2}$, we can invert the system and find the mismatch ratio ρ and the misalignment angle θ that satisfy the matching condition of Eq. (C.3). This means that now $\{m_i, n_i\}_{i=1,2}$ are fixed parameters of Eq. (C.3) while ρ is a variable, along with θ. Next, we find an expression for ρ and θ in terms of $\{m_i, n_i\}_{i=1,2}$ that satisfies Eq. (C.3). In the following paragraph, we address the problem of selecting sets of indices whose corresponding ρ, is close enough the real value fixed by the system ρ_0. We solve Eq. (C.4) for the matrix $\underline{\underline{R}}_\theta$ and for ρ under the constraint that $\underline{\underline{R}}_\theta$ is a rotation

matrix, namely:

$$\begin{cases} \underline{\underline{R}}_\theta = \rho \left(m_1 \mathbb{I} + m_2 \underline{\underline{R}}_\Omega \right)^{-1} \begin{pmatrix} \mathbb{I} & \underline{\underline{R}}_\Omega \end{pmatrix} \cdot \begin{pmatrix} n_1 \\ n_2 \end{pmatrix} \\ \det \underline{\underline{R}}_\theta = 1. \end{cases} \tag{C.5}$$

The first line in Eq. (C.5) is readily solved by

$$\begin{aligned} \underline{\underline{R}}_\theta &= \frac{\rho}{N_\mathrm{b}} \begin{pmatrix} m_1 n_1 + m_2 n_2 + 1/2(m_1 n_2 + m_2 n_1) & -\sqrt{3}/2(m_1 n_2 - m_2 n_1) \\ \sqrt{3}/2(m_1 n_2 - m_2 n_1) & m_1 n_1 + m_2 n_2 + 1/2(m_1 n_2 + m_2 n_1) \end{pmatrix} \\ &= \frac{\rho}{N_\mathrm{b}} \underline{\underline{A}}, \end{aligned} \tag{C.6}$$

where $N_\mathrm{b} = m_1^2 + m_2^2 + m_1 m_2$ is the number of Bravais lattice points in the b lattice [1] and $\underline{\underline{A}}$, implicitly defined in the last step, is a shorthand for the matrix of known coefficients. Substituting Eq. (C.6) into the second line of Eq. (C.5) yields an expression for ρ: $\det \underline{\underline{R}}_\theta = \frac{\rho^2}{N_\mathrm{b}^2} \det \underline{\underline{A}} = 1$. Substituting this back into Eq. (C.6) gives us the solution of (ρ, θ) of Eq. (C.3) at chosen $\{m_i, n_i\}_{i=1,2}$:

$$\begin{cases} \rho &= \frac{N_\mathrm{b}}{\sqrt{\det \underline{\underline{A}}}} \\ \theta &= (\underline{\underline{R}}_\theta)_{11} = \arccos\left(\frac{1}{\sqrt{\det \underline{\underline{A}}}} A_{11} \right) \end{cases} \tag{C.7}$$

Finally, the first vector of the supercell is given by the one of the members of the equality in Eq. (C.3) and the second is obtained by symmetry, namely

$$\boldsymbol{C}_1 = l_\mathrm{a}(n_1 \hat{\boldsymbol{a}}_1 + n_2 \hat{\boldsymbol{a}}_2) \tag{C.8}$$

$$\boldsymbol{C}_2 = \underline{\underline{R}}_\Omega \cdot \boldsymbol{C_1} = -l_\mathrm{a} n_1 \hat{\boldsymbol{a}}_1 + l_\mathrm{a}(n_1 + n_2)\hat{\boldsymbol{a}}_2. \tag{C.9}$$

In order to obtain a system with the desired misalignment θ and a ρ that is an acceptable approximation of the equilibrium mismatch ρ_0, we consider all combinations of integers $n_i,\ m_i$ within the range $(-200, 200)$ and select the supercells which satisfy $\theta \in [0°, 60°]$ and a mismatch ρ satisfying $|\Delta\rho| = |\rho - \rho_0| \leq 1 \times 10^{-7}$. We then bin the resulting supercells with a spacing of $\Delta\theta = 0.01°$ and select the cell with the smaller number of Bravais point within each bin. Note that this procedure does not guarantee that the resulting supercell will be evenly spaced according to the mismatch angle.

The indices defining the supercells used in this work for the MoS_2/G heterostructures are reported in Table C.1, along with the misalignment angle, $\rho - \rho_0$ and number atoms in each layer. For this system $\rho_0 = l_\mathrm{G}/l_{\mathrm{MoS_2}} = 2.460\,187\,8\,\text{Å}/3.093\,682\,7\,\text{Å} = 0.7952295$, the number of atoms in each lattice is given by the number of Bravais lattice points times the number of atoms in the crystal basis, i.e. $N_\mathrm{tot} = N_\mathrm{Bravais} \cdot n_\mathrm{basis}$ with n_basis is 2 and 3 for G and MoS_2, respectively. In creating the supercell, the strain due to the approximated

[1] An equivalent relation holds for the other lattice $N_\mathrm{a} = n_1^2 + n_2^2 + n_1 n_2$

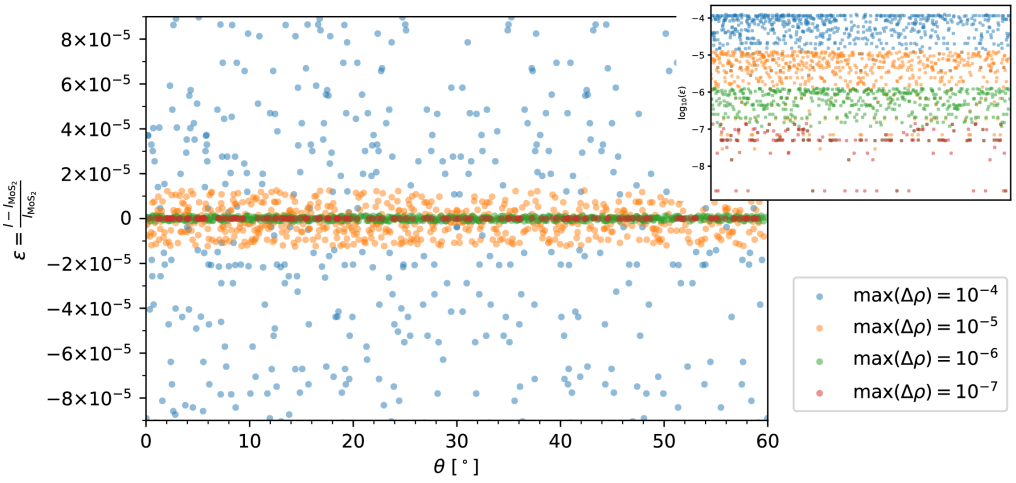

Figure C.2: Strain applied to MoS_2 lattice versus angle imposed to the supercell according to Eq. (C.7) for different values of tolerance. The tolerance value used in the work is $\Delta\rho = 1 \times 10^{-7}$. The value of the lattice parameters is obtained as $l = l_G/\rho$, where ρ is the solution of the Eq. (C.7). The inset in the upper right corner reports the logarithm of the absolute value of the strain ϵ and shows clearly that the spread is the magnitude of the residual strain.

mismatch ρ is applied to MoS_2. The residual strain for different value of the tolerance $\Delta\rho = \rho - \rho_0$ are reported in Fig. C.2.

$\theta[^\circ]$	n_1	n_2	m_1	m_2	$\rho - \rho_0$	N_G	N_{MoS_2}
0.23	**-135**	**-104**	**-108**	**-82**	**9.8e-08**	**86162**	**81732**
0.58	-192	61	-153	50	8.1e-08	57744	54774
0.79	-184	-41	-148	-30	9.8e-08	86162	81732
1.01	-113	-182	-86	-148	-6.2e-08	132916	126081
1.24	-176	-59	-137	-51	4.3e-09	89682	85071
1.39	-109	39	-87	33	-5.7e-08	18300	17361
1.60	-141	-128	-107	-107	2.6e-08	108626	103038
2.11	-138	-99	-104	-85	-2.2e-08	85012	80640
2.88	-184	-41	-140	-42	9.8e-08	86162	81732
3.05	-118	12	-96	15	9e-08	25302	24000
3.21	-182	-113	-134	-102	-6.2e-08	132916	126081
4.17	-184	33	-142	15	8.1e-08	57744	54774
4.93	-191	-48	-140	-55	3.5e-08	95904	90972
5.30	-192	61	-155	62	8.1e-08	57744	54774
5.34	-185	63	-149	63	4.6e-08	53076	50349
5.95	-164	-41	-118	-50	1.5e-08	70600	66969
6.23	-164	-115	-110	-113	6.2e-08	117960	111894
6.64	-123	-185	-71	-169	-8.8e-08	144216	136800
6.75	-164	-145	-154	-89	4.4e-08	143402	136029
7.18	-152	-99	-140	-55	3.5e-08	95906	90972
7.94	-172	169	-146	122	-8.3e-08	58152	55164

8.14	-118	12	-99	24	9e-08	25302	24000
8.42	-163	-125	-156	-68	-9.6e-08	125136	118704
8.64	-145	145	-104	124	1.2e-08	42048	39885
8.75	-138	-99	-85	-104	-2.2e-08	85012	80640
9.01	-184	33	-153	50	8.1e-08	57744	54774
9.04	-176	-59	-117	-76	4.3e-09	89682	85071
9.69	-172	169	-122	146	-8.3e-08	58152	55161
9.75	**-181**	**-95**	**-113**	**-110**	**6.2e-08**	**117960**	**111894**
10.25	-169	-174	-90	-178	7e-08	176484	167409
10.64	-181	-95	-110	-113	6.2e-08	117960	111894
10.81	-164	-145	-89	-154	4.4e-08	143402	136029
11.22	-174	-169	-90	-178	7e-08	176484	167409
11.37	-170	71	-130	31	-4.5e-08	43740	41493
12.17	-113	-182	-134	-102	-6.2e-08	132916	126081
12.27	-185	63	-138	19	4.6e-08	53076	50349
12.60	-192	61	-142	15	8.1e-08	57744	54774
12.99	-135	-104	-140	-42	9.8e-08	86162	81732
13.65	-118	12	-81	-15	9e-08	25302	24000
13.73	-184	33	-155	62	8.1e-08	57744	54774
14.52	-144	-98	-150	-31	1.7e-10	88904	84333
15.20	-184	33	-127	-15	8.1e-08	57744	54774
15.53	-185	63	-149	86	4.6e-08	53076	50349
15.63	-184	-41	-108	-82	9.8e-08	86162	81732
16.39	-182	-113	-86	-148	-6.2e-08	132916	126081
16.66	-135	-104	-148	-30	9.8e-08	86162	81732
17.14	-163	-125	-68	-156	-9.6e-08	125136	118704
17.26	-109	39	-87	54	-5.7e-08	18300	17358
18.47	-192	61	-155	93	8.1e-08	57744	54774
18.74	-118	12	-75	-24	9e-08	25302	24000
18.91	-41	-184	30	-178	9.8e-08	86162	81729
19.89	**-185**	**-123**	**-71**	**-169**	**-8.8e-08**	**144216**	**136800**
20.15	-184	-23	-101	-79	-7.1e-08	77232	73263
20.95	-187	-101	-75	-153	-5.7e-08	128114	121527
21.08	-152	-99	-55	-140	3.5e-08	95906	90972
21.47	-182	-23	-173	48	-8.3e-08	75678	71784
21.55	-135	-104	-42	-140	9.8e-08	86162	81732
22.24	-170	71	-130	99	-4.5e-08	43740	41493
22.58	-184	-41	-182	42	9.8e-08	86162	81732
23.03	-176	-59	-76	-117	4.3e-09	89682	85071
23.20	-192	61	-153	103	8.1e-08	57744	54774
23.63	-192	61	-127	-15	8.1e-08	57744	54774

24.25	-148	-132	-185	-15	-4.9e-08	117728	111675
24.67	-184	-41	-82	-108	9.8e-08	86162	81732
25.00	-113	-182	-174	-52	-6.2e-08	132916	126081
25.23	-135	-104	-30	-148	9.8e-08	86162	81732
26.82	-191	-48	-195	55	3.5e-08	95904	90972
26.86	-185	63	-119	-19	4.6e-08	53076	50349
27.05	-144	-98	-31	-150	1.7e-10	88904	84333
27.74	-164	-41	-168	50	1.5e-08	70600	66969
28.03	-148	-132	-15	-185	-4.9e-08	117728	111675
28.22	-184	-23	-79	-101	-7.1e-08	77232	73263
28.37	-184	33	-103	-50	8.1e-08	57744	54774
29.17	**-176**	**-59**	**-188**	**51**	**4.3e-09**	**89682**	**85071**
30.83	-176	-59	-51	-137	4.3e-09	89682	85071
31.63	-184	33	-153	103	8.1e-08	57744	54774
31.78	-23	-184	79	-180	-7.1e-08	77232	73260
31.97	-148	-132	-200	15	-4.9e-08	117728	111675
32.26	-164	-41	-50	-118	1.5e-08	70600	66969
32.95	-144	-98	-181	31	1.7e-10	88904	84333
33.14	-185	63	-138	119	4.6e-08	53076	50349
34.77	-104	-135	30	-178	9.8e-08	86162	81729
35.33	-41	-184	82	-190	9.8e-08	86162	81729
35.75	-148	-132	15	-200	-4.9e-08	117728	111675
36.37	-192	61	-142	127	8.1e-08	57744	54774
36.80	-192	61	-103	-50	8.1e-08	57744	54774
36.97	-59	-176	76	-193	4.3e-09	89682	85068
37.42	-184	-41	-42	-140	9.8e-08	86162	81732
37.76	-170	71	-99	-31	-4.5e-08	43740	41493
38.45	-135	-104	-182	42	9.8e-08	86162	81732
38.53	-23	-182	-125	-48	-8.3e-08	75678	71784
38.92	-152	-99	-195	55	3.5e-08	95906	90972
39.85	-23	-184	101	-180	-7.1e-08	77232	73260
41.09	-184	-41	-30	-148	9.8e-08	86162	81732
41.26	-118	12	-99	75	9e-08	25302	24000
41.53	-192	61	-93	-62	8.1e-08	57744	54774
42.74	-109	39	-54	-33	-5.7e-08	18300	17361
43.34	-135	-104	30	-178	9.8e-08	86162	81729
44.37	-41	-184	108	-190	9.8e-08	86162	81729
44.47	-185	63	-86	-63	4.6e-08	53076	50349
44.80	-184	33	-142	127	8.1e-08	57744	54774
45.48	-144	-98	31	-181	1.7e-10	88904	84333
46.27	-184	33	-62	-93	8.1e-08	57744	54774

46.35	-118	12	-96	81	9e-08	25302	24000
47.01	-135	-104	42	-182	9.8e-08	86162	81732
47.40	-192	61	-127	142	8.1e-08	57744	54774
47.73	-185	63	-119	138	4.6e-08	53076	50349
48.63	-170	71	-99	130	-4.5e-08	43740	41493
50.31	-172	169	-146	24	-8.3e-08	58152	55164
50.99	-184	33	-50	-103	8.1e-08	57744	54774
51.20	-104	-135	82	-190	9.8e-08	86162	81729
51.25	-138	-99	-189	85	-2.2e-08	85012	80640
51.36	-145	145	-124	20	1.2e-08	42048	39885
51.86	-118	12	-24	-75	9e-08	25302	24000
52.06	-172	169	-24	146	-8.3e-08	58152	55161
52.82	-152	-99	55	-195	3.5e-08	95906	90972
54.05	-164	-41	-168	118	1.5e-08	70600	66969
54.66	-185	63	-63	-86	4.6e-08	53076	50349
55.07	-191	-48	-195	140	3.5e-08	95904	90972
55.83	-184	33	-127	142	8.1e-08	57744	54774
56.95	-118	12	-15	-81	9e-08	25302	24000
57.12	-184	-41	-182	140	9.8e-08	86162	81732
57.89	-138	-99	-189	104	-2.2e-08	85012	80640
58.61	-109	39	-33	-54	-5.7e-08	18300	17358
58.76	-176	-59	-188	137	4.3e-09	89682	85071
59.21	-184	-41	30	-178	9.8e-08	86162	81729
59.42	-192	61	-50	-103	8.1e-08	57744	54774
59.77	-135	-104	82	-190	9.8e-08	86162	81729

Table C.1: Parameters of the rotated supercells used in this work. The lines relative to the four geometries shown in Figure 5 in the main text are highlighted in bold font.

D

Force-Field Parametrization and Benchmark

The G layer is modelled with the REBO potential [172], while the 3-body Stillinger-Weber (SW) potential [171] is used for MoS_2. Interlayer coupling is described by the Lennard-Jones (LJ) potential

$$\begin{aligned} H_{\mathrm{L_1L_2}} &= H^{(\mathrm{LJ})}_{\mathrm{C-(Mo,S)}} \\ &= \sum_{\substack{i\in\mathrm{C} \\ j\in\mathrm{Mo,S}}} 4\epsilon_{ij}\left[\left(\frac{\sigma_{ij}}{r_{ij}}\right)^{12} - \left(\frac{\sigma_{ij}}{r_{ij}}\right)^{6}\right]. \end{aligned} \tag{D.1}$$

The intralayer force fields were benchmarked against experimental results and first principle calculations at DFT level. DFT calculations were performed using using the Vienna *Ab initio* Simulation Package (VASP) [198, 199] within the Projector Augmented-Wave (PAW) framework [124]. The exchange-correlation potential is approximated using the PBE functional [127] and the vdW dispersion is described by the DFT-D2 method [130]. A plane wave cut-off of 800 eV is adopted and the Brillouin zone was sampled using a $13 \times 13 \times 1$ mesh. The results on lattice parameters were deemed satisfactory. Since interlayer interactions are especially relevant for the aim of this work and the LJ parameters reported in Ref. [171] yield unsatisfactory results, it was deemed necessary to conduct a more accurate parametrisation, reported in the following section.

	SW	REBO	DFT	Experimental
Lattice constant graphene(Å)	-	2.4602	2.4668	2.4589 [283],2.464(2) [284]
Lattice constant MoS_2 (Å)	3.0937	-	3.1901	3.15 [285],3.1625 [286]
C-C bond distance (Å)	-	1.4204	1.4242	-
Mo-S bond distance (Å)	2.3920	-	2.4112	-

Table D.1: Structural parameters obtained using the SW model for MoS_2, the REBO model for graphene together with reference data from X-ray diffraction experiments and density functional theory (DFT) calculations. The DFT results were obtained using the computational details reported in Appendix D.

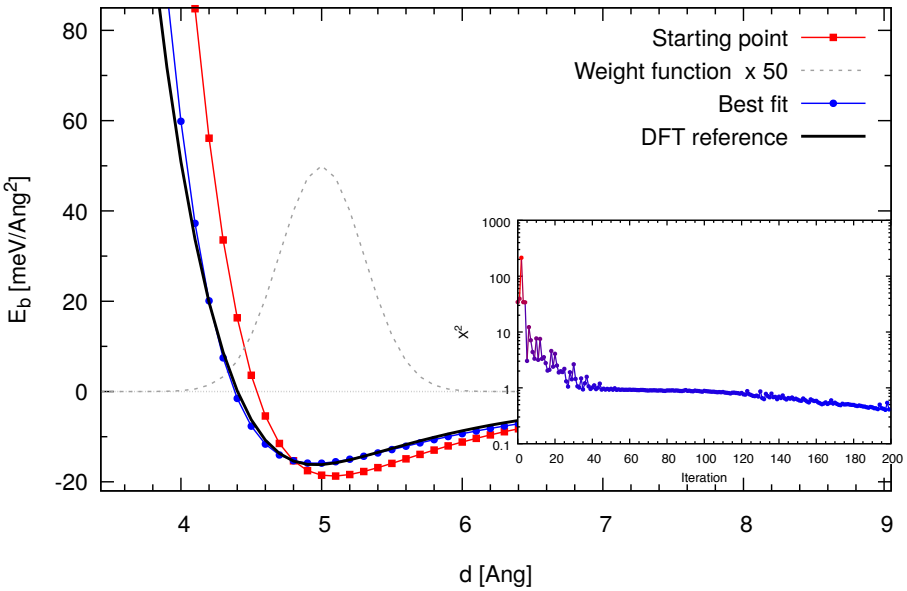

Figure D.1: Refining of LJ-parameters. Energy, in meV/area versus the interlayer distance, in $\mathring{A}$. The black line is the reference BEP from DFT, whereas the red and the blue line are the starting and final binding energies obtained with LAMMPS, respectively. The dashed line represents the weight function around the energy minimum enhanced by a factor of 50, as guide for the eye. The inset shows the goal function χ^2 versus the number of the iterations of the optimization algorithm.

Force Field refinement

In order to improve the unsatisfactory inter-layer description, binding energy profiles (BEP) of the MoS_2/G bilayer system were computed at DFT level used as reference set for the minimisation protocol. The parameters provided in Ref. [171] were used as starting point for the minimisation.

The Simplex algorithm [287] as implemented in SciPy [288] was used as a non-gradient-based minimisation method. This algorithm samples the N-dimensional (N=number of LJ parameters) phase space using a convex polygon. This algorithm acts on the following goal function:

$$\chi^2[f_L] = \frac{1}{W}\int_0^\infty |f_{\mathrm{DFT}}(r) - f_L(r)|^2 w(r)\mathrm{d}r \tag{D.2}$$

which is a squared distance combined with a weight function $w(r)$. The function f_{DFT} is the reference, in our case the Lennard-Jones binding energy profile from DFT, whereas f_L

is same binding energy profile computed with LAMMPS using the current ϵ and σ. The weight function $w(r) = \exp[-(\frac{r-r_0}{\zeta})^2]$ ensures that the most relevant part, the minimum of the Lennard-Jones at $r_0 = 4.94$ Å and its directs surroundings, are represented correctly. The amplitude of the relevant interval around the minimum is tuned with the ζ parameter. In the computation of binding energy profiles the interlayer distance between G and MoS_2 is fixed by freezing in the z direction C atoms and the outermost S layer of MoS_2. The heterostructure used as reference comprises 4×4 MoS_2 unit cell repetition and a 5×5 G unit cell repetition, where the residual stress of 2.6% is applied to MoS_2. The optimised parameters are reported in Table D.2. Fig. D.1 shows the optimised BEP, along with reference and starting point, and the minimisation performance.

Optimized LJ Parameters			
Atoms	ϵ [meV]	σ [Å]	ζ [Å]
C-S	1.64	3.640	0.30
C-Mo	4.55	4.391	0.30

Table D.2: Optimized LJ Parameters for the interlayer interaction between G and MoS_2.

Phonon band structure

Phonon bands were computed with the aid of Phonopy [151], which was coupled to LAMMPS using phonoLAMMPS [289]. In both DFT and classical cases the phonon dispersion was computed using the frozen method employing a 5x5x1 supercell.

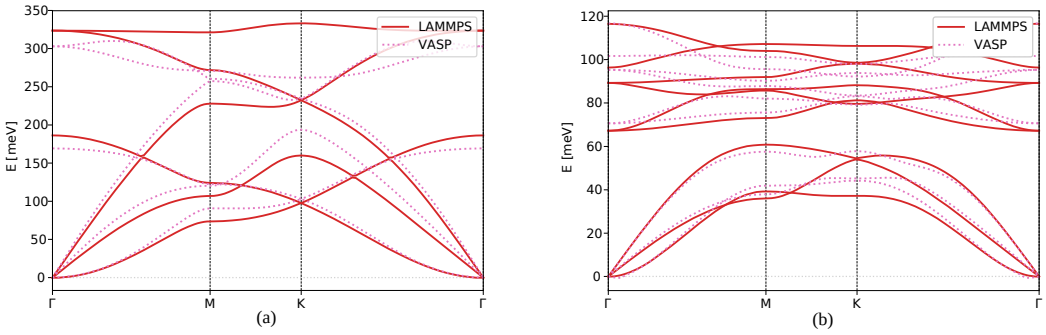

(a) **(b)**

Figure D.2: Phonon band structure of (a) G and (b) MoS_2 computed with LAMMPS (solid lines) and VASP (dashed lines). The y axis reports the phonon energy, while the x axis marks the distance from the origin along the path $\Gamma \to M \to K \to \Gamma$.

Fig. D.2 reports the phonon band structure along the path $\Gamma \to M \to K \to \Gamma$ of G and MoS_2, panels Fig. D.2a and Fig. D.2b respectively, allowing one to compare phonon dispersion computed from quantum forces, at the DFT level, and from classical forces. Acoustic models from quantum and classical dispersion are in good agreement around Γ, the centre of the Brillouin zone. Thus, the long wavelength distortions at the base of NM theory are well-described by the classical force fields. Moving towards the edge of the cell, i.e. distortions occurring over shorter wavelength, the two dispersion deviate. For example,

the splitting of quantum-computed transverse and longitudinal branches observed at M point in G is shifted to a different k in the classical results. Similar observations can be made for the region around K and for the MoS_2 phonon bands. The general trend is that the classical treatment underestimates the energy of acoustic branches and overestimates the optical ones. However, strong quantitative agreement is not needed for the qualitative statements developed in the following discussion and, in order to obtain the sound velocity needed as input of the NM theory, only an accurate description around the Γ point is required.

E

Software: VASP

Many softwares with different implementations of DFT outlined section 2.1 are available, each one characterised by its "dialect". In this work DFT are carried out using the Vienna *ab initio* Software Package (VASP) [197, 119, 198, 199], which is based on a plane-wave expansion of KS orbitals, relies on PP and provides a selection of difference exchange-correlation functionals adn vdW corrections. In this section we report the parameters and technical details used in this work.

All simulations are spin polarised. The tetrahedron smearing with Bloch corrections of amplitude 0.05 eV is used with semiconductors to avoid discontinuity in the energy level occupancy and ease the integration in the BZ. In chapter 4, a Gaussian smearing of 0.05 eV is used, as the metal or semiconductor nature of the large set of compounds studied is unknown. The Pseudo-Potential problem is treated in the augmented-plane wave (PAW) formalism [124, 200]. For the sulfur atoms only the outer p orbitals are considered as valence and for the transition metals the outer s, p and d electron orbital constitute the valence shell. In relaxations, ions positions are optimised using a conjugate gradient algorithm. Depending on the calculations, either all the degrees of freedom, i.e. ions position, cell shape and cell volume, or ions positions only are relaxed; this difference is specified case by case in the main text.

Parallelization Benchmark on Iridis5 HPC In order to test the parallel performances of VASP and define the optimal setup for our machine, we perform a self consistent cycle of fixed length varying the input parameter controlling the numerical aspect of the code. Fig. E.1a shows the N^3 scaling with the system size while Fig. E.1b shows the scaling at fixed system size with the number of cores. Even though in principles there would be

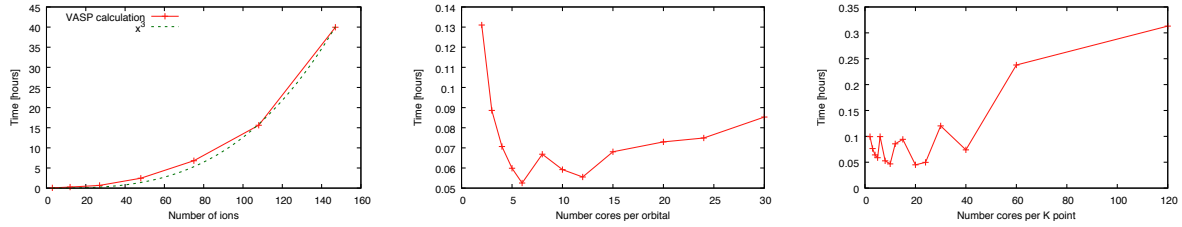

(a) **(b)** **(c)**

Figure E.1: (a) Simulation time versus system size in number of ions. The green dashed line represents a scaling behaviour N^3. (b) Simulation time as function of the number of cores allocated for the computation. (c) Simulation time as function of the number of orbitals treated in parallel.

no limit to the number of cores one could use, the time required to share information between the threads limits this number: on the University of Southampton HCP Iridis5 a Parallelization over 80-120 cores yields the best results for system of 10-30 atoms, while single node jobs (40 cores) suffice for smaller systems of up to 10 atoms. At fixed system size and core number, Fig. E.1c shows the simulation time as function of the number of cores working in parallel on each orbital. Spreading each orbital over ≈ 10 cores yields the best results.

Exchange-correlation Functional Convergence

Following the works by Perdew *et al.* [129] and Bjorkamn *et al.* [290], we use SCAN meta-GGA functional in combination with rVV10 correction for long-ranged vdW interactions. We adopt the values for $C_{\text{vv10}} = 0.0093$ and $b_{\text{vv10}} = 15.6$ used in the Ref. [129]. Being semiconductors with covalent bonds but small bandgaps, TMDs are in between the localised picture implemented in local basis sets, suitable for ionic materials like rock-salts, and the delocalised one of the plane-wave set, suitable for metals. Li *et al.* [291] studied the properties of TMDs and transition metal oxides as function of the functional and the basis set used. They found that, while there is a strong dependence on the functional used, plane-wave are suitable to describe TMDs. Since we want to resolve vdW interaction, which are in the order of 10 meV, we set the tolerance on electrons energy at 1 meV per atom. We found that a tolerance of 1×10^{-4} eV yields satisfying results on the ions minimisation.

SCAN+rVV10 Convergence We test our protocol on two element of the TMDs family: MoS_2 and TiS_2. Experimental results are taken as starting configuration for our calculations. Before optimising the structures, we study the convergence of the total energy with respect to the size plane-wave basis set used in the expansion of the Kohn orbitals and the density of the grid used to sample the reciprocal space. We adopt a cutoff of $E_{\text{cutoff}} = 800$ eV in accordance with Fig. E.2a, which shows difference in total energy between the two systems as function of the energy cutoff of the plane waves[1]. Fig. E.2b shows the convergence of total energy against the number of division in the BZ along each

[1]The error in truncating the basis set is a systematic one and thus it is relevant to check the relative convergence over different systems instead of the absolute one

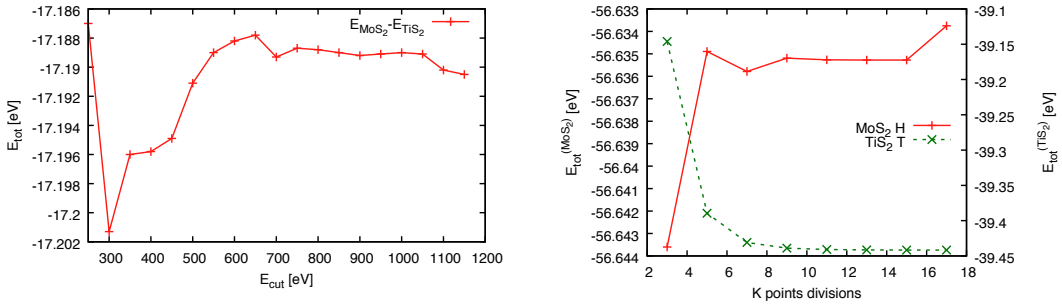

(a) **(b)**

Figure E.2: (a) Total energy difference between H2 MoS_2 and T1 TiS_2 versus the energy cutoff E_{cut}. (b) Total energy versus the number of divisions along each direction in the BZ within a unit cell of prismatic 2H-MoS_2 and octahedral 1T-TiS_2.

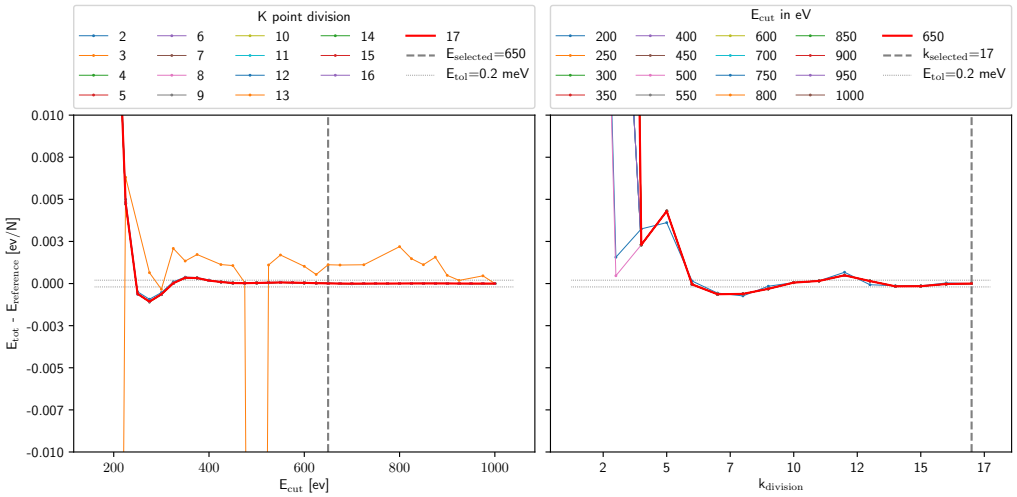

Figure E.3: Convergence study for $CrSe_2$ in octahedral (CdI_2) coordination. (a) Total energy as a function of the energy cutoff E_{cut} for various sampling densities, as reported in the legend. The dashed horizontal line report a threshold value for the total energy accuracy of $E_{\text{tol}} = 0.2\,\text{meV}$. The dashed vertical line marks the adopted value $E_{\text{cut}} = 650\,\text{eV}$. (b) Total energy as a function of the sampling density for various E_{cut}, as reported in the legend. The dashed vertical line marks the adopted value $N_k = 17$.

direction. The total energy does not vary appreciably for more than 11 division [2], which is the value adopted in this work.

PBE Convergence In exploring vast class of materials in HT approach and a coherent DFT parametrisation is needed. Thus, we performed a similar convergence study on a simpler function, PBE [127]. The analysis was carried out on 60 ML reported in Ref. [21]. Fig. E.3 reports an example of this convergence study for $CrSe_2$ in octahedral (CdI_2) coordination. We adopt a cutoff of $E_{\text{cutoff}} = 650\,\text{eV}$ and sample the BZ with a $17 \times 17 \times 1$ mesh. The larger mesh compared to the SCAN parameters is required as some material show a metallic character. The absence of repetition in the k_z direction is dictated by the ML geometry studied.

[2] This correspond to 6600 k-point-per-atom

Compound	a	Reference	c	Reference
MoS_2	3.168	3.161 [230]	12.522	12.295 [230]
TiS_2	3.4085	3.4097 [231]	5.7471	5.7052 [231]

Table E.1: Intralayer a and interlayer c lattice parameters from simulations and references in $\AA$. Intralayer lattice parameter a is within 0.03% and 0.2% of the experimental measured value for TiS_2 and MoS_2, respectively, while the interlayer one c is within 0.7% and 1.8% for TiS_2 and MoS_2, respectively.

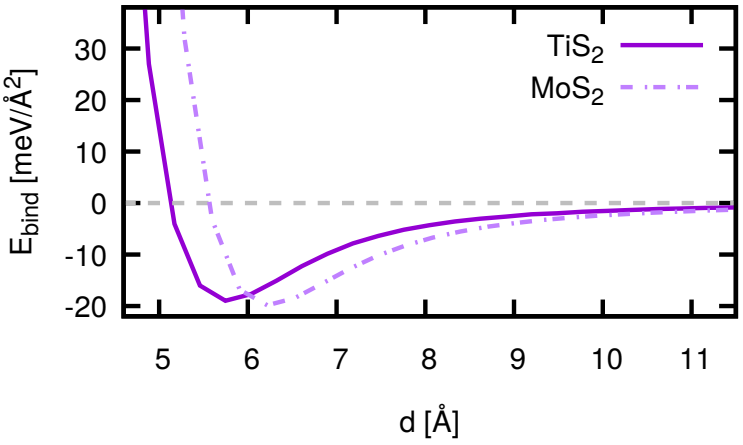

Figure E.4: The BE $E_{\text{bind}}(d)$ of MoS_2 and TiS_2.

Material Properties Benchmark

A relaxation of both ions positions and cell vectors yields the parameters reported in Table E.1.

Binding Energy Profile To estimate the accuracy of our vdW description, we check the binding energy profile defined as $E_{\text{bind}}(d) = E(d) - E(\infty)$ and reported in Fig. E.4. Our protocol is to fix the distance between the layer by rigidly shifting the layers and freezing the z coordinate of the metal ion while all the remaining degrees of freedom are let free to relax. Table E.2 reports the minimum of this profile, which is the binding energy keeping the layers together in the bulk system.

Band Structure Once we have a relaxed structure, we can check that the electronic properties of the system. Fig. E.5b and Fig. E.5c report the band structure and density of state (DOS) of 2H-MoS_2 and 1T-TiS_2, respectively. As a general remark, we note that overlap in the DOS between d metal orbitals and p chalcogenides ones confirms the covalent

Compound	$E_{\text{bind}}(d_{\text{min}})$	Reference
MoS_2	-19.86	-20.53
TiS_2	-18.98	-18.88

Table E.2: Minimum of the BE in meV as computed in this work and reference values from RPA calculation [129].

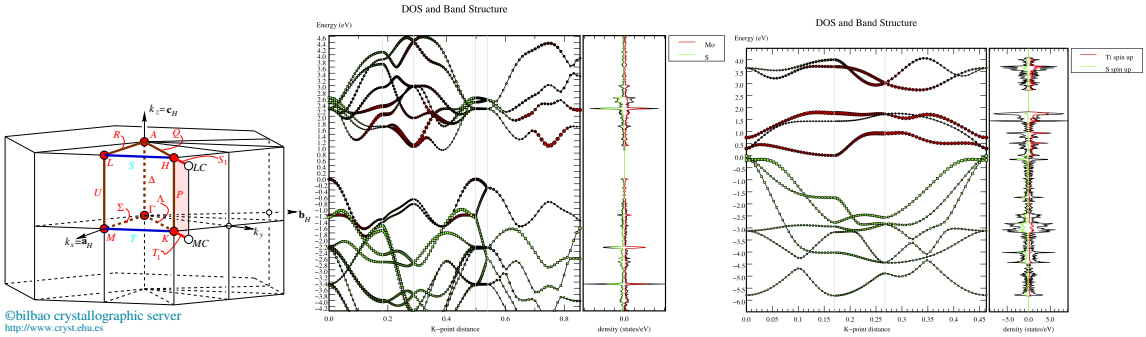

(a) **(b)** **(c)**

Figure E.5: (a) The BZ relative to the hexagonal primitive cell of MoS_2 (space group n. 194) and TiS_2 (space group n. 164). Band structure along the path $\Gamma \to M \to K \to \Gamma \to A \to L$ (each point is marked by a vertical line) within the cell reported in Fig. E.5a and DOS obtained with the SCAN+rVV10 protocol for (b) 2H-MoS_2 and (c) TiS_2. The red and green points represent the projection of the states onto the Mo and S atoms, respectively.

nature of the interaction.

The computed band gap for bulk 2H-MoS_2 of 1 eV underestimate the experimental value of 1.29 eV [16]. The value bandgap of TiS_2 is still debated varying from 0.05 eV to 2.5 eV depending on the experimental technique used [292, 293]. From computational investigation, the material is predicted to be semimetallic and a semiconductor, when going from LDA to hybrid functional. In our simulations TiS_2 is semimetallic, with a small overlap between the minimum of the conduction band at M and the maximum of the valence band at Γ.

F

Software: Phonopy

Phonons dispersion are obtained using the Parlinksi-Li-Kawazoe method [294] as implemented in the Phonopy package [151]. This method is a numerical approach to fit force constants $\underline{\underline{P}}$ from forces $\boldsymbol{F}$ and displacements $\boldsymbol{\Delta}$. The relation for a pair of atoms i and j can be cast in the matrix form

$$\boldsymbol{F} = -\boldsymbol{\Delta} \cdot \underline{\underline{P}}, \tag{F.1}$$

where $\boldsymbol{F}$, $\boldsymbol{\Delta}$ and $\underline{\underline{P}}$ are given by

$$F = \begin{pmatrix} F_x & F_y & F_z \end{pmatrix} \tag{F.2}$$

$$P = \begin{pmatrix} \phi_{xx} & \phi_{xy} & \phi_{xz} \\ \phi_{yx} & \phi_{yy} & \phi_{yz} \\ \phi_{zx} & \phi_{zy} & \phi_{zz} \end{pmatrix} \tag{F.3}$$

$$\boldsymbol{\Delta} = \begin{pmatrix} \Delta r_x & \Delta r_y & \Delta r_z \end{pmatrix}. \tag{F.4}$$

This relation can then be inverted to obtain the force constants $\underline{\underline{P}} = -\boldsymbol{\Delta}^\dagger \boldsymbol{F}$. The number of displacements needed by the fitting procedure is reduce by exploiting the symmetry crystal and the force constants are then used to compute the dynamical matrix $\underline{\underline{D}}$ in Eq. (2.109) and from there the dispersion relation between $\boldsymbol{k}$ and ω and all other properties.

Fig. F.1a reports the dispersion relation for a MoS_2 bulk crystal in the H2 configuration. The dispersion is in agreement with literature [80, 295]: all frequencies are positive, indicating a stable structure, acoustic modes vanish at Γ point and we find the "sliding modes", with frequencies at Γ between 1 THz and 2.4 THz. To test ability to predict unstable structures of this protocol, we computed the phonon dispersion of MoS_2 bulk

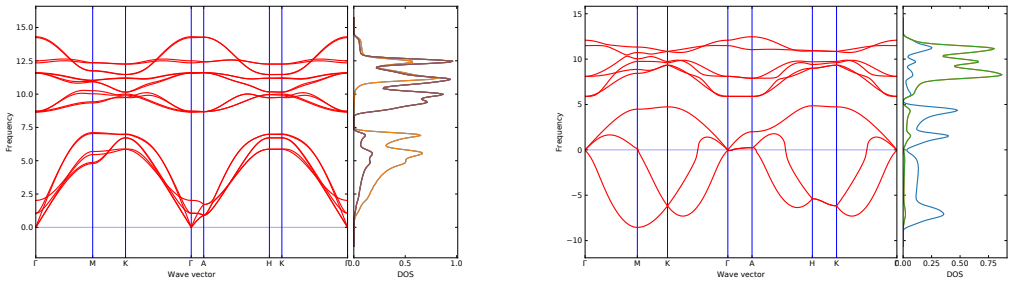

(a) 2H **(b)** 1T

Figure F.1: The phonon dispersion relation and DOS of (a) MoS_2 2H ans (b) artificial MoS_2 T1 crystals computed with SCAN+rVV10 protocol. The path is along the symmetry point of the BZ in Fig. E.5a. Forces are computed in a $2 \times 2 \times 2$ supercell. The dispersion is interpolated on a $41 \times 41 \times 41$ grid.

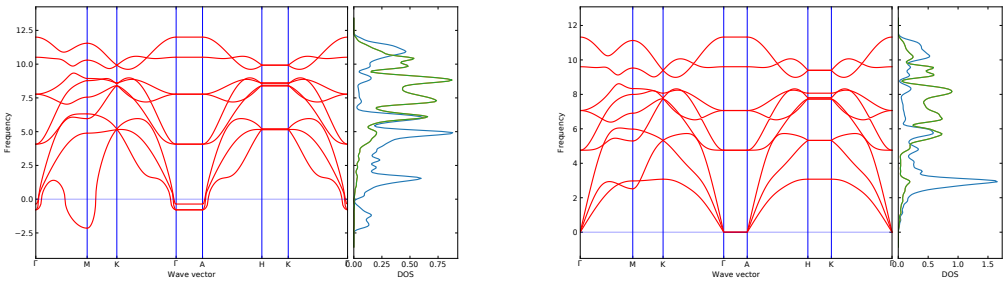

(a) **(b)**

Figure F.2: The phonon dispersion relation and DOS of TiS_2 T1 crystal computed with (a) SCAN+rVV10 and (b) GGA functional and Hubbard correction (GGA+U) $U = 2\,\text{eV}$ protocols. The path is along the symmetry point of the BZ in Fig. E.5a. The phonon displacements are relative to the primitive cell of the T1 polytope but forces are computed in a $2 \times 2 \times 1$ supercell to improve the accuracy on the forces. The lack of replicas along the z direction yields the flat behaviour $\Gamma \to A$; this choice was made to study the CDW instability in the x-y plane. The dispersion is interpolated on a $20 \times 20 \times 20$ grid. Note that in (b) the instability at the M point is gone, but the branch curvature changes sing at this point and the phonon frequencies are lowered, an effect known as Kohn anomaly.

crystal in the T1 configuration, known to be unstable at 0 K. Negative frequencies[1] in Fig. F.1b signal that the structure is indeed unstable: if one were to displace the atoms along the polarisation vector relative to negative frequencies, there would be no recoil force bringing them back to the equilibrium position, and they would be attracted by the real minimum in the configurational space, the prismatic configuration.

Fig. F.2a reports the dispersion relation for a TiS_2 bulk crystal in the H2 configuration. The negative frequencies around the Γ and M points suggest this is an unstable structure. This is in contrast with experimental observation of octahedral coordination of TiS_2.

How do we explain this? This soft mode was previously reported in literature only by Dolui and Sanvit [292], to our knowledge. The authors attribute the instability to a CDW: layered TMDs show strong electron-phonon coupling and CDW ground state

[1]Negative frequencies correspond to imaginary frequency coming from the square root of a negative eigenvector of the dynamical matrix

are found for $TaSe_2$ and $NbSe_2$. The soft mode at M corresponds to a CDW wave vector $q_{\mathrm{CDW}} = \pi/a \begin{pmatrix} 1/2 & 0 & 0 \end{pmatrix}$. Using the LDA functional, the authors found that the system gets stabilised in a 2x2 supercell with the distorted geometry found at the M point: imaginary frequencies disappear and CDW configuration sits 0.85 meV lower than undistorted one. We are currently running simulation to confirm that these results holds with the SCAN+rVV10 protocol. This distortion might be important in all range of TMDs [296] and one should look out for this kind of dynamic instabilities while carrying out DFT simulations. Dolui and coworkers also noted that this instability is stabilised by localising the electrons. As shown in Fig. F.2b, we find as well that the addition of a Hubbard correction $U = 2\,\mathrm{eV}$ that localises the electrons on the Ti atoms removes the instability: electrons are forced to stay around the metal ion, the long range distortion cannot take place and, as a result, all frequencies are positive. This is in agreement with the observation that Khon anomalies, a lowered phonon frequency at a specific $\boldsymbol{k}$ point, can only appear in metallic systems, while the Hubbard correction opens a gap in the electronic structure.

G

Software: ATAT

Since the parametrisation of the CE involves supercell of different size, to be consistent we kept the number of **k** point per atom constant to 6600 through the work. CE models presented in section 2.2 comprise clusters of maximum four points. Bulk models are trained with 113 and 57 structures for 1T and 2H, respectively. Models of the 2D counterparts are trained using 46 and 39 structures for 1T and 2H cases.

Accuracy of the Monte Carlo simulations is affected by finite size effects and it is necessary to study the convergence of quantities of interest against the size of the system. Figures G.1a and G.1b report the convergence study in the two hosts: for MC simulation in the 1T host we adopt a cell containing 4851 atoms and one containing 21904 atoms for the 2H host.

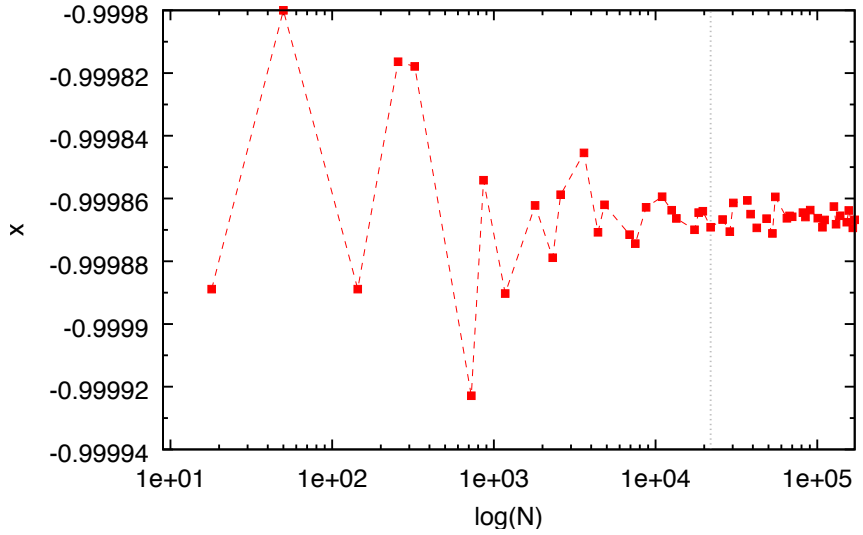

(a)

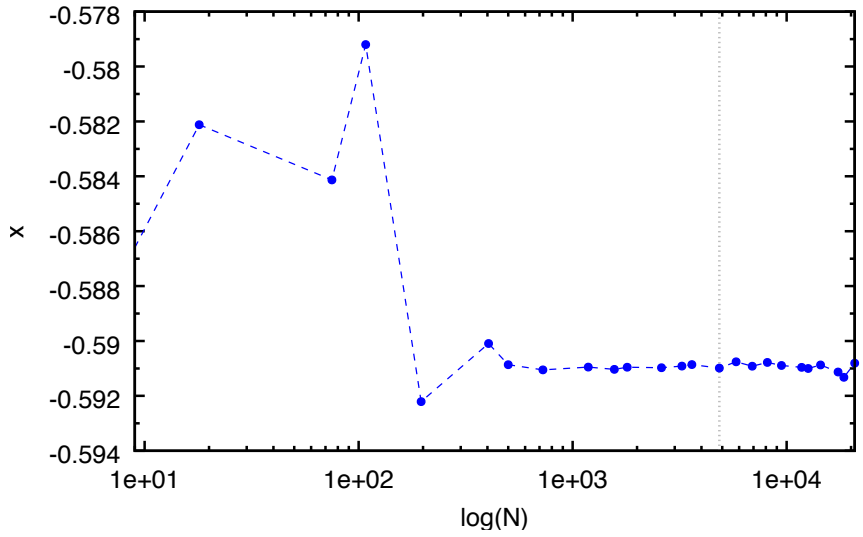

(b)

Figure G.1: Variation of equilibrium concentration in MC simulations as function of the system size in (a) 2H and (b) 1T hosts. Dashed lines are a guide for the eye. Grey vertical line marks the system size chosen for the rest of the simulations.

Bibliography

[1] Andrea Silva, Tomas Polcar, and Denis Kramer. Phase behaviour of (Ti:Mo) S2 binary alloys arising from electron-lattice coupling. *Computational Materials Science*, 186(July 2020):110044, 1 2021.

[2] Andrea Silva, Victor E. P. Claerbout, Tomas Polcar, Denis Kramer, and Paolo Nicolini. Exploring the Stability of Twisted van der Waals Heterostructures. *ACS Applied Materials & Interfaces*, 12(40):45214–45221, 10 2020.

[3] K S Novoselov, A K Geim, S V Morozov, D Jiang, Y Zhang, S V Dubonos, I V Grigorieva, and A A Firsov. Electric field in atomically thin carbon films. *Science*, 306(5696):666–669, 10 2004.

[4] Manish Chhowalla, Hyeon Suk Shin, Goki Eda, Lain-Jong Li, Kian Ping Loh, and Hua Zhang. The chemistry of two-dimensional layered transition metal nanosheets. *Nature Chemistry*, 5(4):263–275, 2013.

[5] Edmund Han, Jaehyung Yu, Emil Annevelink, Jangyup Son, Dongyun A. Kang, Kenji Watanabe, Takashi Taniguchi, Elif Ertekin, Pinshane Y. Huang, and Arend M. van der Zande. Ultrasoft slip-mediated bending in few-layer graphene. *Nature Materials*, 19(3):305–309, 2020.

[6] Andrea Cepellotti and Nicola Marzari. Thermal transport in crystals as a kinetic theory of relaxons. *Physical Review X*, 6(4), 2016.

[7] Shuai Zhang, Tianbao Ma, Ali Erdemir, and Qunyang Li. Tribology of two-dimensional materials: From mechanisms to modulating strategies. *Materials Today*, 26:67–86, 6 2019.

[8] Itai Leven, Dana Krepel, Ortal Shemesh, and Oded Hod. Robust Superlubricity in Graphene/ h -BN Heterojunctions. *The Journal of Physical Chemistry Letters*, 4(1):115–120, 1 2013.

[9] B. Radisavljevic, A. Radenovic, J. Brivio, V. Giacometti, and A. Kis. Single-layer MoS2 transistors. *Nature Nanotechnology*, 6(3):147–150, 3 2011.

[10] Sharon Mitchell and Javier Pérez-Ramírez. Single atom catalysis: a decade of stunning progress and the promise for a bright future. *Nature Communications*, 11(1):10–12, 2020.

[11] Anton Van Der Ven, Zhi Deng, Swastika Banerjee, and Shyue Ping Ong. Rechargeable Alkali-Ion Battery Materials: Theory and Computation, 7 2020.

[12] Silvia Milana. The lab-to-fab journey of 2D materials. *Nature Nanotechnology*, 14(10):919–921, 2019.

[13] Frank Schwierz. Graphene transistors. *Nature Nanotechnology*, 5(7):487–496, 2010.

[14] Gordon E. Moore. Cramming more components onto integrated circuits, Reprinted from Electronics, volume 38, number 8, April 19, 1965, pp.114 ff. *IEEE Solid-State Circuits Society Newsletter*, 11(3):33–35, 9 2006.

[15] CORDIS. SGA-FET-GRAPHENE-2-2019 - Experimental pilot line for devices based on graphene, related 2d materials and heterostructures CORDIS, 2019.

[16] Qing Hua Wang, Kourosh Kalantar-Zadeh, Andras Kis, Jonathan N. Coleman, and Michael S. Strano. Electronics and optoelectronics of two-dimensional transition metal dichalcogenides. *Nature Nanotechnology*, 7(11):699–712, 2012.

[17] E. W. Roberts. Thin solid lubricant films in space. *Tribology International*, 23(2):95–104, 1990.

[18] Kazumasa Shinjo and Motohisa Hirano. Dynamics of friction: superlubric state. *Surface Science*, 283(1-3):473–478, 3 1993.

[19] Yiming Song, Davide Mandelli, Oded Hod, Michael Urbakh, Ming Ma, and Quanshui Zheng. Robust microscale superlubricity in graphite/hexagonal boron nitride layered heterojunctions. *Nature Materials*, 17(10):894–899, 10 2018.

[20] European Union's Horizon 2020. SOLUTION ITN, 2017.

[21] Nicolas Mounet, Marco Gibertini, Philippe Schwaller, Davide Campi, Andrius Merkys, Antimo Marrazzo, Thibault Sohier, Ivano Eligio Castelli, Andrea Cepellotti, Giovanni Pizzi, and Nicola Marzari. Two-dimensional materials from high-throughput computational exfoliation of experimentally known compounds. *Nature Nanotechnology*, 13(3):246–252, 3 2018.

[22] Murat Cihan Sorkun, Séverin Astruc, J. M.Vianney A. Koelman, and Süleyman Er. An artificial intelligence-aided virtual screening recipe for two-dimensional materials discovery. *npj Computational Materials*, 6(1):1–10, 2020.

[23] Jiadong Zhou, Junhao Lin, Xiangwei Huang, Yao Zhou, Yu Chen, Juan Xia, Hong Wang, Yu Xie, Huimei Yu, Jincheng Lei, Di Wu, Fucai Liu, Qundong Fu, Qingsheng Zeng, Chuang Han Hsu, Changli Yang, Li Lu, Ting Yu, Zexiang Shen, Hsin Lin, Boris I. Yakobson, Qian Liu, Kazu Suenaga, Guangtong Liu, and Zheng Liu. A library of atomically thin metal chalcogenides. *Nature*, 556(7701):355–359, 2018.

[24] Haimei Qi, Lina Wang, Jie Sun, Yi Long, Peng Hu, Fucai Liu, and Xuexia He. Production Methods of Van der Waals Heterostructures Based on Transition Metal Dichalcogenides. *Crystals*, 8(1):35, 2018.

[25] A K Geim and I V Grigorieva. Van der Waals heterostructures. *Nature*, 499(7459):419–425, 7 2013.

[26] Yuan Cao, Valla Fatemi, Shiang Fang, Kenji Watanabe, Takashi Taniguchi, Efthimios Kaxiras, and Pablo Jarillo-Herrero. Unconventional superconductivity in magic-angle graphene superlattices. *Nature*, 556(7699):43–50, 2018.

[27] M. Angeli, E. Tosatti, and M. Fabrizio. Valley Jahn-Teller Effect in Twisted Bilayer Graphene. *Physical Review X*, 9(4):041010, 10 2019.

[28] Nick Bultinck, Eslam Khalaf, Shang Liu, Shubhayu Chatterjee, Ashvin Vishwanath, and Michael P. Zaletel. Ground State and Hidden Symmetry of Magic Angle Graphene at Even Integer Filling. *Physical Review X*, 10(3):31034, 2019.

[29] Rebeca Ribeiro-Palau, Changjian Zhang, Kenji Watanabe, Takashi Taniguchi, James Hone, and Cory R. Dean. Twistable electronics with dynamically rotatable heterostructures. *Science*, 361(6403):690–693, 8 2018.

[30] Wang Yao, Xiaodong Xu, Gui-bin Liu, Jianju Tang, and Hongyi Yu. Moiré excitons: From programmable quantum emitter arrays to spin-orbit–coupled artificial lattices. *Science Advances*, 3(11):e1701696, 2017.

[31] D. D.L. Chung. Review: Graphite. *Journal of Materials Science*, 37(8):1475–1489, 2002.

[32] Kian Ping Loh, Qiaoliang Bao, Priscilla Kailian Ang, and Jiaxiang Yang. The chemistry of graphene. *Journal of Materials Chemistry*, 20(12):2277, 2010.

[33] Diana Berman, Ali Erdemir, and Anirudha V Sumant. Graphene: a new emerging lubricant. *Materials Today*, 17(1):31–42, 2014.

[34] Miklos Kertesz and Roald Hoffmann. Octahedral vs. Trigonal-Prismatic Coordination and Clustering in Transition-Metal Dichalcogenides. *Journal of the American Chemical Society*, 106(12):3453–3460, 1984.

[35] Alexander V. Kolobov and Junji Tominaga. *Two-Dimensional Transition-Metal Dichalcogenides*, volume 239. 2016.

[36] A. R. Lansdown. *Molybdenum disulphide lubrication*. Elsevier, 1999.

[37] Federico Raffone, Can Ataca, Jeffrey C. Grossman, and Giancarlo Cicero. MoS2 Enhanced T-Phase Stabilization and Tunability Through Alloying. *Journal of Physical Chemistry Letters*, 7(13):2304–2309, 7 2016.

[38] Ashwin Ramasubramaniam and Doron Naveh. Mn-doped monolayer MoS2: An atomically thin dilute magnetic semiconductor. *Physical Review B - Condensed Matter and Materials Physics*, 87(19):1–7, 2013.

[39] Fredrik Gustavsson, Matthieu Bugnet, Tomas Polcar, Albano Cavaleiro, and Staffan Jacobson. A High-Resolution TEM/EELS Study of the Effect of Doping Elements on the Sliding Mechanisms of Sputtered WS2Coatings. *Tribology Transactions*, 58(1):113–118, 1 2015.

[40] Julija Vinckevičiutė, Maxwell D Radin, and Anton Van der Ven. Stacking-Sequence Changes and Na Ordering in Layered Intercalation Materials. *Chemistry of Materials*, 28(23):8640–8650, 12 2016.

[41] J. W. D. Connolly and A R Williams. Density-functional theory applied to phase transformations in transition-metal alloys. *Physical Review B*, 27(8):5169–5172, 4 1983.

[42] M. Asta, C. Wolverton, D. de Fontaine, and H. Dreyssé. Effective cluster interactions from cluster-variation formalism. I. *Physical Review B*, 44(10):4907–4913, 9 1991.

[43] Jon Gabriel Goiri and Anton Van Der Ven. Phase and structural stability in Ni-Al systems from first principles. *Physical Review B*, 94(9):1–14, 2016.

[44] J. M. Sanchez, J. P. Stark, and V. L. Moruzzi. First-principles calculation of the Ag-Cu phase diagram. *Physical Review B*, 44(11):5411–5418, 1991.

[45] R. McCormack and D. de Fontaine. First-principles study of multiple order-disorder transitions inAgAu Heusler alloys. *Physical Review B - Condensed Matter and Materials Physics*, 54(14):9746–9755, 1996.

[46] G. Ceder, A. Van Der Ven, C. Marianetti, and D. Morgan. First-principles alloy theory in oxides. *Modelling and Simulation in Materials Science and Engineering*, 8(3):311–321, 2000.

[47] B. P. Burton and A. K. Singh. Prediction of entropy stabilized incommensurate phases in the system MoS2-MoTe2. *Journal of Applied Physics*, 120(15):155101, 10 2016.

[48] Takeshi Takahashi, Eric J. Wu, Anton Van Der Ven, and Gerbrand Ceder. First-principles investigation of B-site ordering in Ba(Mg x Ta 1-x)O 3 microwave dielectrics with the complex perovskite structure. *Japanese Journal of Applied Physics, Part 1: Regular Papers and Short Notes and Review Papers*, 39(3 A):1241–1248, 3 2000.

[49] Maxwell D Radin, John C Thomas, and Anton Van der Ven. Order-disorder versus displacive transitions in Jahn-Teller active layered materials. *Physical Review Materials*, 4(4):043601, 4 2020.

[50] K S Novoselov, A Mishchenko, A Carvalho, and A H Castro Neto. 2D materials and van der Waals heterostructures, 7 2016.

[51] Yuan Liu, Nathan O. Weiss, Xidong Duan, Hung-Chieh Cheng, Yu Huang, and Xiangfeng Duan. Van der Waals heterostructures and devices. *Nature Reviews Materials*, 1(9):16042, 9 2016.

[52] Kun Zhang, Xin Fang, Yilun Wang, Yi Wan, Qingjun Song, Wenhao Zhai, Yanping Li, Guangzhao Ran, Yu Ye, and Lun Dai. Ultrasensitive Near-Infrared Photodetectors Based on a Graphene-MoTe2-Graphene Vertical van der Waals Heterostructure. *ACS Applied Materials and Interfaces*, 9(6):5392–5398, 2017.

[53] Martin Dienwiebel, Gertjan S. Verhoeven, Namboodiri Pradeep, Joost W. M. Frenken, Jennifer A. Heimberg, and Henny W. Zandbergen. Superlubricity of Graphite. *Physical Review Letters*, 92(12):126101, 3 2004.

[54] Jianqi Zhu, Zhi Chang Wang, Huijia Dai, Qinqin Wang, Rong Yang, Hua Yu, Mengzhou Liao, Jing Zhang, Wei Chen, Zheng Wei, Na Li, Luojun Du, Dongxia Shi, Wenlong Wang, Lixin Zhang, Ying Jiang, and Guangyu Zhang. Boundary activated hydrogen evolution reaction on monolayer MoS 2. *Nature Communications*, 10(1):1–7, 2019.

[55] Luojun Du, Hua Yu, Mengzhou Liao, Shuopei Wang, Li Xie, Xiaobo Lu, Jianqi Zhu, Na Li, Cheng Shen, Peng Chen, Rong Yang, Dongxia Shi, and Guangyu Zhang. Modulating PL and electronic structures of MoS 2 /graphene heterostructures via interlayer twisting angle. *Applied Physics Letters*, 111(26):263106, 12 2017.

[56] Yu Li Huang, Yifeng Chen, Wenjing Zhang, Su Ying Quek, Chang-Hsiao Chen, Lain-Jong Li, Wei-Ting Hsu, Wen-Hao Chang, Yu Jie Zheng, Wei Chen, and Andrew T. S. Wee. Bandgap tunability at single-layer molybdenum disulphide grain boundaries. *Nature Communications*, 6(1):6298, 5 2015.

[57] Jean Michel Martin and Ali Erdemir. Superlubricity: Friction's vanishing act. *Physics Today*, 71(4):40–46, 4 2018.

[58] R. Zan, Q. M. Ramasse, R. Jalil, J. S. Tu, U. Bangert, and K. S. Novoselov. Imaging Two Dimensional Materials and their Heterostructures. *Journal of Physics: Conference Series*, 902(1), 2017.

[59] Mengzhou Liao, Ze-Wen Wu, Luojun Du, Tingting Zhang, Zheng Wei, Jianqi Zhu, Hua Yu, Jian Tang, Lin Gu, Yanxia Xing, Rong Yang, Dongxia Shi, Yugui Yao, and Guangyu Zhang. Twist angle-dependent conductivities across MoS2/graphene heterojunctions. *Nature Communications*, 9(1):4068, 12 2018.

[60] Ankur Gupta, Tamilselvan Sakthivel, and Sudipta Seal. Recent development in 2D materials beyond graphene. *Progress in Materials Science*, 73:44–126, 2015.

[61] Goki Eda, Hisato Yamaguchi, Damien Voiry, Takeshi Fujita, Mingwei Chen, and Manish Chhowalla. Photoluminescence from chemically exfoliated MoS2. *Nano letters*, 11(12):5111–5116, 2011.

[62] Yu-Chuan Lin, Ning Lu, Nestor Perea-Lopez, Jie Li, Zhong Lin, Xin Peng, Chia Hui Lee, Ce Sun, Lazaro Calderin, Paul N Browning, Michael S Bresnehan, Moon J Kim, Theresa S Mayer, Mauricio Terrones, and Joshua A Robinson. Direct Synthesis of van der Waals Solids. *ACS Nano*, 8(4):3715–3723, 4 2014.

[63] Abhay Shivayogimath, Joachim Dahl Thomsen, David M. A. Mackenzie, Mathias Geisler, Raluca-Maria Stan, Ann Julie Holt, Marco Bianchi, Andrea Crovetto, Patrick R. Whelan, Alexandra Carvalho, Antonio H. Castro Neto, Philip Hofmann, Nicolas Stenger, Peter Bøggild, and Timothy J. Booth. A universal approach for the synthesis of two-dimensional binary compounds. *Nature Communications*, 10(1):2957, 12 2019.

[64] Tomas Polcar and Albano Cavaleiro. Self-adaptive low friction coatings based on transition metal dichalcogenides. *Thin Solid Films*, 519(12):4037–4044, 2011.

[65] T. Polcar and A. Cavaleiro. Review on self-lubricant transition metal dichalcogenide nanocomposite coatings alloyed with carbon. *Surface and Coatings Technology*, 206(4):686–695, 2011.

[66] Paolo Nicolini, Rosario Capozza, Paolo Restuccia, and Tomas Polcar. Structural Ordering of Molybdenum Disulfide Studied via Reactive Molecular Dynamics Simulations. *ACS Applied Materials and Interfaces*, 10(10):8937–8946, 2018.

[67] Joseph C.A. Prentice, Jolyon Aarons, James C. Womack, Alice E.A. Allen, Lampros Andrinopoulos, Lucian Anton, Robert A. Bell, Arihant Bhandari, Gabriel A. Bramley, Robert J. Charlton, Rebecca J. Clements, Daniel J. Cole, Gabriel Constantinescu, Fabiano Corsetti, Simon M.M. Dubois, Kevin K.B. Duff, José Mariá Escartín, Andrea Greco, Quintin Hill, Louis P. Lee, Edward Linscott, David D. O'Regan, Maximillian J.S. Phipps, Laura E. Ratcliff, Álvaro Ruiz Serrano, Edward W. Tait, Gilberto Teobaldi, Valerio Vitale, Nelson Yeung, Tim J. Zuehlsdorff, Jacek Dziedzic, Peter D. Haynes, Nicholas D.M. Hine, Arash A. Mostofi, Mike C. Payne, and Chris Kriton Skylaris. The ONETEP linear-scaling density functional theory program. *Journal of Chemical Physics*, 152(17):174111, 5 2020.

[68] Niccolo R C Corsini, Yuanpeng Zhang, William R Little, Ali Karatutlu, Osman Ersoy, Peter D Haynes, Carla Molteni, Nicholas D M Hine, Ignacio Hernandez, Jesus Gonzalez, Fernando Rodriguez, Vadim V Brazhkin, and Andrei Sapelkin. Pressure-Induced Amorphization and a New High Density Amorphous Metallic Phase in Matrix-Free Ge Nanoparticles. *Nano Letters*, 15(11):7334–7340, 11 2015.

[69] H Peter Jost. *Lubrication: Tribology; Education and Research; Report on the Present Position and Industry's Needs*. H.M.S.O., London, 1966.

[70] Kenneth Holmberg and Ali Erdemir. Influence of tribology on global energy consumption, costs and emissions. *Friction*, 5(3):263–284, 9 2017.

[71] C. R. Woods, F. Withers, M. J. Zhu, Y. Cao, G. Yu, A. Kozikov, M. Ben Shalom, S. V. Morozov, M. M. Van Wijk, A. Fasolino, M. I. Katsnelson, K. Watanabe, T. Taniguchi, A. K. Geim, A. Mishchenko, and K. S. Novoselov. Macroscopic self-reorientation of interacting two-dimensional crystals. *Nature Communications*, 7:1–5, 2016.

[72] Oded Hod, Ernst Meyer, Quanshui Zheng, and Michael Urbakh. Structural superlubricity and ultralow friction across the length scales. *Nature*, 563(7732):485–492, 2018.

[73] Diana Berman, Ali Erdemir, and Anirudha V. Sumant. Graphene: A new emerging lubricant. *Materials Today*, 17(1):31–42, 2014.

[74] V. C. Fox, N. Renevier, D. G. Teer, J. Hampshire, and V. Rigato. The structure of tribologically improved MoS2-metal composite coatings and their industrial applications. *Surface and Coatings Technology*, 116-119:492–497, 1999.

[75] Özlem Baran. Adhesion and fatigue resistance of Ta-doped MoS2 composite coatings deposited with pulsed-DC magnetron sputtering. *Journal of Adhesion Science and Technology*, 31(11):1181–1195, 2017.

[76] Bo N. J. Persson. *Sliding Friction : Physical Principles and Applications*. Springer Berlin Heidelberg, 2000.

[77] P. C. Torche, T. Polcar, and O. Hovorka. Thermodynamic aspects of nanoscale friction. *Physical Review B*, 100(12):125431, 9 2019.

[78] Emanuele Panizon, Giuseppe E Santoro, Erio Tosatti, Gabriele Riva, and Nicola Manini. Analytic understanding and control of dynamical friction. *Physical Review B*, 97(10):104104, 3 2018.

[79] Jeong Young Park and Miquel Salmeron. Fundamental Aspects of Energy Dissipation in Friction. *Chemical Reviews*, 114(1):677–711, 1 2014.

[80] Antonio Cammarata and Tomáš Polcar. Tailoring Nanoscale Friction in MX 2 Transition Metal Dichalcogenides. *Inorganic Chemistry*, 54(12):5739–5744, 2015.

[81] A.I. I. Vakis, V.A. A. Yastrebov, J. Scheibert, L. Nicola, D. Dini, C. Minfray, A. Almqvist, M. Paggi, S. Lee, G. Limbert, J.F. F. Molinari, G. Anciaux, R. Aghababaei, S. Echeverri Restrepo, A. Papangelo, A. Cammarata, P. Nicolini, C. Putignano, G. Carbone, S. Stupkiewicz, J. Lengiewicz, G. Costagliola, F. Bosia, R. Guarino, N.M. M. Pugno, M.H. H. Müser, and M. Ciavarella. Modeling and simulation in tribology across scales: An overview. *Tribology International*, 125(November 2017):169–199, 9 2018.

[82] Sergey Yu. Krylov and Joost W.M. Frenken. The physics of atomic-scale friction: Basic considerations and open questions. *Physica Status Solidi (B) Basic Research*, 251(4):711–736, 4 2014.

[83] J. A. Greenwood and J. B. P. Williamson. Contact of Nominally Flat Surfaces. *Proceedings of the Royal Society A: Mathematical, Physical and Engineering Sciences*, 295(1442):300–319, 1966.

[84] Koji Kato. *History of Tribology*, volume 3. Professional Engineering Publishing, 2011.

[85] Yifei Mo, Kevin T Turner, and Izabela Szlufarska. Friction laws at the nanoscale. *Nature*, 457(7233):1116–1119, 2009.

[86] Binquan Luan and Mark O. Robbins. The breakdown of continuum models for mechanical contacts. *Nature*, 435(7044):929–932, 2005.

[87] Frank Philip Bowden, Frank Philip Bowden, and David Tabor. *The friction and lubrication of solids*, volume 1. Oxford university press, 2001.

[88] Juan J Mazo, Dirk Dietzel, Andre Schirmeisen, J. G. Vilhena, and Enrico Gnecco. Time Strengthening of Crystal Nanocontacts. *Physical Review Letters*, 118(24):1–5, 6 2017.

[89] Enrico Gnecco. *Fundamentals of Friction and Wear*. 2007.

[90] Elisa Riedo and Enrico Gnecco. Thermally activated effects in nanofriction. *Nanotechnology*, 15(4), 2004.

[91] O. Y. Fajardo, E. Gnecco, and J. J. Mazo. Anisotropy effects and friction maps in the framework of the 2d PT model. *Physica B: Condensed Matter*, 455:44–48, 2014.

[92] Antonio Cammarata and Tomas Polcar. Vibrational contributions to intrinsic friction in charged transition metal dichalcogenides. *Nanoscale*, pages 11488–11497, 2017.

[93] M Reguzzoni, A Fasolino, E Molinari, and M C Righi. Potential energy surface for graphene on graphene: Ab initio derivation, analytical description, and microscopic interpretation. *Physical Review B - Condensed Matter and Materials Physics*, 86(24), 2012.

[94] Paolo Nicolini and Tomàš Polcar. A comparison of empirical potentials for sliding simulations of MoS2. *Computational Materials Science*, 115:158–169, 2016.

[95] Victor E.P. Claerbout, Tomas Polcar, and Paolo Nicolini. Superlubricity achieved for commensurate sliding: MoS 2 frictional anisotropy in silico. *Computational Materials Science*, 163:17–23, 6 2019.

[96] L Prandtl. A Conceptual Model to the Kinetic Theory of Solid Bodies. *Zeitschrift für Angewandte*, 8(3):85–106, 1928.

[97] G. Levita, A. Cavaleiro, E. Molinari, T. Polcar, and M. C. Righi. Sliding properties of MoS2 layers: Load and interlayer orientation effects. *Journal of Physical Chemistry C*, 118(25):13809–13816, 2014.

[98] Antonio Cammarata. Phonon-phonon scattering selection rules and control: An application to nanofriction and thermal transport. *RSC Advances*, 9(64):37491–37496, 2019.

[99] G Binnig, C F Quate, and Ch. Gerber. Atomic Force Microscope. *Physical Review Letters*, 56(9):930–933, 3 1986.

[100] Nanosensors. PointProbe ® Plus.

[101] C Mathew Mate, Gary M McClelland, Ragnar Erlandsson, Shirley Chiang, null Mate, null McClelland, null Erlandsson, null Chiang, C Mathew Mate, Gary M McClelland, Ragnar Erlandsson, and Shirley Chiang. Atomic-scale friction of a tungsten tip on a graphite surface. *Physical Review Letters*, 59(17):1942–1945, 10 1987.

[102] E. Gnecco, R. Bennewitz, T. Gyalog, Ch Loppacher, M. Bammerlin, E. Meyer, and H. J. Güntherodt. Velocity dependence of atomic friction. *Physical Review Letters*, 84(6):1172–1175, 2000.

[103] A. Socoliuc, R. Bennewitz, E. Gnecco, and E. Meyer. Transition from stick-slip to continuous sliding in atomic friction: Entering a new regime of ultralow friction. *Physical Review Letters*, 92(13):1–4, 2004.

[104] Andreas Klemenz, Lars Pastewka, S. G. Balakrishna, Arnaud Caron, Roland Bennewitz, and Michael Moseler. Atomic scale mechanisms of friction reduction and wear protection by graphene. *Nano Letters*, 14(12):7145–7152, 2014.

[105] N Manini, O M Braun, E Tosatti, R Guerra, and A Vanossi. Friction and nonlinear dynamics. *Journal of Physics: Condensed Matter*, 28(29):293001, 7 2016.

[106] G A Tomlinson. CVI. A molecular theory of friction. *The London, Edinburgh, and Dublin Philosophical Magazine and Journal of Science*, 7(46):905–939, 1929.

[107] Yakov Il'ich Frenkel and Tatyana Kontorova. The model of dislocation in solid body. *Physikalische Zeitschrift der Sowjetunion*, 13(1340):1, 1938.

[108] Oleg M Braun and Yuri S Kivshar. Nonlinear dynamics of the Frenkel–Kontorova model. *Physics Reports*, 306(1-2):1–108, 12 1998.

[109] Udo Seifert. Stochastic thermodynamics, fluctuation theorems and molecular machines. *Reports on Progress in Physics*, 75(12), 2012.

[110] H Holscher, A Schirmeisen, and U D Schwarz. Principles of atomic friction: from sticking atoms to superlubric sliding. *Philos. Trans. R. Soc. A Math. Phys. Eng. Sci.*, 366(1869):1383–1404, 2008.

[111] S Aubry and P. Y. Le Daeron. The discrete Frenkel-Kontorova model and its extensions. Exact results for the ground-states. *Physica D*, 8(3):381, 1983.

[112] Davide Mandelli, Andrea Vanossi, Nicola Manini, and Erio Tosatti. Friction Boosted by Equilibrium Misalignment of Incommensurate Two-Dimensional Colloid Monolayers. *Physical Review Letters*, 114(10):108302, 3 2015.

[113] Xiaoping Han, Maamar Benkraouda, Naser Qamhieh, and Noureddine Amrane. Understanding ferromagnetism in Ni-doped MoS2 monolayer from first principles. *Chemical Physics*, 528(August 2019):110501, 2020.

[114] Martin Dienwiebel, Namboodiri Pradeep, Gertjan S. Verhoeven, Henny W. Zandbergen, and Joost W.M. Frenken. Model experiments of superlubricity of graphite. *Surface Science*, 576(1-3):197–211, 2 2005.

[115] Andrea Vanossi, Clemens Bechinger, and Michael Urbakh. Structural lubricity in soft and hard matter systems. *Nature Communications*, 11(1):4657, 12 2020.

[116] W. Kohn. Nobel Lecture: Electronic structure of matter—wave functions and density functionals. *Reviews of Modern Physics*, 71(5):1253–1266, 1999.

[117] W. Kohn and L. J. Sham. Self-consistent equations including exchange and correlation effects. *Physical Review*, 140(4A):A1133–A1138, 11 1965.

[118] R. P. Feynman. Forces in molecules. *Physical Review*, 56(4):340–343, 1939.

[119] G Kresse and J. Furthmüller. Efficient iterative schemes for ab initio total-energy calculations using a plane-wave basis set. *Physical Review B*, 54(16):11169–11186, 1996.

[120] R Car and M Parrinello. Unified Approach for Molecular Dynamics and Density-Functional Theory. *Physical Review Letters*, 55(22):2471–2474, 11 1985.

[121] Klaus Capelle. A bird's-eye view of density-functional theory, 2002.

[122] Gregory H Wannier. The Structure of Electronic Excitation Levels in Insulating Crystals. *Physical Review*, 1937.

[123] Nicola Marzari, Arash A Mostofi, Jonathan R Yates, Ivo Souza, and David Vanderbilt. Maximally localized Wannier functions: Theory and applications. *Reviews of Modern Physics*, 84(4):1419–1475, 2012.

[124] P. E. Blöchl. Projector augmented-wave method. *Physical Review B*, 50(24):17953–17979, 1994.

[125] Enrico Fermi. Un metodo statistico per la determinazione di alcune priorieta dell'atome. *Rend. Accad. Naz. Lincei*, 6(602-607):32, 1927.

[126] L H Thomas. The calculation of atomic fields. *Mathematical Proceedings of the Cambridge Philosophical Society*, 23(5):542–548, 1 1927.

[127] John P. Perdew, Kieron Burke, and Matthias Ernzerhof. Generalized Gradient Approximation Made Simple. *Physical Review Letters*, 77(18):3865–3868, 10 1996.

[128] Jianwei Sun, Adrienn Ruzsinszky, and Johnp Perdew. Strongly Constrained and Appropriately Normed Semilocal Density Functional. *Physical Review Letters*, 115(3):036402, 7 2015.

[129] Haowei Peng, Zeng-Hui Yang, John P Perdew, and Jianwei Sun. Versatile van der Waals Density Functional Based on a Meta-Generalized Gradient Approximation. *Physical Review X*, 6(4):041005, 2016.

[130] Stefan Grimme. Semiempirical GGA-type density functional constructed with a long-range dispersion correction. *Journal of Computational Chemistry*, 27(15):1787–1799, 11 2006.

[131] Henrik Rydberg, Bengt I. Lundqvist, David C. Langreth, and Maxime Dion. Tractable nonlocal correlation density functionals for flat surfaces and slabs. *Physical Review B - Condensed Matter and Materials Physics*, 62(11):6997–7006, 2000.

[132] Oleg A Vydrov and Troy Van Voorhis. Nonlocal van der Waals density functional made simple. *Physical Review Letters*, 103(6), 2009.

[133] Gabriel C Constantinescu and Nicholas D.M. Hine. Energy landscape and band-structure tuning in realistic MoS2/MoSe2 heterostructures. *Physical Review B - Condensed Matter and Materials Physics*, 91(19):195416, 5 2015.

[134] A. Walle and G Ceder. Automating first-principles phase diagram calculations. *Journal of Phase Equilibria*, 23(4):348–359, 8 2002.

[135] Christopher Mark Wolverton. *Ground-State Properties and Phase Stability of Binary and Ternary Intermetallic Alloys.* PhD thesis, University of California at Berkeley, 1993.

[136] A van de Walle, M. D. Asta, and G. Ceder. The Alloy-Theoretic Automated Toolkit (ATAT): A User Guide. *Calphad*, 26:539–553, 2002.

[137] J. M. Sanchez. Foundations and Practical Implementations of the Cluster Expansion. *Journal of Phase Equilibria and Diffusion*, 38(3):238–251, 2017.

[138] A. van de Walle and M. Asta. Self-driven Lattice-model Monte Carlo Simulations of Alloy Thermodynamic Properties and Phase Diagrams. *Model. Simul. Mater. Sc.*, 10(1002):521–539, 2002.

[139] Mark E Tuckerman. *Statistical Mechanics: Theory and Molecular Simulation.* Oxford University Press, 2016.

[140] Daan Frenkel and Berend Smit. *Understanding Molecular Simulation*. Academic Press, 2002.

[141] Franz J. Vesely. *Computational Physics*. 2001.

[142] George D Birkhoff. Proof of the Ergodic Theorem. *Proceedings of the National Academy of Sciences*, 17(12):656–660, 1931.

[143] Duane C Wallace and Herbert Callen. Thermodynamics of Crystals. *American Journal of Physics*, 40(11):1718–1719, 11 1972.

[144] Francis Birch. Finite Elastic strain of cubic crystals. *Physical Review*, 71(11):809–824, 1947.

[145] M. Hebbache and M. Zemzemi. Ab initio study of high-pressure behavior of a low compressibility metal and a hard material: Osmium and diamond. *Physical Review B - Condensed Matter and Materials Physics*, 70(22):5–10, 2004.

[146] Eva Pavarini. Crystal-Field Theory, Tight-Binding Method and Jahn-Teller Effect, 2012.

[147] M. T. Hutchings. Point-Charge Calculations of Energy Levels of Magnetic Ions in Crystalline Electric Fields. *Solid State Physics - Advances in Research and Applications*, 1964.

[148] JE Huheey, EA Keiter, and RL Keiter. Inorganic Chemistry: Principles of Structure and Reactivity. In *Inorganic Chemistry*, page 808. Pearson Education, 1993.

[149] Paolo Restuccia, Giacomo Levita, Michael Wolloch, Gabriele Losi, Giulio Fatti, Mauro Ferrario, and M. C. Righi. Ideal adhesive and shear strengths of solid interfaces: A high throughput ab initio approach. *Computational Materials Science*, 154(August):517–529, 11 2018.

[150] N. W. Ashcroft and N. D. Mermin. *Solid State Physics*. Holt, Rinehart and Winston,, 1976.

[151] Atsushi Togo and Isao Tanaka. First principles phonon calculations in materials science. *Scripta Materialia*, 108:1–5, 2015.

[152] Ion Errea, Matteo Calandra, and Francesco Mauri. Anharmonic free energies and phonon dispersions from the stochastic self-consistent harmonic approximation: Application to platinum and palladium hydrides. *Physical Review B - Condensed Matter and Materials Physics*, 89(6):1–16, 2014.

[153] Hartmut Zabel. Phonons in layered compounds. *Journal of Physics: Condensed Matter*, 13(34):7679–7690, 8 2001.

[154] Antonio Cammarata, Paolo Nicolini, Kosta Simonovic, Egor Ukraintsev, and Tomas Polcar. Atomic-scale design of friction and energy dissipation. *Physical Review B*, 99(9):1–8, 3 2019.

[155] Mois I Aroyo, Asen Kirov, Cesar Capillas, J M Perez-Mato, and Hans Wondratschek. Bilbao Crystallographic Server. II. Representations of crystallographic point groups and space groups. *Acta Crystallographica Section A: Foundations of Crystallography*, 62(2):115–128, 3 2006.

[156] Xiaolong Liu, Itamar Balla, Hadallia Bergeron, Gavin P. Campbell, Michael J. Bedzyk, and Mark C. Hersam. Rotationally commensurate growth of MoS2 on epitaxial graphene. *ACS Nano*, 10(1):1067–1075, 2016.

[157] Yumeng Shi, Wu Zhou, Ang-Yu Yu Lu, Wenjing Fang, Yi-Hsien Hsien Lee, Allen Long Hsu, Soo Min Kim, Ki Kang Kim, Hui Ying Yang, Lain-Jong Jong Li, Juan-Carlos Carlos Idrobo, and Jing Kong. van der Waals Epitaxy of MoS 2 Layers Using Graphene As Growth Templates. *Nano Letters*, 12(6):2784–2791, 6 2012.

[158] Chun I. Lu, Christopher John Butler, Jing Kai Huang, Cheng Rong Hsing, Hung Hsiang Yang, Yu Hsun Chu, Chi Hung Luo, Yung Che Sun, Shih Hao Hsu, Kui Hong Ou Yang, Ching Ming Wei, Lain Jong Li, and Minn Tsong Lin. Graphite edge controlled registration of monolayer MoS¡inf¿2¡/inf¿ crystal orientation. *Applied Physics Letters*, 106(18):2–6, 2015.

[159] Marlene Adrian, Arne Senftleben, Silvio Morgenstern, and Thomas Baumert. Complete analysis of a transmission electron diffraction pattern of a MoS2-graphite heterostructure. *Ultramicroscopy*, 166:9–15, 2016.

[160] Horacio Coy Diaz, José Avila, Chaoyu Chen, Rafik Addou, Maria C. Asensio, and Matthias Batzill. Direct observation of interlayer hybridization and dirac relativistic carriers in Graphene/MoS2 van der waals heterostructures. *Nano Letters*, 15(2):1135–1140, 2015.

[161] Debora Pierucci, Hugo Henck, Jose Avila, Adrian Balan, Carl H. Naylor, Gilles Patriarche, Yannick J. Dappe, Mathieu G. Silly, Fausto Sirotti, A. T. Charlie Johnson, Maria C. Asensio, and Abdelkarim Ouerghi. Band Alignment and Minigaps in Monolayer MoS 2 -Graphene van der Waals Heterostructures. *Nano Letters*, 16(7):4054–4061, 7 2016.

[162] Mit H. Naik, Indrajit Maity, Prabal K. Maiti, and Manish Jain. Kolmogorov-Crespi Potential for Multilayer Transition-Metal Dichalcogenides: Capturing Structural Transformations in Moiré Superlattices. *Journal of Physical Chemistry C*, 123(15):9770–9778, 2019.

[163] Roberto Guerra, Merel van Wijk, Andrea Vanossi, Annalisa Fasolino, and Erio Tosatti. Graphene on h-BN: to align or not to align? *Nanoscale*, 9(25):8799–8804, 2017.

[164] Anthony D. Novaco and John P. McTague. Orientational epitaxy-the orientational ordering of incommensurate structures. *Physical Review Letters*, 38(22):1286–1289, 5 1977.

[165] J. P. McTague and A. D. Novaco. Substrate-induced strain and orientational ordering in adsorbed monolayers. *Physical Review B*, 19(10):5299–5306, 5 1979.

[166] T Brazda, Andrea Silva, N Manini, A Vanossi, R Guerra, E Tosatti, and C Bechinger. Experimental Observation of the Aubry Transition in Two-Dimensional Colloidal Monolayers. *Physical Review X*, 8(1):011050, 3 2018.

[167] Emanuele Panizon, Roberto Guerra, and Erio Tosatti. Ballistic thermophoresis of adsorbates on free-standing graphene. *Proceedings of the National Academy of Sciences*, 114(34):E7035–E7044, 8 2017.

[168] Anthony D. Novaco. Theory of orientational epitaxy in the self-consistent phonon approximation. *Physical Review B*, 19(12):6493–6501, 1979.

[169] Ying Wang, Jun Xiao, Hanyu Zhu, Yao Li, Yousif Alsaid, King Yan Fong, Yao Zhou, Siqi Wang, Wu Shi, Yuan Wang, Alex Zettl, Evan J. Reed, and Xiang Zhang. Structural phase transition in monolayer MoTe2 driven by electrostatic doping. *Nature*, 550(7677):487–491, 10 2017.

[170] Zi Jian Wang, Tian Bao Ma, Yuan Zhong Hu, Liang Xu, and Hui Wang. Energy dissipation of atomic-scale friction based on one-dimensional Prandtl-Tomlinson model. *Friction*, 3(2):170–182, 2015.

[171] Zhiwei Ding, Qing-Xiang Pei, Jin-Wu Jiang, Wenxuan Huang, and Yong-Wei Zhang. Interfacial thermal conductance in graphene/MoS2 heterostructures. *Carbon*, 96:888–896, 1 2016.

[172] Donald W Brenner, O A Shenderova, J A Harrison, S J Stuart, B Ni, and S B Sinnott. A second-generation reactive empirical bond order (REBO) potential energy expression for hydrocarbons. *Journal of Physics-Condensed Matter*, 14(4):783–802, 2002.

[173] Steve Plimpton. Fast parallel algorithms for short-range molecular dynamics. *Journal of Computational Physics*, 117(1):1–19, 3 1995.

[174] D. Tomer, S. Rajput, and L. Li. Spatial inhomogeneity in Schottky barrier height at graphene/MoS2 Schottky junctions. *Journal of Physics D: Applied Physics*, 50(16), 2017.

[175] D Mandelli, I Leven, O Hod, and M Urbakh. Sliding friction of graphene/hexagonal -boron nitride heterojunctions: A route to robust superlubricity. *Scientific Reports*, 7(1), 2017.

[176] Saptarshi Das, Marcellinus Demarteau, and Andreas Roelofs. Nb-doped single crystalline MoS2 field effect transistor. *Applied Physics Letters*, 106(17), 2015.

[177] No Title.

[178] Xiumei Geng, Weiwei Sun, Wei Wu, Benjamin Chen, Alaa Al-Hilo, Mourad Benamara, Hongli Zhu, Fumiya Watanabe, Jingbiao Cui, and Tar Pin Chen. Pure and stable metallic phase molybdenum disulfide nanosheets for hydrogen evolution reaction. *Nature Communications*, 7, 2016.

[179] Yichao Huang, Yuanhui Sun, Xueli Zheng, Toshihiro Aoki, Brian Pattengale, Jier Huang, Xin He, Wei Bian, Sabrina Younan, Nicholas Williams, Jun Hu, Jingxuan Ge, Ning Pu, Xingxu Yan, Xiaoqing Pan, Lijun Zhang, Yongge Wei, and Jing Gu. Atomically engineering activation sites onto metallic 1T-MoS 2 catalysts for enhanced electrochemical hydrogen evolution. *Nature Communications*, 10(1):1–11, 2019.

[180] Brian Pattengale, Yichao Huang, Xingxu Yan, Sizhuo Yang, Sabrina Younan, Wenhui Hu, Zhida Li, Sungsik Lee, Xiaoqing Pan, Jing Gu, and Jier Huang. Dynamic evolution and reversibility of single-atom Ni(II) active site in 1T-MoS2 electrocatalysts for hydrogen evolution. *Nature Communications*, 11(1):4114, 12 2020.

[181] A. C. Domask, R. L. Gurunathan, and S. E. Mohney. Transition Metal–MoS2 Reactions: Review and Thermodynamic Predictions. *Journal of Electronic Materials*, 44(11):4065–4079, 2015.

[182] Xiaoqiang Yao and Hugo F. Franzen. Nb1.72Ta3.28S2: A Novel Phase in the Ta-Nb-S Ternary System with a Layered Structure. *Journal of the American Chemical Society*, 113(4):1426–1427, 1991.

[183] K. Koepernik, D. Kasinathan, D. V. Efremov, Seunghyun Khim, Sergey Borisenko, Bernd Büchner, and Jeroen Van Den Brink. TaIrTe4: A ternary type-II Weyl semimetal. *Physical Review B*, 93(20):1–5, 2016.

[184] M Saeki and M Onoda. Preparation of 3s-type Mo$_{0.5}Ta$_{0.5}S$_2$. *Journal of the less-common metals*, 135(1):L1–L3, 1987.

[185] F J Di Salvo, C H Chen, R M Fleming, J V Waszczak, R G Dunn, S A Sunshine, and James A Ibers. Physical and structural properties of the new layered compounds Ta2NiS5 and Ta2NiSe5. *Journal of the Less Common Metals*, 116(1):51–61, 1986.

[186] Hui Gao, Hui Gao, Joonki Suh, Joonki Suh, Michael C. Cao, Andrew Y. Joe, Fauzia Mujid, Kan Heng Lee, Kan Heng Lee, Saien Xie, Saien Xie, Preeti Poddar, Jae Ung Lee, Jae Ung Lee, Kibum Kang, Kibum Kang, Philip Kim, David A. Muller,

and Jiwoong Park. Tuning Electrical Conductance of MoS2Monolayers through Substitutional Doping. *Nano Letters*, 20(6):4095–4101, 2020.

[187] A. Banerji, S. Bhowmick, and A. T. Alpas. Role of temperature on tribological behaviour of Ti containing MoS2 coating against aluminum alloys. *Surface and Coatings Technology*, 314:2–12, 2017.

[188] Sean M. Oliver, Ryan Beams, Sergiy Krylyuk, Irina Kalish, Arunima K. Singh, Alina Bruma, Francesca Tavazza, Jaydeep Joshi, Iris R. Stone, Stephan J. Stranick, Albert V. Davydov, and Patrick M. Vora. The structural phases and vibrational properties of Mo1-xWxTe2 alloys. *2D Materials*, 4(4), 2017.

[189] Yanfeng Chen, Jinyang Xi, Dumitru O. Dumcenco, Zheng Liu, Kazu Suenaga, Dong Wang, Zhigang Shuai, Ying Sheng Huang, and Liming Xie. Tunable band gap photoluminescence from atomically thin transition-metal dichalcogenide alloys. *ACS Nano*, 7(5):4610–4616, 2013.

[190] M. Worsdale, A. Rabis, E. Fabbri, T. J. Schmidt, and D. Kramer. Conductivity Limits of Extrinsically Doped SnO2 Supports. *ECS Transactions*, 69(17):1167–1178, 10 2015.

[191] Davide Mandelli and Erio Tosatti. Nanophysics: Microscopic friction emulators, 2015.

[192] Benjamin J. Irving, Paolo Nicolini, and Tomas Polcar. On the lubricity of transition metal dichalcogenides: an ab initio study. *Nanoscale*, 9(17):5597–5607, 2017.

[193] Gabriele Losi, Paolo Restuccia, and Maria Clelia Righi. Superlubricity in phosphorene identified by means of ab initio calculations. *2D Materials*, 2020.

[194] Jonas L. Kaufman, Julija Vinckevičiūtė, Sanjeev Krishna Kolli, Jon Gabriel Goiri, and Anton Van Der Ven. Understanding intercalation compounds for sodium-ion batteries and beyond. *Philosophical Transactions of the Royal Society A: Mathematical, Physical and Engineering Sciences*, 377(2152), 2019.

[195] Kaline Pagnan Furlan, Patricia Bodanese Prates, Thayna Andrea Dos Santos, Matheus Vinícius Gouvêa Dias, Heitor Tavares Ferreira, João Batista Rodrigues Neto, and Aloisio Nelmo Klein. Influence of alloying elements on the sintering thermodynamics, microstructure and properties of Fe-MoS2 composites. *Journal of Alloys and Compounds*, 652:450–458, 2015.

[196] T. W. Scharf, R. S. Goeke, P. G. Kotula, and S. V. Prasad. Synthesis of Au-MoS2 nanocomposites: Thermal and friction-induced changes to the structure. *ACS Applied Materials and Interfaces*, 5(22):11762–11767, 2013.

[197] G. Kresse and J. Furthmüller. Efficiency of ab-initio total energy calculations for metals and semiconductors using a plane-wave basis set. *Computational Materials Science*, 6:15–50, 1996.

[198] G Kresse and J Hafner. Ab initio molecular dynamics for open-shell transition metals. *Physical Review B*, 48(17):13115–13118, 1993.

[199] G. Kresse and D. Joubert. From ultrasoft pseudopotentials to the projector augmented-wave method. *Physical Review B*, 59(3):1758–1775, 1999.

[200] Carsten Rostgaard. *The Projector Augmented-wave Method*, volume 837 of *Lecture Notes in Physics*. Springer Berlin Heidelberg, Berlin, Heidelberg, 2009.

[201] Łukasz Mentel. {mendeleev} – A Python resource for properties of chemical elements, ions and isotopes.

[202] W Lawrence Bragg M.A. XVIII. The arrangement of atoms in crystals. *The London, Edinburgh, and Dublin Philosophical Magazine and Journal of Science*, 40(236):169–189, 1920.

[203] Beatriz Cordero, Verónica Gómez, Ana E. Platero-Prats, Marc Revés, Jorge Echeverría, Eduard Cremades, Flavia Barragán, and Santiago Alvarez. Covalent radii revisited. *Journal of the Chemical Society. Dalton Transactions*, (21):2832–2838, 2008.

[204] Pekka Pyykkö and Michiko Atsumi. Molecular single-bond covalent radii for elements 1-118. *Chemistry - A European Journal*, 15(1):186–197, 2009.

[205] J. C. Slater. Atomic radii in crystals. *The Journal of Chemical Physics*, 41(10):3199–3204, 1964.

[206] Y Wang, S Curtarolo, C Jiang, R Arroyave, T Wang, G Ceder, L.-Q. Chen, and Z.-K. Liu. Ab initio lattice stability in comparison with CALPHAD lattice stability. *Calphad*, 28(1):79–90, 2004.

[207] Ian Ford. *Statistical Physics: an entropic approach*. John Wiley & Sons, 2013.

[208] Xue Xia, Siow Mean Loh, Jacob Viner, Natalie C Teutsch, Abigail J Graham, Viktor Kandyba, Alexei Barinov, Ana M Sanchez, David C Smith, Nicholas D. M. Hine, and Neil R. Wilson. Atomic and electronic structure of two-dimensional Mo(1-x)WxS2 alloys. *arXiv*, pages 5–8, 9 2020.

[209] Nicolas Onofrio, David Guzman, and Alejandro Strachan. Novel doping alternatives for single-layer transition metal dichalcogenides. *Journal of Applied Physics*, 1221(10):185102–185305, 2017.

[210] Anton Van der Ven. CASM, v0.2.1, 2017.

[211] A. Van der Ven, J. C. Thomas, Qingchuan Xu, and J. Bhattacharya. Linking the electronic structure of solids to their thermodynamic and kinetic properties. *Mathematics and Computers in Simulation*, 80(7):1393–1410, 2010.

[212] B. Puchala and A. Van Der Ven. Thermodynamics of the Zr-O system from first-principles calculations. *Physical Review B - Condensed Matter and Materials Physics*, 88(9):1–15, 2013.

[213] John C. Thomas and Anton Van Der Ven. Finite-temperature properties of strongly anharmonic and mechanically unstable crystal phases from first principles. *Physical Review B - Condensed Matter and Materials Physics*, 88(21):1–13, 2013.

[214] Félix-Antoine Fortin, François-Michel De Rainville, Marc-André Gardner, Marc Parizeau, and Christian Gagné. {DEAP}: Evolutionary Algorithms Made Easy. *Journal of Machine Learning Research*, 13:2171–2175, 7 2012.

[215] F Pedregosa, G Varoquaux, A Gramfort, V Michel, B Thirion, O Grisel, M Blondel, P Prettenhofer, R Weiss, V Dubourg, J Vanderplas, A Passos, D Cournapeau, M Brucher, M Perrot, and E Duchesnay. Scikit-learn: Machine Learning in {P}ython. *Journal of Machine Learning Research*, 12:2825–2830, 2011.

[216] Shyue Ping Ong, Lei Wang, Byoungwoo Kang, and Gerbrand Ceder. Li - Fe - P - O2 phase diagram from first principles calculations. *Chemistry of Materials*, 20(5):1798–1807, 2008.

[217] Anubhav Jain, Shyue Ping Ong, Geoffroy Hautier, Wei Chen, William Davidson Richards, Stephen Dacek, Shreyas Cholia, Dan Gunter, David Skinner, Gerbrand Ceder, and Kristin A. Persson. Commentary: The materials project: A materials genome approach to accelerating materials innovation. *APL Materials*, 1(1), 2013.

[218] Roberto Guerra, Andrea Vanossi, and Mauro Ferrario. Nonlinear mobility of a driven system: Temperature and disorder effects. *Surface Science*, 601(18):3676–3681, 9 2007.

[219] Bogdan Guster, Enric Canadell, Miguel Pruneda, and Pablo Ordejón. First principles analysis of the CDW instability of single-layer 1 T -TiSe 2 and its evolution with charge carrier density. *2D Materials*, 5(2):025024, 3 2018.

[220] Jaydeep Joshi, Heather M. Hill, Sugata Chowdhury, Christos D. Malliakas, Francesca Tavazza, Utpal Chatterjee, Angela R. Hight Walker, and Patrick M. Vora. Short-range charge density wave order in 2H- T a S2. *Physical Review B*, 99(24):1–9, 2019.

[221] Emanuele Panizon, Torben Marx, Dirk Dietzel, Franco Pellegrini, Giuseppe E. Santoro, Andre Schirmeisen, and Erio Tosatti. Friction anomalies at first-order transition spinodals: 1T-TaS 2. *New Journal of Physics*, 20(2):023033, 2 2018.

[222] Layne B. Frechette, Christoph Dellago, and Phillip L. Geissler. Consequences of Lattice Mismatch for Phase Equilibrium in Heterostructured Solids. *Physical Review Letters*, 123(13):135701, 2019.

[223] P. Fratzl and O. Penrose. Ising model for phase separation in alloys with anisotropic elastic interaction—I. Theory. *Acta Metallurgica et Materialia*, 43(8):2921–2930, 8 1995.

[224] P. Fratzl and O. Penrose. Ising model for phase separation in alloys with anisotropic elastic interaction - II. A computer experiment. *Acta Materialia*, 44(8):3227–3239, 1996.

[225] Yoyo Hinuma, Giovanni Pizzi, Yu Kumagai, Fumiyasu Oba, and Isao Tanaka. Band structure diagram paths based on crystallography. *Computational Materials Science*, 128:140–184, 2017.

[226] A Cammarata and T Polcar. Electro-vibrational coupling effects on "intrinsic friction" in transition metal dichalcogenides. *RSC Advances*, 5(129):106809–106818, 2015.

[227] N.M Renevier, V.C Fox, D.G Teer, and J Hampshire. Coating characteristics and tribological properties of sputter-deposited MoS2/metal composite coatings deposited by closed field unbalanced magnetron sputter ion plating. *Surface and Coatings Technology*, 127(1):24–37, 5 2000.

[228] Wen Kuang Hsu, Yah Qiu Zhu, Nan Yao, Steven Firth, Robin J H Clark, Harold W. Kroto, and David R M Walton. Titanium-doped molybdenum disulfide nanostructures. *Advanced Funtional Materials*, 11(1):69–74, 2001.

[229] Oleg A. Vydrov and Troy Van Voorhis. Nonlocal van der Waals density functional: The simpler the better. *Journal of Chemical Physics*, 133(24):1–9, 2010.

[230] Roscoe G. Dickinson and Linus Pauling. The crystal structure of molybdenite. *Journal of the American Chemical Society*, 45(6):1466–1471, 6 1923.

[231] R. R. Chianelli, J. C. Scanlon, and A. H. Thompson. Structure refinement of stoichiometric TiS2. *Materials Research Bulletin*, 10(12):1379–1382, 12 1975.

[232] Hugh Baker. *ASM Handbook: Alloy Phase Diagrams Volume 3*. 1998.

[233] Matteo Calandra. Phonon-Assisted Magnetic Mott-Insulating State in the Charge Density Wave Phase of Single-Layer 1T-NbSe2. *Physical Review Letters*, 121(2):026401, 7 2018.

[234] Quanshui Zheng, Bo Jiang, Shoupeng Liu, Yuxiang Weng, Li Lu, Qikun Xue, Jing Zhu, Qing Jiang, Sheng Wang, and Lianmao Peng. Self-Retracting Motion of Graphite Microflakes. *Physical Review Letters*, 100(6):067205, 2 2008.

[235] Alexander E Filippov, Martin Dienwiebel, Joost W. M. Frenken, Joseph Klafter, and Michael Urbakh. Torque and Twist against Superlubricity. *Physical Review Letters*, 100(4):046102, 1 2008.

[236] Duoming Wang, Guorui Chen, Chaokai Li, Meng Cheng, Wei Yang, Shuang Wu, Guibai Xie, Jing Zhang, Jing Zhao, Xiaobo Lu, Peng Chen, Guole Wang, Jianling Meng, Jian Tang, Rong Yang, Congli He, Donghua Liu, Dongxia Shi, Kenji Watanabe, Takashi Taniguchi, Ji Feng, Yuanbo Zhang, and Guangyu Zhang. Thermally Induced Graphene Rotation on Hexagonal Boron Nitride. *Physical Review Letters*, 116(12):126101, 3 2016.

[237] Wei Yang, Guorui Chen, Zhiwen Shi, Cheng-Cheng Liu, Lianchang Zhang, Guibai Xie, Meng Cheng, Duoming Wang, Rong Yang, Dongxia Shi, Kenji Watanabe, Takashi Taniguchi, Yugui Yao, Yuanbo Zhang, and Guangyu Zhang. Epitaxial growth of single-domain graphene on hexagonal boron nitride. *Nature Materials*, 12(9):792–797, 9 2013.

[238] He Li, Jinhuan Wang, Song Gao, Qing Chen, Lianmao Peng, Kaihui Liu, and Xianlong Wei. Superlubricity between MoS 2 Monolayers. *Advanced Materials*, 29(27):1701474, 7 2017.

[239] Baowen Li, Jun Yin, Xiaofei Liu, Hongrong Wu, Jidong Li, Xuemei Li, and Wanlin Guo. Probing van der Waals interactions at two-dimensional heterointerfaces. *Nature Nanotechnology*, 14(6):567–572, 6 2019.

[240] J M Martin, C Donnet, T Lemogne, and T Epicier. Superlubricity of Molybdenum-Disulfide. *Physical Review B*, 48(14):10583–10586, 1993.

[241] D. Berman, S. A. Deshmukh, S. K. R. S. Sankaranarayanan, Ali Erdemir, and Anirudha V. Sumant. Macroscale superlubricity enabled by graphene nanoscroll formation. *Science*, 348(6239):1118–1121, 2015.

[242] Dirk Dietzel, Michael Feldmann, Udo D Schwarz, Harald Fuchs, and André Schirmeisen. Scaling laws of structural lubricity. *Physical Review Letters*, 111(23):235502, 12 2013.

[243] A. S. De Wijn. (In)commensurability, scaling, and multiplicity of friction in nanocrystals and application to gold nanocrystals on graphite. *Physical Review B - Condensed Matter and Materials Physics*, 86(8):1–11, 2012.

[244] Martin H. Müser, Ludgar Wenning, and Mark O Robbins. Simple Microscopic Theory of Amontons's Laws for Static Friction. *Physical Review Letters*, 86(7):1295–1298, 2 2001.

[245] Matthew Yankowitz, Jiamin Xue, Daniel Cormode, Javier D Sanchez-Yamagishi, K Watanabe, T Taniguchi, Pablo Jarillo-Herrero, Philippe Jacquod, and Brian J LeRoy. Emergence of superlattice Dirac points in graphene on hexagonal boron nitride. *Nature Physics*, 8(5):382–386, 5 2012.

[246] Eryin Wang, Xiaobo Lu, Shijie Ding, Wei Yao, Mingzhe Yan, Guoliang Wan, Ke Deng, Shuopei Wang, Guorui Chen, Liguo Ma, Jeil Jung, Alexei V Fedorov, Yuanbo Zhang,

Guangyu Zhang, and Shuyun Zhou. Gaps induced by inversion symmetry breaking and second-generation Dirac cones in graphene/hexagonal boron nitride. *Nature Physics*, 12(12):1111–1115, 12 2016.

[247] Dan Cao, Tao Shen, Pei Liang, Xiaoshuang Chen, and Haibo Shu. Role of chemical potential in flake shape and edge properties of monolayer MoS2. *Journal of Physical Chemistry C*, 119(8):4294–4301, 2015.

[248] Linfeng Wang, Xiang Zhou, Tianbao Ma, Dameng Liu, Lei Gao, Xin Li, Jun Zhang, Yuanzhong Hu, Hui Wang, Yadong Dai, and Jianbin Luo. Superlubricity of a graphene/MoS2 heterostructure: A combined experimental and DFT study. *Nanoscale*, 9(30):10846–10853, 2017.

[249] S. Yu Krylov, K. B. Jinesh, H. Valk, M. Dienwiebel, and J. W.M. M Frenken. Thermally induced suppression of friction at the atomic scale. *Physical Review E - Statistical, Nonlinear, and Soft Matter Physics*, 71(6):1–4, 2005.

[250] C Mathew Mate, Gary M McClelland, Ragnar Erlandsson, and Shirley Chiang. Atomic-scale friction of a tungsten tip on a graphite surface. *Physical Review Letters*, 59(17):1942–1945, 1987.

[251] S Fujisawa, Y Sugawara, S Ito, S Mishima, T Okada, and S Morita. The two-dimensional stick-slip phenomenon with atomic resolution. *Nanotechnology*, 4(3):138–142, 7 1993.

[252] André Andrá André Schirmeisen, Lars Jansen, Hendrik Hölscher, and Harald Fuchs. Temperature dependence of point contact friction on silicon. *Applied Physics Letters*, 88(12):123108, 3 2006.

[253] Lars Jansen, Hendrik Hölscher, Harald Fuchs, and André Schirmeisen. Temperature dependence of atomic-scale stick-slip friction. *Physical Review Letters*, 104(25):1–4, 6 2010.

[254] Tania Tĝnia Tomé and Mário J. De Oliveira. Entropy production in nonequilibrium systems at stationary states. *Physical Review Letters*, 108(2):1–5, 2012.

[255] A. Vanossi, N. Manini, and E. Tosatti. Static and dynamic friction in sliding colloidal monolayers. *Proceedings of the National Academy of Sciences*, 109(41):16429–16433, 2012.

[256] Itay Barel, Michael Urbakh, Lars Jansen, and André Schirmeisen. Temperature dependence of friction at the nanoscale: When the unexpected turns normal. *Tribology Letters*, 39(3):311–319, 2010.

[257] Alexandre Tkatchenko and Matthias Scheffler. Accurate Molecular Van Der Waals Interactions from Ground-State Electron Density and Free-Atom Reference Data. *Physical Review Letters*, 102(7):073005, 2 2009.

[258] Yanmin Liu, Aisheng Song, Zhi Xu, Ruilong Zong, Jie Zhang, Wenyan Yang, Rong Wang, Yuanzhong Hu, Jianbin Luo, and Tianbao Ma. Interlayer friction and superlubricity in single-crystalline contact enabled by two-dimensional flake-wrapped atomic force microscope tips. *ACS Nano*, 12(8):7638–7646, 2018.

[259] Yang Gao, Suenne Kim, Si Zhou, Hsiang Chih Chiu, Daniel Nélias, Claire Berger, Walt De Heer, Laura Polloni, Roman Sordan, Angelo Bongiorno, and Elisa Riedo. Elastic coupling between layers in two-dimensional materials. *Nature Materials*, 14(7):714–720, 2015.

[260] Tevis D. B. Jacobs, C. Mathew Mate, Kevin T. Turner, and Robert W. Carpick. Understanding the Tip-Sample Contact. In *Scanning Probe Microscopy in Industrial Applications*, number June 2016, pages 15–48. John Wiley & Sons, Inc, Hoboken, NJ, 11 2013.

[261] E. Gnecco, R. Bennewitz, T. Gyalog, and E. Meyer. Friction experiments on the nanometre scale. *Journal of Physics Condensed Matter*, 13(31), 2001.

[262] K. L. Johnson. Normal contact of elastic solids – Hertz theory. *Contact Mechanics*, pages 84–106, 2013.

[263] Weinan E, Weiqing Ren, and Eric Vanden-Eijnden. Simplified and improved string method for computing the minimum energy paths in barrier-crossing events. *The Journal of Chemical Physics*, 126(16):164103, 4 2007.

[264] Pauli Virtanen, Ralf Gommers, Travis E Oliphant, Matt Haberland, Tyler Reddy, David Cournapeau, Evgeni Burovski, Pearu Peterson, Warren Weckesser, Jonathan Bright, Stéfan J van der Walt, Matthew Brett, Joshua Wilson, K Jarrod Millman, Nikolay Mayorov, Andrew R J Nelson, Eric Jones, Robert Kern, Eric Larson, C J Carey, İlhan Polat, Yu Feng, Eric W Moore, Jake VanderPlas, Denis Laxalde, Josef Perktold, Robert Cimrman, Ian Henriksen, E A Quintero, Charles R Harris, Anne M Archibald, Antônio H Ribeiro, Fabian Pedregosa, and Paul van Mulbregt. SciPy 1.0: fundamental algorithms for scientific computing in Python. *Nature Methods*, 17(3):261–272, 3 2020.

[265] C. Van Den Broeck and M. Esposito. Ensemble and trajectory thermodynamics: A brief introduction. *Physica A: Statistical Mechanics and its Applications*, 418:6–16, 2015.

[266] Tânia Tomé and Mário J. De Oliveira. Stochastic approach to equilibrium and nonequilibrium thermodynamics. *Physical Review E - Statistical, Nonlinear, and Soft Matter Physics*, 91(4):042140, 4 2015.

[267] Nolan C Harris, Yang Song, and Ching-Hwa Kiang. Experimental Free Energy Surface Reconstruction from Single-Molecule Force Spectroscopy using Jarzynski's Equality. *Physical Review Letters*, 99(6):68101, 2007.

[268] Jan Liphardt. Equilibrium Information from in an Experimental Test of Jarzynski ' s Equality. *Science*, 1832(2002):1832–1835, 2007.

[269] Elizabeth A Shank, Ciro Cecconi, Jesse W Dill, Susan Marqusee, and Carlos Bustamante. The folding cooperativity of a protein is controlled by its chain topology. *Nature*, 465(7298):637–640, 2010.

[270] I A Martínez, É. Roldán, L Dinis, D Petrov, J M R Parrondo, and R A Rica. Brownian Carnot engine. *Nature Physics*, 12(1):67–70, 1 2016.

[271] Shoichi Toyabe, Takahiro Sagawa, Masahito Ueda, Eiro Muneyuki, and Masaki Sano. Experimental demonstration of information-to-energy conversion and validation of the generalized Jarzynski equality. *Nature Physics*, 6(12):988–992, 2010.

[272] V Blickle, T Speck, L Helden, U Seifert, and C Bechinger. Thermodynamics of a colloidal particle in a time-dependent nonharmonic potential. *Physical Review Letters*, 96(7):24–27, 2006.

[273] J R Gomez-Solano, L Bellon, A Petrosyan, and S Ciliberto. Steady-state fluctuation relations for systems driven by an external random force. *Epl*, 89(6):0–6, 2010.

[274] Franco Pellegrini, Emanuele Panizon, Giuseppe E. Santoro, and Erio Tosatti. Thermally assisted lubricity and negative work tails in sliding friction. *Physical Review B*, 99(7):75428, 2 2019.

[275] Ken Sekimoto. Langevin Equation and Thermodynamics. *Progress of Theoretical Physics Supplement*, (130):17–27, 1998.

[276] U Seifert and T Speck. Fluctuation-dissipation theorem in nonequilibrium steady states. *Epl*, 89, 2010.

[277] Ilya Prigogine. Introduction to thermodynamics of irreversible processes. *itti*, 1967.

[278] Gavin E Crooks. Nonequilibrium Measurements of Free Energy Differences for Microscopically Reversible Markovian Systems. *Journal of Statistical Physics*, 90(5/6):1481–1487, 1998.

[279] J Schnakenberg. Network theory of microscopic and macroscopic behavior of master equation systems. *Reviews of Modern Physics*, 48(4):571–585, 1976.

[280] Anisoara Socoliuc, Enrico Gnecco, Sabine Maier, Oliver Pfeiffer, Alexis Baratoff, Roland Bennewitz, and Ernst Meyer. Nanometer-Sized Contacts. *Science*, 313:207–211, 2006.

[281] Yalin Dong, Ajay Vadakkepatt, and Ashlie Martini. Analytical Models for Atomic Friction. *Tribology Letters*, 44(3):367–386, 12 2011.

[282] Giacomo Levita, Elisa Molinari, Tomas Polcar, and Maria Clelia Righi. First-principles comparative study on the interlayer adhesion and shear strength of transition-metal dichalcogenides and graphene. *Physical Review B - Condensed Matter and Materials Physics*, 92(8):1–8, 2015.

[283] Y. Baskin and L. Meyer. Lattice constants of graphite at low temperatures. *Physical Review*, 100(2):544, 1955.

[284] Peter Trucano and Ruey Chen. Structure of graphite by neutron diffraction. *Nature*, 258(5531):136–137, 11 1975.

[285] N. Wakabayashi, H. G. Smith, and R. M. Nicklow. Lattice dynamics of hexagonal MoS2 studied by neutron scattering. *Physical Review B*, 12(2):659–663, 1975.

[286] M. A. Py and R. R. Haering. Structural destabilization induced by lithium intercalation in MoS 2 and related compounds. *Canadian Journal of Physics*, 61(1):76–84, 1 1983.

[287] J. A. Nelder and R. Mead. A Simplex Method for Function Minimization. *The Computer Journal*, 7(4):308–313, 1965.

[288] Travis E Oliphant. SciPy: Open source scientific tools for Python, 2007.

[289] Abel Carreras. phonoLAMMPS, 2019.

[290] T. Björkman, A Gulans, A V Krasheninnikov, and R M Nieminen. Van der Waals bonding in layered compounds from advanced density-functional first-principles calculations. *Physical Review Letters*, 108(23):235502, 6 2012.

[291] Wenqing Li, Christian F.J. Walther, Agnieszka Kuc, and Thomas Heine. Density functional theory and beyond for band-gap screening: Performance for transition-metal oxides and dichalcogenides. *Journal of Chemical Theory and Computation*, 9(7):2950–2958, 2013.

[292] Kapildeb Dolui and Stefano Sanvito. Dimensionality-driven phonon softening and incipient charge density wave instability in TiS2. *EPL*, 115(4):47001, 8 2016.

[293] Rui-Zhi Zhang, Chun-Lei Wan, Yi-Feng Wang, and Kunihito Koumoto. Titanium sulphene: two-dimensional confinement of electrons and phonons giving rise to improved thermoelectric performance. *Physical Chemistry Chemical Physics*, 14(45):15641, 2012.

[294] K Parlinski, Z Q Li, and Y Kawazoe. First-principles determination of the soft mode in cubic ZrO2. *Physical Review Letters*, 78(21):4063–4066, 5 1997.

[295] A. Molina-Sánchez and L. Wirtz. Phonons in single-layer and few-layer MoS2 and WS2. *Physical Review B - Condensed Matter and Materials Physics*, 84(15):1–8, 2011.

[296] D S Inosov, V B Zabolotnyy, D V Evtushinsky, A A Kordyuk, B Büchner, R Follath, H Berger, and S V Borisenko. Fermi surface nesting in several transition metal dichalcogenides. *New Journal of Physics*, 10(12):125027, 12 2008.